Title
Exploring the Dysregulation of Iron Metabolism in Cancer: Leveraging Fenton Chemistry for Selective Drug Delivery

Author
Spangler, Benjamin

Publication Date
2015

Peer reviewed|Thesis/dissertation

Exploring the Dysregulation of Iron Metabolism in Cancer: Leveraging Fenton Chemistry for Selective Drug Delivery

by

Benjamin Spangler

DISSERTATION

Submitted in partial satisfaction of the requirements for the degree of

DOCTOR OF PHILOSOPHY

in

Chemistry and Chemical Biology

in the

GRADUATE DIVISION

Dedications and Acknowledgements

I would like to thank everyone who has helped me make it to this point. It is a long list. From my parents who raised me to always ask questions, strive for knowledge, and work hard for the things I cared about, to all those who have taught me along my academic progression; I am here because of you. So thank you, for taking the time to help me learn and grow.

Special thanks are due to the following people for helping me along my way in this project:

- Dr. Adam Renslo and Dr. James Wells: for being excellent P.I.'s and steering me towards success in so many ways.
- Dr. Michelle Arkin and Dr. Martin McMahon for their excellent input and advice as members of my thesis committee.
- Dr. Shaun Fontaine: for sharing intermediates, many useful discussions of chemistry, and being an all-around great guy.
- Dr. Charles Morgan: for many useful discussions and contributing towards the cell culture work presented in Chapter 2 by assisting in the development of the high-throughput immunofluorescence assay, help with qRT-PCR, and preforming knock-downs and over-expressions for studies of the reactive iron pool.
- Dr. Byron Hann and the preclinical therapeutics core at UCSF: for their assistance planning and executing all of the mouse studies presented here.

- Dr. Samantha Zeitlin: for helping me remember how to do cell culture when I started.
- Mr. Steven Chen: for assistance with automated imaging and image analysis
- Dr. Yihui Shi: for preforming the toxicity experiments across a panel of the NCI 60 cell lines presented in Chapter 3.
- Dr. Tetsuya Matsuguchi for assistance with qRT-PCR experiments.
- Dr. Alan Wolfe for the calculation of pharmacokinetic parameters.

Aspects of Chapter 2 were adapted from a manuscript currently under review with Nature Chemical Biology: Spangler, B. et al., A reactivity-based probe of the intracellular labile ferrous iron pool. Manuscript submitted for publication. (2015).

Aspects of Chapter 3 were adapted from a manuscript in preparation. Spangler, B. et al., Leveraging the reactive iron pool for selective drug delivery in cancer. Manuscript in preparation. (2015).

The work presented in Chapter 4 was done in collaboration with Sutro Biopharma (Toni Kline, Xiaofan Li, Jeff Hanson, Sihong Zhou, Krishna Bajjuri, Gang Yin, Alexander Steiner, and Aaron Sato) which provided materials for chemistry and preformed all antibody conjugations and cell culture experiments.

This manuscript is dedicated to my amazing fiancée Naomi Yonis who has somehow managed to handle the stresses of these last few months while taking care of me as I have floundered my way through completing a PhD. I could not have done it without you.

Exploring the Dysregulation of Iron Metabolism in Cancer: Leveraging Fenton Chemistry for Selective Drug Delivery

Benjamin Spangler

Abstract

Most cancer chemotherapeutics are administered at or near their maximum tolerated dose, yet poor efficacy and insufficient therapeutic index remain major causes of attrition in oncology drug development. New pharmacological approaches that selectively target tumor cells are therefore of significant interest. Emerging evidence suggests that an augmented pool of intracellular labile Fe(II) is a metabolic signature of many cancers and thus may represent a targetable chemical environment. We have leveraged Fe(II)-dependent, Fenton-type reactivity of the 1,2,4-trioxolane ring to develop highly selective, reactivity-based probes of the ferrous iron pool and a prototypical scaffold for Fe(II)-dependent drug delivery of chemotherapeutics. These probes reveal higher reactive Fe(II)-pools in cancer cells as compared to non-tumorigenic cells, changes that can be linked to alteration of iron metabolism. Our findings suggest that many cancers alter iron metabolism to increase intracellular Fe(II)-pools and these changes can be exploited for cell-

selective drug delivery. By using this scaffold to mask a highly potent DNA-alkylator we illustrate that this prodrug system is capable of stabilizing and selectively delivering such potent cytotoxins *in vivo*. Overall our results establish that Fe(II)-dependent prodrug/delivery strategies can be used to enhance the therapeutic index of cancer chemotherapeutics. Encouraged by these results further efforts were made to apply trioxolane-based systems as novel, tumor-selective cleavable linkers for antibody-drug conjugate strategies. Preliminary results indicate trioxolane-based linkers are capable of efficiently releasing drugs from ADC's in cancer cells but optimization will be required before further development.

Short-hand and abbreviations used in this text:

ADC: antibody-drug conjugate
BCN: bicyclo[6.1.0]nonyne
BME: β-mercaptoethanol
Bpy: bipyridy
CBI: cyclopropylbenzindoline
CMB: combretastatin
CTG: CellTiter-Glo®
DBCO: Dibenzocyclooctyl
DCM: dichloromethane
DFO: desferrioxamine
DMS: dimethylsulfide
FAC: ferric ammonium citrate
FAS: ferrous ammonium sulfate
GSH: glutathione
hTf: holo-transferrin
IRE: iron responsive element
MMAE/F: Monomethyl auristatin E/F
MOA: mechanism of action
NAC: N-acetyl cysteine
PK: pharmacokinetics
Puro: puromycin
ROS: reactive oxygen species
TAP: tumor-activated prodrug
TEA: trimethylamine
TPP: triphenylphosphine
Trx: 1,2,4-trioxolane
UTR: untranslated region

Table of Contents

Dedications and Acknowledgements iii
Abstract v
Short-hand and abbreviations used in this text: vii
Table of Contents viii
List of Figures, Schemes, and Tables x
Chapter 1: Iron Metabolism and Cancer 1
Regulation of iron metabolism in mammalian cells 1
Dysregulation of iron metabolism in cancer cells 5
Currently available tools to study the labile iron pool 7
Chapter 2: Development of trioxolane-derived reactivity-based probes of the reactive iron(II) pool. 11
Sterically hindered endoperoxides 11
Synthesis of a trioxolane-based probe for intracellular reactive Fe(II) 21
Validation of trioxolane-conjugates as reactivity-based probes of the intracellular labile Fe(II) pool 25
Profiling cell-type specific changes the labile pool of ferrous iron 31
Understanding the consequences of iron-metabolism dysregulation on the presence of intracellular reactive Fe(II)-species: 34
Genetic Alterations to the Labile Fe(II) pool 35
In vivo applications of trioxolane-derived, reactivity-based probes of the labile Fe(II) pool in a PC-3 tumor xenograft model 39
Discussion 41
Chapter 3: Leveraging the dysregulation of iron-metabolism in cancer as a trigger for selective drug delivery 44
Selective drug release strategies in cancer 45
Trioxolane-mediated delivery of cytotoxic agents to cancer cells 49
Profiling the effects of oncogenic transformation on iron metabolism and sensitivity to trioxolane-conjugates 52
Development of trioxolane-conjugates of highly potent DNA alkylators 54
Pharmacokinetics and safety of trioxolane-drug conjugates 57

Studying the fate of the cyclohexenone byproduct 60
Efficacy of trioxolane-drug conjugates in xenograft models 62
Discussion 65
Chapter 4: Development of trioxolane-based tumor-selective cleavable linkers for antibody drug conjugates 69
Active targeting TAP approaches: 69
Synthesis of trioxolane-based ADC linkers 72
Initial cell culture experiments with trioxolane-linked ADCs 78
Returning to DBCO-mediated ADC conjugation strategies 81
Development of trioxolane-linked ADCs bearing MMAE drug payloads 83
Discussion 87
Chapter 5: Conclusions and future directions 91
Methods and Materials 95
General Procedures and Materials 95
Reagents: 96
In vitro Assays: 97
Cell Culture Assays: 98
In vivo Assays: 103
Synthesis: 106
Supplementary Data: 161
Supplemental Figures: 161
Schemes: 172
Tables: 175
References: 179

List of Figures, Schemes, and Tables

Figure 1: Scheme of iron metabolism pathways in normal cells..... 3

Figure 2: Scheme of iron metabolism dysregulation in cancer cells 7

Figure 3: Sterically hindered endoperoxides used as malaria chemotherapeutics... 13

Figure 4: Influence of sterics on Fe(II) reactivity of 1,2,4-trioxolanes 18

Figure 5: Mechanism of Fe(II)-dependent payload delivery from trioxolane-based conjugates. 20

Figure 6: A turn-on fluorescent probe reveals selective Fe(II)-reactivity of hindered 1,2,4-trioxolanes. 22

Figure 7: Trioxolane-conjugates of puromycin can be used as peroxide dependent cellular probes of Fe(II)..... 24

Figure 8: Reactivity-based probe 3 is a highly selective and sensitive tool for reporting on Fe(II) in cells. 28

Figure 9: Comparing reactive Fe(II) pools across cell lines. 33

Figure 10: Genetic manipulation of the reactive iron pool. 37

Figure 11: *In vivo* comparisons of the reactive Fe(II) pool across tissues..... 40

Figure 12: Trioxolane-mediated drug delivery strategies in cancer. 45

Figure 13: Exploiting augmented reactive iron pools for selective drug delivery..... 51

Figure 14: Profiling the effects of oncogenic transformation on the Fe(II) pool of MCF10A cells. 54

Figure 15: Synthesis and in vitro characterization of amino-CBI conjugates. 57

Figure 16: Pharmacokinetics and tolerability of amino-CBI conjugates in non-tumor bearing NSG mice. 60

Figure 17: Clearance of glutathione adducts of the produced cylcohexenone in mice 62

Figure 18: Efficacy of amino-CBI conjugates in mouse xenograft models..... 64

Figure 19: Synthesis of DBCO-bearing trioxolane-CBI conjugates 74

Figure 20: Alternative routes to DBCO-bearing trioxolane-CBI conjugates 75

Figure 21: Synthesis of BCN-bearing trioxolane-drug conjugates..... 77

Table 1: Efficiency of antibody conjugation with trioxolane linker 22 and comparators under various conditions..... 78

Table 2: Cell toxicity for ADC conjugates derived from 22 80
Figure 22: Synthesis of DBCO-bearing trioxolane-conjugates of 5 and control compounds 82
Figure 23: Synthesis of DBCO-Trx-MMAE conjugates 84
Table 3: Antibody conjugation with 28 and comparators under various conditions 85
Table 4: Cell Toxicity for trioxolane-linked ADCs bearing MMAE drug payloads 86
Supplementary Figure 1: Fluorescence intensity over time and rates of fluorescence increase from 1 treated with metal ions and redox active compounds. 161
Supplementary Figure 2: Plasma and media stability of Trx-puro conjugate 3..... 162
Supplementary Figure 3: Representative images of Fe(II)-conditioning dose responses. 163
Supplementary Figure 4: Fe(II)-conditioning with FAS and DFO. 164
Supplementary Figure 5: Selectivity of Trx-puro probe 3 for reporting on Fe(II) in cells 165
Supplementary Figure 6: Effects of hepcidin treatment on Fe(II) levels. 166
Supplementary Figure 7: Baseline-corrected puro incorporation for cell lines treated with 2 or 3 167
Supplementary Figure 8: qRT-PCR panels for iron regulator proteins across cells 168
Supplementary Figure 9: Oncogenic perturbation of iron metabolism protein expression 169
Supplementary Figure 10: Stability of amino-CBI analogs 9, 10, and 11 170
Supplementary Figure 11: Efficacy of amino-CBI analogs 9, 10, and 11 in xenograft models 171
Supplementary Scheme 1: Synthesis of trioxolane-based FRET probe 1 172
Supplementary Scheme 2: Synthesis of puromycin conjugates 3 and 4. 173
Supplemental Scheme 3: Synthesis of microtubule inhibitor conjugates 2 and 3.... 174
Supplementary Table 1: Intrinsic permeability of puromycin and trioxolane-conjugate 3 175
Supplementary Table 2: Toxicity of 6 and 7 across cell lines 176
Supplementary Table 3: Expanded toxicity panel of trioxolane-conjugate 7 177
Supplementary Table 4: Pharmacokinetic parameters of compounds of 9 and 10. 178

Chapter 1: Iron Metabolism and Cancer

Iron plays a key role in biology as a nutrient required for cell growth and maintenance. Organisms from bacteria to humans all utilize the reduction potential of ferrous iron to enable a wide variety of enzymatic processes. Unharnessed however, the reactivity of ferrous iron can promote the formation of reactive oxygen species (ROS) that are toxic to cells. The processes involved in controlling the presence iron in organisms are thus highly regulated. The dysregulation of these processes has been implicated in a wide variety of disease states; therefore the study of iron in biological systems is of substantial importance to human health.

Iron metabolism and its regulation in mammalian cells under normal and disease states has been previously reviewed in detail[1–5]. For the purposes of this dissertation, a brief summary of the pathways of iron metabolism in mammalian cells and how they are altered in cancers is provided below.

Regulation of iron metabolism in mammalian cells

Iron is transported in the blood stream in the ferric (Fe^{III}) state and bound to transferrin (holotransferrin). Cells which require iron express the transferrin receptor (TfR) and upon binding of holotransferrin the complex is endocytosed. Acidification of the endosome leads to release of Fe(III) from transferrin and reduction of the liberated Fe(III) to ferrous iron (Fe^{II}) by ferrireductases such as STEAP3. Once in the ferrous form, Fe(II) can be transported into the cytosol via the divalent metal ion transporter (DMT-1).

Cells can also import iron through the less well understood lipocalin-2 (LCN-2) pathway. This pathway utilizes mammalian siderophores that chelate free iron. After chelation, the siderophores are then bound by LCN-2. Recognition of the complex at the lipocalin-2 receptor (LCN2R) then allows for internalization and release of iron into the cell. There is further evidence to suggest that small-molecule chelates of iron can be imported into cells under some circumstances based on cell culture studies using iron complexes such as ferric ammonium citrate (FAC)[2]. These mechanisms are likely to be relevant mainly in iron-overload diseases however as the levels of non-protein bound iron in the blood stream are considered to be vanishingly small under normal physiological conditions[5].

Once imported, Fe(II) contributes to what is commonly termed the labile iron pool, which is experimentally defined as the pool of "chelatable" cytosolic iron. From there it is transported, through largely uncharacterized processes, to the mitochondria for Fe-S cluster biosynthesis and heme generation. Fe-S clusters are a required co-factor in more than 200 identified enzymes and proteins[6]. These co-factors are essential for a wide variety of enzymatic functions required to maintain cellular homeostasis and promote cell growth including de novo nucleotide synthesis, cell cycle regulation, maintenance of genomic stability, and respiratory function in the mitochondria[6–8]. Redox cycling between ferrous and ferric iron is exploited in these enzymes to complete their catalytic cycles[7]. However, ferrous iron in its unbound and unregulated form, promotes the disproportionation of hydrogen peroxide (Fenton reaction) to produce hydroxyl and hydroperoxyl radicals - reactive oxygen species (ROS) that confer cellular damage and can lead to

apoptosis[4,9–11]. Accordingly, iron homeostasis is rigorously regulated to ensure that cells have access to sufficient labile iron to support essential enzyme function, while limiting exposure to ferritoxic species[1–3]. Under normal physiological conditions Fe(II) that is not incorporated into enzymes is thus rapidly oxidized and exported via the iron exporter ferroportin or oxidized and stored as Fe(III) in the iron storage protein ferritin.

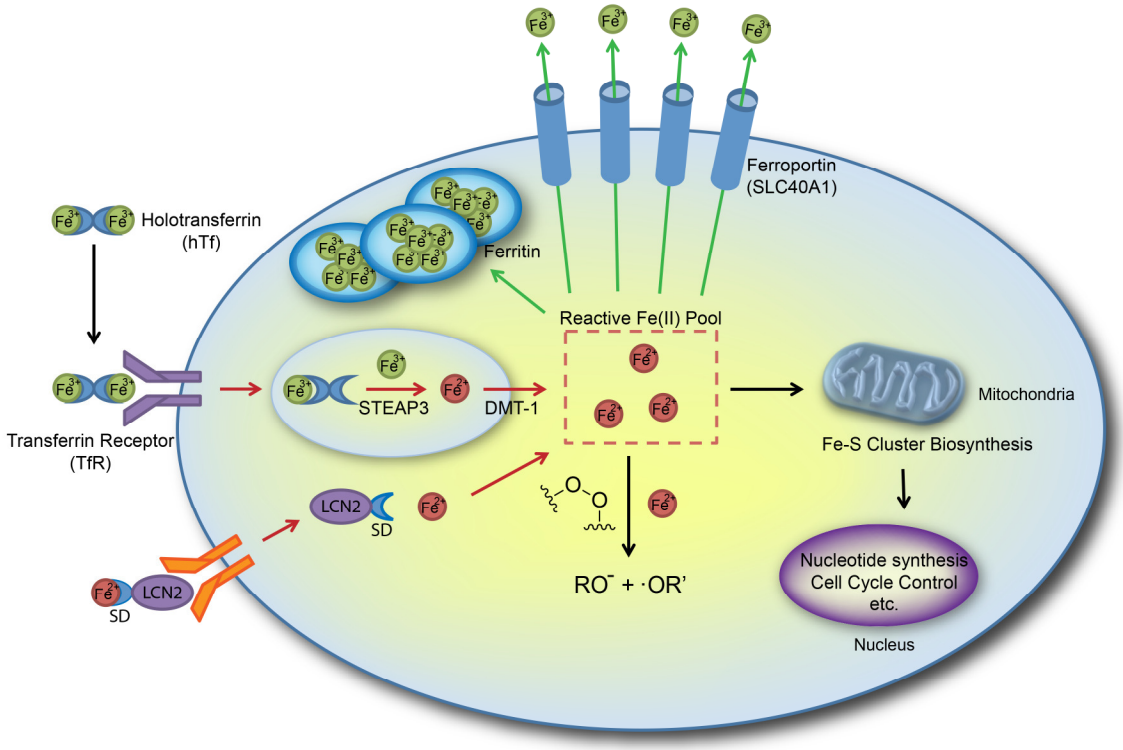

Figure 1: Scheme of iron metabolism pathways in normal cells
Iron import, storage, and export are key determinants of the reactive Fe(II) pool in cells. Prevalent aspects of each pathway are illustrated here with ferric iron shown in green and ferrous iron shown in red. Pathways that act to increase ferrous iron species are highlighted with red arrows while pathways responsible for removing or sequestering iron are shown in green. Lipocalin 2 is abbreviated as LCN2 and SD stands for any small molecule siderophore substrate of LCN2.

The processes of iron import, export, and storage are all actively regulated at the post-transcriptional level via the iron sensing proteins IRP1 (Aco1) and IRP2[3]. The mRNAs encoding for TfR, DMT1, ferroportin, and ferritin all contain iron responsive elements (IREs) in their 3' or 5' untranslated regions (UTRs). Under low iron conditions these IRE's are recognized by IRP1 or IRP2 with high affinity ($K_d \sim 10^{-12}$ M) and binding results in stabilization of mRNA encoding TfR and DMT1 and translational inhibition of ferritin and ferroportin mRNA, effectively increasing iron import while decreasing iron storage and export to provide more available iron for the cell. Under high iron conditions IRP2 is degraded while IRP1 binds iron and gains activity as a cytosolic aconitase, in turn losing function as an iron regulatory protein. This loss of IRP activity serves to reduce iron import while increasing iron storage and export to protect the cell from excess reactive Fe(II) species.

Consistent with the importance of iron metabolism in cellular processes, knockout of both IRP1 and IRP2 in mice results in embryonic lethality while tissue specific knockouts result in profound growth defects and death within 4 weeks of birth[1]. Single IRP1$^{-/-}$ mice however, show no obvious phenotype, while IRP2$^{-/-}$ mice display signs of aberrant iron homeostasis yet remain viable[3]. These results suggest that the two proteins have a degree of functional redundancy *in vivo* yet play differential roles in iron metabolism. IRP2 appears to be the primary regulator under normal conditions while IRP1 serves mainly as c-aconitase, perhaps only actively regulating iron metabolism under conditions of iron overload or the loss of IRP2 activity[3].

Dysregulation of iron metabolism in cancer cells

Rapidly proliferating cancer cells have increased requirements for DNA synthesis, repair, and mitochondrial respiration, thus necessitating an augmented labile iron pool. Accordingly, iron metabolism pathways have been shown to be substantially dysregulated in many cancers[8]. Analysis of 61 genes with functions related to iron metabolism in tissue samples from cancer patients revealed nearly half of the genes (49%) were significantly associated with distant metastasis-free survival, supporting the important role iron metabolism plays in tumor growth and metastasis[12]. From this study two gene dyads stood out as particularly important in patient outcomes: those involved in transferrin-mediated iron uptake and those involved in iron export via ferroportin.

The transferrin Receptor (TfR) is highly expressed in many cancers from diverse origins[13–15], suggesting increased iron import is a characteristic of many cancers. Consistent with these observations, multiple components of the transferrin receptor iron import pathway have been observed to be up-regulated in cancers, including members of the STEAP family of metalloreductases, and the divalent metal ion transporter (DMT1)[16,17]. Expression of LCN2 has also been observed to be up-regulated in a number of cancers, indicating increased iron import is not limited to the canonical pathways[18].

Down-regulation of iron export via ferroportin is another means by which cancer cells can increase their labile iron pools. Human breast cancer cell lines and tissue samples have been shown to have decreased levels of ferroportin expression

compared to normal breast tissue[19]. Downregulation of iron export was associated with larger labile iron pools in cells and increased tumorigenicity in xenograft models[19]. Even more compellingly, expression levels of ferroportin in breast cancer patient tissue samples were found to significantly correlate with disease-specific and metastasis-free survival in these studies. Patients expressing higher levels of ferroportin had better clinical outcomes, suggesting that reduced availability of intracellular iron may limit the ability of tumors to grow aggressively and metastasize[19].

Prevalent oncogenes like Myc have also been associated with changes in iron homeostasis that increase the labile iron pool. Induced expression of c-Myc in cells has been shown to substantially reduce ferritin expression and increase TfR and DMT1 expression, yielding a net increase in labile iron[17,20]. These changes appeared to be driven at least in part by increased expression of IRP2, suggesting that Myc expression may drive an increase in the available iron pool in cells by affecting the iron regulatory proteins that control iron metabolism. This may be a key promoter of tumorigenesis as IRP2 overexpression has been shown to promote tumor growth *in vivo*[21].

It is thus clear that iron plays a significant role in tumorigenesis and disease progression in cancer. Cancer cells have been consistently observed to alter their pathways of iron metabolism in ways that are predicted to augment the available iron in the cell to enable the rapid growth characteristic of cancer (**Fig. 2**).

Correlating these changes to the relative abundance of reactive Fe(II) species in cells has been challenging however, due to a paucity of valuable cellular probes of Fe(II).

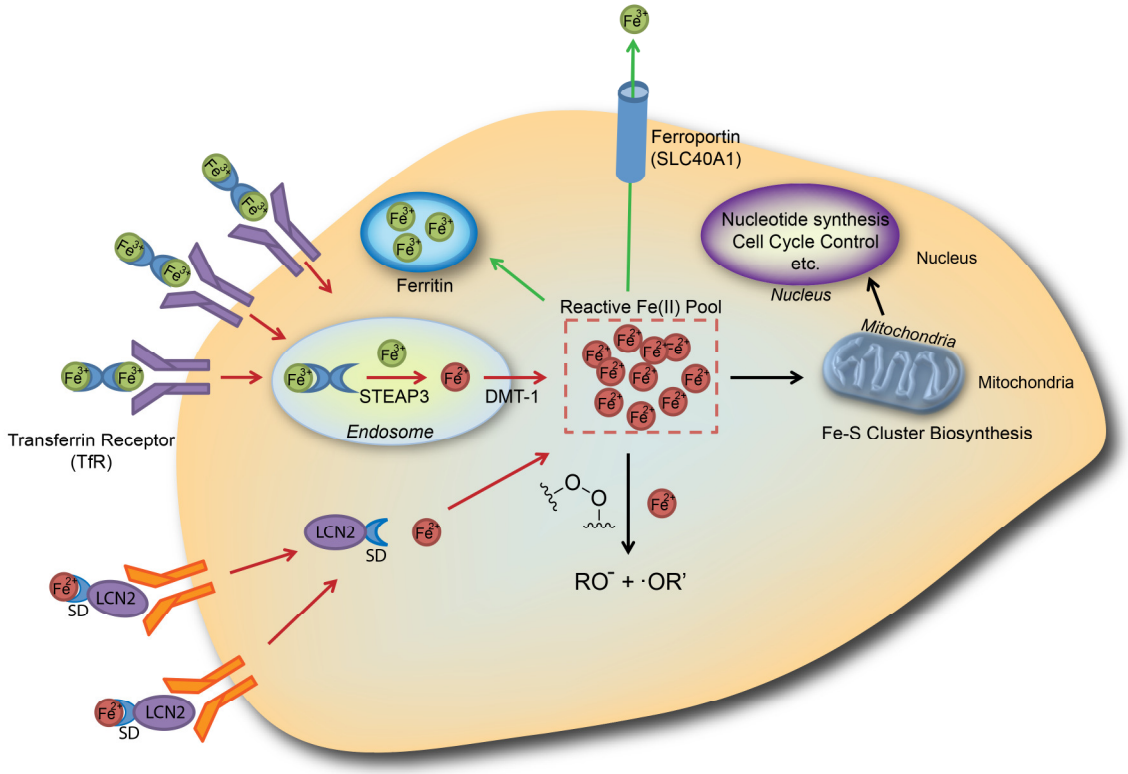

Figure 2: Scheme of iron metabolism dysregulation in cancer cells
Iron import, storage, and export have all been shown to be dysregulated in various ways in cancer cells. It is thought that this dysregulation may lead to an increased pool of reactive, labile Fe(II) species. Prevalent aspects of each pathway are illustrated here as compared in normal cells depicted in Figure 1. Ferric iron is shown in green balls and ferrous iron shown in red. Pathways that act to increase ferrous iron species are highlighted with red arrows while pathways responsible for removing or sequestering iron are shown in green. Lipocalin 2 is abbreviated as LCN2 and SD stands for any small molecule siderophore substrate of LCN2.

Currently available tools to study the labile iron pool

Due to the crucial role iron plays in both normal and disease state physiologies several attempts have been made to build selective tools to study the labile iron pool

in cells. Early efforts to study the labile iron pool utilized cell fractionation followed by a variety of detection strategies (EPR, radiolabeling, etc.)[22]. These studies required disruption of the cell membrane which can lead to de-compartmentalization. This approach thus results in substantial perturbation to the components of the labile iron pool and thus raises significant questions about the validity of results from these studies[22].

Later efforts combined iron chelation with fluorescent moieties to yield probes wherein binding of iron leads to quenching of fluorescence. Examples include PhenGreen SK and Calcein AM which have been used to non-invasively study the pool of chelatable iron in live cells[22–27]. While such reagents are not intrinsically selective for binding iron, their fluorescence is partially quenched upon binding either ferric or ferrous iron. Subsequent sequestration of the bound iron with a (non-fluorescent) iron chelator such as 2,2'-bipyridyl (Bpy) or desferrioxamine (DFO) is then used to infer labile iron concentrations based on the extent of de-quenching, and reference to some *in situ* or *ex situ* fluorescence calibration standard. The significant challenges and caveats associated with these existing tools and approaches have been comprehensively reviewed[22,26,28]. The probes and chelators are generally used at μM concentrations which can cause cytotoxicity over longer periods of exposure making them poorly suited to longer term observations. Furthermore, the application of high concentrations of iron chelators such as DFO can represent a substantial perturbation to the very system studied and has been shown in some cases to extract iron from protein complexes such as ferritin[29]. The chelation moieties used also tend to rely on siderophores which bind Fe(III)

preferentially thus making their application to study the presence of Fe(II) species indirect at best.

More recently several groups have sought to leverage the reductive potential of Fe(II) to make reactivity-based cellular probes. This strategy is appealing for several reasons. Unlike chelation based approaches, application of the probes would not need to sequester the iron pool to report on it. Furthermore, as Fe(II) has the greatest redox potential of biologically relevant metal cations there is good reason to believe that an appropriately tuned system could be highly selective for reporting on Fe(II) over Fe(III) and other metal cations in cells.

The first reported reactivity based probe of Fe(II) utilized an N-oxide form of the dye rhodamine[30]. Oxidation of rhodamine to the N-oxide significantly reduces its fluorescence, which is restored upon Fe(II) mediated reduction of the N-O bond. This system proved highly selective for reporting on Fe(II) *in vitro* and showed some utility in cell culture assays. However, in our hands, the substantial instability of the N-oxide probe limited its application.

The Chang group at UC Berkeley has more recently reported a hybrid chelation/reactivity-based probe that utilizes an iron(II)-mediated C-O bond cleavage to release a fluorescent reporter after chelation[31]. By relying on an Fe(II)-mediated reaction which occurs only after chelation to produce signal, this strategy provided good selectivity for detecting Fe(II) over Fe(III) and most other metal cations *in vitro*. The probe was also successfully applied in cell culture studies to report on intracellular changes to Fe(II) induced by treatment with exogenous iron

sources or chelators. Unfortunately, this probe showed significant cross reactivity with Co(II) (albeit at higher concentration than those likely to be relevant in cells). Furthermore, due to its reliance on chelation it is still subject to some of the same caveats as previous, less elegant and selective, chelation-based tools.

The encouraging *in vitro* selectivity observed with these recently reported reactivity-based probes of Fe(II) speaks strongly for such approaches. However, the drawbacks of both previously reported reactivity-based probes suggest that such a compound must possess finely tuned reactivity with Fe(II) to maintain good selectivity over other metal cations and sufficient stability for useful applications.

Chapter 2: Development of trioxolane-derived reactivity-based probes of the reactive iron(II) pool.

Improved methods for selectively reporting on intracellular labile iron(II) are of significant interest for studies of iron metabolism and disease relevant changes in iron homeostasis. Useful new methodologies require probes which are highly selective for reporting on labile Fe(II) over other metal ions and reductants in the complex environment of the cell. These probes also need to be sensitive enough to report on endogenous levels of labile Fe(II) while maintaining good stability in the absence of Fe(II)-species. We felt that such a probe could be developed from the well-studied endoperoxide-based class of antimalarials typified by the natural product artemisinin and structurally simplified synthetic analogs[32,33]. These compounds rely on their reactivity with Fe(II)-species to kill malarial parasites yet maintain excellent stability, even in the hot and humid climates where they are often administered[34,35].

Sterically hindered endoperoxides

Therapeutics derived from the natural product artemisinin have become indispensable tools to combat malaria, a disease that still claims more than 400,000 lives every year, primarily in the developing world[36]. While there is some amount of debate concerning the precise mechanism of action of the artemisinins[37], there is a clear consensus that Fe(II)-dependent fragmentation of its sterically hindered

endoperoxide bond is a key aspect of drug action[34,35] (**Fig. 3**). This fragmentation is thought to be caused by free heme produced in the food vacuole of the parasite as it digests hemoglobin. Fe(II) induced homolysis of the endoperoxide bond in artemisinin produces oxygen radicals which subsequently rearrange to carbon-centered radicals capable of forming toxic adducts with heme and other proteins. These radicals and adducts are thought to be responsible for much of its efficacy against parasites[38].

Inspired by the unique mechanism of action (MOA) of artemisinin and its excellent antimalarial activity, many groups have subsequently developed structurally simplified analogs which retain a sterically hindered endoperoxide moiety[9,39–48]. These compounds generally retain the excellent potency of artemisinin against malarial parasites and require the peroxide bond for activity, consistent with their Fe(II)-mediated MOA[49]. Of the synthetic endoperoxides explored for malarial applications, 1,2,4-trioxolanes (or ozonides) have arguably seen the most success with the recent approval of arterolane maleate (Synriam) in India[50] (**Fig. 3**). These compounds are easy and inexpensive to make and have been extensively studied both as intermediates in the cleavage of olefins[51] and, more recently, as drug candidates for applications in a variety of diseases including malaria[33,43], *fasciola hepatica* infections[52], schistosomiasis[53], and cancer[54].

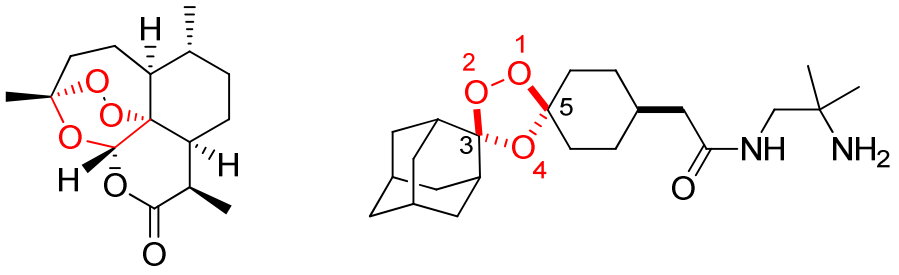

Figure 3: Sterically hindered endoperoxides used as malaria chemotherapeutics
The chemical structures of artemisinin and the structurally simplified synthetic trioxolane arterolane. The key sterically hindered endoperoxide bond of each molecule is highlighted in red.

The formation of ozonides and cyclic peroxides in general has been previously reviewed[55]. The most common means of 1,2,4-trioxolane formation is Griesbaum ozonolysis in which oximes are reacted with ketones in the presence of ozone to produce tetra-substituted 1,2,4-trixolanes in excellent yields. This reaction is thought to proceed through a series of 3+2 cycloadditions and reversions to yield the final ozonides. The stereochemistry of the products obtained[56,57] and their stability are both heavily influenced by the nature of substitutions around the peroxide bond.

Stability of sterically hindered endoperoxides

While simple ozonides are somewhat notorious for thermal instability and the potential to undergo explosive decomposition[58,59], the literature describes a surprisingly large range of reactivities across this class of compounds. Some ozonides have been observed to cause violent explosions upon warming to room temperature and reduce readily in the presence of triphenyl phosphine (TPP) or

dimethyl sulfide (DMS)[60], while others have been found to be stable up to 175 °C and withstood $LiBH_4$ reductions and Mitsunobu reaction conditions[61].

A critical factor in the instability of simple 1,2,4-trioxolanes is the presence of α-protons at the 3 and 5 positions of the trioxolane ring (**Fig. 3**). Early work by Story et al. showed that the availability of protons at these positions for intramolecular hydrogen abstractions was correlated with thermal instability[58]. This was corroborated by work from Hull *et al.* where gas phase thermal decomposition reactions of simple ozonides showed that the tetra-substituted 2-butene ozonide and the bicyclic 1,2-dimethylcyclopentene ozonide had far greater thermal stability than less substituted ozonides with α-protons available for abstraction. Indeed, with each increasing alkyl substitution at the 3 and 5 positions the rate of thermal decomposition decreased by approximately an order of magnitude[62]. Methoxy and ethoxy substitutions were shown to be even more stabilizing to the trioxolane as compared to alkyl substituents[63] while α-oxo ozonides are notorious for their instability[64], indicating that the electronic nature of the substituents is also a determining factor in the thermal stability of the molecule.

Based on the decomposition products observed in these studies it has been concluded that the thermal and photochemical decomposition of trioxolanes compounds proceeds via initial homolysis of the peroxide bond. By utilizing sterically hindered, tetra-substituted trioxolane rings, excellent thermal stability has been achieved in the case of the antimalarial trioxolanes. These compounds have

been found to be stable at elevated temperatures (>50 °C)[56] as high as 175 °C in some cases[61].

Consistent with the observed effects of electronics on the thermal stability of trioxolanes, Kuwabara *et al*. showed in competitive reduction assays that the inductive effects of substituents around the trioxolane ring correlates with the reactivity of ozonides with reductants* such that CN > CF_3> CO_2Me > H in descending order of reactivity[65]. While dimethylsulfide and PPh_3 are commonly used to reduce simple ozonides in organic synthesis[60,63,65–68], the tetra-substituted scaffolds pursued as malarial chemotherapeutics have been shown to be stable to both reagents in the context of Swern oxidations[56] and Mitsunobu reactions[46,61,69]. They have also shown good stability to more traditional reducing agents such as sodium and lithium borohydrides[61,69–72]. Importantly, these compounds retain peroxide dependent antimalarial activity illustrating a surprising selectivity for Fe(II)-mediated reduction of the peroxide bond in these sterically-hindered, electron-rich scaffolds.

Other factors which have been shown to induce trioxolane degradation are acidic and basic conditions. The presence of an α-proton is critical in determining the stability of the trioxolane to basic conditions. While ozonides with available α-protons have been observed to decompose in the presence of triethylamine and sodium hydroxide[67,68], tetra-substituted ozonides have been shown to be stable to strongly basic conditions including ester hydrolysis with potassium hydroxide and

* Triphenylphospine was used as the reductant in this study.

Grignard reagents[56,61,73,74]. Taken together with observations of the factors contributing to thermal and reductive stability of trioxolane scaffolds, these findings indicate that, for optimal stability, trioxolane systems should be fully substituted at the 3 and 5 positions with electron rich moieties.

In contrast to their excellent stability under basic conditions, tetra-substituted trioxolanes are known to participate in Hock-type fragmentations when exposed to either Bronsted[75–77] or Lewis acids[78–80]. In spite of these potential instabilities however, a wide array of reactions have been carried out in the presence of both Lewis and protic acids[61,66,73,74,81,82]. One potential driving factor in acid stability is the presence of water. In our hands, many tetrasubstituted trioxolanes have been completely stabile for hours at room temperature in 4 M HCl in dioxanes, provided the reaction is carried out under strictly anhydrous conditions. A full account of the factors determining acidic stability has yet to be compiled however; thus particular care must be taken to limit prolonged exposure to strongly acidic conditions while working with trioxolanes. It is worth noting however that arterolane and other endoperoxides are dosed orally and known to have good bioavailability and PK parameters indicating that these compounds are largely stable to the range of acidic conditions relevant *in vivo*.

Fe(II)-reactivity of sterically hindered endoperoxides

Trioxolane-based antimalarials must not only possess excellent stability under physiological conditions but must also maintain reactivity with Fe(II)-species in the parasite for efficacy. Early studies determined that Fe(II)-mediated reduction of

1,2,4-trioxolanes proceeds via inner-sphere single electron transfer processes[83]. Based on the products observed from Fe(II)-mediated reduction of ^{18}O-labelled trioxolanes, Abe et al. concluded that the reaction is sensitive to steric effects. Thus, these workers observed preferential formation of reaction products arising from regioselective attack of Fe(II) on the less hindered side of unsymmetrically substituted trioxolanes[83]. Molecular orbital calculations supporting these studies suggested Fe(II) attack on the O-O σ^* LUMO orbital from the less hindered direction generated an oxy radical intermediate in a regioselective manner. Subsequent electron transfer reactions and a C-C bond scission were then proposed to explain the experimentally observed reaction products in a manner consistent with observations from similar studies of artemisinin and related compounds[84,85].

Steric hindrance around the peroxide bond was accordingly found to be the major determinant of reaction rate with Fe(II)[86]. Work by Creek et al. showed that highly hindered endoperoxides with adamantyl substitutions on both sides of the peroxide bond were found to be largely unreactive with Fe(II) ($k = 0.008\ h^{-1}$) whereas a substantially less hindered bis-cyclohexyl analog reacted rapidly ($k = 0.85\ h^{-1}$) [86] (**Fig. 4**). Trioxolane analogs pursued as antimalarials are unsymmetrical with an adamantyl moiety to one side and a cyclohexyl on the other, which provides an optimal balance of reactivity ($k = 0.41\ h^{-1}$) and stability.

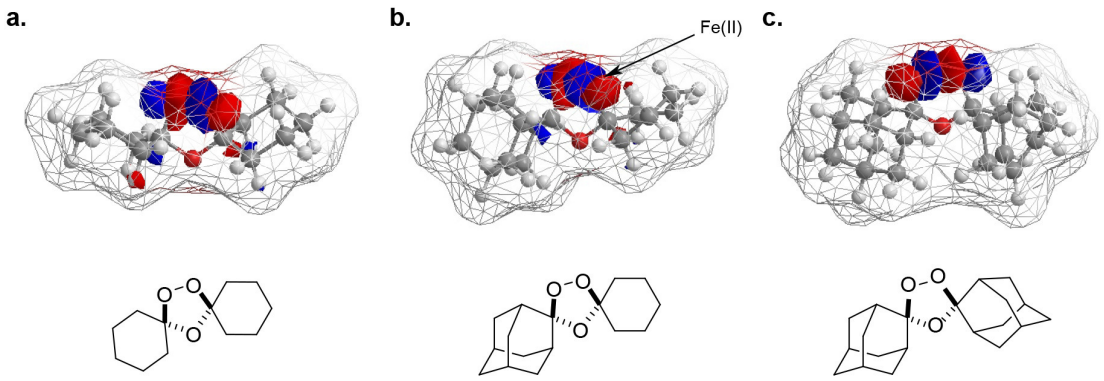

Figure 4: Influence of sterics on Fe(II) reactivity of 1,2,4-trioxolanes
MM2 energy minimized 3D structures of previously reported trioxolane-bearing spirocycles with differing steric bulk around the peroxide bond dictating differential Fe(II) reactivity. Connolly molecular surfaces are shown in wireframe colored by atom (white = C, red = O) and the predicted LUMO orbital for each molecule is shown. The corresponding two-dimensional compound structures are shown beneath each model for clarity. Compounds are shown in decreasing rank of iron(II) reactivity from left to right (**a**>**b**>**c**).

Substitutions on the cyclohexyl ring were used to further fine tune the Fe(II)-reactivity and stability of the molecule. Incorporation of heteroatoms was found to generally increase the rate of Fe(II)-reactivity with the incorporation of basic moieties increasing reaction rates more than acidic functionalities[86]. These effects were minor in comparison to those mediated by changes in sterics and were largely rationalized on the basis of their ability to loosely chelate iron thus increasing local concentration. Bulkier cyclohexane substituents oriented *cis* to the peroxide bond on the other hand, were found to significantly slow reaction rates, consistent with the importance of steric effects on reactivity, as described above[86]. The conformation of the peroxide bond[†] was also found to substantially effect rates of Fe(II) reactivity. Compounds in which the peroxide bond was equatorial were much

[†] Disposed either axially or equatorially from the cyclohexyl ring

more reactive with Fe(II) than axial comparators, an observation rationalized by the increased steric crowding imparted by 1,3-diaxial interactions between the peroxide bond and axial protons of the cyclohexyl ring[86,87]. Trioxolanes with the best properties for antimalarial applications were found to have an axial peroxide bond, suggesting the increased stability achieved from this conformation is beneficial, particularly for *in vivo* applications.

Consistent with the substantial influence of sterics on reactivity, Fe(II)-mediated reduction of unsymmetrical trioxolanes such as that in arterolane (**Fig. 3**, **Fig. 4b**) was found to be highly regioselective for reaction at the less hindered oxygen atom of the peroxide bond. This resulted in quantitative yields of the corresponding cyclohexanone after subsequent β-scission and rearrangement[86]. The quantitative evolution of cyclohexanone upon Fe(II)-mediated peroxide reduction was leveraged by previous members of the Renslo Lab to construct an arterolane-like scaffold for Fe(II)-triggered drug/payload delivery (**Fig. 5**). This was accomplished by modifying the cyclohexane ring such that the cyclohexanone product evolved upon reduction by Fe(II) possesses a carbamate bond to the payload which is positioned beta to the carbonyl function. This unstable intermediate then undergoes spontaneous β-elimination to evolve CO_2 and release the amine-linked payload (**Fig. 5**). Since the carbamate bond is stable while the trioxolane is intact (no β-elimination can occur[‡]), payload release is thus coupled to Fe(II)-mediated reduction of the peroxide bond. Trioxolane-based, Fe(II)-dependent payload

[‡] This is due to the dramatic change in pKa for the α-protons in the intact conjugate (pKa ~ 59) as compared to the cyclohexanone intermediate (pKa ~ 18).

delivery strategies of this nature have thus far been validated and utilized to deliver payloads to Fe(II)-rich compartments of the malaria parasite both *in vitro*[57,88] and *in vivo*[89].

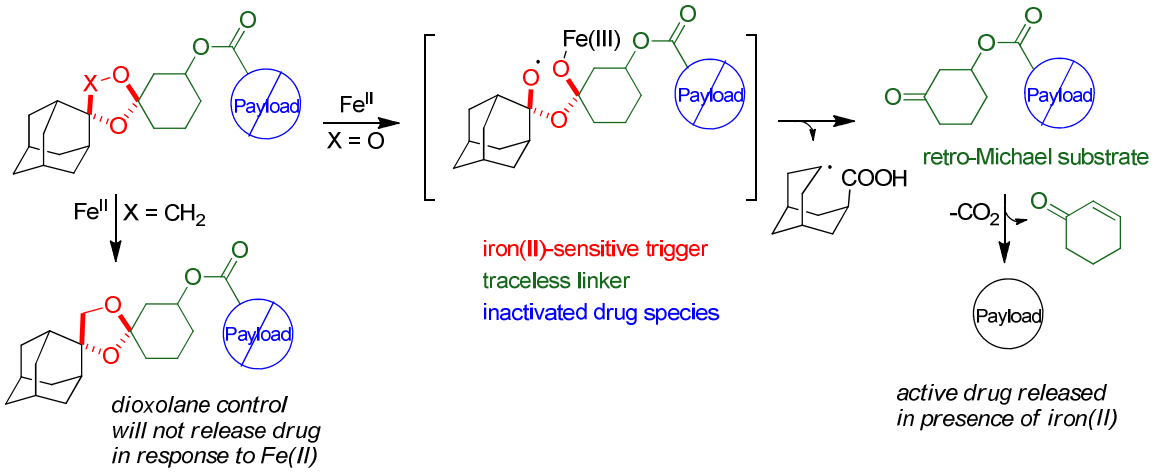

Figure 5: Mechanism of Fe(II)-dependent payload delivery from trioxolane-based conjugates.
The trioxolane scaffold reacts with Fe(II) species through single-electron reduction of the peroxide bond to produce radical intermediates which rearrange through β-scission to cleave the molecule in half. This process produces a cyclohexanone substituted at the beta position with carbamate-tethered payload. This intermediate is unstable and degrades to evolve CO_2 and release free payload via retro-Michael reaction. Dioxolane controls where the peroxide bond has been replaced with an ether linkage are non-reactive with Fe(II) and are thus important negative controls.

We reasoned that, due to the finely tuned Fe(II)-reactivity of this trioxolane scaffold, such a system could be engineered to produce selective probes for Fe(II)-species which would have utility in cell culture models and *in vivo*. Such a system could, in theory, be constructed by employing the trioxolane-based payload delivery scaffold for the Fe(II)-dependent unmasking of either fluorescent moieties or cell active compounds such as puromycin which would leave observable marks on the cell.

Synthesis of a trioxolane-based probe for intracellular reactive Fe(II)

The development of a reactivity-based probe of the ferrous iron pool required mechanistically linking reduction of the Fe(II)-reactive 1,2,4-trioxolane moiety to a readily observable and quantifiable signal. We reasoned that a FRET probe could be designed in which Fe(II)-induced trioxolane fragmentation served to dissociate the FRET pair (**Fig. 6a**). Thus, we synthesized the probe **1** in which the fluorophore-quencher pair is separated by a tetrasubstituted trioxolane related to arterolane (**Fig. 6a, Supplementary Scheme. 1**). As expected, the DANSYL moiety in probe **1** is internally quenched, with negligible fluorescence signal observed when excited at the absorbance maximum (337 nm) (**Fig. 6b**). Upon exposure to Fe(II) species however, a strong fluorescence signal with an emission maximum at 465 nm appeared in a time and concentration dependent fashion (**Fig. 6b**). Significantly, compound **1** exhibited negligible reactivity with Fe(III) or other biologically relevant metal ions, even at very high (1.5 mM) concentrations (**Fig. 6c, Supplementary Fig. 1**). Similarly, treatment with holotransferrin (transferrin-bound Fe^{III}), or biologically relevant oxidants or reductants did not lead to significant activation of **1** (**Fig. 6d, Supplementary Fig. 1**). While these studies were invaluable for demonstrating the Fe(II)-specific reactivity of the 1,2,4-trioxolane moiety, compound **1** was not useful for studies in intact cells due to poor cellular permeability.

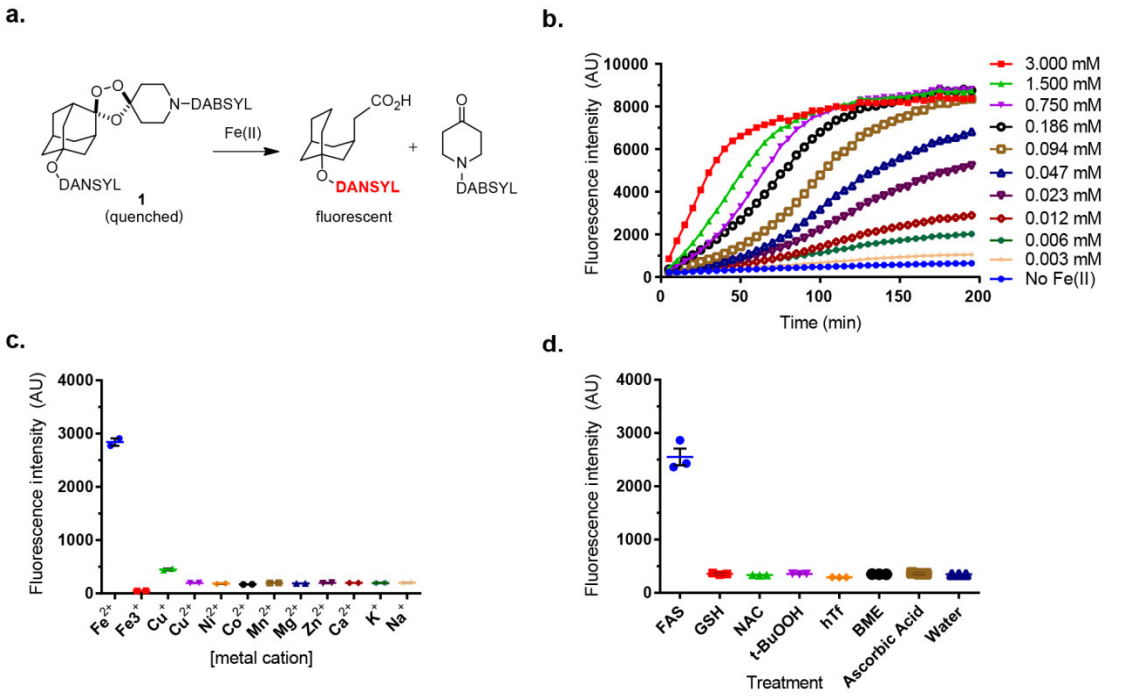

Figure 6: A turn-on fluorescent probe reveals selective Fe(II)-reactivity of hindered 1,2,4-trioxolanes.

(**a**) Chemical structure and mechanism of turn-on fluorescent probe **1**. (**b**) Fluorescence signal at 465 nm (E_{max}) of trioxolane-based fluorescent probe **1** over time when exposed to the indicated concentrations of $FeBr_2$. (**c**) Fluorescence signal at 465 nm of **1** when treated with 1.5 mM (1 M for Na^+) solutions of the indicated metal ions for 2 hours. Error bars represent s.e.m. (n=2). (**d**) Fluorescence signal at 465 nm of **1** when treated with 3 mM solutions of the indicated biologically relevant redox-active reagents for 5 hours. Error bars represent s.e.m. (n=3).

A cell-active probe (**3**) was ultimately produced by conjugating puromycin (**2**) to our previously described 1,2,4-trioxolane scaffold (**Fig. 7a, Supplementary Scheme 2**)[88,90]. Puromycin is incorporated in nascent polypeptides at the ribosome, producing a permanent and dose-dependent mark on cells that can be detected with anti-puromycin antibodies. Significantly, the α-amino functionality of puromycin (**2**) required for incorporation is acylated in the trioxolane-conjugate **3**, thus the activity of **2** is blocked in the intact conjugate prior to reaction with Fe(II). As an important

negative control we also prepared the bioisosteric but non-peroxidic dioxolane conjugate **4**, which is unreactive with Fe(II) (**Fig. 7a, Supplementary Scheme 2**)[57].

Incubation of **3** in cell culture media for 24 hours at 37 °C produced no observable release of **2**, demonstrating good stability under cell culture conditions in the absence of Fe(II) (**Supplementary Fig. 2a**). When ferrous ammonium sulfate (FAS) was added to the media however, the trioxolane ring in **3** fragmented completely within 30 minutes to yield the expected cyclohexanone intermediate (peak denoted with ***; Fig. 7b**). This unstable intermediate then underwent spontaneous retro-Michael reaction to release free **2** as desired; thus confirming that, when exposed to reactive Fe(II)-species in solution probe **3** releases free puromycin (**2**) as designed (**Fig. 7b**).

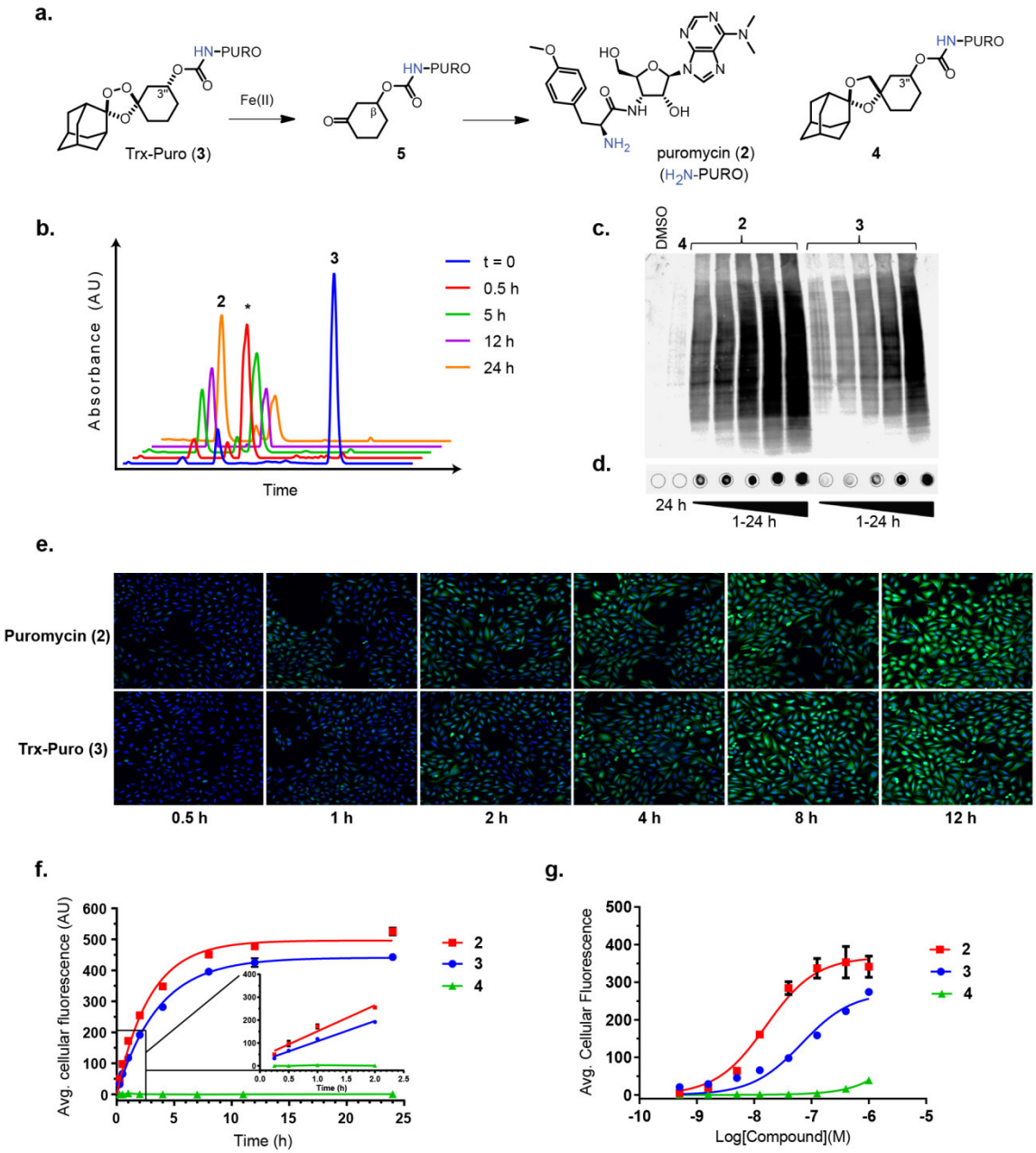

Figure 7: Trioxolane-conjugates of puromycin can be used as peroxide dependent cellular probes of Fe(II).

(**a**) Chemical structure and mechanism of Fe(II)-triggered trioxolane-puromycin conjugate **3** and dioxolane-control **4**. (**b**) LCMS spectra (UV absorbance at 275 nm) illustrating the efficient conversion of **3** to the cyclohexanone intermediate (*) and subsequently free puromycin (**2**) in cell culture media following addition of ferrous ammonium sulfate (FAS). (**c**) Time-dependent incorporation of puromycin in cellular proteins of U-2 OS cells treated with 1 μM solutions of **2**, **3**, or **4** as assessed by western or (**d**) dot blot analysis with anti-puromycin antibodies. (**e**) Representative images of incorporation of puromycin over time in U-2 OS cells treated with 0.1 μM solutions of trioxolane-puromycin conjugate **3** or free puromycin (**2**) visualized via immunofluorescence. (**f**) Quantification of average cellular

puromycin incorporation over time in U-2 OS cells treated with 0.1 μM solutions of **2**, **3**, or **4** then fixed, stained and imaged. Images were analyzed at the single cell level for immunofluorescence density in over 2000 cells per condition and well mean intensity values across triplicates were reported with error bars depicting +/- s.e.m. The inset shows initial rates of puromycin incorporation in the linear regime, which were 7.4 and 3.7 AU/h for **2** and **3** respectively. The initial incorporation rate in cells treated with dioxolane-puromycin control **4** was indistinguishable from zero. (**g**) Quantification of average cellular puromycin incorporation in cells treated with a dose response of **2**, **3**, or **4** for 8 h then fixed, stained, and imaged as in (e) and (f). Values represent the well mean intensity values across triplicates as in (f) with error bars depicting +/- s.e.m.

Validation of trioxolane-conjugates as reactivity-based probes of the intracellular labile Fe(II) pool

To determine if probe **3** responded to the labile Fe(II) pool in mammalian cells we compared the rate and extent of puromycin (**2**) incorporation over 24 hours in U-2 OS cells treated with equimolar concentrations of **2** or trioxolane-puromycin probe **3**. Encouragingly, we found that both compounds produced a time-dependent increase in puromycin incorporation as determined by western and dot blot analysis with α-puromycin antibodies (**Fig. 7c-d**). Cells treated with trioxolane-conjugate **3** showed a small lag in puromycin incorporation compared to those treated with free puromycin (**2**). Total levels of incorporation at 24 hours were nearly identical, consistent with efficient release of **2** from trioxolane-conjugate **3**, presumably mediated by intracellular Fe(II). By contrast, puromycin incorporation was undetectable in U-2 OS cells treated with dioxolane-puromycin control **4**, indicating that intracellular release of puromycin from **3** is peroxide dependent, and by extension Fe(II)-dependent (**Fig. 7c-d**).

To characterize the response of **3** under a broader range of conditions, we developed a robust, cell based immunofluorescence assay using high-content imaging with single cell resolution. This assay allowed us to study the time and dose dependence of the cellular effects of **3** by visualizing cellular puromycin incorporation with fluorophore labelled secondary antibodies and high-throughput fluorescence microscopy (**Fig. 7e-g**). We found that U-2 OS cells treated with equimolar concentrations (0.1 μM) of probe **3** or free puromycin (**2**) showed similar incorporation half-lives (2.5 h and 2.0 h respectively) and fluorescence saturation points (441 vs 496 AU), indicating that activation of **3** and release of **2** occurs rapidly and efficiently within the cells (**Fig. 7f**). As the intrinsic permeability of **2** and **3** were found to be very similar in the PAMPA assay we expect the differences in rates of puromycin incorporation observed are related to the rate and extent of Fe(II)-mediated release of **2** from **3** as opposed to differential cell permeability between the two compounds (**Supplementary Table 1**). Interestingly, the rate-determining retro-Michael reaction of the cyclohexanone intermediate (*) to liberate **2** appears to be appreciably accelerated in cells (**Fig. 7c-f**) when compared to cell-free media containing Fe(II) (**Fig. 7b**). While the reason(s) for this are unclear, we have observed similarly accelerated rates of intracellular retro-Michael reaction with different trioxolane conjugates in malaria parasites[57], suggesting a common feature of both environments which is not represented in the *in vitro* assays may enhance the rate of the β-elimination. U-2 OS cells treated with non-peroxidic control **4** again showed negligible immunofluorescence signal under all

conditions studied, confirming that puromycin release from **3** is peroxide dependent (**Fig. 7f-g**).

Defining the sensitivity and selectivity of probe 3 in response to intracellular iron:

To determine whether **3** could be used to detect changes to intracellular Fe(II) concentrations, PC-3 cells were pre-treated for two hours with various concentrations of ferrous ammonium sulfate (FAS) or the iron chelator 2,2'-bipyridyl (Bpy) in serum free media, washed, and then probed with 1 μM **3** for four hours. The cells pre-treated with FAS showed dose dependent increases in signal from puromycin incorporation compared to cells that were pre-treated with vehicle (**Fig. 8a-b** and **Supplementary Fig. 3**). Pre-conditioning with as little as single-digit μM concentrations of FAS induced an observable response over control conditions, demonstrating that probe **3** exhibits excellent sensitivity to changes in intracellular Fe(II) levels. Cells pre-treated with Bpy correspondingly showed a dose-dependent decrease in signal consistent with the expected Fe(II)-dependent reactivity of **3** (**Fig. 8a-b** and **Supplementary Fig. 3**). An analogous dose-dependent decrease in immunofluorescence was also observed when PC-3 cells were pretreated with the iron chelator DFO[22,23,26,30] rather than Bpy (**Supplemental Fig. 4**). When PC-3 cells pre-conditioned with FAS or DFO were treated with free **2** instead of **3**, no changes in the immunofluorescence signal were observed, indicating that these pre-treatments do not affect rates of protein synthesis or puromycin incorporation but rather the rate and extent of puromycin release from **3** (**Supplementary Fig. 4**).

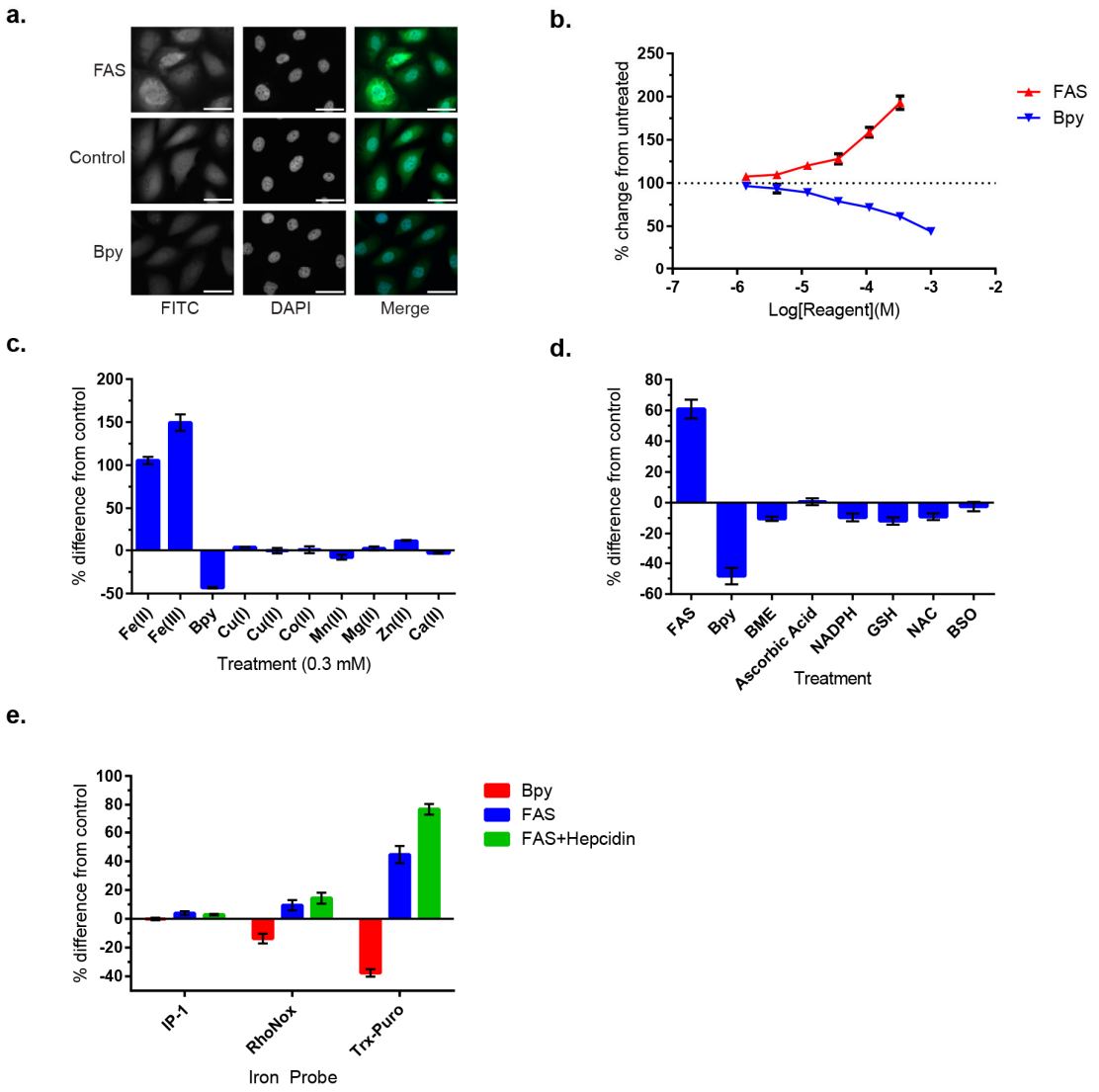

Figure 8: Reactivity-based probe 3 is a highly selective and sensitive tool for reporting on Fe(II) in cells.

(**a**) Representative images of PC-3 cells pre-treated with FAS (0.3 mM), Bpy (1 mM), or vehicle for 2 h then washed and exposed to 1 μM of **3** for 4 h. Puromycin incorporation is visualized with Alexafluor488-labelled secondary antibodies shown in green (FITC cannel) and nuclei are visualized with Hoechst nuclear stain shown in blue in the merged image. Scale bars denote 50 μm. (**b**) Average cellular puromycin incorporation in PC-3 cells pretreated with the indicated doses of FAS or Bpy for 2 h in serum free media then washed with PBS and exposed to 1 μM solutions of trioxolane-conjugate **3** for 4 h. Greater than 2000 cells were imaged and analyzed per condition and well mean intensity values across triplicates are reported with error bars depicting +/- s.e.m. (**c**) Average cellular puromycin incorporation in PC-3 cells treated pretreated with 0.3 mM solutions of the indicated metal ions in serum free media for 2 h then washed with PBS and exposed to 1 μM solutions of trioxolane-conjugate **3** for 4 h. Greater than 2000 cells were imaged and analyzed per condition and well mean intensity values across duplicates are reported with error bars

depicting +/- s.e.m. (**d**) Average cellular puromycin incorporation in PC-3 cells treated pretreated with solutions of GSH (1 mM for 22 h), NAC (10 mM for 20 h), BSO (1 mM for 20 h), BME (0.1 mM for 20 h), Ascorbic Acid (1 mM for 3 h), or NADPH (1 mM for 3 h) in cell culture media and then washed with PBS and exposed to 1 μM solutions of trioxolane-conjugate **3** for 4 h. (**e**) Dynamic response of cell iron conditioning in PC-3 cells as measured by Fe(II)-probes IP-1, RhoNox-1, and **3**. The percent change from non-iron conditioned cells is compared for each probe when treated with 0.3 mM FAS, Bpy, or FAS after pretreatment with Hepcidin. For all panels greater than 2000 cells were imaged and analyzed per condition and well mean intensity values across triplicates are reported with error bars depicting +/- s.e.m.

To provide further evidence that probe **3** is responding to changes in intracellular Fe(II) and not other metal ions, we performed an analogous set of pre-conditioning experiments applying various biologically relevant metal ions (**Fig. 8c**). Thus, PC-3 cells were pre-treated with dose responses of various metal ions in serum-free media for two hours, washed, and probed with **3** (1 μM) for four hours, and then fixed, stained, and imaged. From these experiments, only cells pre-treated with Fe(II) or Fe(III) elicited a notable response from probe **3** at any of the tested concentrations (**Fig. 8c** and **Supplementary Fig. 5e**). Since trioxolanes are unreactive with Fe(III) (**Fig. 6c and Supplementary Fig. 2b**), the robust response of **3** in cells pre-treated with Fe(III) reflects the detection of increased intracellular Fe(II) resulting from internalization and reduction of Fe(III), consistent with known iron biology[8,91].

To confirm signal from the probe was selective for Fe(II) over other biologically relevant reductants PC-3 cells were treated with various reagents previously shown to alter intracellular gluthathione (GSH) levels and redox status. The concentrations and manner of application were based on those reported previously for the various reagents[92–97]. Notably, none of these conditions produced any substantial, dose-

dependent effects on signal from puromycin release in cells treated with **3,** consistent with the excellent stability of hindered trioxolanes towards biologically relevant reductants we observed in our studies of FRET-probe **1** in solution(**Fig. 6d and Supplementary Fig. 5a-b**). To verify that pre-treatment with GSH, N-acetyl cysteine (NAC), or the gluthathione synthesis inhibitor buthionine sulfoximine (BSO) in fact altered intracellular GSH concentrations, we also employed a commercial fluorometric GSH detection kit. While the pre-treatment conditions we employed substantially altered the intracellular GSH concentrations in a dose dependent manner, the effects on signal from **3** were minor (ca. 10% or less change from control) and did not track with the observed dose dependent changes to GSH levels (**Supplementary Fig. 5c-d**). Taken together with the metal ion specificity experiments these results confirm that probe **3** is selective for reporting on intracellular Fe(II).

Comparing probe 3 with fluorescent turn-on probes IP1 and RhoNox-1:

We next sought to compare the sensitivity of probe **3** and immunofluorescence detection with the recently reported fluorescent turn-on probes IP-1 and RhoNox-1. We compared the response of IP-1 and RhoNox-1 in pre-conditioned PC-3 cells using the same high-throughput high-content imaging approach described above for studies of **3**. The iron-conditioning treatments were identical to those used with **3** and the application of IP-1 (2 μM, 2 h) and RhoNox-1 (5 μM, 4h) were based on conditions reported previously, with some optimization. All three probes produced a qualitatively similar response following pre-treatment with high concentrations (0.3 mM) of Bpy or FAS (**Fig. 8e**). However, the magnitude of response under all

conditions was notably higher with **3** and only probe **3** was able to report on changes induced by the peptide hormone hepcidin (HP), a post-translational regulator of the iron exporter ferroportin (**Fig. 8e**). Probe **3** detected an increased labile iron(II) pool in cells that were treated with 10 μg/mL of HP in cell culture media for 16 h prior to and during FAS pre-treatment compared to cells treated with FAS alone (**Fig. 8e**). These results are consistent with expectations following the reduction in iron export capacity caused by HP induced ferroportin degradation. This effect was observed for all doses of FAS studied with probe **3** (**Supplementary Fig. 6**). These findings are consistent with previous observations using IP-1 to monitor changes to the labile iron pool induced by HP and FAS using lower throughput confocal microscopy methods[31]. Immunofluorescence imaging with probe **3** thus affords greater sensitivity than fluorescence imaging with IP-1 and RohNox1 in the context of a high-throughput plate-based based imaging assay. The advantages of this screening approach include the ability to rapidly image large fields of cells (2,000-10,000 cells per condition) with single-cell resolution and to simultaneously explore multiple treatment conditions in parallel by employing cells seeded in 96- or 384-well plates.

Profiling cell-type specific changes the labile pool of ferrous iron

Having established the utility of trioxolane-puromycin conjugate **3** as a selective and sensitive reactivity-based probe of labile iron(II) pools in cells we were interested in exploring its application to studying labile iron pools in the context of disease-specific cellular metabolism. For example, iron homeostasis is known to be altered

in many cancers. To explore whether these changes affect the presence of reactive Fe(II) species in the cancer cells, we used **3** to compare the labile iron(II) pools of cancer cells with non-tumorigenic cells. We found that the immunofluorescence response of **3** in non-tumorigenic MCF10A cells was significantly diminished as compared to that of **3** in RKO cancer cells, reflecting a larger labile iron pool in RKO as compared to MCF10A cells (**Fig. 9a-b**). As different cell lines may have differing endogenous rates of protein synthesis and puromycin incorporation we normalized the fluorescence signal in cells treated with probe **3** to the signal obtained from equimolar treatment with free puromycin at saturation (**2**). This provided a convenient metric – normalized signal (%) - to compare Fe(II) pools across cell lines. We profiled additional of cancer cell lines and a second non-tumorigenic cell line (IMR-90) using this methodology and found the cancer cell lines exhibited normalized signal values of ~75-90% as compared to ~40-45% for the non-tumorigenic cell lines (**Fig. 9c** and **Supplemental Fig. 7**). Thus, across a small panel of cell lines, probe **3** revealed augmented pools of labile Fe(II) in cancer cell lines compared to non-tumorigenic cell lines. Probe **3** therefor provides a means to identify tumorigenic cells possessing an altered and potentially targetable metabolic state characterized by increased concentrations of reactive Fe(II).

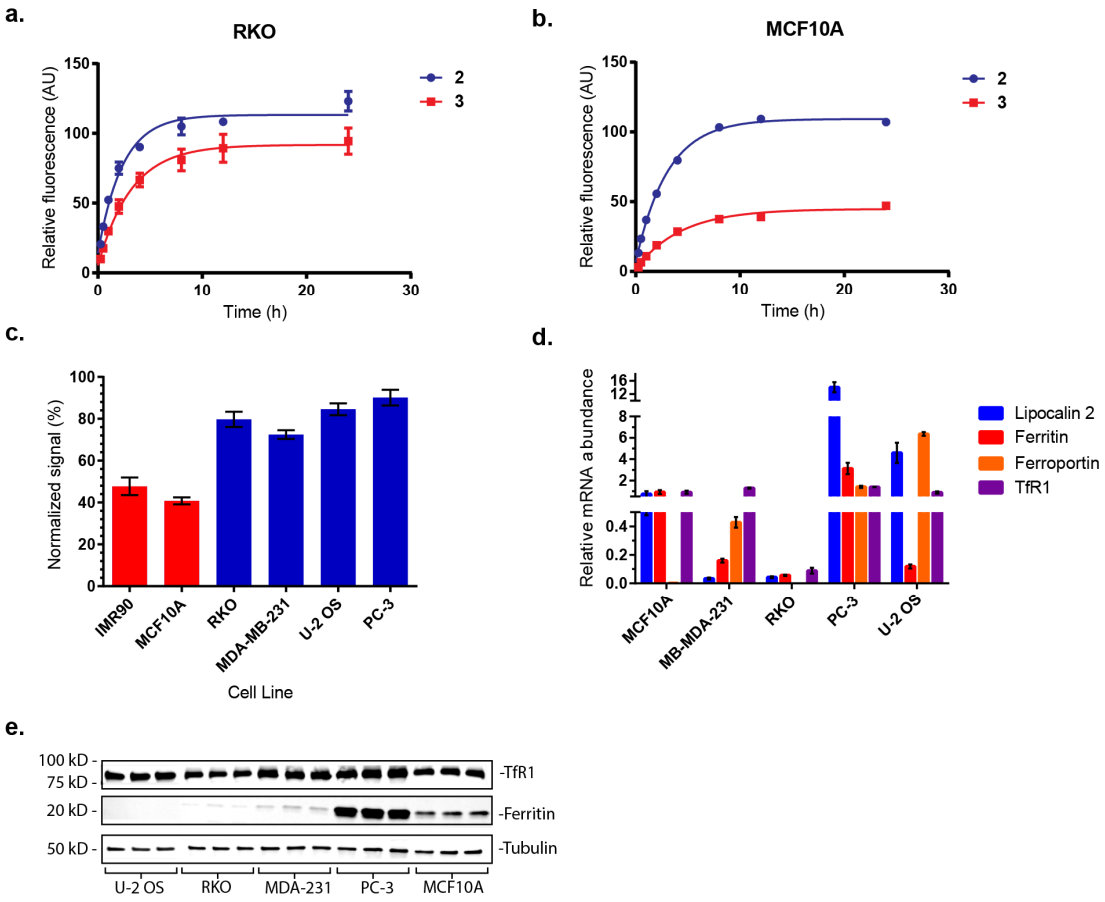

Figure 9: Comparing reactive Fe(II) pools across cell lines.

(**a**) Puromycin incorporation over time in RKO cells treated with 0.1 μM solutions of **2** or **3** in cell culture medium. Background in vehicle treated cells is subtracted and data is normalized to puromycin incorporation at saturation in cells treated with free puromycin. More than 10,000 cells were imaged and analyzed per condition and values represent the well mean intensity across triplicates with error bars depicting +/- s.e.m. (**b**) Puromycin incorporation over time in MCF10A cells treated with 0.1 μM solutions of **2** or **3** in cell culture medium. Background in vehicle treated cells is subtracted and data is normalized to incorporation at saturation in cells treated with free puromycin. Greater than 2500 cells were imaged and analyzed per condition and values represent well mean intensity across triplicates with error bars depicting +/- s.e.m. (**c**) Puromycin incorporation at saturation in cells treated with 0.1 μM **3** normalized to that in cells treated with free puromycin (**2**) across cell lines from diverse origins. Non-tumorigenic cell lines are indicated in red with cancer derived cell lines shown in blue. Values are presented as the percent of signal at saturation in cells treated with **2** comparing well averages across triplicates +/- s.e.m. (greater than 1000 cells analyzed per condition). (**d**) Relative mRNA levels for ferritin heavy chain (FTH-1), lipocalin 2 (LCN2), ferroportin (SLC40A1), and transferrin receptor (TfR1) across a selection of cell lines profiled in (c). Measurements were made in biological triplicates and internally normalized to GAPDH expression levels. Relative mRNA levels were determined from a standard curve for of pooled cDNA samples from all cell lines for each qPCR primer set. Error bars represent s.e.m. (n = 3). (**e**) Expression levels of ferritin

(FTH-1) and transferrin receptor (TfR) by western blot compared to tubulin loading controls. Immunoblot confirms the observed changes to ferritin expression translate to changes at the protein level.

Understanding the consequences of iron-metabolism dysregulation on the presence of intracellular reactive Fe(II)-species:

To identify factors that could be contributing to the increased reactive Fe(II)-pool observed in the cancer cells we profiled the expression levels of key iron metabolism proteins across the same panel of cells. Preliminary studies revealed only minimal changes for most of the proteins studied (**Supplementary Fig. 8a**); however, the transcript levels of the iron storage protein ferritin heavy chain (FTH-1) showed a marked decrease (5.7 to 16-fold) in many of the cancer cell lines when compared to the more resistant MCF10A cells (**Fig. 9d**). These decreased levels of FTH-1 mRNA were correlated with reduced ferritin protein levels as measured by immunoblot (**Fig. 9e**). These observations are consistent with reduced iron storage capacity in the cells which could contribute to increased levels of reactive Fe(II)-species. Interestingly, PC-3 cells showed a small *increase* in FTH-1 transcripts levels (3.4-fold) compared to the MCF10A cells while maintaining a larger labile Fe(II) pool as determined with probe **3**. These cells, however, also showed a 19-fold increase in transcripts for the iron import protein lipocalin-2 (LCN-2), suggesting that the augmented reactive Fe(II)-pool in PC-3 cells is driven by increased iron import capacity as opposed to decreased iron storage as in the other cell lines. On the other hand, three of the four cancer cell lines studied paradoxically had

significantly higher transcript levels for the iron exporter ferroportin when compared to MCF10A cells, suggesting that transcript analysis alone is insufficient to fully explain the differential response of cancer cells and non-tunorigenic cells to **3**. Overall however, these results do reveal that alteration of the reactive iron pool can occur in distinct ways, via differential regulation of iron metabolism in different cancer cell types.

Genetic Alterations to the Labile Fe(II) pool

To study how changes in the expression of iron regulatory proteins could contribute to the changes in labile iron(II) pools we observed between cell lines we altered the expression levels of both iron storage and export proteins and measured the resulting changes to the intracellular reactive iron pool using **3**. We selected the non-tumorogenic MCF10A cell line for knock-down studies because of its small reactive iron pool and high endogenous expression of the iron storage protein, ferritin. We predicted that knockdown of ferritin would substantially increase the levels of reactive intracellular iron. However, transfection of a pool of siRNAs targeting FTH-1 led to only a modest increase in the reactive iron pool when compared to scrambled siRNA transfected cells (**Fig. 10a**). Incomplete knockdown of FTH-1 could not explain the modest effect observed, as FTH-1 knockdown in these experiments was robust (>90%) (**Fig. 10b,e**). We thus hypothesized that the cells mount a rapid response to FTH-1 knockdown that restores iron homeostasis. Consistent with this hypothesis, we observed a compensatory reduction in transcript levels of the iron import protein lipocalin-2 following FTH-1 knockdown

(**Fig. 10b, Supplementary Fig. 8b**). We further observed a reduction in the levels of the iron regulatory protein IREB2. Decreased IREB2 levels would result in reduced translational inhibition of what ferritin mRNA remains after knockdown, allowing the cells to better maintain iron homeostasis. Further attempts to affect iron homeostasis in the MCF10A cells via knock down of the iron exporter ferroportin (SLC40A1) did not induce any observable increase in the reactive iron pool (**Fig. 10a**). This was not unexpected given these cells were found to have very low endogenous levels of ferroportin (so low that we were unable to observe further decrease from knockdown) (**Fig. 10b**). Thus MCF10A cells appear to rely heavily on regulation of iron import and storage to achieve homeostasis.

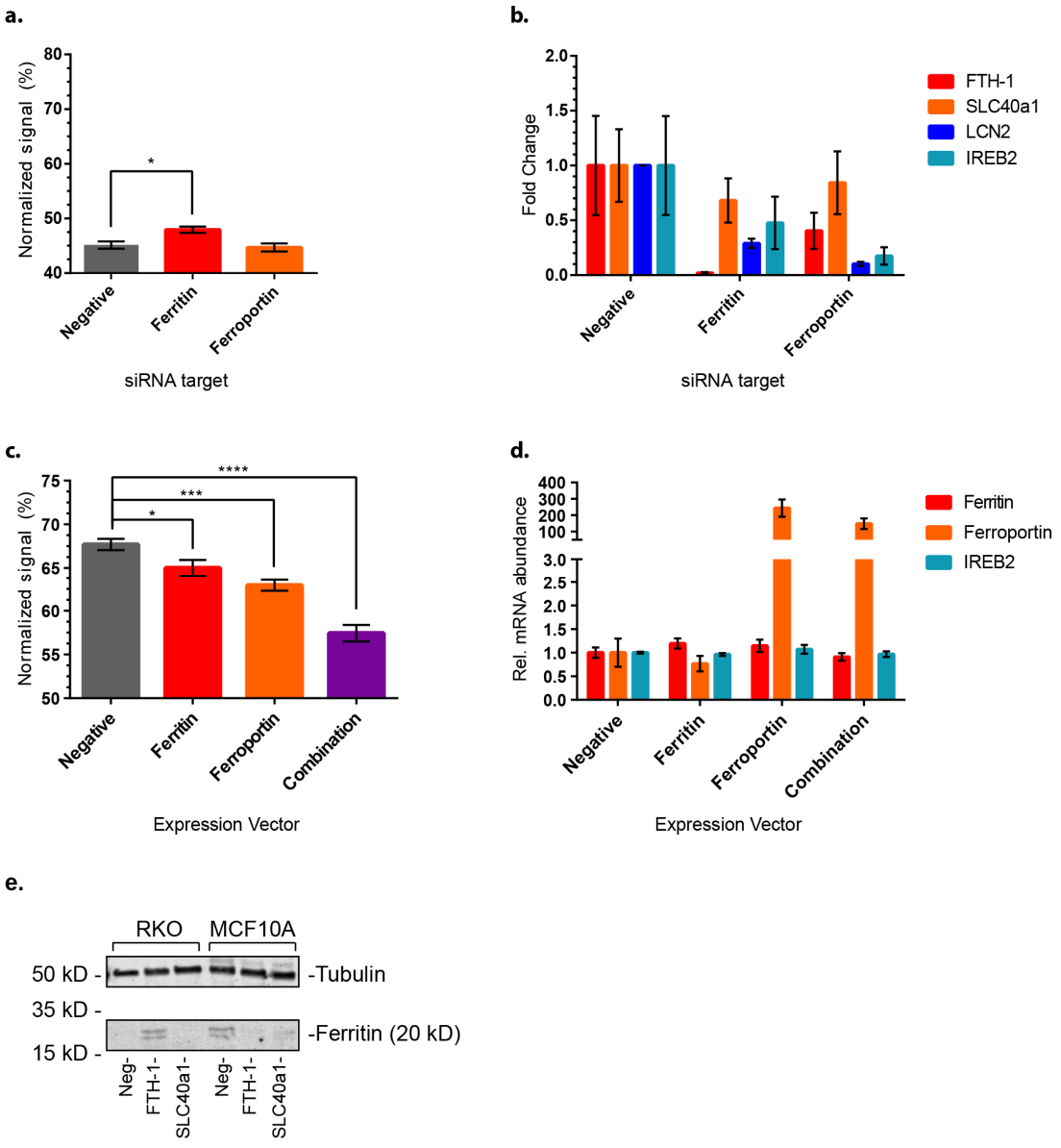

Figure 10: Genetic manipulation of the reactive iron pool.

(**a**) Changes in the reactive iron pool measured by probe **3** in MCF10A cells transfected with siRNA targeting the iron storage protein ferritin or the iron export protein ferroportin 24 hours before addition of **3**. The effect of these siRNA manipulations on other iron regulatory proteins was assessed by transcriptional profiling. (**b**) Transcriptional changes to selected iron regulator proteins in MCF10A cells treated with ferritin or ferroportin siRNA. Knockdown of ferroportin in MCF10A cells could not be confirmed due to insufficient assay sensitivity to detect the low endogenous levels of ferroportin in these cells. (**c**) Changes in the reactive iron pool as measured by **3** in RKO cells 24 hours after transient transfection with expression vectors for ferritin, ferroportin, or the combination. (**d**) Relative mRNA expression levels for select iron regulatory proteins in RKO cells transiently transfected with expression vectors for ferritin, ferroportin, or the combination. Over expression of

ferritin could not be confirmed by qRT-PCR, however over expression was confirmed at the protein level by immunoblot (**e**). Error bars in (a-d) represent s.e.m. for experiments run in biological triplicate. For panels (a) and (c) differences in the reactive iron pool were compared across treatments and cell types (n=3; error bar, mean ± s.e.m.; *P≤0.05, ***P≤0.001, ****P≤0.0001, Two-Way ANOVA with Dunnett's multiple comparisons test).

To explore whether ectopic expression of ferritin or ferroportin would limit reactive Fe(II) concentrations in cancer cells we chose to use RKO cells, which have low endogenous levels of both proteins and a large reactive iron pool as determined with **3** (**Fig. 9**). Indeed, ectopic expression of either FTH-1 or ferroportin by transient transfection of RKO cells resulted in a significant decrease in the reactive iron pool (**Fig. 10c**). Co-transfection of ferritin and ferroportin decreased reactive iron levels even further, consistent with their orthogonal roles in iron sequestration and export (**Fig. 10c**). Interestingly, while overexpression of ferroportin was readily observable by qRT-PCR, overexpression of ferritin was not observed with the probes used (**Fig. 10d**). Overexpression of ferritin was however confirmed at the protein level via western blot (**Fig. 10e**).

In contrast to the knockdown experiments in MCF10a cells detailed above, reduction of reactive iron in RKO cells by ectopic expression of ferritin and/or ferroportin was not accompanied by compensatory changes to iron regulatory proteins (**Fig. 10d, Supplementary Fig. 8b**). This may indicate that the cells are programmed to respond rapidly to a (potentially toxic) increase in reactive iron concentration, whereas a decrease in reactive iron is tolerated, at least over the time frame of our experiments.

These studies combining genetic modulation of iron regulatory proteins with expression profiling and the evaluation of reactive iron pools with probe **3** thus comprise a useful methodology for studying how cells respond and adapt to maintain iron homeostasis.

In vivo applications of trioxolane-derived, reactivity-based probes of the labile Fe(II) pool in a PC-3 tumor xenograft model

Since puromycin incorporation leaves a permanent detectable mark on exposed cells/tissues, we reasoned that probe **3** might also be used to evaluate reactive Fe(II)-pools *in vivo*. Female NSG mice engrafted subcutaneously with PC-3 tumors were thus administered puromycin (**2**) (25 mg/kg) or **3** (25, 50, or 100 mg/kg) over 24 hours via osmotic pump to provide sustained exposure over the course of the experiment. The mice were then euthanized and tissues were collected for analysis of puromycin incorporation by dot-blot analysis. We observed that mice treated with **3** incorporated puromycin in a dose dependent manner in tumor tissue whereas there was substantially less incorporation across all other tissues studied, with the exception of liver (**Fig. 11a-b**). As in the cell culture studies, we normalized signal in tissues from mice treated with **3** to that in the same tissues from mice treated with free **2** to account for tissue specific differences in rates of protein synthesis and puromycin incorporation (**Fig. 11c)**. When taking intrinsic rates of protein synthesis into account our results suggest that the tumors possess an augmented labile Fe(II) compared to the endogenous tissues studied, consistent with our observations in cell culture. These preliminary experiments establish that

it is possible to utilize probe **3** *in vivo* to observe differences in tissue specific labile iron(II)-pools.

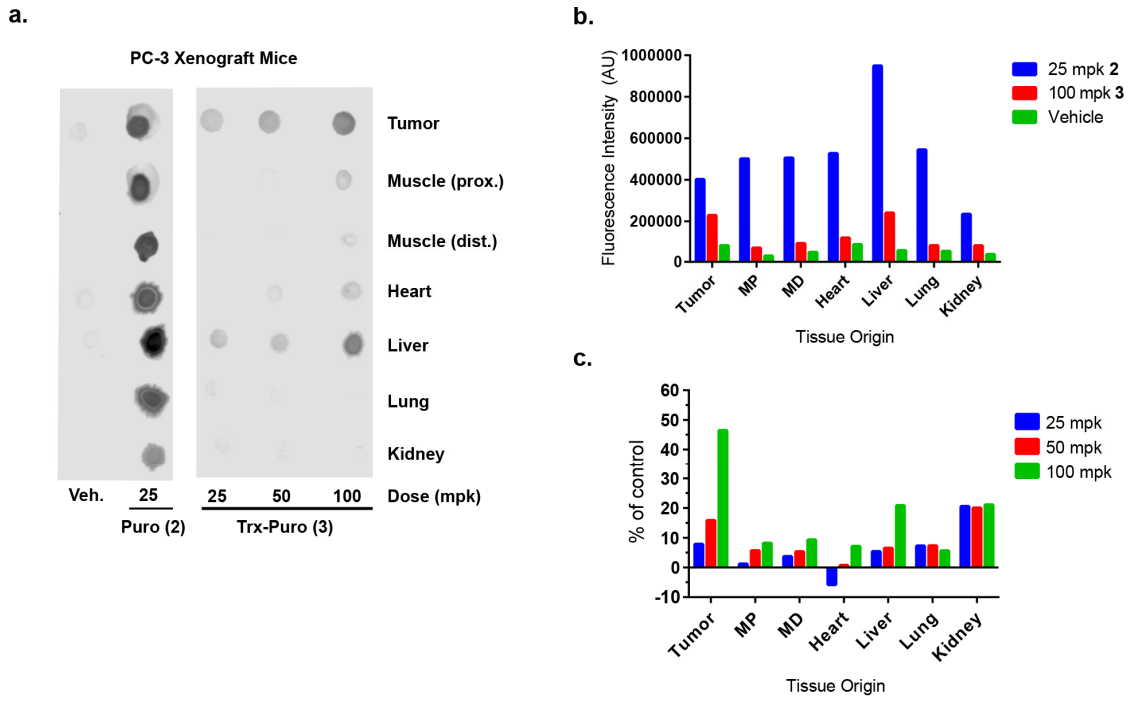

Figure 11: *In vivo* comparisons of the reactive Fe(II) pool across tissues.
(**a**) Dot blots of puromycin incorporation in tissue homogenates from PC-3 xenograft bearing mice treated with the indicated doses of **2** or **3** via osmotic pump over 24 h then sacrificed and dissected for samples. Homogenates from each tissue were prepared via cryofracturing tissues and homogenizing in RIPA lysis buffer. Samples were normalized for total protein content prior to spotting and analysis with α-puromycin antibodies. (**b**) Quantification of puromycin incorporation in each tissue from mice treated with 25 mpk of free puromycin (**2**) or 100 mpk of trioxolane-conjugate **3**. (**c**) Puromycin incorporation in tissues from mice treated with 25, 50, or 100 mpk of **3** normalized to that in samples from the same tissues in mice treated with free puromycin (**2**) to account for tissue specific differences in rates of protein synthesis and puromycin incorporation.

Discussion

Studies of iron metabolism and intracellular labile iron pool have traditionally relied on fluorescent probes like Calcein-AM and PhenGreen-SK, or have employed iron chelators like deferoxamine and deferiprone[22,25,26]. However, Calcein and PhenGreen lack intrinsic binding selectivity iron over other metals (e.g. Ca^{2+}, Zn^{2+}, Mg^{2+}) and are experimentally challenging to use[29]. At the same time, iron chelators like DFO and deferiprone bind Fe(III) much more avidly than Fe(II) and can even compete for Fe(III) bound to ferritin, artificially perturbing the homeostatic system being studied[29]. Here we describe a new reactivity-based probe (**3**) that directly interrogates the intracellular iron species of greatest interest (labile ferrous iron) via an Fe(II)-dependent chemical reaction with a chemically optimized trioxolane scaffold. In contrast to traditional tools, probe **3** is useful at non-cytotoxic nanomolar concentrations and its novel mechanism of action involves neither the binding nor sequestration of the Fe(II) species being interrogated.

We also describe a high-content, plate-based immunofluorescence assay for puromycinylated proteins that has been optimized for applications involving probe **3**. Using this new methodology it is possible to profile large numbers of chemical and genetic manipulations to the labile iron(II) pool in parallel using automated processes. Our results indicate that this system can be used to detect even subtle changes in labile iron pools with significantly greater sensitivity than is achievable with previously reported fluorescent, reactivity-based probes of Fe(II) under comparable conditions[30,31].

Using the described methodology we observe changes in labile iron(II) levels induced by post-translational modulation of ferroportin levels with the biologically relevant peptide hormone hepcidin. Similarly, probe **3** detected altered labile iron(II) pools in cells where the iron export and storage proteins ferroportin and ferritin were overexpressed or knocked down. The impact of these genetic manipulations (separately or in combination) on labile iron(II) could be assessed and compared quantitatively using **3**. The system we have developed thus provides a useful methodology for studying the relative impact various perturbations, both chemical and genetic, have on the labile ferrous iron content of the cell.

Additional advantages of **3** and its companion assay include the flexibility of the antibody-based readout used. While our studies to date employed fluorophore labelled secondary antibodies, one could readily modify the assay to use primary or secondary antibodies labelled with a wide variety of detectable moieties (radiolabels, enzymes, nanoparticles, etc.). This flexibility not only allows for application-specific optimization but also makes the assay widely available for use without specialized equipment as simple measurements can be conducted with dot-blot analysis and chemiluminescent readers. Because puromycin incorporation occurs secondary to reaction with Fe(II), analysis of fixed cells or prepared organs/tissue can be performed at leisure without concerns of time-dependent loss of signal, etc. Naturally probe **3** will not be useful for imaging live cells or animals, nor for studying the sub-cellular distribution of labile iron in cells and thus will not replace fluorescent and other imaging probes for such applications. Nevertheless, due to the excellent sensitivity and throughput of the assays described here, probe **3**

should find general utility in studies of iron metabolism and cellular homeostasis. Significantly, the *in vivo* application of **3** further distinguishes this probe from previously reported turn-on fluorescent probes, which cannot be administered to animals and are useful only for *ex-vivo* analysis of tissue preparations [98].

Utilization of probe **3** to compare labile iron(II) pools across diverse cell lines revealed that the cancer cells profiled had significantly augmented iron pools compared to non-tumorigenic cells, a finding that is consistent with expectations based on existing knowledge about iron metabolism and its dysregulation in cancer[8]. Application of probe **3** *in vivo* in PC-3 xenograft models supported these findings, suggesting that, relative to endogenous tissues, tumors likely have increased concentrations of reactive iron(II). These results encourage further applications of our trioxolane-based scaffold to explore the selective delivery of cytotoxic payloads to cancer cells and tumor microenvironments.

Chapter 3: Leveraging the dysregulation of iron-metabolism in cancer as a trigger for selective drug delivery

The much-celebrated development of molecularly targeted cancer therapeutics in recent years has been accompanied by renewed interest in technologies for the tumor/cell-selective delivery of highly potent but intrinsically non-selective cellular toxins. Recent evidence suggests that an increase in reactive intracellular iron is another metabolic signature of cancer[8]. The results of our previous studies utilizing trioxolane-derived, reactivity based probes of cellular Fe(II) are consistent with this notion and indicate that many cancers have augmented reactive Fe(II) pools that could potentially be targeted (**Fig. 12**). Chemical methods to exploit differences in iron metabolism in cancer remain underdeveloped however, despite the fact that a pharmacological role for reactive ferrous iron species has clinical precedent in antimalarial therapy with the sesquiterpene endoperoxide artemisinin[32,99,100].

This chapter describes the application of trioxolane-drug conjugates in a novel tumor activated prodrug (TAP) strategy wherein augmented Fe(II) pools in cancer cells/tumor serve as the trigger for prodrug activation and drug release. This strategy allows us to selectively deliver extremely potent cytotoxins to cancer cells and tumor microenvironments, thus mitigating off target toxicities and increasing therapeutic windows for more efficacious application of potent cytotoxins.

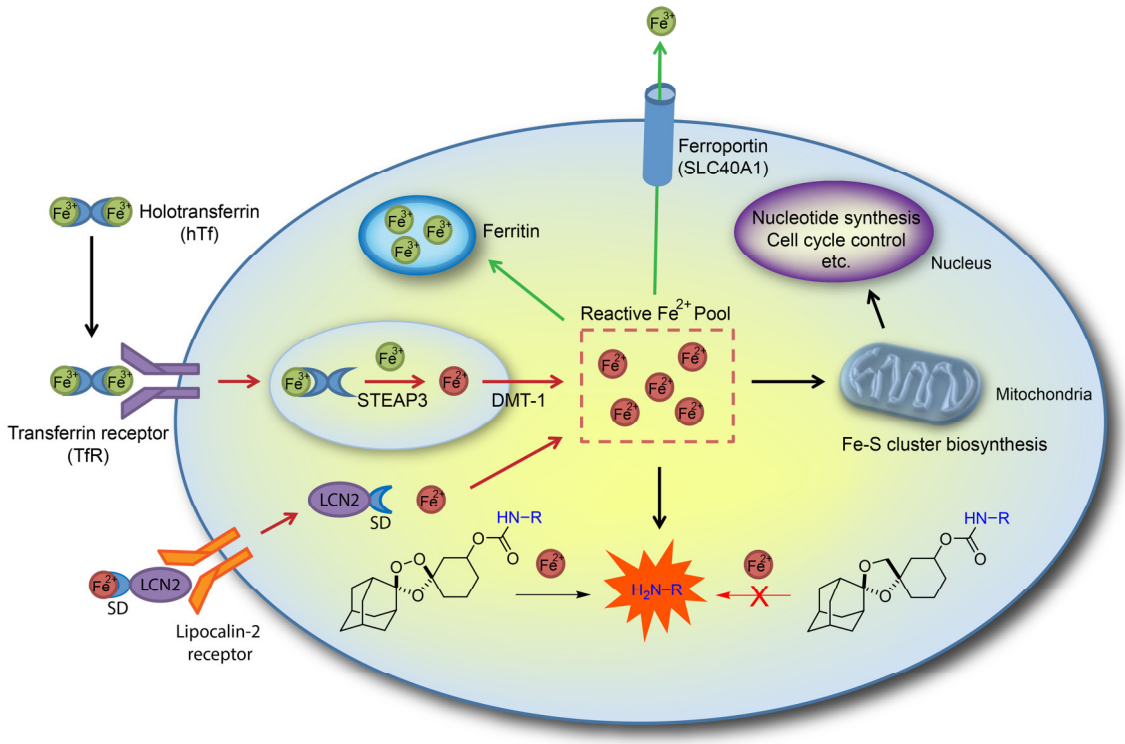

Figure 12: Trioxolane-mediated drug delivery strategies in cancer.
Iron metabolism is regulated through three distinct pathways: import (via transferrin receptor, lipocalin-2, etc.), storage (ferritin), and export (ferroportin). Specific nodes of iron metabolism act to increase (red arrows) or decrease (green arrows) iron pool and the sum of these processes modulate the size of the labile iron(II) pool. The novel tumor activated prodrugs described here leverage the dysregulation of the labile iron(II) pool in cancer by coupling the Fe(II)-specific reactivity of a 1,2,4-trioxolane to release of toxic payloads (H_2N-R). Bioisosteric probes lacking the peroxide bond (1,3-dioxolanes) are unreactive with iron(II) and thus constitute important controls.

Selective drug release strategies in cancer

There are two general classes of TAP strategies: those that seek to utilize differences in enzymatic activity to activate the prodrug, and those that seek to leverage differences in chemical environment between cancer cells and normal cells. Both strategies have advantages but also drawbacks which have limited their application.

Enzymatically activated prodrugs have been heavily researched for applications in cancer. These strategies generally work by either targeting endogenous differences in protein function or expression in cancer cells[101–107], or as part of more complicated targeting strategies involving exogenous enzymes delivered to the tumor via antibodies (ADEPT) or genetic engineering strategies (GDEPT and VDEPT)[108–110]. The use of exogenous enzymes is appealing both for reasons of selectivity and for efficiency of drug release, however the substantial difficulties associated with achieving selective delivery of enough enzyme to the target site in a safe manner have prevented clinically successful applications of these strategies[105,109]. Conversely, strategies taking advantage of changes in endogenous enzyme expression in tumors have seen some success in the clinic. Notable examples include prodrugs of 5-fluorouracil (5-FU) such as capecitabine (which is activated via multiple sequential enzymatic reactions[103]), and prodrugs activated by cytochrome P450's such as dacarbazine and cyclophosphamide[105,111]. This approach has inherent issues with selectivity however, as the endogenous enzymes which are leveraged tend to also be expressed in non-target tissues (albeit at lower levels). Furthermore, as these strategies rely on the expression and activity of their target enzymes for drug activation it is relatively easy for tumors to escape exposure to the active drug. By simply altering the expression or activity of that enzyme the cancer cells can prevent release of the active drug, thus making such approaches sensitive to resistance and recrudescence after treatment.

Tumor activated prodrug strategies that seek to leverage changes to the chemical environment within the tumor have also been explored[112–117]. These strategies have

thus far focused on the hypoxic tumor environment induced by poor tumor vasculature and leaky blood vessels[118]. This environment is well known to reduce the effectiveness of radiotherapy[119] and standard chemotherapies[117]. Substantial effort has thus gone into targeting the hypoxic environment of solid tumors. Most strategies have focused on modifications of parent drugs to relatively non-toxic prodrugs that are prone to reduction and activation via single electron reductases such as P450's whose activity is promoted by the hypoxic environment of the tumor. This reduction can then produce the toxic, radical-based effector or in many cases an intermediate that is then back-oxidized or further processed to yield the toxic species[117].

Such strategies have seen some success in the clinic as evidenced by tirapazamine, a prodrug which is reduced under hypoxic conditions to yield a highly reactive radical capable of inducing double-strand breaks in DNA[114,120]. Initial cell culture studies suggested tirapazamine possessed significant selectivity for killing hypoxic cells over oxic cells (50-300 fold therapeutic window)[120]. Subsequent mouse studies however showed only a 3-fold difference in toxicity between hypoxic and oxic cells and consistent with these results, clinical applications of tirapazamine as a single agent have unilaterally failed[120]. Applications in combination with radiotherapies and cisplatin have seen more success however, and this compound was found to synergize with both radiotherapy and cisplatin in solid tumors, presumably due to its ability to kill the hypoxic cells which are resistant to other therapies. Clinical results have been variable however, and in some cases tirapazamine was found to enhance off-target toxicities[114]. While the application of hypoxia activated prodrugs

in combination with standard chemotherapies remains an appealing strategy to target the hypoxic core of many solid tumors, substantial off-target toxicities have often be found to limit applications, suggesting that this approach may suffer from selectivity issues[114,117]. One contributing factor may be the highly heterogeneous nature of tumor hypoxia as changes to blood flow and oxygen tension have been found to vary substantially even within different regions of the same tumor[114]. The fact that hypoxia activated prodrugs generally rely on enzymatic reduction could also contribute to issues with efficacy and resistance due to tumor heterogeneity in expression of the requisite enzymes[114].

Our previous results with trioxolane derived reactivity-based probe **3** suggest that many cancer cells have substantially dysregulated iron metabolism and larger pools of labile Fe(II) species. This dysregulation is thought to be induced by the need for Fe(II) as a critical co-factor in many enzymes involved in growth and cell maintenance, making Fe(II) a required nutrient for growth. This dysregulation thus induces an Fe(II)-rich chemical environment that could, in principle, be exploited as a trigger for selective drug release in a novel TAP approach. This strategy could have advantages over enzymatic approaches as such an environment might be more challenging for the cancer cell to alter in order to avoid TAP activation and exposure to active drug.

Trioxolane-mediated delivery of cytotoxic agents to cancer cells

To explore whether trioxolane-based Fe(II)-dependent payload release strategies could be used to release toxic payloads in cancer cells we synthesized a known small molecule microtubule toxin (**5**)[121] and its trioxolane conjugate **6** (**Fig. 13a and Supplementary Scheme 3**). In contrast to puromycin and other amines we have conjugated in the past, we found electron-poor anilines to react poorly with *para*-nitrophenylcarbonates resulting in low yields. Carbamate formation was thus achieved via reaction of the trioxolane alcohol intermediate with an isocyanate, which was in turn prepared from the action of phosgene on the aniline. In the case of aniline **5**, this approach provided the trioxolane conjugate **6** in good yield. A non-peroxidic dioxolane conjugate (**7**) was prepared in an analogous manner to confirm that the cytotoxicity of **5** is ablated while in conjugated forms and that intracellular release of active **5** from **6** is peroxide-dependent (**Fig. 13a and Supplementary Scheme 3**). We further utilized a previously reported trioxolane analog (**8**)[90] lacking the toxin **5** as a control for the intrinsic cytotoxicity of the peroxide moiety (**Fig. 13a**).

The cytotoxicity of the trioxolane conjugate **6** and control compounds **5**, **7**, and **8** were assessed across a small panel of cell lines. The results were unequivocal. In MDA-MB-231 cells, trioxolane-conjugate **6** displayed efficacy in the low nM range (EC_{50} = 21 nM), three orders of magnitude more potent than either of the negative controls (**7** or **8**), and nearly as potent as the free payload (**5**) applied directly (EC_{50} = 11 nM) (**Fig. 13b**). These results confirm the efficient, peroxide-dependent release

of **5** from trioxolane-conjugate **6** in cancer cells. Moreover, the lack of measurable toxicity exhibited by **7** demonstrates that the intrinsic cytotoxicity of **5** can be effectively blocked in the conjugated form, a highly desirable feature of the scaffold for therapeutic applications.

Normalizing the efficacy of the trioxolane-conjugate **6** to that of its cytotoxic payload (**5**) provided an "EC_{50} ratio" – a convenient metric to measure the efficiency of payload release from **6** across cell lines. In MDA-MB-231 cells, this ratio was found to be 0.54 (EC_{50} = 11 nM and 21 nM for **5** and **6**, respectively). Amongst the other cell lines examined, U-2 OS and RKO cells were nearly as sensitive to **6** as MDA-MB-231 cells, with EC_{50} ratio of 0.46, while PC-3 and HeLa cells were somewhat less sensitive (EC_{50} ratio of 0.30-0.32), though **6** was still effective in these cells at therapeutically relevant, low-nM concentrations (**Fig. 13d and Supplementary Table 2**). Consistent with the smaller reactive iron pool we previously observed in non-tumorigenic cells (**Fig. 9c**), MCF10A cells were highly resistant to the trioxolane-conjugate **6** with an EC_{50} ratio of just 0.04 (**Fig. 13c-d**). While this is an extremely encouraging finding, some caution is warranted in comparing these ratios given that the MCF10A cells require different cell culture media which could contribute to the observed differences.

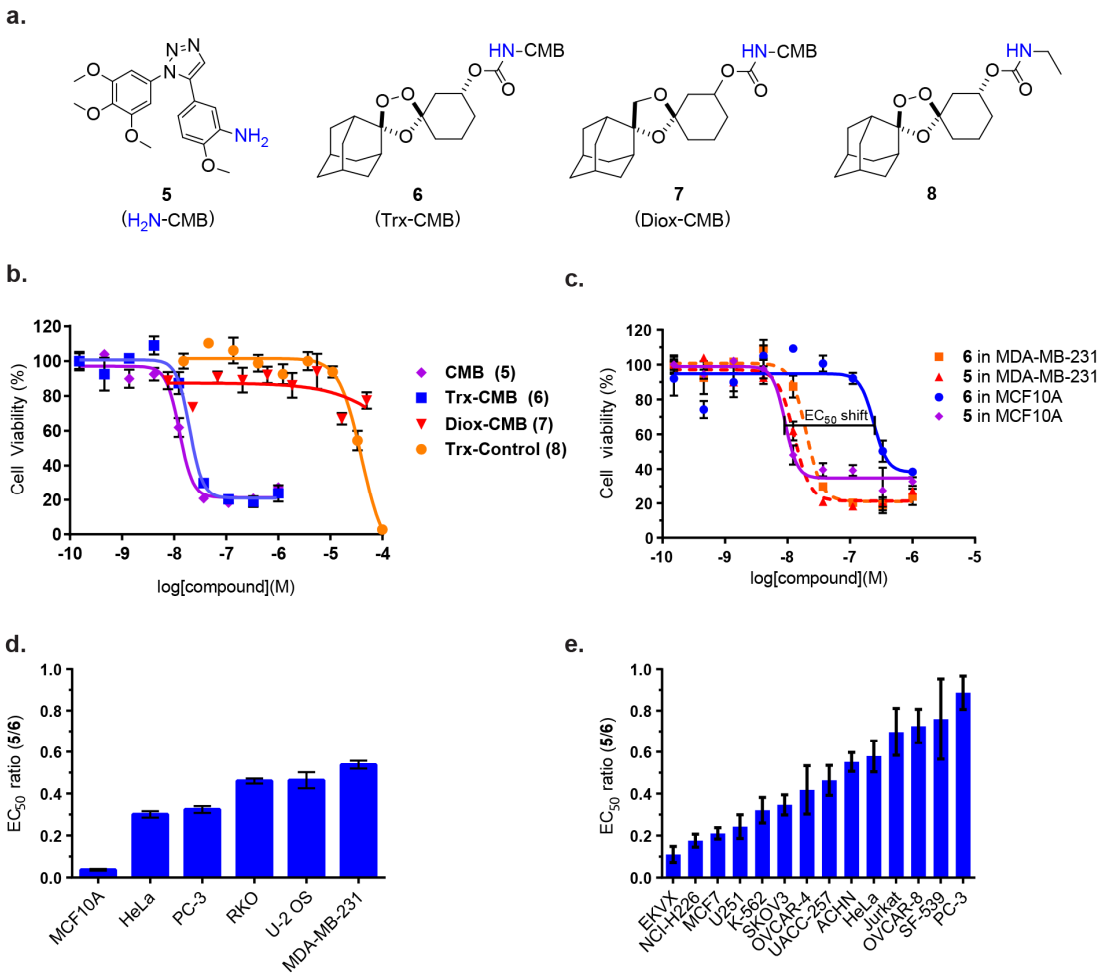

Figure 13: Exploiting augmented reactive iron pools for selective drug delivery

(**a**) Chemical structure of microtubule inhibitor **5** and corresponding conjugates and controls **6-8**. (**b**) Cytotoxicity of compounds **5-8** in MB-MDA-231 cells after 24 h of exposure as determined by cell counting (n=3; error bar, mean ± s.e.m.). (**c**) Cytotoxicity of **1** and its trioxolane-conjugate **6** in MDA-MB-231 and MCF10A cells as determined by cell counting (n=3; error bar, mean ± s.e.m.). The shift in EC_{50} value for **5** and its trioxolane conjugate **6** is illustrated. Dividing the EC_{50} value for **5** by that for **6** in a given cell line produces an "EC_{50} ratio" that is used to compare the efficiency of drug release across cell lines. This ratio is 0.54 for the sensitive MDA-MB-231 cells (2-fold EC_{50} shift), and 0.04 for the resistant, non-tumorigenic MCF10A cells (25-fold EC_{50} shift). (**d**) EC_{50} ratios calculated as described in (c) for a small panel of cell lines. Error bars represent s.e.m. from three experiments conducted in triplicate. (**e**) EC_{50} ratios for an expanded panel of mammalian cell lines. The EC_{50} values for **5** and **6** were determined after a 72 hour incubation using the CellTiter-Glo® cell viability assay. Error bars represent s.e.m. (n = 3).

Encouraged by our initial findings we next explored the cytotoxicity of **5** and **6** across a larger panel of cancer cell lines from diverse origins using a CellTiter-Glo® assay to assess viability (**Fig. 13e**). We observed a range of sensitivities to **6** across the different cell lines, with EC_{50} ratios ranging from 0.89 for PC-3 cells (**5** and **6** essentially equipotent) to 0.11 for EKVX cells (9-fold shift in EC_{50}). Even the least sensitive cancer cell line produced an EC_{50} in the nM range for conjugate **6** and most showed less than a three-fold shift in EC_{50} from the free payload **5** (**Supplementary Table 3**), suggesting that this approach could be broadly useful for the delivery of cytotoxic chemotherapeutic agents.

Profiling the effects of oncogenic transformation on iron metabolism and sensitivity to trioxolane-conjugates

Considering the possible therapeutic applications of this TAP approach, we were interested in exploring how oncogenic transformations alter the reactive iron pool in cells and if oncogene induced changes would sensitize cells to payload delivery from trioxolane conjugates. The Bandyopadhyay lab at UCSF has previously reported the generation of a library of non-tumorigenic MCF10A derived cell lines constitutively expressing a panel of known oncogenes[122]. This panel represented an excellent opportunity to study the effects of oncogene expression on cellular iron metabolism. Accordingly, we employed trioxolane-conjugate **6** and transcriptional profiling to study the effects of the oncogenes Ras and Myc, which have previously been associated with changes in iron metabolism[8,17,20]. First, we used qRT-PCR to evaluate the transcriptional profile of iron regulatory proteins in MCF10A cells

constitutively expressing the oncogene Hras[122]. In contrast to literature reports[19], we observed no significant transcriptional changes that would contribute to an increased reactive iron pool (**Fig. 14a and Supplementary Fig. 9**). Consistent with these findings, no increase in sensitivity to **6** was observed for MCF10A cells overexpressing Ras as compared to those transformed with the empty vector (**Fig. 14b**). In contrast, when we examined Myc transformed MCF10A cells, we observed substantial down regulation of the iron exporter ferroportin and up regulation of the ferrireductase STEAP3 when compared to MCF10A cells transformed with the empty vector (**Fig. 14a**). Both of these changes predict for an increased reactive iron pool (**Fig. 1** and **2**). Consistent with these findings, the Myc-transformed MCF10A cells were found to be more sensitive to trioxolane-conjugate **6** than cells transformed with the empty vector as evidenced by a significant 3.2-fold shift in the EC_{50} ratio (**Fig. 14b**). These results suggest that oncogene induced changes to the reactive iron pool can sensitize cells to the delivery of potent cytotoxins from trioxolane-conjugates in an otherwise isogenic background.

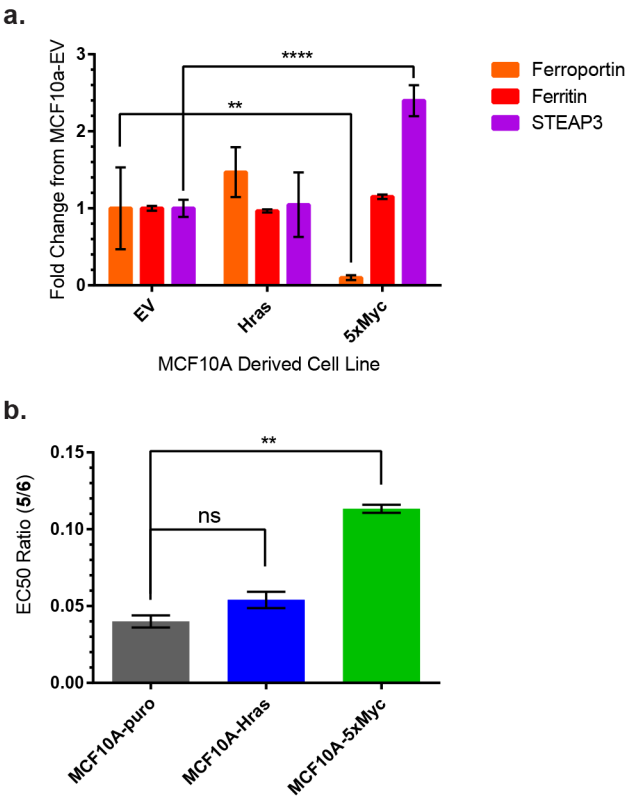

Figure 14: Profiling the effects of oncogenic transformation on the Fe(II) pool of MCF10A cells. (**a**)Relative mRNA levels for ferroportin, ferritin, and the ferrireductase STEAP3 in MCF10A cells stably transfected with empty vector (control) or with vectors expressing the oncogenes Myc or Hras (n=3; error bar, mean ± s.e.m.; **P≤0.01, ****P≤0.0001, Two-Way ANOVA with Dunnett's multiple comparisons test). (**b**) EC_{50} ratio (**5/6**) for MCF10A cells stably transfected with H-ras or c-Myc oncogenes as compared to the empty vector (control). Error bars represent s.e.m from three independent experiments conducted in triplicate (**P≤0.01, One-Way ANOVA)

Development of trioxolane-conjugates of highly potent DNA alkylators

Encouraged by our findings with the microtubule inhibitor conjugate (**6**) we sought to expand upon the strategy by employing a well-known class of highly potent and cytotoxic DNA-alkylators based on the natural product duocarmycin[123,124]. Accordingly, we masked the *seco*-form of a previously reported amino-cyclopropylbenzindoline analog (amino-CBI) (**9**)[125] by conjugating at the aniline

position to form the desired trioxolane-CBI conjugate (**10**) and negative control dioxolane-CBI conjugate **11** (**Fig. 15a**). We again utilized formation of the isocyanate intermediate to facilitate formation of the desired carbamate conjugates. In contrast to the isocyanate of combretastatin analog **5** which was stable enough to observe via LCMS analysis, the isocyanate of **9** was found to be highly unstable and neither LCMS nor TLC analysis were useful for following the progress of the reaction. Instead, small aliquots of the reaction mixture (ca. 10 μL) were sampled and quenched with excess benzylamine (ca. 10 μL) to form a stable urea *in situ* and the reaction was determined complete when no sign of the starting amine was observed in samples thus prepared. Upon completion of the reaction, solvent was removed *in vacuo* and the resulting red solid was dried on high vacuum for > 1 h to remove residual phosgene. The crude isocyanate was then dissolved in a minimal volume of a solution of the requisite alcohol in DCM which had been dried over 4 Å molecular sieves. To facilitate and accelerate this bimolecular reaction, we found it was helpful to slowly concentrate the reaction mixture by passing an argon stream over the solution until the reaction was deemed complete (24-48 h). Notably, this procedure produced substantially improved yields as compared to previously reported procedures for formation of carbamate analogs of the same amino-CBI analog **9** (60-80% vs 25% previously[126]).

The *seco*-form of amino-CBI analogs such as **9** is known to spontaneously cyclize in aqueous solution to give the highly electrophilic cyclopropylbenzindoline species. We found that **9**, which is known to slowly hydrolyze in solution after cyclization[126], was substantially stabilized by carbamoylation of the aniline. Thus while free **9**

degraded over a matter of hours after thawing a DMSO stock solutions at room temperature, the conjugates **10** and **11** were found to be completely stable for more than a year at room temperature in DMSO (**Supplementary Fig. 10**). No traces of released payload (**9**) or any cyclization or hydrolysis byproducts were observed from either **10** or **11** (**Supplementary Fig. 10**). More importantly, trioxolane-conjugate **10** was found to be completely stable in cell culture media for over a week at 37 °C indicating the conjugate has substantially improved stability over the free payload **9** and excellent properties for cell culture studies.

In cell culture studies trioxolane conjugate **10** was found even more potent than free drug payload (**9**) in both MDA-MB-231 and PC-3 cells with a sub-nanomolar EC_{50} reflecting the increased stability of **9** in conjugated form (**Fig. 15b-c**). Given that the dioxolane conjugate (**11**) we prepared as a negative control was found to be completely non-toxic at all concentrations tested, the peroxide-dependent toxicity of **10** indicates efficient intracellular release of payload **9** from **10**induced by labile Fe(II) of the cancer cells, consistent with our previous findings with other trioxolane-conjugates.

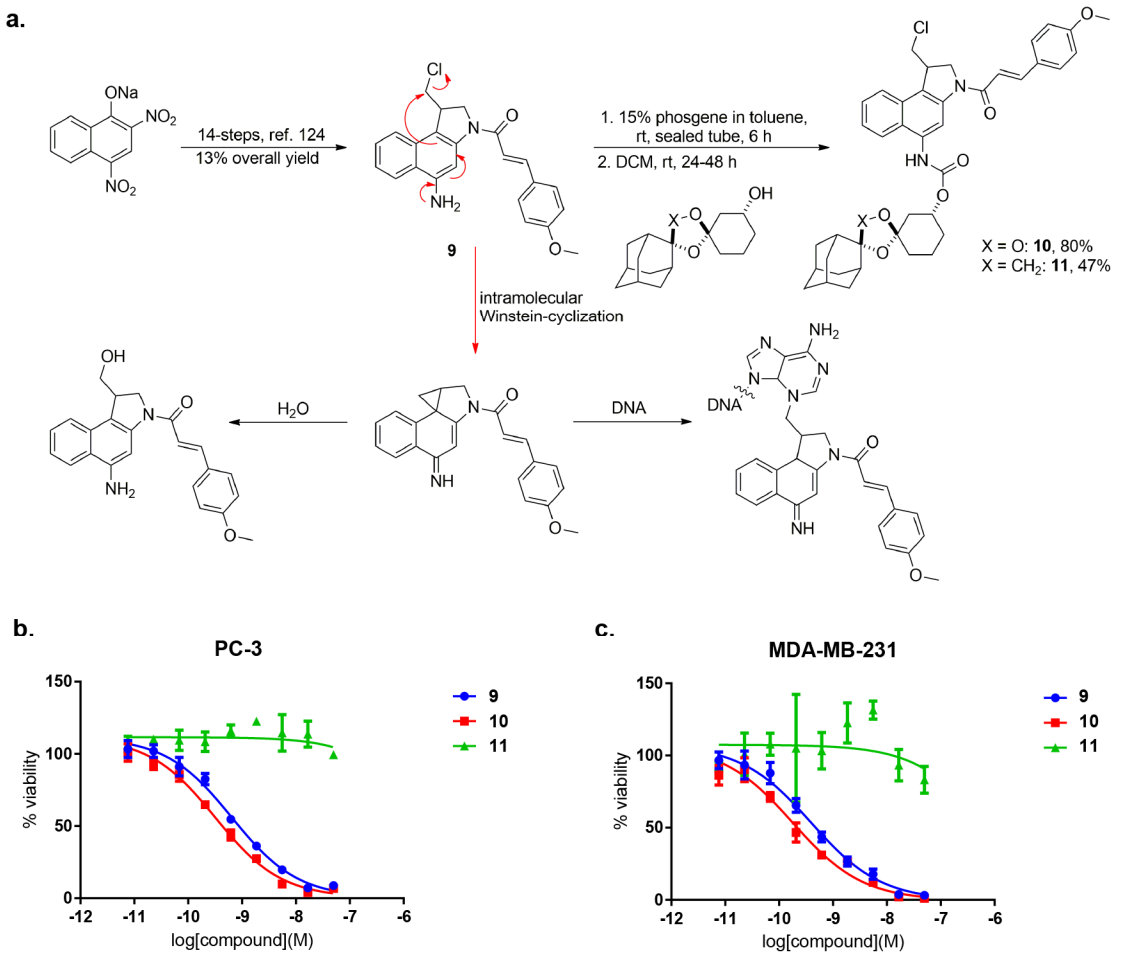

Figure 15: Synthesis and in vitro characterization of amino-CBI conjugates.
(**a**) Synthesis of DNA-alkylator **9**, trioxolane-conjugate **10**, and negative control dioxolane-conjugate **11**. Compound **9** will spontaneously cyclize in solution to give the active cyclopropylbenzindoline alkylator shown below it. That species is then prone to hydrolysis as observed in Supplementary Figure 10. (**b**) Cytotoxicity of compounds **9-11** in PC-3 cells after 72 h of exposure as determined by cell counting (n=3; error bar, mean ± s.e.m.). (**c**) Cytotoxicity of compounds **9-11** in MB-MDA-231 cells after 72 h of exposure as determined by cell counting (n=3; error bar, mean ± s.e.m.).

Pharmacokinetics and safety of trioxolane-drug conjugates

Encouraged that conjugation of **9** to the trioxolane scaffold appeared to not only stabilize the parent drug payload but also to mask its toxicity until Fe(II)-mediated

payload release, we were interested in studying the toxicity and efficacy of **10** *in vivo*. Dose escalation studies in non-tumor bearing NSG mice illustrated that the free drug (**9**) is highly toxic to mice with a maximum tolerated dose (MTD) of 0.3 mg/kg when dosed three times at four day intervals via i.p. administration, consistent with previous observations of similar analogs[125]. In contrast, the trioxolane-conjugate (**6**) was 25-fold better tolerated with an MTD of 7.5 mg/kg using the same dosing regimen.

Pharmacokinetic studies revealed the rapid disappearance of **9** after a single i.p. dose ($t_{1/2}$ = 3.8 h) while conjugate **10** displayed a significantly longer half-life ($t_{1/2}$ = 20.4 h), likely reflecting the improved aqueous stability of the conjugate (**Fig. 16a-b**, **Supplementary Table 4**). At early time points, low concentrations of the cyclohexanone intermediate arising from trioxolane cleavage were observed in plasma from mice treated with **10** suggesting a small amount of instability *in vivo*. Correspondingly, small amounts of free **9** were also noted in these samples as would be expected following the spontaneous retro-Michael reaction. The maximum plasma concentrations of free **9** observed in mice treated with 7.5 mg/kg of **10** were lower than that observed in mice treated directly with 0.3 mg/kg of **9** (C_{max} = 48 ng/mL vs 108 ng/mL respectively) however, overall exposure to **9** over 24 h was somewhat higher in mice treated with **10** than in mice treated with **9** ($AUC_{0\text{-}24\ h}$ = 641 h*ng/mL vs. 246 h*ng/mL respectively). This was presumably due to the gradual release of small amounts of free **9** from **10** *in vivo* resulting in prolonged exposure to **9**. While the small amounts of released **9** observed in these studies could well contribute to off-target toxicities, **10** was still expected to

possess an enhanced therapeutic index compared to **9** due to the substantially increased exposure achievable with conjugate **10** at its MTD ($AUC_{0\text{-}24\ h}$ = 5050 h*ng/mL) (**Fig. 16a-b, Supplementary Table 4**). As **10** is expected to release its payload predominantly within tumor in the context of xenograft models we expected that the increased exposure achievable with **10** would translate to increased efficacy at the MTD.

As compounds like **9** have been previously shown to cause dose-limiting hepatotoxicity when dosed in mice[127], we explored whether administration in the conjugate form **10** could protect from these toxicities. Consistent with this hypothesis, blood tests revealed substantial induction of liver enzymes in mice treated with **9** at MTD while normal levels were observed in mice treated with **10** at its higher MTD, apparently reflecting significantly reduced exposure to free payload (**9**) in the livers of mice treated with **10** (**Fig. 16c**).

The hepatotoxicity of duocarmycin-class toxins like **9** has been observed to occur with a delayed onset so we followed the mice for a minimum of 50-days post dosing then collected livers from the treated mice and assessed them for altered morphology and signs of toxicity. Even at tolerated doses mice treated with **9** had altered liver morphology and texture indicative of hepatotoxicity in addition to enlarged intestines and serosanguinous ascites near the site of administration. In contrast, the livers of mice treated with 7.5 mg/kg of **10** appeared normal and the dose limiting toxicity appeared to be localized toxicity at the site of administration as evidenced by enlarged intestines.

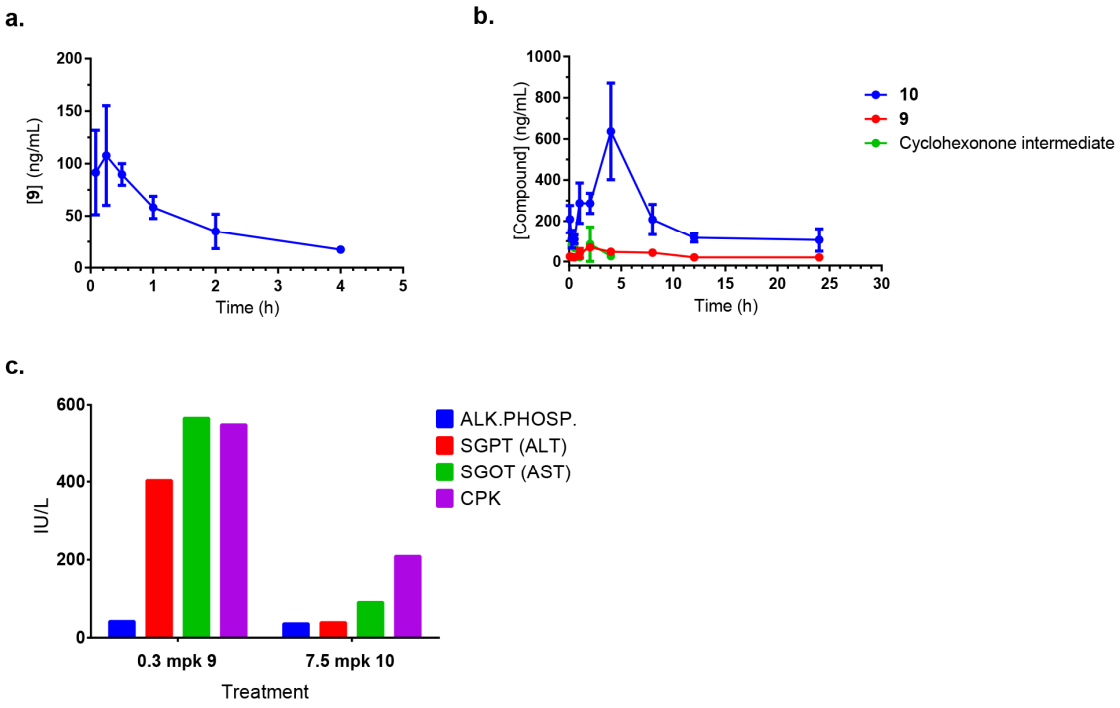

Figure 16: Pharmacokinetics and tolerability of amino-CBI conjugates in non-tumor bearing NSG mice.

(**a**) Plasma concentrations of **9** in mice following a single 0.3 mg/kg doses of **9** via i.p. administration in NSG mice. (**b**) Plasma concentrations of **10** and the cyclohexyl intermediate produced by iron-mediated trioxolane cleavage as well as free **9** in mice following a single 7.5 mg/kg dose of **6** via i.p. administration. (**c**) Alkaline Phosphatase (Alk. Phos.), serum alanine aminotransferases (ALT), aspartate aminotransferase (AST) levels, and creatine phosphokinase (CPK) levels in blood samples from mice treated with either free **9** (0.3 mg/kg) or trioxolane-conjugate **10** (7.5 mg/kg).

Studying the fate of the cyclohexenone byproduct

A potential concern with utilizing trioxolane-conjugates of this chemotype *in vivo* is the formation of potentially reactive cyclohexenone byproduct from the payload-releasing retro-Michael reaction. This α,β-unsaturated ketone could, in principal, react with intracellular nucleophiles to produce protein adducts that might induce immune reactions or other toxicities. As glutathione represents the most prevalent intracellular nucleophile, we prepared a mass-labeled glutathione (GSH) adduct of

cyclohexenone (**12**) to explore the fate of this species *in vivo.* This GSH adduct (**12**) was dosed to male BALB/c mice i.v. and plasma samples were analyzed over time for concentrations of **12** as well as any 'light' GSH conjugate (**13**) that would arise from exchange with endogenous GSH (**Fig. 17**). Encouragingly, we observed that **12** was cleared rapidly (124 mL/min/kg) with a half-life of only 6.6 min. We observed a very small concentration of endogenous glutathione adducts (**13**) within the first 10 min after treatment. This finding indicates that rate of clearance of the GSH conjugate is significantly greater than rates of retro-Michael reaction/Michael addition of endogenous GSH. These data are consistent with previous toxicity studies of cyclohexenone in rats, where daily doses of up to 100 mg/kg were tolerated with no observable toxicity and the compound was found to be cleared rapidly as glucuronide adducts[128]. Trioxolane-drug conjugates should thus be able to be applied *in vivo* without significant concern of toxicities arising from the formation of cyclohexenone during the process of drug release.

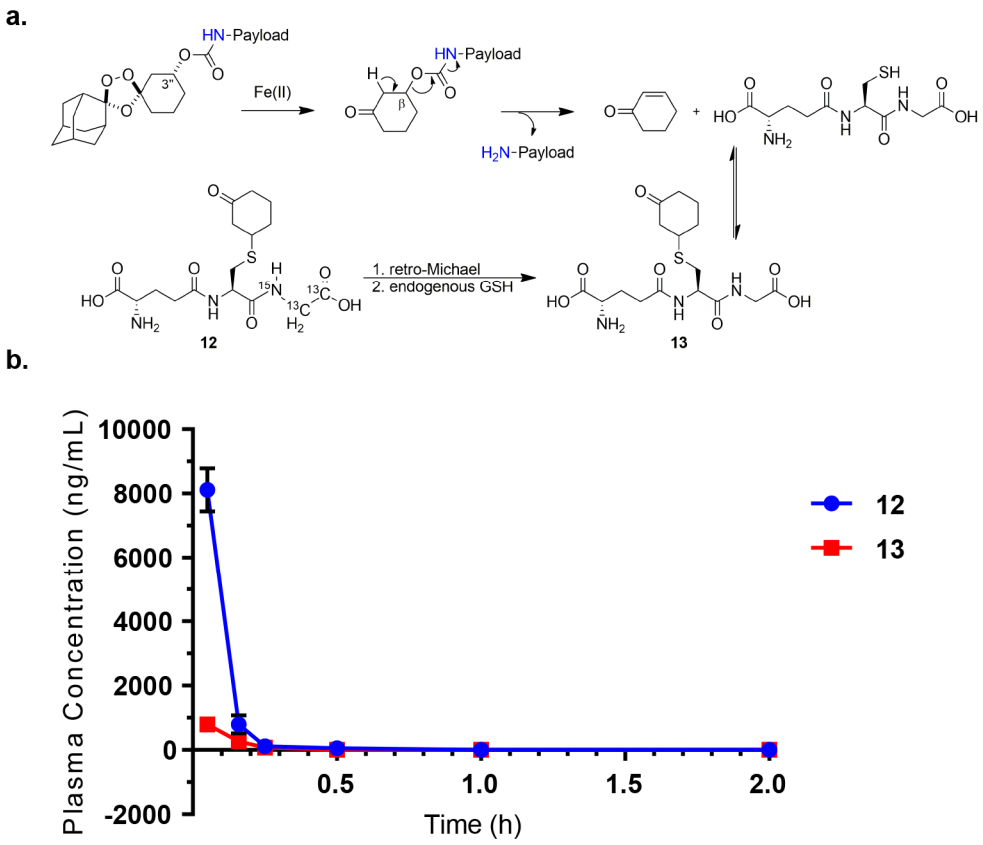

Figure 17: Clearance of glutathione adducts of the produced cylcohexenone in mice
(**a**) Scheme illustrating the formation of cyclohexenone as a byproduct of payload release from trioxolane-conjugates and the potential reactivity of cyclohexanone with cellular nucleophiles such as glutathione. (**b**) Plasma concentration levels of the glutathione conjugate **12** following a single intravenous dose of 10 mg/kg in male BALB/c mice. Samples were also analyzed for the presence of non-mass labelled conjugates (**13**) that would arise from exchange of glutathione.

Efficacy of trioxolane-drug conjugates in xenograft models

Confident that trioxolane conjugate **10** safely masks the toxic payload **9** prior to Fe(II)-mediated release, we next sought to confirm that **10** retained efficacy against tumors *in vivo*. For these studies we chose to make xenografts from two cell lines from diverse origins, PC-3 and MDA-MB-231 cells, which had augmented reactive

Fe(II) pools in our previous studies (**Fig. 9**) and were shown to be sensitive to conjugate **10** in cell culture experiments (**Fig. 15**). We thus treated PC-3 and MDA-MB-231 xenograft bearing mice with trioxolane-conjugate (**10**) or the free payload (**9**) and compared body weights and rates of tumor growth under the different dosing conditions (**Fig. 18a-d**). In MDA-MB-231 xenograft mice **9** was found to confer a minor reduction in tumor growth rate when dosed at the MTD, consistent with previous preclinical and clinical applications of duocarmycin-like drug candidates[129] (**Fig. 18a**). Significantly, at these doses compound **9** caused substantial weight loss in the treated mice, reflecting poor tolerability of the compound and a negligible therapeutic window for *in vivo* applications (**Fig. 18b**). In contrast, mice treated with 2.5 mg/kg of the trioxolane conjugate **10** showed identical levels of tumor growth inhibition while showing negligible weight loss, effectively demonstrating that the conjugate (**10**) is capable of masking off-target toxicities while still delivering the active payload (**9**) to the tumor environment (**Fig. 18a**). Increasing the dose of **10** to the MTD of 7.5 mg/kg gave substantially better efficacy than obtained with the MTD of **9** while maintaining better tolerance (**Fig. 18a-b**). Consistent with the expected peroxide-dependence of delivery, dioxolane control **11** produced no effect on tumor growth at doses equivalent to efficacious doses of trioxolane conjugate **10** (**Supplementary Fig. 11**). In PC-3 xenograft-bearing mice a similar trend was observed, with **10** being substantially better tolerated at equipotent doses (**Fig. 18c-d**).

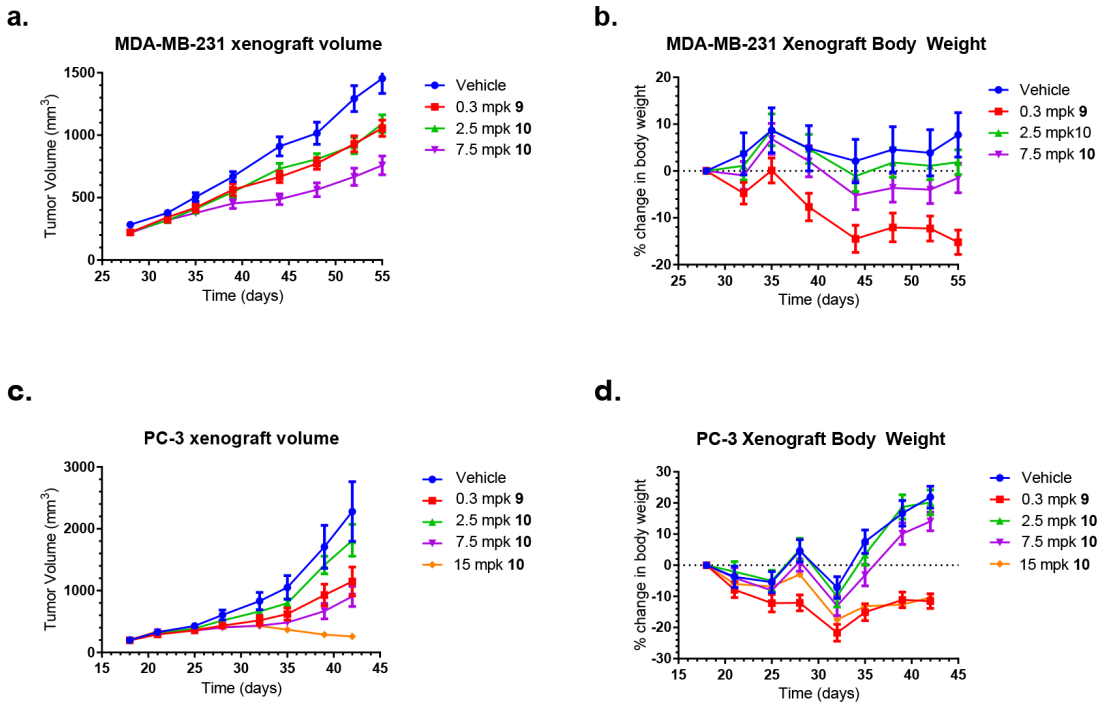

Figure 18: Efficacy of amino-CBI conjugates in mouse xenograft models.
(**a**) Changes in tumor volume over time as determined by calipers in MDA-MB-231 xenograft bearing mice treated with the indicated doses of **9** or **10** on days 28, 32, and 36 as compared to mice treated with vehicle. (**b**) Changes in mouse weight over time for the mice in (a). (**c**) Changes in tumor volume over time as determined by calipers in PC-3 xenograft bearing mice treated with the indicated doses of **9** or **10** as on days 17, 21, and 25 (or 17, 24, and 31 for 15 mg/kg dose) compared to mice treated with vehicle. (**d**) Changes in mouse weight over time for the mice in (c).

As the MTD and pathology studies revealed that the dose limiting toxicity of conjugate **10** appeared to be localized G.I. toxicity near the site of administration rather than hepatotoxicity as observed with **9**, an effort was made to explore alternate dosing regimens which might mitigate these toxicities. By extending the interval between doses to a week, the dose of **10** could be increased to 15 mg/kg in PC-3 xenograft bearing mice while realizing similar tolerance as free drug **9** at the MTD. Excitingly, this altered dosing regimen produced robust tumor regression (**Fig. 18c**). The effect on tumor growth was found further to be quite durable with

no evidence of further growth observed for the remainder of the study, several weeks after the final dose. Together, these results illustrate that trioxolane-conjugate **10** is able to effectively rescue the potent, yet non-specific cytotoxin **9** for effective therapeutic applications in multiple contexts via selective, Fe(II)-dependent, payload release within the tumor microenvironment.

Discussion

The trioxolane-based, Fe(II)-dependent prodrug strategy developed herein has several appealing characteristics from a therapeutic standpoint. Concentrations of unbound Fe(II) in blood and plasma have been estimated to be vanishingly small, implying excellent extracellular stability of the system[5]. As iron metabolism is also rigorously controlled intracellularly to avoid excess exposure to reactive Fe(II)-species in normal tissues our system appears to be highly selective for releasing payloads in cancer cells and tumors where this regulation has been substantially altered[8]. This is evidenced by the resistance of non-tumorigenic cells lines to trioxolane conjugates we observed in cell culture and the observed 55-fold increase in MTD for trioxolane-conjugate **10** over the free drug **9** when dosed weekly. By harnessing this selectivity to mask highly potent yet intrinsically non-selective cytotoxins such as **9** we were able to achieve excellent on-target activity and tumor regression while mitigating off-target toxicities that previously limited efficacious applications. Importantly, this strategy is potentially applicable to a wide range of known cytotoxins given the broad scope of the conjugation chemistry. Trioxolane-based prodrugs might thus be utilized not only to “rescue” compounds too cytotoxic

for therapeutic use such as those illustrated here, but also to improve the efficacy and side effect profile of diverse classes of approved cancer therapeutics (e.g. kinase inhibitors, PARP inhibitors, imides, etc).

The flexibility to utilize a wide variety of toxic effectors represents a substantial benefit of this strategy over previously reported approaches seeking to leverage changes in the chemical environment of the tumor (i.e. hypoxia) which have been found serendipitously or developed on a case by case basis. By carefully exploring a wide array of potential partner drugs for conjugation the trioxolane-based drug delivery platform described here can be readily optimized for a given application. The ability to select an appropriate toxin can thus allow trioxolane-based drug delivery systems to be efficacious as single agents unlike previously reported hypoxia activated prodrugs such as tirapazamine.

From a practical standpoint, the ease of development of trioxolane-based drug delivery systems provides a substantial benefit over more complicated strategies such as ADEPT, VDEPT, and GDEPT. These approaches rely on the delivery of exogenous enzymes to the tumor via antibody-protein conjugates or gene therapy approaches. If the exogenous enzyme can be delivered safely and in sufficient quantities to the tumor then drugs can be released in a highly selective and efficient manner within the tumor; however, the extensive technical challenges associated with this process and the dangers of gene therapy approaches have thus far precluded the successful application of such complicated strategies. In comparison, the trioxolane-based drug delivery platform described here relies on the simple

chemical activation of the prodrug by the augmented reactive Fe(II) pools in cancer cells induced by their increased metabolic demands.

To the best of our knowledge, the trioxolane-based prodrugs reported here represent the first example of a prodrug system that exploits a nutrient that is dysregulated in cancer cells as a trigger for selective drug release. This strategy could provide significant advantages over other targeted cancer therapeutics that rely on the expression of a single protein to provide therapeutic benefit such as molecularly targeted therapies (i.e. gleevec) and enzymatically activated TAPs. Such therapies can be relatively easy for cancers to circumvent via mutation to the target protein; resistance and recrudescence is thus a major issue in the field. By instead targeting an altered metabolic state that is both a consequence and requirement for rapid cell-growth (i.e., augmented labile ferrous iron), we hypothesize that our approach may be less susceptible to resistance than single-protein targeted therapies. Consistent with this hypothesis we observed excellent durability of response in xenograft models dosed with trioxolane-conjugate **10**.

We have thus leveraged the intrinsic reactivity of the trioxolane moiety to develop an Fe(II)-triggered drug release platform that is efficacious against human cancer lines in culture and xenograft models. Our promising results encourage further studies in genetic cancer models and patient-derived xenografts to define the scope and optimal applications for the strategy. Further research exploring additional examples of partner drugs optimized to provide on-target efficacy to tumor targets while mitigating off-target systemic toxicities are also warranted. Overall, our

initial results suggest these systems may be able to substantially improve therapeutic windows for a number of known cytotoxins and approved drugs to afford more efficacious and better tolerated treatment regimens.

Chapter 4: Development of trioxolane-based tumor-selective cleavable linkers for antibody drug conjugates

Encouraged by the successful application of trioxolane-derived payload delivery systems to selectively target cancer cells, we were interested in exploring further expansions of the technology. An exciting and active area of research in cancer therapy is the field of antibody-drug conjugates (ADCs). ADCs are an example of active targeting TAP strategies that seek to utilize antibody recognition of cancer specific epitopes to facilitate the delivery of extremely potent cytotoxins to cancer cells. Given the success of trioxolane-conjugates as passive (not actively targeted) TAPs we felt that combination with an active targeting moiety like an antibody could prove a synergistic approach to further enhance the selectivity of delivery.

Active targeting TAP approaches:

Active targeting strategies that deliver drug payloads to tumor microenvironments have seen a wealth of attention recently due to the success of the ADC's brentuximab vedotin and trastuzumab emtansine in the clinic[130,131]. These approaches seek to target cell surface receptors or nutrient transporters (e.g. folate) to exploit active uptake of the drug conjugates into the cell. Such systems commonly consist of three components: the targeting moiety, a small molecule or protein toxic payload, and a linker used to connect the two[132,133]. All three components are critical determinants of efficacy and as such have been extensively studied[131,133–136].

While antibody-based strategies have seen the most attention recently, a wide variety of active targeting moieties have been previously explored, from actively transported small molecule nutrients like folate[137–140], to carrier proteins like transferrin that are endocytosed at their cognate receptor[141,142]. Of these, only antibody-based strategies have seen clinical success, though recent preclinical and clinical trials with folate-drug conjugates have shown some promise[138,140,143]. Regardless of targeting moiety, all of these strategies struggle with issues arising from heterogeneity in target receptor expression and presentation on tumor cells[108,135]. As there are a limited number of receptors presented on the cell surface at a given time, the quantity of drug payload that can be delivered is limited, even when targeting highly expressed receptors. The careful selection of well validated target receptors that are strongly expressed and presented on cancer cells is thus of paramount importance. Tumor heterogeneity further contributes to these inherent challenges in achieving sufficient concentrations of the toxic payloads within tumor cells to achieve efficacious responses.

Addressing these issues requires the use of highly cytotoxic payloads capable of killing cells at sub-nanomolar concentrations. Extremely potent cytotoxins like duocarmycins and auristatins – DNA alkylators and microtubule inhibitors – kill cells with very little exposure, thus providing good efficacy even if intracellular concentrations are relatively low compared to what would be achieved with traditional chemotherapeutics. It is also desirable for these toxic payloads to be able to diffuse from the targeted cell to kill nearby cells. This ability to kill nearby cells – known as the bystander effect – helps address issues of tumor heterogeneity[144,145].

Due to tumor heterogeneity, some cells within a tumor may not display enough of the target antigen to internalize sufficient amounts of the payload to induce cell death. If cells which *are* expressing high enough levels of the target protein release the toxic payload to their neighbor cells, local concentrations of payload within the tumor environment will be higher thus providing better efficacy. This is a challenging game to play however, as systemic exposure to the toxic payloads must be avoided to prevent off-target toxicities. Utilizing such potent payloads is thus a double-edged sword and exceptional care must be taken to insure the intact conjugate is stable and selectively targeted to the tumor environment to prevent excess exposure to endogenous tissues.

Linker chemistry is fundamental in determining the stability and efficacy of ADCs and other active-targeting strategies. The linker between the antibody and drug payload must exhibit excellent extracellular stability to prevent systemic release of the toxin; however, once endocytosed, the linker should quickly and efficiently release the payload to provide the desired on-target efficacy. The most prevalent linker strategy currently utilizes peptide-based linkers. Drug release from these systems is mediated within the endosome/lysosome by proteolytic cleavage of the linker to release drug payload[146,147]. Alternative strategies utilize acid sensitive or reducible linkers which evolve their drug payloads upon acidification of the endosome or exposure to the reducing environment of the cell[144,148,149].

Not all linkers need immediately cleave to release drug payloads in a traceless manner however. Trastuzumab emtansine utilizes a maytansine payload stably

conjugated to the antibody[148]. Once the intact conjugate reaches the lysosome of target cells it is proteolysed to evolve the payload bearing a small residual fragment of the antibody. This species is highly toxic and proceeds to kill the cell. While stable linker strategies may preclude a bystander effect, they do possess advantages with respect to conjugate stability and so help to minimize systemic exposure to the free payload.

Of the various linker strategies explored to date, none exhibit substantial intrinsic selectivity for cleavage within cancer cells over normal cells. Most of the selectivity achieved from active targeting strategies is thus supplied by the targeting moiety. This represents a potential pitfall of such strategies as it places enormous importance on the selection of an appropriate targeting moiety when the target receptors/ antigens will always be expressed to some extent on some normal tissues. This issue is reflected in the fact that both approved ADCs are currently dosed at their MTD to achieve efficacy. The dose limiting toxicities are largely thought to be due to on-target delivery to normal tissues that express low levels of the target receptor. Having a linker system with inherent selectivity for releasing payload in tumor cells would thus be a very appealing strategy to further improve targeted delivery.

Synthesis of trioxolane-based ADC linkers

Our initial attempts at developing trioxolane-based ADC linkers focused on conjugation of trioxolane-duocarmycin analogs such as **10** to antibodies via strain-promoted Huisgen cycloaddition. This approach was enabled by site specific

incorporation of unnatural azido amino acids in the antibodies via technology developed at Sutro Biopharma Inc. with whom we collaborated for this endeavor.

We utilized an earlier generation of trioxolane scaffolds for this work as these systems provided the additional chemical handles needed for incorporation of the strained cyclooctyne (**Fig. 19**)[150]. Thus, the previously reported trioxolane lactone **14**[150] was opened with 1-N-Boc-ethylendiamine to afford Boc-protected intermediate **15**. Removal of the Boc-protecting group was accomplished with 4 M HCl in dioxanes under strictly anhydrous conditions to avoid potential instabilities of the trioxolane ring to aqueous acidic conditions. The resulting free amine was then exposed to the commercially available NHS-ester of a dibenzylcycylooctyne (DBCO) analog containing a PEG linker (DBCO-PEG_4-NHS ester) for improved solubility properties. This afforded the requisite trioxolane analog (**16**) with DBCO functionality for antibody conjugation and the free alcohol needed for addition of drug payloads. Addition of duocarmycin analog **9** to alcohol **16** was then accomplished via isocyanate formation and condensation in minimal volumes of rigorously dried solvents as previously described. Initial analysis indicated the reaction proceeded smoothly and material consistent with the desired product by LCMS (**17**) was obtained. Characterization by NMR in *d*-chloroform resulted in decomposition of the product however indicating substantial instability to even mildly acidic conditions. This instability appeared to be related to the DBCO moiety which is known to be acid sensitive. Indeed all steps after the incorporation of the DBCO moiety suffered poor yields due to challenges with purification and stability of the intermediates.

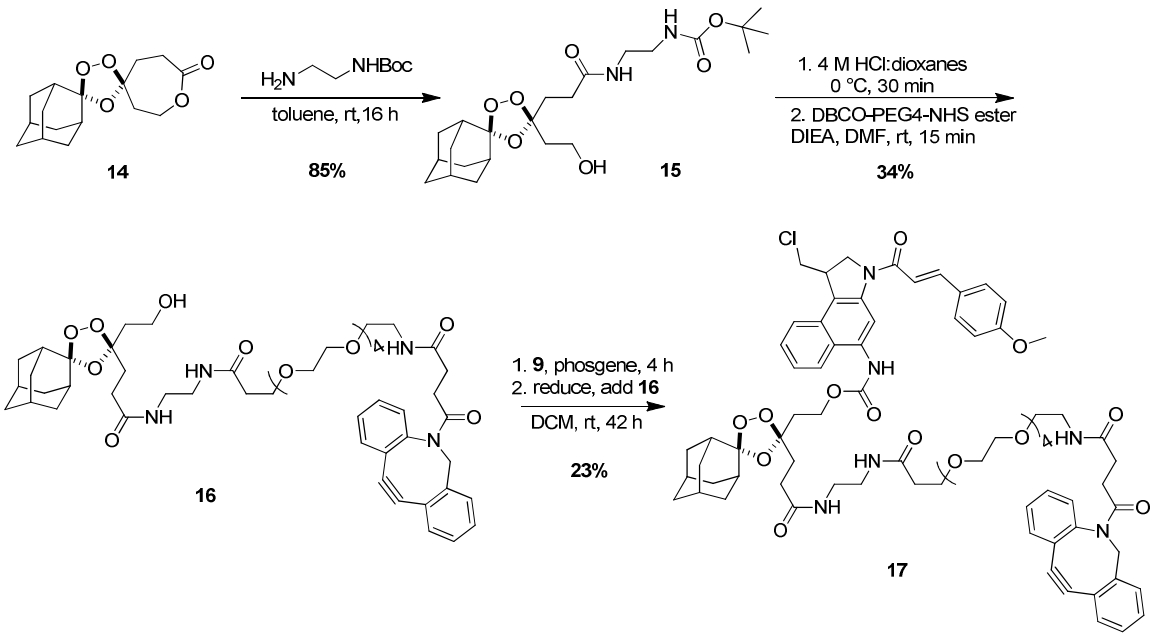

Figure 19: Synthesis of DBCO-bearing trioxolane-CBI conjugates
Synthetic methodology for formation of DBCO-bearing trioxolane-conjugates of **9** to be used in antibody conjugation strategies. Detailed procedures for each step can be found in the methods section.

To minimize the number of reaction steps with the DBCO moiety present, the route was modified so the drug payload (**9**) was conjugated prior to amine de-protection and addition of the DBCO moiety (**Fig. 20**). Addition of alcohol **15** to the isocyanate of **9** thus afforded the drug conjugate **18** in good yield. Amine de-protection followed by condensation with DBCO-PEG_4-NHS-ester then gave the desired DBCO containing trioxolane-drug conjugate **17**. A further conjugate was also prepared using DBCO-C6-NHS-ester (**19**) to test the effects of the PEG linker on solubility and antibody conjugation (**Fig. 20**).

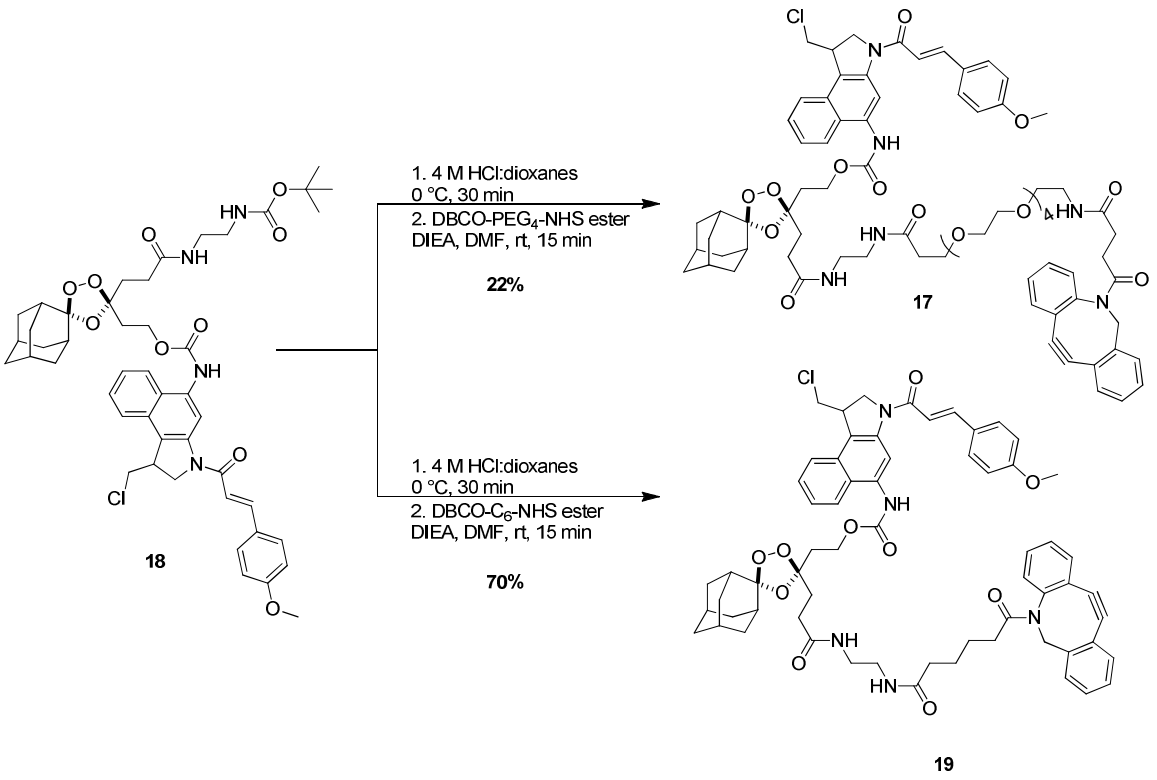

Figure 20: Alternative routes to DBCO-bearing trioxolane-CBI conjugates
Alternative synthetic methodology for formation of DBCO-bearing trioxolane-conjugates of **9** to be used in antibody conjugation strategies. Detailed procedures for each step can be found in the methods section.

Both **17** and **19** performed well in preliminary conjugation studies with para-azidomethyl-L-phenylalanine (*p*AMF) indicating the DBCO moiety was intact and the conjugates were reactive with azido amino acids to form adducts via Huisgen cycloaddition as designed. Conjugations of both intermediates to antibodies with site specific *p*AMF incorporations failed to produce efficient conjugation however under all attempted conditions. Similar results were obtained with a control compound prepared at Sutro with an industry standard ValCit pAB linker in place of the trioxolane linker. The repeated failure of attempted antibody conjugations to substrates containing both DBCO and amino-CBI moieties (**9**) combined with the

substantial difficulty observed in obtaining stable intermediates for conjugation suggested a possible incompatibility between the two moieties. These results thus prompted exploration of alternative drug payloads and conjugation strategies.

Combretastatin analog **5** has several attributes that made it appealing for use as a drug payload for preliminary ADC studies. Synthesis of the drug payload **5** is substantially easier than that of amino-CBI analog **9** (4 vs. 14 steps) and it has much better stability properties since **5** is not a reactive electrophile. Trioxolane conjugates of **5** were also previously shown to be of utility in cell culture studies exploring payload release efficiencies, suggesting it would be similarly useful for proof of concept studies in the context of ADC strategies. Trioxolane conjugates of **5** bearing two different cyclooctyne moieties were thus pursued as intermediates for ADC conjugations (**Fig. 21-22**).

Opening of trioxolane lactone **14** with the commercially available bicyclo[6.1.0]nonyne (BCN) bearing amine **20** thus afforded alcohol intermediate **21**. Isocyanate formation from amine **5** followed by condensation with alcohol **21** then afforded the desired BCN bearing trioxolane-drug conjugate **22** (**Fig. 21**). Notably, pyridine was added to this reaction in an effort to prevent exposure to HCl generated during the course of the reaction. This was found to promote formation of the urea dimer of **5** resulting in reduced yields and thus all further condensations were pursued without the addition of amine bases.

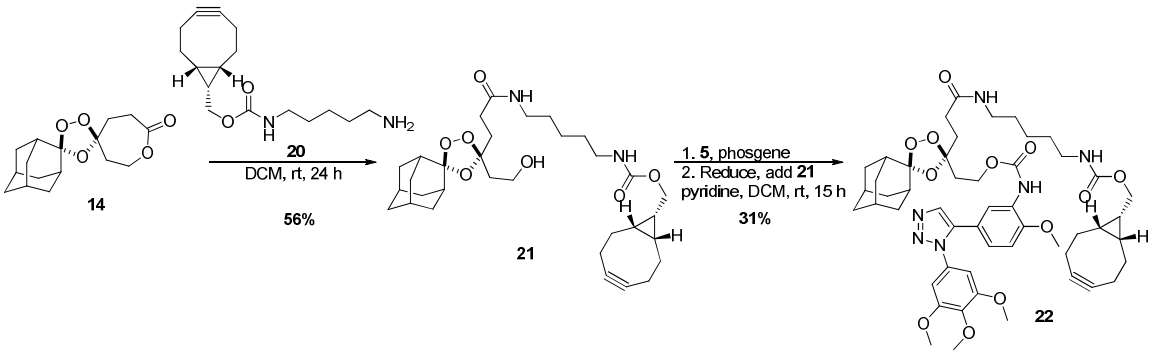

Figure 21: Synthesis of BCN-bearing trioxolane-drug conjugates
Synthetic methodology for formation of BCN-bearing trioxolane-conjugates of **5** to be used in antibody conjugation strategies. Detailed procedures for each step can be found in the methods section.

The BCN moiety is substantially less reactive than DBCO giving it improved stability but also reduced reactivity with azide bearing substrates. This proved problematic as conjugate **22** behaved poorly in initial antibody conjugation reactions suggesting the decreased reactivity might make conjugation to intact antibodies inefficient. A control compound comprising of a previously validated payload (MMAF) with a BCN alkyne moiety also failed to conjugate well to antibodies in these studies. In contrast, an MMAF-DBCO substrate performed well, indicating that the issue was likely the reduced reactivity of the BCN handle as opposed to an issue with the trioxolane linker (**Table 1**).

As surrogate conjugations with *p*AMF worked well for the BCN bearing compounds, we concluded that some aspect of the local protein environment surrounding the antibody conjugation site significantly inhibits the conjugation reaction. Consistent with this hypothesis, when 1.1 M guanidinium was added to attempt conjugation with unfolded antibody, the conjugation reaction proceeded more smoothly. After refolding the antibody a drug-to-antibody ratio (DAR) of 1.47 was achieved, as

compared to DAR = 0.5 in the absence of guanidinium (**Table 1**). Substantial amounts of precipitates were observed after refolding the antibodies however suggesting that material was lost during this unfolding-refolding process. This strategy is thus not viable as a long-term solution. That being said, as the maximum DAR using the site-specific approach is 2 and the state of the art systems commonly achieve DAR's of 1.8-1.9, the ADCs produced by the unfolding-refolding approach were determined to be of sufficient quality to proceed with cell culture studies to establish proof of concept.

Table 1: Efficiency of antibody conjugation with trioxolane linker 22 and comparators under various conditions

Description	Rxn conditions	DAR
Trastuzumab-**22**-1	30:1 Drug:antibody, 40% DMSO, 48 Hrs	0.50
Trastuzumab-BCN-MMAF-1	30:1 Drug:antibody, 40% DMSO, 48 Hrs	nd
Trastuzumab-**22**-2	30:1 Drug:antibody, 40% DMSO, 1.1 M Guanidinium, 48 Hrs	1.47
Trastuzumab-BCN-MMAF-2	30:1 Drug:antibody, 40% DMSO, 1.1 M Guanidinium, 48 Hrs	nd
Trastuzumab-DBCO-MMAF	10:1 Drug:antibody, 4% DMSO	1.78

Initial cell culture experiments with trioxolane-linked ADCs

With trioxolane-linked ADCs in hand, cell killing experiments were initiated to assess the viability of the trioxolane linker. A key question in this regard was whether or not the linker would be cleaved in the endosome to release free drug (endosomal escape). Encouragingly, while the unconjugated drug-linker control **22** was essentially non-toxic as compared to the free drug payload (302 nM vs 2 nM), the trioxolane-based ADCs (Trastuzumab-**22**-2) showed cytotoxicity nearly equipotent (EC_{50} = 4.1 nM) to the free payload **5** (EC_{50} = 2 nM), suggesting effective uptake of the ADC by the endocytic pathway, and efficient endosomal escape of free

drug. These results support the validity of trioxolanes as novel ADC linkers. In spite of the lower observed DAR, ADCs produced under standard conditions (Trastuzumab-**22**-1) showed very similar EC_{50} to those conjugated under denaturing conditions suggesting the conjugation reaction may have proceeded more efficiently than indicated by mass spec analysis (**Table 2**).

Table 2: Cell toxicity for ADC conjugates derived from 22

Potency of ADC's derived from **22** and control compounds in antigen positive (SKBR3) and antigen negative (MDA-MB-468) cell lines as determined by CTG analysis. The therapeutic ratio for a conjugate is defined as the fold change in EC_{50} between antigen positive and antigen negative cell lines.

ADC Description	EC50 (nM)		Therapeutic Ratio
	SKBR3	MDA-MB-468	
Trastuzumab-**22**-1	2.7	21	7.8
Trastuzumab-**22**-2	4.1	17	4.1
22	302	412	
5 (free CMB payload)	2	~ 3.6	
Trastuzumab-BCN-MMAF-1	0.24	3.7	15.4
Trastuzumab-BCN-MMAF-2	0.26	1.4	5.4
BCN-MMAF	0.15	6.7	
Trastuzumab-DBCO-MMAF	0.019	>100	> 5000
DBCO-MMAF	237	137	

Unfortunately, in antigen negative cells the trioxolane-linked ADCs also showed significant toxicity (EC_{50} of 17-21 nM), indicating a potentially narrow 5-fold therapeutic window between antigen positive and negative cells. This suggested some spurious release of payload from the trioxolane-linked ADC, since ValCit-pAB based ADCs (represented here by Trastuzumab-DBCO-MMAF) commonly see greater than 1000-fold shifts in EC_{50} between antigen positive and negative cell lines (**Table 2**). Free drug could result from either linker instabilities or contaminating starting material from the conjugations. As similar results were also obtained with the BCN-bearing MMAF analog, which also conjugated poorly, our findings suggest this off-target toxicity may derive from issues inherent to the BCN-mediated conjugation strategy (**Table 2**).

Returning to DBCO-mediated ADC conjugation strategies

As combretastatin analog **5** has substantially fewer liabilities than duocarmycin analog **9** an attempt was made to return to the more reactive, DBCO mediated conjugation strategies with these drug payloads. Trioxolane lactone **14** was thus opened with lithium hydroxide in methanol and THF to afford intermediate alcohol **23**. Condensation with the isocyanate of **5** gave the desired trioxolane-conjugate **24**, and then saponification of the methyl ester followed by peptide coupling to DBCO-PEG_4-NH_2 produced the desired intermediate **25** ready for conjugation.

To test the possibility of trioxolane-related linker instability we also sought to compare the trioxolane linker directly to the state-of-the-art ValCit pAB linker utilizing the same drug payload and antibody. Control conjugate **26** was thus formed in an analogous matter to **25** via condensation of Fmoc-protected ValCit pAB with the isocyanate of **5** to yield intermediate **27**, followed by Fmoc removal and peptide coupling to DBCO-PEG_4-NH_2 (**Fig. 22**). Notably, poor yields were observed in the condensation reaction with the isocyanate of **5** due to solubility issues with the ValCit pAB alcohol starting material and product, which led to reduced reactivity and significant loss of the final product. However, due to the minimal material needed for conjugation, sufficient material was produced to proceed with antibody conjugations. Unfortunately, these compounds failed to conjugate well to antibodies and low DAR (0.7) were obtained with both **25** and **26**.

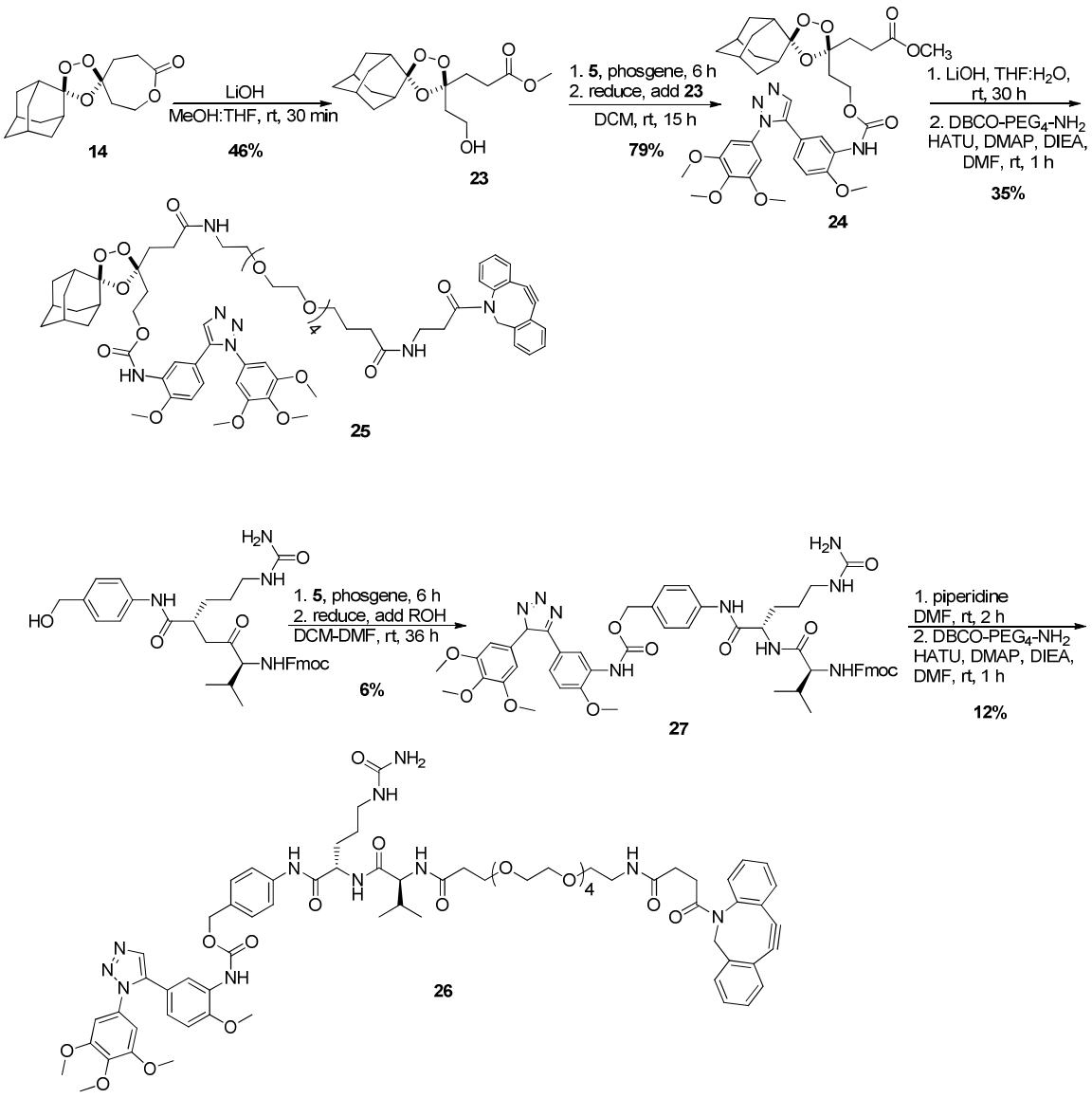

Figure 22: Synthesis of DBCO-bearing trioxolane-conjugates of 5 and control compounds

Synthetic methodology for formation of DBCO-bearing conjugates of **5** utilizing both trioxolane-based linkers and ValCit pAB linkers. Detailed procedures for each step can be found in the methods section.

In cell culture studies, these ADCs showed weak activity in both antigen positive and antigen negative cells. These findings held for both the trioxolane-linker based ADC's from **25** and the ValCit pAB linked conjugates from **26** with the trioxolane

linked ADCs showing more activity than the ValCit pAB linked ADCs, which were largely inactive in both cell lines. Due to the poor conjugation and activity of both sets of drug linker systems the results were inconclusive. To obtain a better comparison we decided to pursue a second direct comparison study, this time using an industry standard drug payload.

Development of trioxolane-linked ADCs bearing MMAE drug payloads

As the original proof of concept ADCs developed by Sutro utilized monomethyl auristatin drug payloads (MMAE/F) we pursued a DBCO-trioxolane-MMAE conjugate. Conjugates produced from these analogs would be directly comparable to the ADCs developed by Sutro, differing only in the trioxolane linker (compared to ValCit pAB). Accordingly, alcohol **23** was reacted with *p*-nitrophenyl chloroformate to produce the corresponding activated *p*-nitrophenylcarbonate **28**. Condensation of **28** with MMAE then afforded the corresponding trioxolane-MMAE conjugate **29**. Ester hydrolysis followed by peptide coupling to DBCO-PEG_4-NH_2 then gave the desired intermediate (**30**) for antibody conjugation.

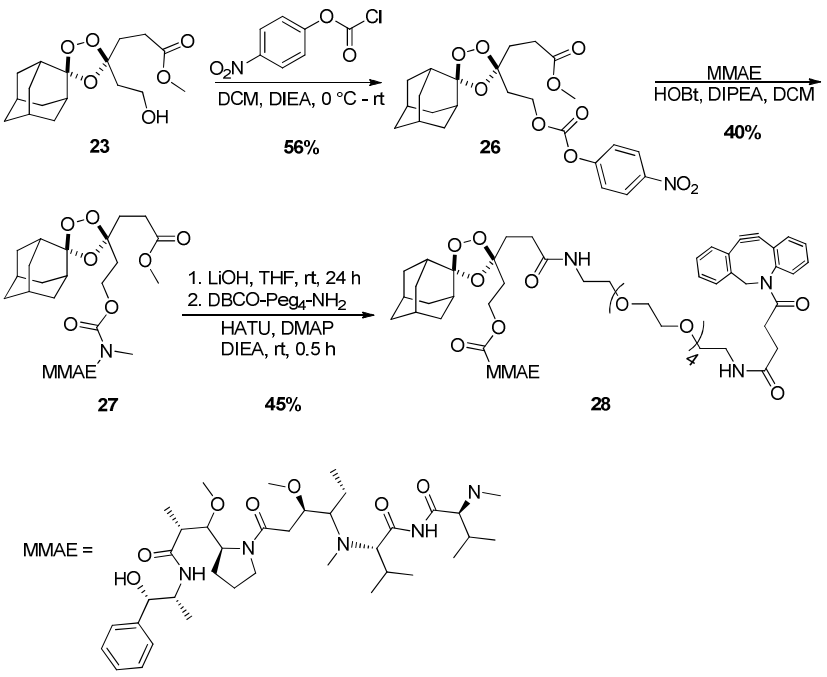

Figure 23: Synthesis of DBCO-Trx-MMAE conjugates
Synthetic methodology for formation of DBCO-bearing trioxolane conjugates of MMAE. Detailed procedures for each step can be found in the methods section.

This conjugate appeared to display enhanced properties for ADC conjugation compared to previous studies with DAR of 1.4 obtained (**Table 3**). Notably, a second attempt at conjugation of CMB conjugate **25** also gave better results than the initial findings when run in parallel (DAR ~ 1.8). These results held up for conjugations at each of two different locations on the antibody (**Table 3**). It is unclear why these results vary so significantly between the two attempts, or why the drug payload might have such an effect on the efficiency of antibody conjugation. However, with multiple trioxolane linked ADCs in hand and direct comparators utilizing ValCit pAB linkers for positive controls we were encouraged to proceed with cell culture characterization.

Table 3: Antibody conjugation with 28 and comparators under various conditions

ADC Description	Description of compound	DAR
Trastuzumab(site 1)-VC pAB MMAE	DBCO PEG4 VC pAB MMAE	1.87
Trastuzumab(site 2)-VC pAB MMAE	DBCO PEG4 VC pAB MMAE	1.96
Trastuzumab(site 1)-**25**	DBCO PEG4 TRX **5**	1.80
Trastuzumab(site 2)-**25**	DBCO PEG4 TRX **5**	1.49
Trastuzumab(site 1)-**30**	DBCO PEG4 TRX MMAE	1.44
Trastuzumab(site 2)-**30**	DBCO PEG4 TRX MMAE	1.42

Consistent with our previously results, trioxolane-linked ADCs bearing MMAE payloads showed activity comparable to free MMAE in antigen positive cells, reflecting efficient payload delivery from the conjugate (**Table 4**). As MMAE in an ADC must escape the endosome/lysosome to achieve efficacy, these results clearly indicate that the trioxolane-linker is efficiently cleaved to release free drug payload within the endosome/lysosome system. The trioxolane linked ADCs were also nearly equipotent to ADCs based on the industry standard ValCit pAB linker, suggesting the novel linker does not significantly reduce the efficiency of payload release compared to current technologies. These encouraging findings were consistent across both of the conjugation sites explored in these studies (**Table 4**).

Table 4: Cell Toxicity for trioxolane-linked ADCs bearing MMAE drug payloads
Potency of ADCs derived from **25** and **30** and control compounds in antigen positive (SKBR3) and antigen negative (MDA-MB-468) cell lines as determined by cell titer glow assay.

Compound	EC_{50}		Therapeutic Ratio
	SKBR3	MDA-MB-468	
Trastuzumab(site 1)-**30**	0.07	0.61	8.7
Trastuzumab(site 2)-**30**	0.071	2.1	29.6
Trastuzumab(site 1)-VC pAB MMAE	0.046	>100	>2000
Trastuzumab(site 2)-VC pAB MMAE	0.003	4.6	1533
Trastuzumab(site 1)-**25**	2.4	8.7	3.6
Trastuzumab(site 2)-**25**	4.3	~ 10	~ 2.3
MMAE	0.072	0.17	
DBCO PEG4 VC pAB MMAE	281	726	
30	22	57	
25	260	~ 743	

While the trioxolane-linked ADCs in these studies displayed significantly better cell-type selectivity than in the previous studies, with therapeutic index as high as ~30, they still compared poorly to ADCs with ValCit pAB linkers which displayed therapeutic indexes over 1000 (**Table 4**). These results suggest the trioxolane-linker is more prone to extracellular degradation and release of drug payloads than the best existing linker technology. Interestingly, the site of conjugation appeared to have substantial effects on the stability of the conjugates. Trioxolane-linked ADCs conjugated at site 2 on trastuzumab were four-fold less toxic toward antigen-negative cell lines, when compared to ADCs conjugated site 1. These results may speak to an antibody dependent instability of the linker that is partially mitigated by conjugation at site 2, producing more stable ADCs. A similar effect was not noted in

the ValCit pAB linked conjugates, likely reflecting their superior intrinsic stability regardless of conjugation site.

Discussion

The substantial challenges encountered in developing trioxolane-based linkers for ADCs underscore the complexity of these systems and the importance of optimizing every aspect of the conjugates. Throughout our work we observed that changes to the drug payload, linker composition, or even the site of antibody conjugation could have significant impacts on the efficiency of antibody conjugation in addition to the efficacy and stability of the final conjugates. Given this complexity and the need to empirically determine the effect a given change will have, it is thus important to carefully interrogate and optimize each component of the system individually.

Our initial attempts focused on developing conjugates utilizing **9** as the drug payload. While this drug payload proved of great utility in our earlier studies, application of this class of compounds in ADC conjugations involving strained alkyne cycloadditions is unprecedented and we observed apparent incompatibilities between **9** and the DBCO moiety. The resulting stability and purification issues thus precluded further exploration of this warhead in combination with DBCO-mediated conjugation strategies.

Likewise, while the microtubule inhibitor **5** proved of utility in our previous studies, we experienced issues achieving efficient antibody conjugations with drug-linker intermediates using this payload. Even when using DBCO-mediated conjugations at

well-validated sites on a heavily studied antibody, poor conjugation efficiencies were observed. This was true for both the trioxolane-based linker and the well-established ValCit pAB linker used in clinically approved ADCs. The reasons for this are not immediately evident as in both conjugates the drug payload is located distal from the site of conjugation. Regardless, since **5** was also unprecedented for application as an ADC drug payload we decided to further reduce the number of variables and use the established ADC drug payload MMAE.

Having thus settled on a direct comparison between the validated DBCO-ValCitpAB-MMAE system and an exactly analogous trioxolane-based DBCO-Trx-MMAE system we were finally able to achieve efficient conjugations. This then allowed for unambiguous analysis of the efficacy and stability of the trioxolane linker as compared to the industry standard linker (ValCitpAB).

We were encouraged to find that the ADCs with trioxolane linkers were substantially more potent than the unconjugated precursors (**25, 30**). Indeed, the ADCs displayed cytotoxicity equivalent to free MMAE, reflecting efficient drug release once internalized. In antigen positive cell lines they performed nearly as well as the state of the art systems with just a two-fold decrease in potency. Overall, these data indicate efficient endosomal/ lysosomal escape of drug from trioxolane linkers and suggest that such systems could be developed into viable ADC linkers.

Unfortunately, trioxolane-linked ADCs also exhibited substantial activity against antigen-negative cell lines. These findings appear to reflect an antibody-dependent instability of the current trioxolane linkers. Throughout our studies the drug-linker

moieties showed negligible toxicity when not conjugated to antibodies (i.e., **25**, **30**) compared to the free drug payloads (**5**, MMAE) (>100-fold shift in EC_{50}). The trioxolane-linker moiety is thus stable in the absence of the antibody since any substantial (>1%) release of free drug would results in an EC_{50} within 100-fold of that of the free drug. In comparison, the ADCs produced with those same linkers were as little as 4-fold less potent than the free drug in antigen negative cells, indicative of substantial release of the drug payload in an antigen-independent fashion. The impact that site of conjugation had on the potency of the trioxolane-linked ADCs in antigen negative cell lines further supports our hypothesis of antibody-dependent instability. ADCs produced from linkage to site 2 were ~4-times less potent in antigen negative cells than those linked to site 1. This suggests that the local environment at the conjugation site on the antibody can affect the stability of the conjugate with the site 2 site giving more stable intact conjugates in this context. As site 2 is known to be more solvent exposed than site 1 this further supports the theory that local interactions with the antibody may be contributing to the observed instability.

Overall our findings indicate that trioxolane-linked ADCs are capable of releasing their drug payloads in an efficient manner in cells, consistent with our previous studies of trioxolane-based TAPs. Poor selectivity (5 to 30-fold) for antigen positive over antigen negative cells however suggests there are stability issues related to the linker in the context of the intact ADC. This issue appears to be, at least in part, related to the local environment at the site of conjugation. Further optimization of the site of conjugation could thus potentially work to further stabilize future

conjugates. Alternatively, given the significant body of literature describing the factors which influence trioxolane stability, one could rationally design improved trioxolane-linker scaffolds with enhanced stability in the context of an ADC. Once stabilized ADCs are produced via either approach or a combination thereof, in depth studies exploring the toxicity of the ADCs in cell culture and mouse xenograft models would provide insight into the benefits (if any) that might be obtained by utilizing trioxolane-based linkers over state-of-the-art linker strategies. We hypothesize that the additional layer of selectivity conferred at the stage of intracellular drug release would serve to further reduce off-target toxicities and thus allow for safer, more efficacious dosing than ADCs utilizing current linker technologies.

Chapter 5: Conclusions and future directions

The carefully tuned ferrous iron reactivity of sterically hindered antimalarial endoperoxides has provided an excellent foundation for the work presented here. This scaffold facilitated the development of novel reactivity-based probes of the cellular labile Fe(II) pool which proved to be highly sensitive and selective for reporting on Fe(II) in the complex environment of the cell. These probes were found to be significantly more sensitive than previously reported probes of cellular Fe(II) and were compatible with *in vivo* applications, thus providing significant utility in the study of labile Fe(II) pools in biological systems. While here we reported simple dot-blot studies to measure gross levels of reactive Fe(II) species in entire organs, one could readily envisage using histopathological methods to provide greater spatial resolution about iron(II) pools within specific organs and tissues. It is further worth noting that the ease, flexibility, and high-throughput nature of the companion immunofluorescence assay we describe for probe **3** represent substantial improvements over previous probes and methods which require confocal microscopy for sensitive measurements. The application of these probes should thus prove useful for a wide variety of future studies of iron metabolism.

Our application of these probes in cancer models revealed that the dysregulation of iron metabolism in cancer cells/tumors contributes to an increased pool of reactive Fe(II) species compared to normal tissues. Based on these observations we were able to further utilize the trioxolane scaffold to leverage those changes in chemical environment as a trigger for selective drug release from trioxolane-conjugates in a

novel TAP strategy. This strategy provided considerable benefit in reducing off target toxicities when used to mask a potent DNA-alkylator for selective release within tumor microenvironments. This allowed us to dose the conjugate 55-times higher than the free drug, which in turn provided substantially improved efficacy over that achievable with the free drug at maximally tolerated doses. We further observed that masking the active drug species until Fe(II)-mediated release within the tumor environment provided substantially increased compound stability which translated to better PK properties and increased potency in on-target cells in cell culture studies. We were thus able to effectively demonstrate that trioxolane-based payload delivery systems are capable of safely masking a variety of cytotoxins until Fe(II)-mediated drug release within the tumor environment.

This strategy was applicable in multiple tumor types and based on cell culture studies could be even more broadly applied. Our promising initial results thus encourage further research to explore the scope and utility of this approach in other cancer models. As the payload delivery system developed by the Renslo lab is quite flexible to various conjugation strategies depending on the chemical handles available, this system could potentially be applied to a wide variety of known cytotoxic payloads to improve safety and efficacy profiles. Thus further research into identifying additional partner drugs that would benefit from this approach is also warranted.

The promising results obtained using trioxolane-based payload delivery scaffolds as a novel TAP strategy encouraged exploring the expanded use of this system as a

tumor selective cleavable linker for ADCs. Our initial results indicate such a strategy could be feasible, as the trioxolane-linked ADCs studied appeared to effectively release their drug payloads within antigen presenting cancer cells. Substantial activity against antigen negative cells however indicated that these systems might possess insufficient stability in their current form. These issues appeared to be mediated to some extent by the antibody, as unconjugated systems were largely non-toxic (stable) by comparison. Consistent with this hypothesis, changing the site of conjugation on the antibody reduced toxicity in antigen-negative cells, suggesting the environment at the site of conjugation has an impact on the stability of the conjugate. Further optimization of conjugation conditions and the site of conjugation could thus prove beneficial for stability.

While the trioxlane-conjugates reported here were generally found to have good stability properties in cell culture media, the results from the ADC studies suggest the systems might benefit from additional optimization to improve chemical stability. As the factors that influence the stability of the peroxide bond are well defined, additional research into building a trioxolane system optimized for stability as an ADC linker might prove fruitful. Alternatively, as the instabilities observed here appeared to be at least partially mediated by the antibody, a change of strategies towards small molecule based targeting approaches such as folate-conjugates might be desirable. Such a shift in strategy would also be appealing from the standpoint of the challenges observed in achieving acceptable antibody conjugation efficiencies; small molecule conjugates would reduce the complexity of

the endeavor and remove the need for bioorthogonal coupling strategies which caused us substantial difficulties.

In conclusion, we have leveraged the finely tuned Fe(II)-dependent reactivity of sterically hindered 1,2,4-trioxolanes to develop highly selective, reactivity-based probes of the ferrous iron pool and a prototypical scaffold for Fe(II)-dependent drug delivery of chemotherapeutics. Our encouraging findings indicate that many cancer cells have augmented reactive Fe(II)-pools which can be utilized to selectively release potent cytotoxins within cells and/or the tumor microenvironment. We find that using such a strategy can provide substantial benefits to the application of cytotoxic payloads that otherwise lack specificity for killing cancer cells. This work thus encourages continued efforts to explore and optimize trioxolane-based payload delivery scaffolds for applications in cancer chemotherapies.

Methods and Materials

General Procedures and Materials

^{1}H and ^{13}C NMR spectra were recorded on Varian INOVA-400 400 MHz and Bruker 500 MHz spectrometers. Chemical shifts are reported in δ units (ppm). NMR spectra were referenced relative to residual NMR solvent peaks. Coupling constants (*J*) are reported in hertz (Hz). Air and/or moisture sensitive reactions were carried out under an argon atmosphere in oven-dried glassware using anhydrous solvents from commercial suppliers. Air and/or moisture sensitive reagents were transferred via syringe or cannula and were introduced into reaction vessels through rubber septa under an atmosphere of argon. Solvent removal was accomplished with a rotary evaporator at ca. 10-50 Torr. Column chromatography was carried out using a Biotage SP1 flash chromatography system and silica gel cartridges from Silicycle. Analytical TLC plates from EM Science (Silica Gel 60 F_{254}) were employed for TLC analyses. Mass analyses and compound purity were determined using Waters Micromass ZQTM, equipped with Waters 2795 Separation Module, Waters 2996 Photodiode Array Detector, and Waters 2424 ELS detector Separations were carried out with an XTerra® MS C18, 5μm, 4.6 x 50 mm column, at ambient temperature (unregulated) using a mobile phase of water-methanol containing a constant 0.10 % formic acid. Fluorescence and absorbance data was collected on a Molecular Devices Flex Station 3.

Mammalian cell lines were maintained in an atmosphere of 5% CO_2 in Dulbecco's Modified Eagle Medium (DMEM) or RPMI 1640 media purchased from HyClone

supplemented with 10% FBS (Gibco), Pen/Strep (1x final concentration, Gemini Bio-Products), and non-essential amino acids (UCSF Cell Culture Facility). MCF10A derived cell lines were cultured as previously reported[122].

All Western Blot and Dot Blot images were analyzed with Licor Image Studio Software to determine signal intensity. Graphing and analysis of data was done using GraphPad Prism 6 Software and Microsoft Excel 2010. Figures were prepared with Adobe Design Standard CS6 software.

Statistics: Error bars in all figures represent s.e.m. unless otherwise indicated. When three or more means were compared, one or two-way ANOVA tests were applied as required with Dunnett's multiple comparisons tests used to determine significance. Statistical significance is indicated as follows: * = P≤0.05, ** = P≤0.01, *** = P≤0.001, **** = P≤0.0001.

Reagents:

Unless otherwise noted all chemical reagents and solvents used were purchased from Sigma-Aldrich. Dichloromethane was purchased from Fisher Scientific. Puromycin dihydrochloride was purchased from P212121. Oxime **10** was prepared as previously described[74]. Trioxolane alcohol **15** was prepared as described previously[90]. Dioxolane alcohol **17** and puromycin conjugate **4** were prepared as described previously[57]. Combretastain analog **6** was prepared as described previously[121]. Zinc sulfate was purchased as a 100 mM aq. Soln. from Alfa Aesar. Cobalt(II) sulfate heptahydrate was purchased from Sigma-Aldrich: SIAL.

Magnesium(II) chloride hexahydrate was purchased from Amresco. Ferrous ammonium sulfate was purchased from Santa Cruz. Sodium chloride was purchased from Fisher Scientific. Nickel(II) sulfate, Fe(II) bromide, Fe(III) sulfate hydrate, copper(II) chloride, copper(I) chloride, calcium chloride, potassium chloride, and manganese(II) chloride were all purchased from Sigma Aldrich. DBCO-PEG_4-NHS Ester, DBCO-C_6-NHS Ester, and DBCO-PEG_4-NH_2 were all purchased from Click Chemistry Tools.

In vitro Assays:

Fluorescence Assays of 1: Solutions of the indicated metal ions as sulfate, chloride, or bromide salts were prepared in milli-Q purified water to the specified concentrations. 10 μL of each of these solutions was added to 10 μL of a 30 μM solution of **1** in DMSO in white, low volume, flat bottom 384-well plates (Corning, #3824) and mixed thoroughly. The fluorescence signal at E_{max} (465 nm) for each well when excited at 337 nm was then measured every five minutes for 3 hours. Rates of fluorescence increase were determined for each sample using the initial rate method and compared to determine reactivity.

***In vitro* Fragmentation Studies:** Solutions of trioxolane conjugates in DMSO (10 mM) were spiked into 1 mL of RPMI cell culture media (supplemented as in cell culture studies) that had been warmed with stirring to 37 °C to give a final solution of 300 μM compound with 3% DMSO co-solvent which was stirred at 37 °C. Aliquots were taken at various time points and analyzed by LC/MS. The chromatography method involved gradient elution from 0-95% MeOH in water (constant 0.1%

formic acid) over 8 min. Stability of the compounds was followed by observing signal at absorbance maxima for each compound (**2**: λ = 275 nM **6:** λ = 250 nM) of the peaks corresponding to the parent compounds and free payloads as determined by authentic samples**.** For iron conditioned samples 0.5 mL of 0.6 mM solutions of compound in DMSO were spiked into 0.5 mL of RPMI cell culture media containing 60 mM FAS while stirring at 37 °C. 50 µL aliquots of the resulting mixture were removed periodically and analyzed via LC/MS for trioxolane fragmentation and release of free payload.

Antibody conjugation reactions: Antibody conjugation reactions were carried out under proprietary conditions at Sutro BioPharma. The efficiency of antibody conjugation reactions (i.e. the DAR of the final conjugate) was determined via LCMS and MALD-TOF spectrometry analysis. Conjugate purity was determined with an Agilent TapeStation Instrument and concentrations of the final conjugates were determined from their absorption at 280 nm.

Cell Culture Assays:

Western Blots: Cells were plated at 300,000 cells per well in 6-well plates and grown to confluence. Media was then removed, cells were washed twice with PBS, and 200 µL of RIPA lysis buffer containing sigma protease inhibitor cocktail (P8340, 1:100) was added to each well. Cells were incubated in lysis buffer for 10 min at RT then scrapped and collected. Lysates were analyzed by BCA and normalized for total protein content with lysis buffer then denatured in Laemmli loading buffer with 0.01 M DTT at 100 °C for 10 min. 10 µg of protein from each sample was then loaded

onto Biorad Mini-PROTEAN® TGX™ 4-15% gels and run @ 150V for 55 min then transferred to Immobilon PVDF membrane at 35 V for 1 h. The membrane was blocked with 5% non-fat milk in TBS-T for 1 h at rt then incubated with the indicated antibodies in 2.5% non-fat milk overnight at 4 °C. The blot was then washed three-times with TBS-T and once with PBS-T before incubating with Licor IRDye secondary antibodies in Odyssey blocking buffer (#927-40000) + 0.2% Tween-20 and 0.01% Sodium dodecyl sulfate (SDS). The blot was washed 3 times with PBS-T for 5 min and once with PBS then imaged for fluorescent signal on an Odessey Classic Infrared Imaging System.

Dot Blots: Samples prepared as for Western Blots were spotted on to Immobilon PVDF membrane which was activated with MeOH then allowed to dry completely prior to spotting 1 μg of total protein per sample. Samples were allowed to completely adsorb onto the membrane and dry before blocking with with 5% non-fat milk in TBST for 1 h at rt and then staining and imaging as done in Western Blots.

Puromycin incorporation via in cell immunofluorescence: Cells were plated in 96-well greiner black μClear tissue culture plates at 5,000-7,000 cells per well and incubated at 37 °C in 5% CO_2 incubators for 24 h (or until ca. 80% confluent) prior to exposure to compounds. Cells were then exposed to puromycin (**2**) or conjugates thereof (**3**,**4**) at the specified concentrations in media for the indicated periods of time prior to removing media, washing cells with PBS, and fixing cells in 4% paraformaldehyde for 10 min at rt then washing twice with PBS and once with PBS containing 0.1% Triton X-100. Cells were then stained with Kerafast α-puromycin

antibody [3RH11] (1:500) in 10% FBS in PBS with 0.1% Triton X-100 for 30 min at 37 °C. Cells were washed once with PBS and once with PBS containing 0.1% Triton X-100 then stained with α-mouse secondary FITC (488 nm excitation, 535 nm emission) antibody (1:100) and DAPI in 10% FBS in PBS with 0.1% Triton X-100 for 30 min at 37 °C. Cells were washed once with PBS containing 0.1% Triton X-100 and once with PBS then stored in PBS and imaged using an IN Cell 2000 automated cell imager at 10x magnification with 9 images per well (imaging the entire well) in FITC and DAPI channel fluorescence. Images were analyzed for nuclei count and puromycin incorporation by IN Cell developer software. Puromycin incorporation was assessed by mean cellular fluorescence density in the FITC channel for each cell as defined by targets seeded with nuclei in the DAPI channel (ca. 3,000-9,000 cells per well). Average cellular fluorescence density under each condition was determined and reported values represent the average of three experiments +/- s.e.m.. Background signal from cells treated with DMSO was subtracted for each condition. For cross cell line comparisons and genetic modulation experiments signal in cell treated with the trioxolane-conjugate **3** was normalized to that in cells treated with free puromycin (**2**) and reported as percent of labelling at 8 h of compound exposure.

Iron Conditioning: Cells were exposed to the indicated doses of FAS or DFO in RPMI 1640 cell culture medium for 2.5 h and then washed with PBS to remove any residual extracellular iron. Cells were then treated with a 1 μM solution of **2** or **3** in cell culture medium for 4 h. Post-treatment cells were washed, fixed, and stained as in the puromycin incorporation studies described above.

Quantitative PCR: Cells were seeded 300,000 cells per well in 6-well plates and grown to confluency then collected with trypsin (0.05%), washed with PBS, and snap frozen in liq. N_2 then stored at -78 °C. Cell pellets were processed for mRNA isolation using Qiagen RNeasy Mini Kit with QIAshredder lysate homogenizers and on column DNA digest. Issolated mRNA was analyzed for concentration and purity on a ThermoScientific NanoDrop 2000c spectrophotometer and 1000 ng of mRNA from each sample was translated to cDNA using Invitrogen SuperScript® III First-Strand Synthesis System. The resulting cDNA was used for qRT-PCR analysis (10 ng/reaction) with SsoAdvanced™ Universal SYBR® Green Supermix in a Roche LightCycler 480. The following gene specific primers obtained from IDT were used for amplification: STEAP3 (Hs.PT.58.39767601), TFRC (Hs.PT.39a.22214826), SLC40A1 (Hs.PT.58.2024686), SLC11A2 (Hs.PT.58.25936698), FTH1 (Hs.PT.58.24667858), GAPDH (Hs.PT.39a.22214836), ACO1 (Hs.PT.56a.15210081), IREB2 (Hs.PT.58.24702746), LCN2 (Hs.PT.58.27617685), HAMP (Hs.PT.58.21516221), ABCB6 (Hs.PT.58.39710929), and MYC (Hs.PT.58.26770695). GAPDH was used as an endogenous control and relative mRNA levels were calculated from a standard curve of pooled samples with LightCycler 480 software used for 2nd derivative maximum analysis and standard curve fitting. Samples were prepared and run in biological triplicates and error bars represent s.e.m..

Transient Transfection: A standard lipofectamine 2000 (Life Technologies) transient transfection protocol was used for both siRNA and ectopic plasmid DNA transfections. Briefly, cells were plated the day before transfection. A quarter of the suggested amount of lipofecatamine2000 was used for plasmid transfection. The

standard ratio of siRNA:lipofectamine was used for siRNA knockdown experiments. The nucleotide-lipid complexes were added to cells growing in Optimem and allowed to incubate for 6 hours at 37C prior to exchanging into fresh standard growth media for each cell line. Cells were allowed to recover overnight, prior to re-plating for experimental treatments.

Toxicity by Nuclei Counting: Cells were plated in 96-well greiner black μClear tissue culture plates at the indicated densities in DMEM cell culture media and incubated at 37 °C in 5% CO_2 incubators for 24 h prior to exposure to compounds. Cells were then treated in triplicate with dose dilutions of compounds performed in media containing 0.1% DMSO (100 μL of media, per well). 24 h post–treatment media was removed and cells were washed with 100 μL of PBS then stained with Hoechst nuclear stain at a final concentration of 10 μg/mL in PBS for 10 min at rt and fixed in 4% paraformaldehyde for 10 min at rt. After fixing the cells were and stored in 100μL of PBS for imaging. Wells were imaged with an inCell 2000 automated cell imager at 10x magnification with 3-4 images per well in bright field and DAPI channel fluorescence and images were analyzed for nuclei count by inCell developer software. EC_{50} values were calculated in GraphPad Prism from normalized dose response curves and are reported as the average of three experiments +/- s.e.m..

Toxicity by CellTiter-Glo®: Cells were harvested, re-suspended and plated with a Wellmate liquid handler (Thermo Scientific) into 384-well plates and cultured for 24 hours before dosing. Master compound plates were made with a Janus

(PerkinElmer), then further diluted to achieve uniform final concentrations of DMSO of 0.1% in media for all treatment conditions. Compound treatments in media were added to the cell plates with a Matrix Platemate (Thermo Scientific). Cell viabilities were determined 72 hours after treatment by Cell-Titer Glo Assay (Promega) on the Envision Multilabel Plate Reader (Perkin Elmer). Relative Luminescent Units (RLU) were plotted against corresponding drug concentrations and fitted with a standard four parameter sigmoidal curve with GraphPad Prism 6. Data was further fit for EC_{50} shift parameters in GraphPad Prism 6 to determine EC_{50} ratios for **6/7**. Data is reported as the EC_{50} ratio, error bars represent s.e.m. (n=3). Data for cell lines in which EC_{50} ratio fits were ambiguous, R^2 values were less than 0.9, or response to the free drug was less than 40% was not reported.

In vivo Assays:

In vivo puromycin studies: To evaluate relative changes in reactive iron pools across tissue types *in vivo*, we used the heterotopic indirect tumor xenograft model in nude mice (NCR nu/nu, Taconic). Early passage PC-3 cells were harvested and a cell suspension (1:1 serum free DMEM: Matrigel) was injected subcutaneously (s.c.) into the right flank of anesthetized donor nude mice (10^6 cells/mouse in 0.1 ml). When the mean tumor volume was 250-400 mm^3, tumor-bearing mice were treated with the indicated doses of compounds **2** or **3** formulated in 50:40:10 PEG 400:20% 2-hydroxypropyl-cylcodextrine in water: DMSO via ALZET® Osmotic Pump 2001D over the course of 24 h. Upon completion of dosing mice were sacrificed and organs were harvested and snap frozen. Frozen tissue samples were

cyrofractured with BioSpec Products BioPulverizer and ca. 20 mg of each tissue was further homogenized in RIPA lysis buffer supplemented with sigma protease inhibitor cocktail (P8340, 1:100) on ice for 30 min with frequent vortexing. Homogenized samples were clarified by centrifugation at 14,000 rpm for 10 min at 4 °C and standardized for total protein content by BCA. Lysates were assayed by dot blot analysis (1 µL of 1000 ng/µL solution per sample) for puromycin incorporation using Kerafast α-puromycin antibody [3RH11] (1:1000) in 2.5% non-fat milk overnight at 4 °C. The blot was then washed three-times with TBS-T and once with PBS-T before incubating with Li-cor IRDye 2° antibodies in Odyssey blocking buffer (#927-40000) + 0.2% Tween-20 and 0.01% Sodium dodecyl sulfate (SDS). The blot was washed 3 times with PBS-T for 5 min and once with PBS then imaged for fluorescent signal on an Odessey Classic Infrared Imaging System. Images were analyzed using Licor Image Studio Software to determine signal intensity.

Dose Escalation Studies: To evaluate the tolerability of the experimental agents, we treated nude mice (NCR nu/nu, Taconic) in triplicate with the indicated compounds in 50:40:10 PEG 400:20% 2-hydroxypropyl-cylcodextrine in water: DMSO via i.p. injections at the indicated intervals. Doses were increased in 2- or 3-fold steps until a given dose caused one or more mice in the group to reach protocol limits for tolerance (>20% weight loss) at any point post dosing.

Pharmacokinetics Studies: To evaluate the in vivo pharmacokinetic properties of the experimental agents, we treated nude mice (NCR nu/nu, Taconic) in triplicate with the indicated compounds at their respective MTD's formulated in 50:40:10 PEG

400:20% 2-hydroxypropyl-cylcodextrine in water: DMSO via i.p. injections. Blood samples were collected 5 min, 15 min, 30 min, 1 h, 2 h, 4 h, 8 h, 12 h, and 24 h post dosing and analyzed for plasma concentrations of each compound via MS/MS analysis conducted by Integrated Analytical Solutions, Inc. The resulting data was analyzed with WinNonlin software to calculate standard PK parameters.

Efficacy Studies: To evaluate the in vivo properties of the experimental agents, we used the heterotopic indirect tumor xenograft model in nude mice (NCR nu/nu, Taconic). Early passage PC-3 cells were harvested and a cell suspension (1:1 serum free DMEM: Matrigel) was injected subcutaneously (s.c.) into the right flank of anesthetized donor nude mice (10^6 cells/mouse in 0.1 ml). For MDA-MB-231 xenografts the cells were injected into the mammary fat pad of anesthetized donor nude mice (10^6 cells/mouse in 0.1 ml of PBS). When the mean tumor volume was 250-400 mm^3, tumor-bearing mice were treated with the indicated doses of compounds formulated in 50:40:10 PEG 400:20% 2-hydroxypropyl-cylcodextrine in water: DMSO via i.p. administration with the indicated frequency. Tumor volume (by caliper) and mouse weight was monitored twice weekly

Synthesis:

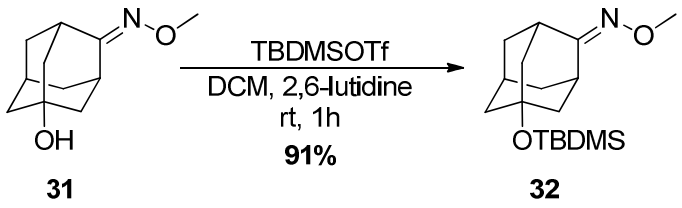

31 **32**

Synthesis of 5-[(tert-butyldimethylsilyl)oxy]-N-methoxyadamantan-2-imine (32). A 15-mL pear-shaped flask equipped with a rubber septa and argon inlet was charged with a teflon stir bar and a solution of **31**[74] (1.00 g, 5.12 mmol, 1 equiv.) in 1 mL of dry dichloromethane. 2,6-lutidine (1.19 mL, 10.24 mmol, 2 equiv.) was added and the solution was cooled to 0° C. TBDMS-triflate (1.77 mL, 7.68 mmol, 1.5 equiv.) was added dropwise to the reaction vessel while stirring under argon at 0° C. The reaction was then allowed to warm to room temperature and stirred for 1 h, then diluted with 75 mL of diethyl ether and washed with two, 50-mL portions of 1 N HCl and one, 50-mL portion of satd aq NaCl solution. The organic layer was dried over $MgSO_4$, filtered, and concentrated to afford an orange oil. Purification via column chromatography on 40 g of silica gel elluting with 5% EtOAc/hexanes afforded 1.438 g (91%) of **32**, as a clear oil : ^{1}H NMR (300MHz, $CDCl_3$): δ = 3.84 (s, 3 H), 3.60 (br. s, 1 H), 2.68 (br. s, 1 H), 2.25 (br. s, 1 H), 1.89 (br. s., 4 H), 1.83 (br. s., 2 H), 1.67 - 1.80 (m, 3 H), 1.62 (s, 1 H), 0.87 (s, 9 H), 0.09 ppm (s, 6 H). ^{13}C NMR (75MHz, $CDCl_3$): δ = 70.3, 61.3, 46.4, 45.3, 45.2, 38.1, 37.9, 36.7, 31.0, 30.6, 25.9, 18.1, -1.6 ppm. LRMS (ESI) *m/z* $[M+H]^+$ calcd for $C_{17}H_{31}NO_2Si$: 310.2; found: 310.1.

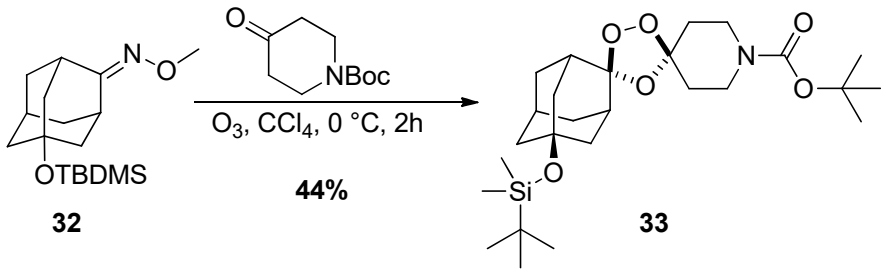

Synthesis of tert-butyl 7-[(tert-butyldimethylsilyl)oxy]dispiro[adamantane-2,2'-[1,3,5]trioxolane-4',4''-piperidine]-1''-carboxylate (33). A 200-mL recovery flask was charged with **32** (1.438 g, 4.64 mmol, 1 equiv.), 1-Boc-4-piperidone (1.853 g, 9.28 mmol, 2 equiv.), and a Teflon stir bar. To this was added 46 mL of carbon tetrachloride and the reaction mixture cooled to 0° C. Ozone was bubbled through the reaction mixture at a rate of 0.6 L/ min while stirring at 0 °C for 2.5 h. The reaction was then purged with O_2 for 5 min followed by argon for 5 min. The reaction mixture was concentrated and the resulting clear oil was purified by column chromatography on 120 g of silica gel eluting with 5% EtOAc/Hexanes to yield 1.0 g (44%) of **33** as a clear oil. ^{1}H NMR (300MHz, $CDCl_3$): δ = 3.41 - 3.67 (m, 4 H), 2.08 (br. s., 4 H), 1.93 (br. s., 3 H), 1.79 (d, *J*=2.8 Hz, 4 H), 1.73 (br. s., 2 H), 1.55 - 1.69 (m, 4 H), 1.52 (br. s., 9 H), 0.84 (s, 9 H), 0.03 - 0.18 ppm (m, 6 H). ^{13}C NMR (75MHz, $CDCl_3$): δ = 111.2, 107.6, 80.0, 70.0, 60.6, 47.5, 46.0, 45.5, 42.8, 38.6, 38.5, 38.4, 34.6, 34.4, 33.7, 33.7, 29.1, 28.6, 26.0, 25.9, 21.3, 18.1, 14.4, -1.6, -1.6 ppm. LRMS (ESI) *m/z* $[M\text{-Boc+H}]^+$ calcd $C_{21}H_{37}NO_4Si$: 396.2; found: 396.2 $[M\text{-Boc+H}]^+$.

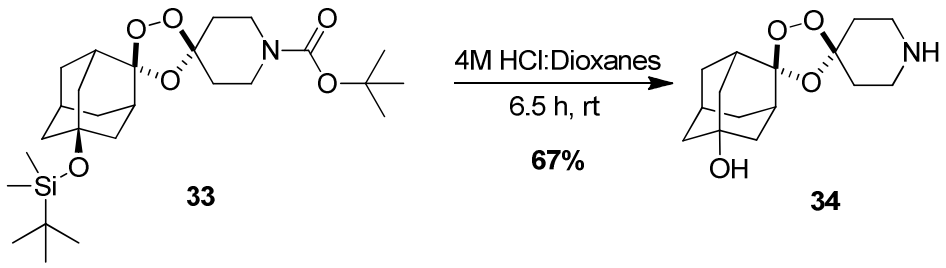

33 **34**

Synthesis of dispiro[adamantane-2,2'-[1,3,5]trioxolane-4',4''-piperidine]-7-ol (34). A 20-mL scintillation vial containing **33** (0.238 g, 0.48 mmol) was charged with a Teflon stirbar and equipped with a rubber septa and argon inlet. The atmosphere was replaced with argon and 5 mL of 4 M HCl in dioxane was added with stirring under argon at rt. The reaction was stirred for 6.5 h at rt then diluted with 20 mL of deionized water and washed with three, 25-mL portions of EtOAc. A 5 N NaOH solution (25 mL) was then added to the aqueous layer, and this was then extracted with three, 30-mL portions of 10% MeOH in chloroform. The combined organic layers were dried over $MgSO_4$, filtered, and concentrated to afford 0.090 g (67%) of **34** as an off-white solid. ^{1}H NMR (400MHz, CD_3OD): δ = 4.82 (s, 1 H), 2.76 - 2.94 (m, 4 H), 2.05 (br. s., 3 H), 2.01 (br. s., 2 H), 1.86 - 1.95 (m, 2 H), 1.81 (br. s., 1 H), 1.72 - 1.78 (m, 4 H), 1.68 (br. s., 2 H), 1.57 ppm (dd, *J*=18.4, 11.8 Hz, 4 H). ^{13}C NMR (100MHz, CD_3OD): δ = 110.6, 110.6, 107.3, 107.3, 67.0, 66.5, 66.1, 61.0, 44.1, 44.0, 43.6, 41.4, 38.5, 38.3, 35.0, 34.9, 33.4, 33.3, 29.4, 29.0 ppm. LRMS (ESI) *m/z* $[M+H]^+$ calcd for $C_{15}H_{23}NO_4$: 282.2; found: 282.0.

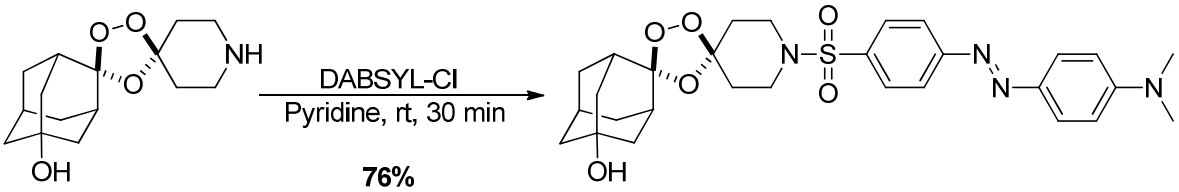

34 **35**

Synthesis of 1''-{4-[(E)-2-[4-(dimethylamino)phenyl]diazen-1-yl]benzenesulfonyl}dispiro[adamantane-2,2'-[1,3,5]trioxolane-4',4''-piperidine]-7-ol (35). A 10-mL round-bottomed flask equipped with a rubber septa and an argon inlet was charged with **34** (0.031 g, 0.11 mmol, 1 equiv.) and a Teflon stir bar. The material was dissolved in 0.9 mL of pyridine and DABSYL chloride (0.038g, 0.115 mmol, 1.05 equiv.) was added in one portion while stirring under argon. The reaction was stirred at rt under argon for 3 h then diluted with 10 mL of EtOAc and washed with 2, 10-mL portions of deionized water and one, 10-mL portion of satd aq NaCl solution. The organic layer was dried over $MgSO_4$, filtered, and concentrated to afford an orange oil which was purified on 12 g of silica gel eluting with 50% EtOAc/Hexanes to yield 0.048 g (76%) of **35**: ^{1}H NMR (400MHz, $CDCl_3$): δ = 7.87 - 8.01 (m, 4 H), 7.84 (d, *J*=8.4 Hz, 2 H), 6.75 (d, *J*=8.8 Hz, 2 H), 3.21 - 3.34 (m, 2 H), 3.17 (d, *J*=6.0 Hz, 2 H), 3.11 (s, 6 H), 2.04 (br. s., 4 H), 1.88 - 1.97 (m, 5 H), 1.78 (d, *J*=12.5 Hz, 2 H), 1.68 (br. s., 2 H), 1.47 - 1.62 (m, 4 H), 1.25 ppm (t, *J*=7.1 Hz, 1 H). ^{13}C NMR (100MHz, $CDCl_3$): δ = 156.0, 153.3, 143.8, 135.9, 128.6, 125.9, 122.8, 122.8, 111.6, 111.3, 106.4, 106.3, 67.5, 67.1, 60.6, 44.4, 44.4, 42.0, 42.0, 40.4, 38.3, 38.0, 34.1, 34.0, 33.4, 29.1, 28.8, 14.4 ppm. LRMS (ESI) *m/z* $[M+H]^+$ calcd for $C_{29}H_{36}N_4O_6S$: 569.2; found: 569.2.

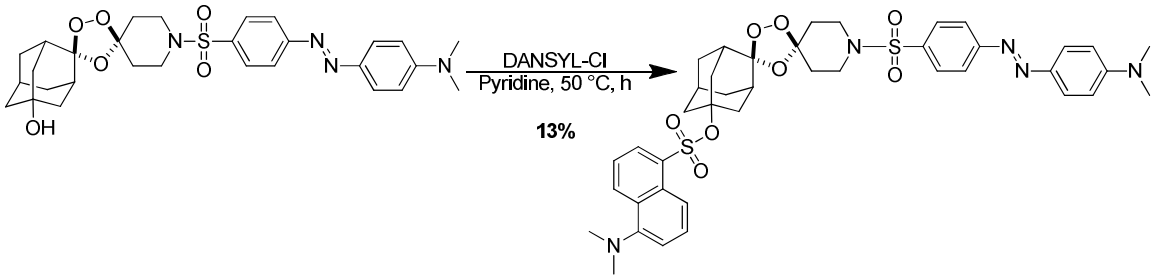

Synthesis of 1''-{4-[(E)-2-[4-(dimethylamino)phenyl]diazen-1-yl]benzenesulfonyl}dispiro[adamantane-2,2'-[1,3,5]trioxolane-4',4''-piperidine]-7-yl 5-(dimethylamino)naphthalene-1-sulfonate (1). A 10-mL round-bottomed flask equipped with a rubber septa and argon inlet was charged with **35** (0.048 g, 0.084 mmol, 1 equiv.), DANSYL chloride (0.113 g, 0.42 mmol, 5 equiv.), and a Teflon stirbar. The reagents were dissolved in 0.7 mL of pyridine with stirring under argon and the reaction mixture was warmed to 50 °C. The reaction was stirred under argon at 50 °C for 44 h, and then diluted with 10 mL of EtOAc and washed with 2, 10-mL portions of deionized water and one, 10-mL portion of satd aq NaCl solution. The organic layer was dried over $MgSO_4$, filtered, and concentrated to afford oil which was dissolved in CH_2Cl_2:MeOH and deposited onto ca. 5 g of silica. Purification on 12 g of silica gel eluting with 35% EtOAc/Hexanes yielded the desired material which was further purified over 12 g of silica gel eluting with 30% EtOAc/Hexanes to afford 0.009g (13%) of **1**.^{1}H NMR (300MHz, $CDCl_3$): δ = 8.55 (d, *J*=8.7 Hz, 1 H), 8.23 (dd, *J*=12.4, 8.1 Hz, 2 H), 7.81 - 8.00 (m, 6 H), 7.52 (dt, *J*=15.3, 7.9 Hz, 2 H), 7.18 (d, *J*=7.5 Hz, 1 H), 6.72 - 6.81 (m, 2 H), 3.45 (s, 1 H), 3.30 - 3.39 (m, 1 H), 3.14 (d, *J*=1.3 Hz, 6 H), 2.88 (s, 6 H), 2.56 (s, 1 H), 2.40 (d, *J*=8.7 Hz, 2 H), 2.11 (d, *J*=12.6 Hz, 5 H), 1.85 - 1.98 (m, 4 H), 1.76 (d, *J*=13.8 Hz, 2 H), 1.49 - 1.65 ppm (m, 5 H). ^{13}C NMR (75MHz, $CDCl_3$): δ = 156.0, 153.4, 143.9, 136.1, 135.6, 131.0, 130.0, 128.8, 128.7, 128.5, 126.0, 123.4, 122.9, 111.7, 110.2, 106.8, 89.6, 77.4, 60.6, 45.7, 44.4, 41.9, 40.5, 39.8, 38.9, 34.1, 33.0, 31.8, 29.5, 22.9,

21.3, 14.4, 14.3 ppm**.** LRMS (ESI) *m/z* $[M+H]^+$ calcd for $C_{41}H_{47}N_5O_8S_2$: 802.3; found: 802.3.

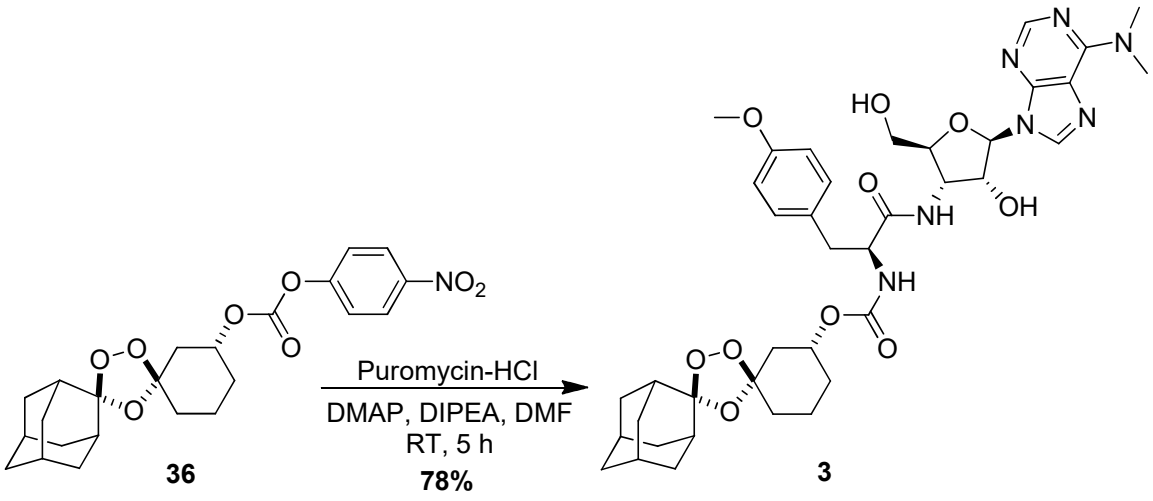

Synthesis of dispiro[adamantane-2,2'-[1,3,5]trioxolane-4',1''-cyclohexane]-3''-yl N-[(1S)-1-{[(2S,3S,4R,5R)-5-[6-(dimethylamino)-9H-purin-9-yl]-4-hydroxy-2-(hydroxymethyl)oxolan-3-yl]carbamoyl}-2-(4-methoxyphenyl)ethyl]carbamate (3). Prepared as previously described[57], except using trioxolane intermediates with *trans* stereochemistry (~90:10 dr) at the 3" position.[30] A two-necked, 15-mL round-bottomed flask equipped with a stir bar, septa, and argon inlet was charged with puromycin dihydrochloride from Streptomyces alboniger (0.064 g, 0.1 mmol, 1.1 equiv.), 4-dimethylaminopyridine (ca. 0.002 g, 0.01 mmol, 0.15 equiv.), and 4-nitrophenyl carbonate **36**[90] (0.048 g, 0.1 mmol, 1.0 equiv.) and the atmosphere was replaced with argon. This material was then dissolved in N,N-dimethylformamide (4 mL) and N,N-diisopropylethylamine (0.10 ml, 0.6 mmol, 5.3 equiv.) was added to this solution. The reaction mixture was allowed to stir at room temperature under argon for 5 hours then diluted with 10 mL of EtOAc and washed with four, 15-mL portions of sat. $NaHCO_3$. The aqueous layer was back extracted with 20mL of EtOAc and the organic layers were combined, washed with 20 mL of satd aq NaCl solution, and then dried over $MgSO_4$, filtered, and concentrated to afford a light yellow oil. Purification via column

chromatography on 25 g of silica gel (gradient elution with 0-10% MeOH/CH_2Cl_2) afforded the desired material with minor impurities. Further purification via reverse phase chromatography on a Silicycle 12 g C-18 column with gradient elution 0-100% MeOH/H_2O with constant 0.05% formic acid yielded 65 mg (78%) of **3** as a white solid. ^{1}H NMR (400MHz, CD_3OD): δ = 7.70 - 7.80 (m, 2 H), 6.68 (d, *J*=8.6 Hz, 2 H), 6.39 (dd, *J*=8.6, 1.5 Hz, 2 H), 6.11 (d, *J*=7.5 Hz, 1 H), 5.30 - 5.34 (m, 1 H), 4.15 (s, 3 H), 4.06 - 4.12 (m, 1 H), 3.99 - 4.05 (m, 1 H), 3.83 - 3.92 (m, 1 H), 3.51 (br. s., 1 H), 3.40 (d, *J*=12.8 Hz, 1 H), 3.13 (d, *J*=12.5 Hz, 1 H), 3.03 (br. s., 6 H), 2.85 - 2.88 (m, 1 H), 2.40 - 2.55 (m, 2 H), 1.69 - 1.78 (m, 1 H), 1.07 - 1.56 (m, 19 H), 0.89 - 1.04 (m, 1 H), 0.72 - 0.87 ppm (m, 2 H); ^{13}C NMR (100MHz, CD_3OD): δ = 191.2, 173.6, 159.4, 156.8, 155.6, 152.4, 149.6, 138.5, 131.0, 129.4, 125.9, 121.4, 114.7, 112.3, 109.4, 91.6, 84.7, 74.3, 72.3, 62.0, 59.9, 55.7, 52.4, 51.3, 51.3, 40.9, 39.1, 38.3, 37.4, 37.1, 37.0, 35.4, 34.3, 31.2, 27.6, 27.2, 20.4 ppm; LRMS (ESI) *m/z* $[M+H]^+$ calcd for $C_{39}H_{51}N_7O_{10}$: 778.4; found: 778.3.

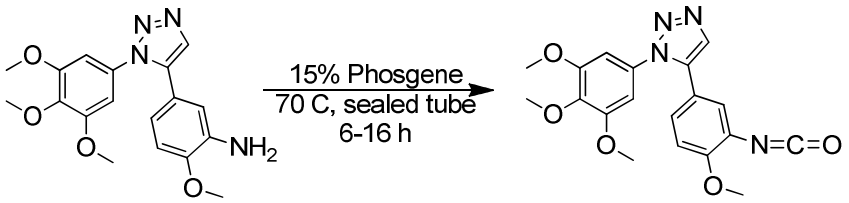

5 **37**

Synthesis of 5-(3-isocyanato-4-methoxyphenyl)-1-(3,4,5-trimethoxyphenyl)-1H-1,2,3-triazole (37). A 15-mL sealed reaction vessel fitted with a septa, argon inlet, and teflon stir bar was charged with 15.0% solution of phosgene in toluene (1.540 g, 2.3 mmol, 10.0 equiv.) (Caution! Toxic!). A solution of 2-methoxy-5-[1-(3,4,5-trimethoxyphenyl)-1H-1,2,3- triazol-5-yl]aniline (**5**)[121] (83 mg, 0.2 mmol, 1.0 equiv.) in anhydrous CH_2Cl_2 (4 mL) kept over 4Å molecular sieves was added drop wise to this solution. The septa was then quickly exchanged for a threaded cap and the sealed reaction vessel was heated to 70 °C behind a blast shield for 6-16 h. After cooling, the solution transferred to a 35-mL round-bottomed flask and concentrated to afford a light yellow solid that was further dried at high vaccum for at least 1 h to yield **37**. This material was carried used in subsequent reactions without further purification. LRMS (ESI) m/z $[M+H]^+$ calcd for $C_{19}H_{18}N_4O_5$: 383.1; found: 383.2.

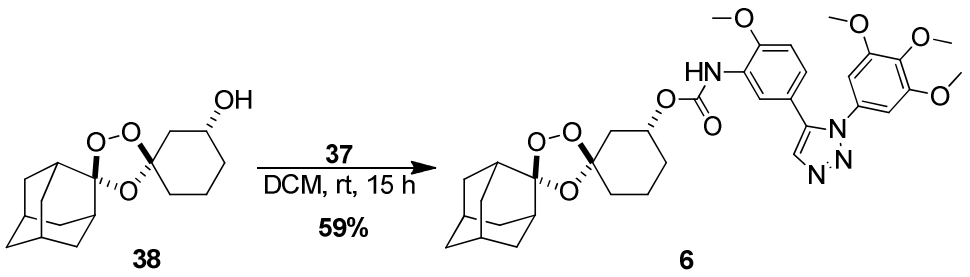

Synthesis of dispiro[adamantane-2,2'-[1,3,5]trioxolane-4',1''-cyclohexane]-3''-yl N-{2-methoxy-5-[1-(3,4,5-trimethoxyphenyl)-1H-1,2,3-triazol-5-yl]phenyl}carbamate (6). A 15-mL round-bottomed flask equipped with rubber septa and argon inlet was charged with isocyanate **37** (0.03 mmol, 1.0 equiv.) and a stir bar, and the atmosphere was replaced with argon. A solution of alcohol **38**[90] (0.046 g, 0.16 mmol, 5.3 equiv) in 1 mL of dry CH_2Cl_2 was added in bulk to the reaction and the reaction was stirred at rt and slowly concentrated to dryness under argon stream over the course of ca. 15 h. The resulting yellow solid was suspended in CH_2Cl_2 (10 mL) and washed with 10 mL of deionized water and 10 mL of satd aq NaCl solution, dried over $MgSO_4$, filtered, and concentrated to afford a light yellow oil. Purification via column chromatography on 12 g of silica gel (elution with 50% EtOAc/hexanes) afforded 0.012 g (59% over two steps) of carbamate **6** as an off-white solid: ^{1}H NMR (500MHz, $CDCl_3$): δ = 8.20 (br. s., 1 H), 7.83 (s, 1 H), 7.18 (s, 1 H), 6.80 (s, 2 H), 6.62 (s, 2 H), 4.75 - 4.87 (m, 1 H), 3.90 (br. s., 6 H), 3.73 - 3.78 (m, 6 H), 2.29 (dd, *J*=10.9, 1.8 Hz, 1 H), 1.84 - 2.06 (m, 9 H), 1.75 - 1.83 (m, 4 H), 1.60 - 1.74 (m, 8 H), 1.49 - 1.58 (m, 1 H), 1.32 - 1.41 (m, 1 H), 1.22 - 1.29 ppm (m, 1 H); ^{13}C NMR (126MHz, $CDCl_3$): δ = 153.6, 152.5, 148.1, 138.7, 138.0, 133.2, 132.5, 128.3, 123.2, 119.7, 118.4, 111.9, 110.1, 108.8, 103.5, 71.8, 61.2, 56.5, 56.0, 40.2, 36.9, 36.5, 36.5, 35.0, 35.0, 34.9, 34.0, 30.7, 27.1, 26.6, 19.9 ppm; HRMS (ESI) *m/z* $[M+H]^+$ calcd for $C_{35}H_{42}N_4O_9$: 663.3025; found: 663.2998.

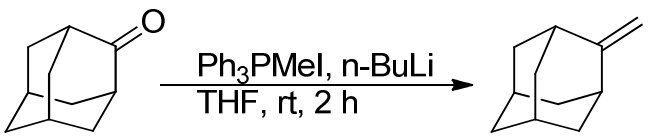

39

Synthesis of 2-methylideneadamantane (39): A 200-mL, round-bottomed flask equipped with a stir bar, rubber septa, and an argon inlet needle was charged with a solution of methyltriphenylphosphonium iodide (3.39 g, 8.38 mmol, 1.2 equiv) dissolved in THF (31 mL). A solution of n-BuLi (1.42 M in THF) was added dropwise to this suspension until the starting material dissolved and a bright orange color persisted (ca. 8 mL, 11 mmol, 1.6 equiv). The reaction mixture was stirred at rt for 15 minutes and then a solution of 2-adamantanone (1.049 g, 6.98 mmol, 1 equiv) dissolved in THF (10 mL) was added dropwise to the reaction mixture while stirring under Ar. After stirring for 2 hours the reaction mixture was diluted with CH_2Cl_2 and washed with H_2O. The aqueous layer was extracted with CH_2Cl_2 and the organic phases were combined, washed with satd aq NaCl solution, dried over $MgSO_4$, filtered, and concentrated to a yellow oil which was purified via silica chromatography eluting with 100% hexanes to yield 0.680 g (66%) of **39** as a fine white solid. ^{1}H NMR (400 MHz, $CDCl_3$) δ 4.51 (s, 2H), 2.49 (br. s., 2H), 1.92 - 1.97 (m, 2H), 1.85 - 1.92 (m, 4H), 1.79 - 1.85 (m, 5H), 1.78 (br. s., 1H), ^{13}C NMR (100 MHz, $CDCl_3$) δ 158.7, 100.8, 77.5, 77.4, 76.9, 39.9, 39.3, 37.5, 28.5.

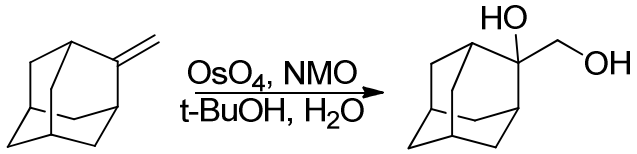

39 **58%** **40**

Synthesis of 2-(hydroxymethyl)adamantan-2-ol (40): A 35-mL, round-bottomed flask was charged with **39** (0.212 g, 1.4 mmol, 1 equiv) dissolved in 5 mL of tert-butanol, and 5 mL of H_2O. A solution of osmium tetroxide in (2.5% w/v in tert-butanol, 0.25 mL, 0.32 mmol, 0.2 equiv) was added to this solution followed by N-methylmorpholine oxide (0.465 g, 4.0 mmol, 2.8 equiv). This mixture was allowed to stir at rt for 12 hours then diluted with 20 mL of EtOAc and washed with 50 mL of satd aq $NaHCO_3$ solution. The aqueous phase was extracted with two 50-mL portions of EtOAc. The organic phases were washed with satd aq NaCl solution, dried over $MgSO_4$, and concentrated to give a light brown solid which was purified via silica chromatography eluting with 40% EtOAc in Hexanes to yield 0.152 g of **40** (58%). ^{1}H NMR (400MHz, CD_3OD): δ 3.67 (s, 2 H), 2.27 (d, *J*=11.9 Hz, 2 H), 1.83 - 1.91 (m, 2 H), 1.77 - 1.83 (m, 4 H), 1.71 - 1.77 (m, 4 H), 1.50 - 1.58 ppm (m, 2 H); ^{13}C NMR (100MHz, $CDCl_3$) δ 75.4, 67.3, 38.3, 34.6, 34.6, 33.0, 27.8, 27.4; LRMS (ESI) m/z $[M+Na]^+$ calcd for $C_{11}H_{18}O_2$: 205.1; found: 204.9.

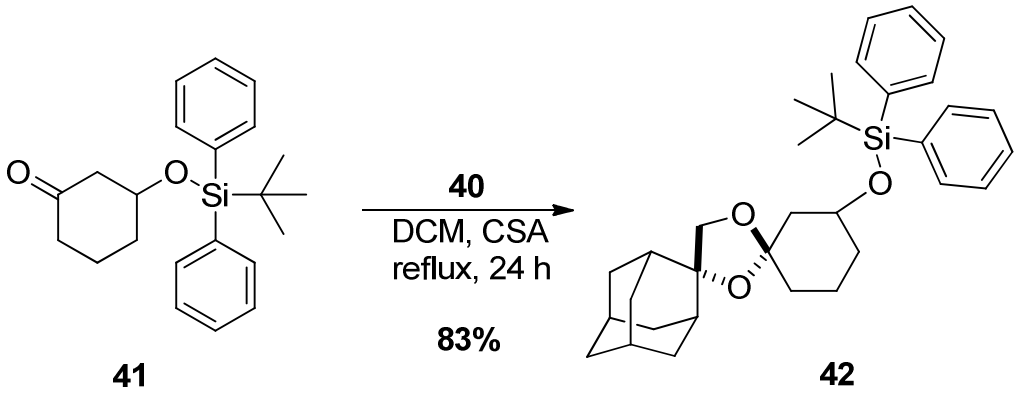

Synthesis of tert-butyl({dispiro[adamantane-2,4'-[1,3]dioxolane-2',1''-cyclohexane]-3''-yloxy})diphenylsilane (42): A 50 mL, 2-neck round-bottomed flask equipped with a stirbar, rubber septa, and reflux condenser fitted with an argon inlet adapter was charged with diol **40** (0.126 g, 0.69 mmol, 1 equiv), ketone **41**[90] (0.260 g, 0.74 mmol, 1.07 equiv), CH_2Cl_2 (20 mL), and camphor sulfonic acid (0.038 g, 0.016 mmol, 0.24 equiv). The reaction mixture was heated at reflux for 24 h, allowed to cool to rt, diluted with 20 mL of CH_2Cl_2, and washed with 25 mL of H_2O. The aqueous phase was extracted with two, 25-mL portions of CH_2Cl_2. The combined organic phases were washed with satd aq NaCl solution, dried over $MgSO_4$, filtered, and concentrated to afford a pale yellow oil. Purification via column chromatography on silica gel (elution with 10% EtOAc/Hexanes) to yield 0.295 g (83%) of **42** as clear oil. ^{1}H NMR (400 MHz, $CDCl_3$) δ 7.69 - 7.72 (m, 1 H), 7.67 - 7.69 (m, 1 H), 7.39 - 7.46 (m, 1 H), 7.38 (d, *J*=1.5 Hz, 1 H), 7.35 - 7.37 (m, 1 H), 3.90 - 3.99 (m, 1 H), 3.77 (dd, *J*=50.9, 9.5 Hz, 2 H), 1.99 - 2.06 (m, 1 H), 1.86 - 1.94 (m, 1 H), 1.82 (d, *J*=11.5 Hz, 1 H), 1.69 - 1.77 (m, 2 H), 1.66 (br. s., 2 H), 1.43 - 1.59 (m, 3 H), 1.36 - 1.43 (m, 2 H), 1.27 - 1.36 (m, 1 H), 1.05 - 1.10 ppm (m, 5 H); ^{13}C NMR (100MHz, $CDCl_3$) δ 136.0, 135.9, 134.9, 134.8, 129.6, 127.6, 109.5, 84.6, 84.2, 72.3, 72.1, 70.8, 70.4, 46.6, 45.8, 37.5, 37.5, 37.3, 37.2, 36.6, 36.3,

36.1, 35.9, 35.1, 34.8, 34.0, 33.8, 33.6, 27.2, 27.0, 26.8, 20.6, 20.5, 19.3, 19.3; LRMS (ESI) m/z $[M+H]^+$ calcd for $C_{33}H_{44}O_3Si$: 517.3; found: 517.3.

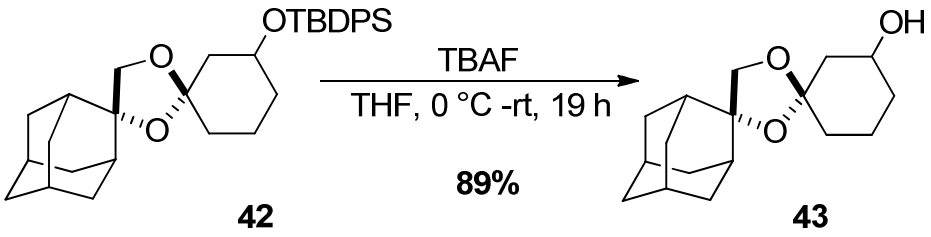

42 **43**

Synthesis of dispiro[adamantane-2,4'-[1,3]dioxolane-2',1''-cyclohexane]-3''-ol (43): A 25-mL, round-bottomed flask equipped with a stir bar, rubber septa, and an argon inlet needle was charged with a solution of dioxolane **42** (0.139 g, 0.56 mmol, 1 equiv) in dry THF (6 mL) and cooled to 0 °C. A solution of TBAF (1.0 M in THF, 2.8 mL, 2.8 mmol, 5 equiv) was added dropwise to this solution while stirring at 0 °C. The reaction was stirred at 0 °C for 30 minutes, allowed to warm to rt, stirred at rt for 19 hours, and then diluted with 20 mL of EtOAc and washed with 50 mL of H_2O. The aqueous layer was extracted with 30 mL of EtOAc. The combined organic phases were washed with satd aq NaCl solution, dried over $MgSO_4$, filtered, and concentrated to afford a clear oil. Purification via column chromatography on silica gel (elution with 25% EtOAc/hexanes) afforded 0.139 g (89%) of **43** as a foamy, white oil: ^{1}H NMR (400MHz, $CDCl_3$): δ 3.98 (br. s., 1 H), 3.86 - 3.92 (m, 2 H), 2.67 (br. s., 1 H), 2.11 - 2.19 (m, 2 H), 1.88 (d, *J*=3.8 Hz, 1 H), 1.74 - 1.84 (m, 7 H), 1.66 - 1.72 (m, 3 H), 1.54 - 1.62 (m, 7 H), 1.44 - 1.54 ppm (m, 1 H); ^{13}C NMR (100MHz, $CDCl_3$) δ 109.5, 109.4, 85.6, 84.9, 72.4, 72.1, 68.6, 68.1, 44.1, 37.5, 37.5, 37.4, 37.4, 37.2, 37.2, 36.6, 36.5, 36.1, 36.0, 36.0, 36.0, 33.9, 33.7, 33.7, 33.6, 33.5, 27.1, 26.9, 26.8, 26.8, 19.4, 18.9; LRMS (ESI) m/z $[M+H]^+$ calcd for $C_{17}H_{26}O_3$: 279.2; found: 279.1.

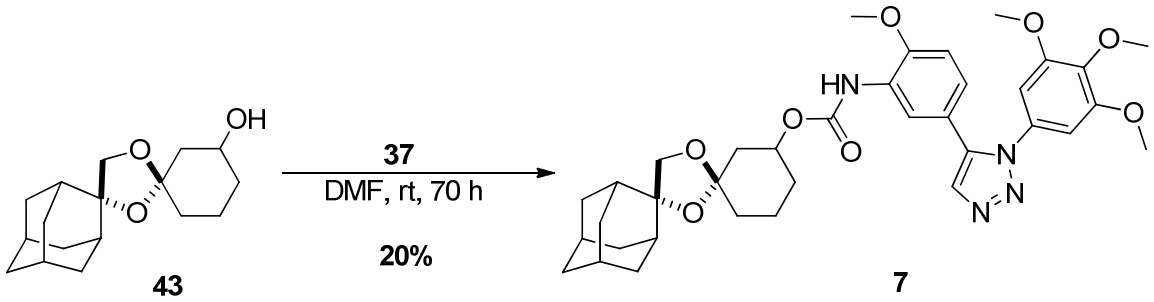

43 7

Synthesis of dispiro[adamantane-2,2'-[1,3]dioxolane-4',1''-cyclohexane]-3''-yl N-{2-methoxy-5-[1-(3,4,5-trimethoxyphenyl)-1H-1,2,3-triazol-5-yl]phenyl}carbamate (7). In a manner analogous to the preparation of trioxolane-conjugate **6** the requisite alcohol starting material **43** (0.035 g, 0.13 mmol, 1.7 equiv) was reacted with isocyanate **37** (0.028 g, 0.07 mmol, 1 equiv) in anhydrous DMF (2.5 mL) stored over 2 Å molecular sieves for 70 h at rt under an atmosphere of argon. The reaction mixture was then diluted with 10 mL of CH_2Cl_2 and washed with 10 mL of deionized water. The aqueous layer was extracted with three, 5-mL portions of CH_2Cl_2 and the organic layers were combined, dried over $MgSO_4$, filtered, and reduced to yield a yellow oil. Purification via column chromatography on 25 g of silica gel (elution with 25-50-75% EtOAc/Hexanes) afforded the desired material contaminated with trace amounts of analine **5**, which was further purified via rpHPLC with gradient elution from 0-90% MeOH:H_2O with constant 0.1% formic acid to yield 0.020 g (20% over two steps) of carbamate **7** as a white solid. ^{1}H NMR (400MHz, $CDCl_3$): δ 7.78 - 7.87 (m, 1 H), 7.19 (s, 1 H), 6.73 - 6.82 (m, 2 H), 6.54 - 6.65 (m, 2 H), 3.95 (s, 1 H), 3.88 (s, 6 H), 3.76 (s, 6 H), 2.24 (d, *J*=14.5 Hz, 2 H), 2.14 (s, 1 H), 2.06 - 2.13 (m, 1 H), 1.78 (s, 3 H), 1.82 (s, 3 H), 1.51 - 1.73 (m, 8 H), 1.38 ppm (d, *J*=5.1 Hz, 2 H); ^{13}C NMR (75MHz, $CDCl_3$): δ = 162.7, 153.6, 152.9, 148.2, 138.7, 138.0, 133.3, 132.5, 128.5, 123.1, 119.7, 118.4, 110.1, 109.0, 103.4, 85.3, 77.4, 73.1, 72.6, 61.2, 56.5, 56.0, 43.0, 37.5, 36.7, 36.5, 36.1, 33.8, 31.7, 31.4, 27.1, 26.9, 20.3 ppm; HRMS (ESI) m/z $[M+H]^+$ calcd for $C_{36}H_{44}N_4O_8$: 661.3232; found: 661.3203.

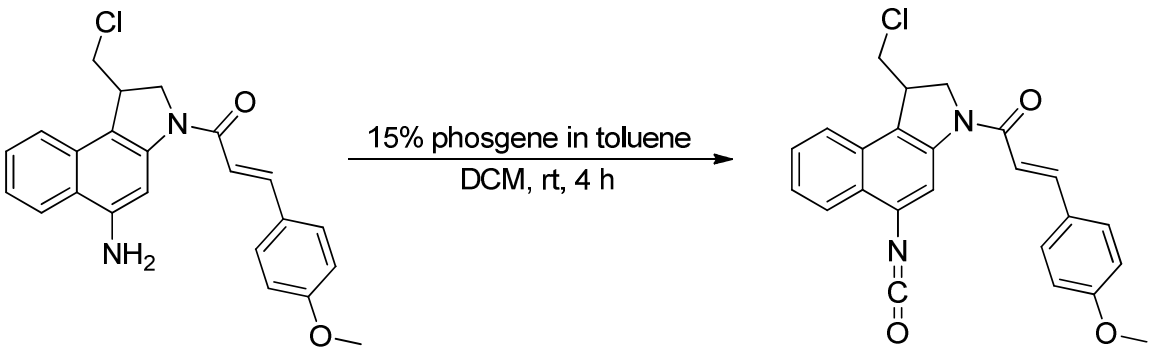

Preparation of (2E)-1-[1-(chloromethyl)-5-isocyanato-1H,2H,3H-benzo[e]indol-3-yl]-3-(4-methoxyphenyl)prop-2-en-1-one (44): A 15-mL sealed tube reaction vessel which had been heat dried under vacuum and covered in argon was charged with a stirbar and a solution of 15.0% Phosgene (1.090 ml, 1.5 mmol, 10.0 equiv.) in toluene. To this solution was added a solution of aniline **5** (60 mg, 0.2 mmol, 1.0 equiv.) dissolved in 4 mL of dry DCM in a dropwise fashion over the course of ca. 5 min. This transfer was completed with an additional 2mL of dry DCM and the rubber septa was then quickly exchanged for the threaded cap and the reaction was stirred at rt for 4 h over which the reaction gradually changed from yellow to deep red. An aliquot of the reaction (10 µL) was quenched with benzylamine (50 µL) and a sample analyzed my LCMS indicated no aniline starting material (**9**) remained with only benzylamine and the expected formed urea present. The reaction was reduced under vacuum to a light red solid (**44**) which was further dried under high vacuum for >1 h then carried on for subsequent reactions without further purification or characterization due to instability.

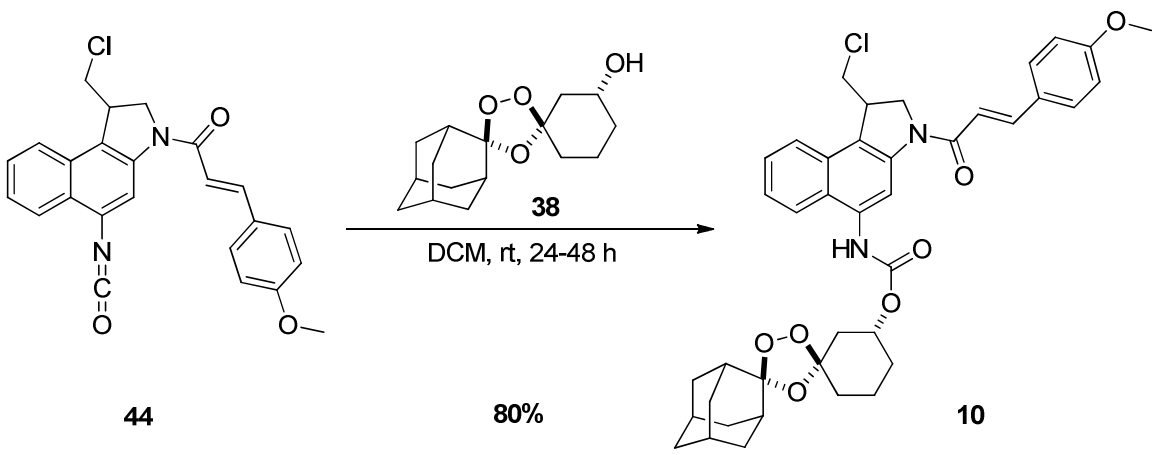

Preparation of dispiro[adamantane-2,2'-[1,3,5]trioxolane-4',1''-cyclohexane]-3''-yl N-[1-(chloromethyl)-3-[(2E)-3-(4-methoxyphenyl)prop-2-enoyl]-1H,2H,3H-benzo[e]indol-5-yl]carbamate (10): A 15-mL, sealed tube reaction vessel equipped with a stir bar, rubber septa, and an argon inlet needle containing isocyanate **44** (0.09 mmol, 1 eq.) was charged with a solution of alcohol **38**[90] (0.089 g, 0.3 mmol, 3.6 equiv.) in dichloromethane (2.000 mL) and the reaction was stirred at rt under argon for 42 h. During this time the reaction was concentrated to dryness twice via argon stream then re-suspended in 2 mL of dry DCM. After the second concentration the reaction was complete by LCMS and the reaction was deposited directly on to a 25 g silica column in 1 mL of DCM eluting with 25-50% EtOAc:Hex to afford 0.050 g (80%) of **10** as a foamy yellow solid: ^{1}H NMR (400MHz, $CDCl_3$): δ 8.85 (br. s., 1 H), 7.77 - 7.88 (m, 2 H), 7.71 (d, *J*=8.2 Hz, 1 H), 7.55 (br. s., 1 H), 7.50 (t, *J*=7.4 Hz, 1 H), 7.40 (t, *J*=7.4 Hz, 1 H), 6.92 (d, *J*=8.2 Hz, 2 H), 6.73 (br. s., 1 H), 4.84 - 4.95 (m, 1 H), 4.44 - 4.55 (m, 1 H), 4.33 (t, *J*=9.4 Hz, 1 H), 4.05 (br. s., 1 H), 3.92 (d, *J*=10.9 Hz, 1 H), 3.85 (s, 3 H), 3.44 (t, *J*=10.7 Hz, 1 H), 2.37 (s, 1 H), 2.10 (br. s., 1 H), 1.84 - 2.05 (m, 9 H), 1.72 - 1.83 (m, 5 H), 1.63 - 1.71 (m, 5 H), 1.48 - 1.61 (m, 2 H), 1.34 - 1.44 ppm (m, 1 H). ^{13}C NMR (100MHz, $CDCl_3$): δ 161.5, 161.4, 144.0, 134.4, 134.3, 130.1, 127.8, 127.8, 127.4, 124.7, 123.1, 114.4,

111.8, 111.8, 108.9, 73.3, 72.1, 55.6, 55.5, 46.2, 41.4, 40.3, 40.2, 36.9, 36.8, 36.5, 36.4, 36.4, 35.9, 35.0, 35.0, 34.9, 34.9, 34.0, 33.9, 31.1, 30.8, 27.0, 26.6, 26.0, 24.9, 23.6, 19.9 ppm; HRMS (ESI) m/z $[M+H]^+$ calcd for $C_{40}H_{43}ClN_2O_7$: 699.2837; found: 699.2858.

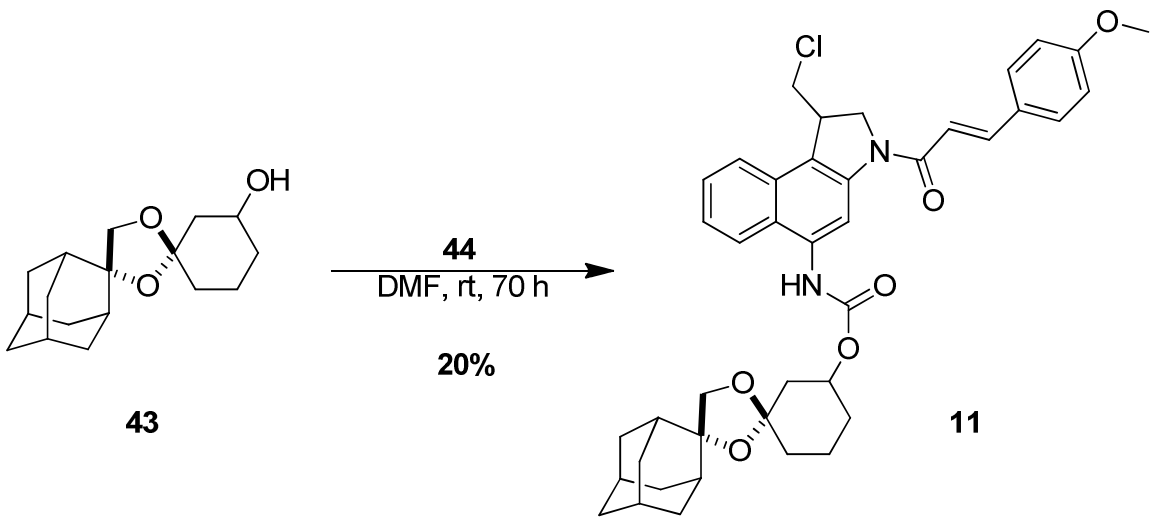

43 11

Preparation of dispiro[adamantane-2,4'-[1,3]dioxolane-2',1''-cyclohexane]-3''-yl N-[1-(chloromethyl)-3-[(2E)-3-(4-methoxyphenyl)prop-2-enoyl]-1H,2H,3H-benzo[e]indol-5-yl]carbamate (11): A 15-mL vacuum dried round-bottomed flask equipped with a teflon stir bar, septa and argon inlet was charged with a solution of isocyanate **44** (0.032 g, 0.1 mmol, 1.0 equiv.) in dry DCM, then reduced and dried on high vac for > 2 h. To this material was added a solution of alcohol **43** (0.043 g, 0.2 mmol, 2.0 equiv.) in N,N-dimethylformamide (1.500 ml) while stirring under argon. The solution was stirred under argon for 21 h then diluted with 15 mL of EtOAc, washed with two, 20-mL portions of deionized water and one 20-mL portion of sat. NaCl solution. The organic layer was dried over $MgSO_4$, filtered, and reduced to a deep red oil which was purified on 25 g of silica elluting with 25% EtOAc:Hexanes to afford 0.025 g (0.021 mmol, 47%) of **11** as a yellow solid. ^{1}H NMR (400MHz, $CDCl_3$): δ 8.89 (br. s., 1 H), 7.91 (s, 1 H), 7.80 - 7.88 (m, 1 H), 7.76 (d, *J*=7.9 Hz, 1 H), 7.60 (br. s., 1 H), 7.53 (t, *J*=7.3 Hz, 1 H), 7.43 (ddd, *J*=8.3, 7.0, 1.0 Hz, 1 H), 6.94 (d, *J*=8.6 Hz, 2 H), 6.86 (br. s., 1 H), 4.98 - 5.07 (m, 1 H), 4.55 (d, *J*=10.1 Hz, 1 H), 4.39 (t, *J*=9.4 Hz, 1 H), 4.07 - 4.13 (m, 1 H), 3.96 (d, *J*=10.1 Hz, 1 H), 3.89 - 3.92 (m, 2 H), 3.85 - 3.87 (m, 3 H), 3.47 (t, *J*=11.0

Hz, 1 H), 2.09 - 2.29 (m, 4 H), 1.79 - 1.88 (m, 3 H), 1.77 (br. s., 4 H), 1.64 - 1.71 (m, 4 H), 1.51 - 1.62 (m, 5 H), 1.49 (d, *J*=4.6 Hz, 1 H), 1.44 - 1.47 (m, 1 H), 1.37 ppm (d, *J*=11.2 Hz, 1 H). ^{13}C NMR (100MHz, $CDCl_3$): δ 161.5, 134.6, 130.1, 127.9, 124.8, 114.5, 109.0, 85.2, 72.6, 55.6, 46.2, 42.9, 37.6, 37.5, 37.5, 37.4, 36.6, 36.2, 36.0, 33.9, 33.8, 31.3, 27.1, 26.9, 20.3 ppm. HRMS (ESI) m/z $[M+H]^+$ calcd for $C_{41}H_{45}ClN_2O_6$: 697.3044; found: 697.3056.

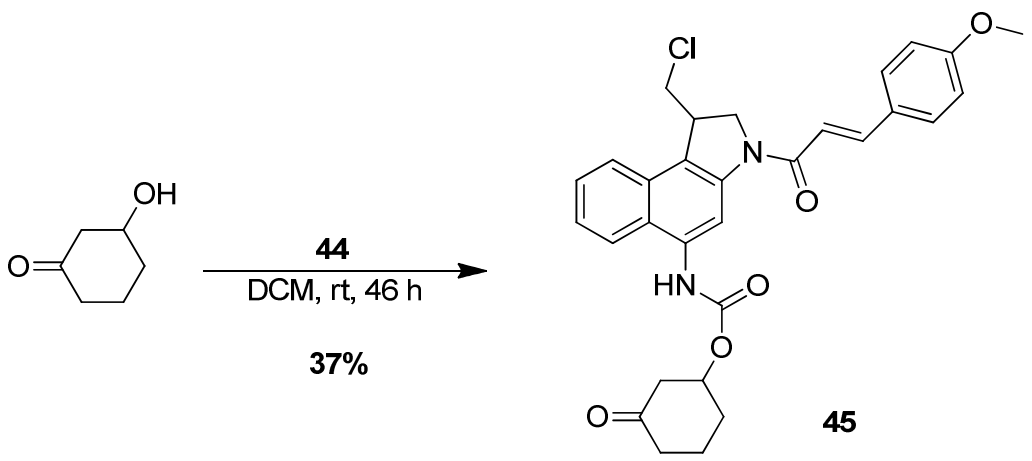

Preparation of 3-oxocyclohexyl N-[1-(chloromethyl)-3-[(2E)-3-(4-methoxyphenyl)prop-2-enoyl]-1H,2H,3H-benzo[e]indol-5-yl]carbamate (45): A 5-mL round-bottomed flask equipped with a rubber septa and argon inlet was charged with isocyanate **44** (0.010 g, 0.025 mmol, 1 eq.) and a teflon stirbar. The atmosphere was replaced with argon and a solution of 3-hydroxycyclohexan-1-one (0.020 g, 0.2 mmol, 6.9 equiv.) in dichloromethane (0.571 ml, 8.9 mmol, 350.2 equiv.) was added in bulk to the formed isocyanate under argon and the reaction was stirred at rt under argon for 46 h then concentrated and loaded directly onto 12 g of silica, elluting with 25-50% EtOAc:Hex to afford 0.005 g (0.009 mmol, 37%) of carbamate XX contaminated with a small amount of an unknown material. Due to instability of the desired product the material was used as is for an authentic sample in plasma concentration determination for PK studies: ^{1}H NMR (400MHz, CD_2Cl_2) δ 8.89 (1H, br. S.), 7.89 (1H, d, J = 6.8 Hz), 7.81 (1H, d, J = 8.5 Hz), 7.62 (2H, br. s.), 7.57 (1H, br. s.), 7.47 (1H, br. s.), 7.03 (1H, br. s.), 6.96 (2H, d, J = 6.6 Hz), 6.84 (1H, br. s.), 4.56 (1H, d, J = 9.1 Hz), 4.44 (1H, br. s.), 4.17 (3H, br. s.), 3.99 (1H, d, J = 10.5 Hz), 3.86 (3H, br. s.), 3.59 (1H, d, J = 10.1 Hz), 2.73 (1H, d, J = 11.9 Hz), 2.60 (3H, d, J = 13.5 Hz), 2.23 - 2.41 (9H, m), 1.95 - 2.11 (7H, m), 1.86 (1H, br. s.), 1.71 (4H, br. s.), 1.60 (9H, br. s.), 1.27 (3H, br. s.), 0.85 (3H, br. s.); HRMS (ESI) m/z $[M+H]^+$ calcd for $C_{30}H_{29}ClN_2O_5$: 533.1843; found: 533.1842.

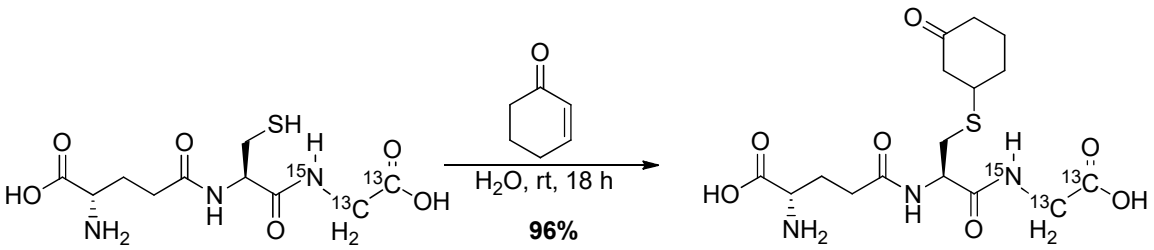

Reaction to produce (2S)-2-amino-4-{[(1R)-1- {[carboxy($^{13}C_2$)methyl](^{15}N)carbamoyl}-2-[(3- oxocyclohexyl)sulfanyl]ethyl]carbamoyl}butanoic acid (12):

A 5 mL round-bottomed flask equipped with a rubber septa and argon inlet was charged with Glutathione-(glycine-$^{13}C_2$,^{15}N) (0.025 g, 0.1 mmol, 1.0 equiv.) and a Teflon stir bar and the atmosphere was replaced with argon. The material was dissolved in 0.5mL of millipure water which had been degassed with argon for 1 h to give a clear solution to which 2-Cyclohexen-1-one (0.040 ml, 0.4 mmol, 5.1 equiv.) was added. The reaction was allowed to stir at rt under argon for 18 h then dilluted with 5 mL of millipure water and washed with three, 5 mL portions of ethyl ether. The aqueous fraction was isolated and lyophilized to yield 0.0313 g of **12** (96%) as a white solid: ^{1}H NMR (400MHz, D_2O): δ = 4.56 (dd, *J*=8.2, 5.3 Hz, 1 H), 4.15 (d, *J*=5.7 Hz, 1 H), 3.92 (t, *J*=6.5 Hz, 1 H), 3.80 (d, *J*=5.7 Hz, 1 H), 3.29 (tt, *J*=8.5, 4.5 Hz, 1 H), 3.13 - 3.20 (m, 1 H), 3.07 (ddd, *J*=14.0, 6.9, 5.5 Hz, 1 H), 2.90 (ddd, *J*=14.1, 8.2, 6.2 Hz, 1 H), 2.76 (ddd, *J*=14.2, 9.5, 4.5 Hz, 1 H), 2.47 - 2.60 (m, 2 H), 2.41 - 2.46 (m, 1 H), 2.33 - 2.41 (m, 2 H), 2.11 - 2.22 (m, 2 H), 1.93 - 2.11 (m, 2 H), 1.69 - 1.82 (m, 2 H), 1.57 - 1.67 (m, 1 H), 1.29 - 1.38 (m, 1 H), 1.25 (t, *J*=7.3 Hz, 1 H), 1.15 (t, *J*=7.1 Hz, 1 H), 0.91 ppm (t, *J*=7.4 Hz, 1 H). ^{13}C NMR (100MHz, D_2O): d = 174.7, 173.2, 173.2, 172.8, 53.2, 47.1, 43.1, 41.3, 40.5, 31.2, 30.2, 25.9, 13.0 ppm. Mass labelled ^{13}C clearly visible at 41.3 (dd, *J*=58.7, 12.2; 1 C) and 173.2 (d, *J*=58.7, 1 C). HRMS m/z $[M+H]^+$ calcd for $C_{14}{}^{13}C_2H_{25}N_2{}^{15}NO_7S$: 407.1529; found: 407.1464.

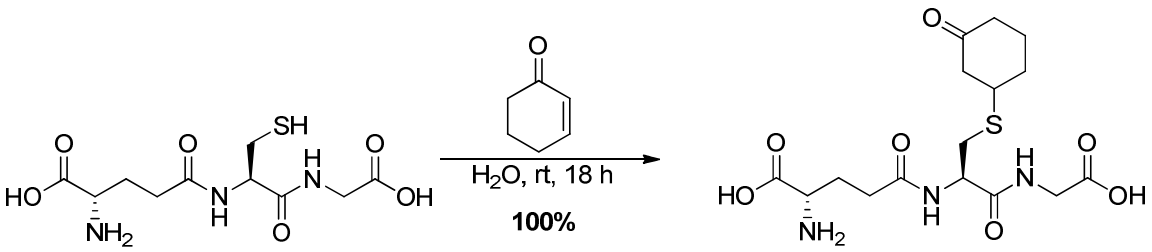

Reaction to produce (2S)-2-amino-4-{[(1R)-1-[(carboxymethyl)carbamoyl]-2-[(3-oxocyclohexyl)sulfanyl]ethyl]carbamoyl}butanoic acid (13): A 10 mL round-bottomed flask equipped with a rubber septa and argon inlet was charged with L-Glutathione (0.060 g, 0.2 mmol, 1.0 equiv.) and a Teflon stir bar and the atmosphere was replaced with argon. The material was dissolved in 1 mL of millipure water which had been degassed with argon for 1 h to give a clear solution to which 2-Cyclohexen-1-one (0.1 ml, 1.0 mmol, 5.3 equiv.) was added. The reaction was allowed to stir at rt under argon for 20 h then dilluted with 5 mL of millipure water and washed with three, 5 mL portions of ethyl ether. The aqueous fraction was isolated and lyophilized to yield 0.079 g of **13** (100%) as a white solid: ^{1}H NMR (400MHz, D_2O): δ = 4.56 (dd, *J*=8.4, 5.3 Hz, 1 H), 3.94 (s, 2 H), 3.80 (t, *J*=6.4 Hz, 1 H), 3.23 - 3.33 (m, 1 H), 3.08 (ddd, *J*=13.7, 7.8, 5.4 Hz, 1 H), 2.90 (ddd, *J*=14.3, 8.1, 6.8 Hz, 1 H), 2.47 - 2.57 (m, 2 H), 2.41 - 2.47 (m, 1 H), 2.32 - 2.41 (m, 1 H), 2.14 (q, *J*=7.5 Hz, 3 H), 2.00 - 2.08 (m, 1 H), 1.75 ppm (dd, *J*=7.5, 2.7 Hz, 2 H). ^{13}C NMR (100MHz, D_2O): δ = 174.8, 173.6, 173.6, 172.6, 164.4, 128.2, 53.9, 47.1, 41.7, 40.5, 31.4, 26.2, 25.5, 23.5, 23.4, 22.2 ppm. HRMS m/z $[M+H]^+$ calcd for $C_{16}H_{25}N_3O_7S$: 404.1491; found: 404.1461.

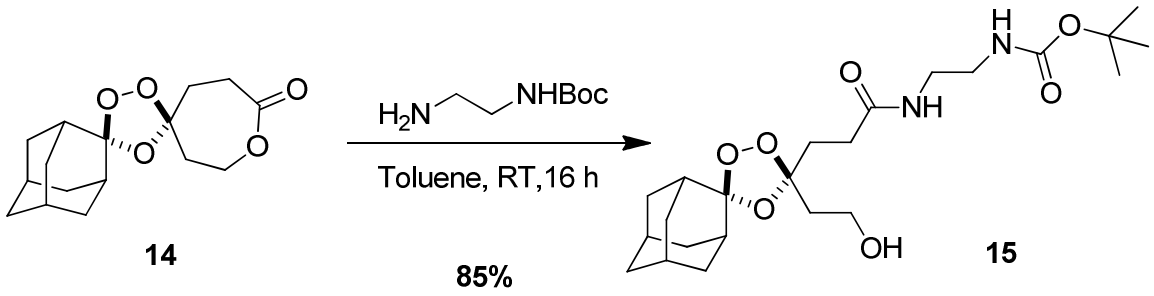

14 **85%** **15**

Preparation of tert-butyl N-(2-{3-[5'-(2-hydroxyethyl)spiro[adamantane-2,2'-[1,3,4]trioxolane]-5'-yl]propanamido}ethyl)carbamate (15): A 4-mL screw top scintillation vial was charged with a solution of lactone **14** (0.052g, 0.2 mmol, 1.0 equiv.) in toluene (0.5 mL) and a Teflon stir bar. Tert-Butyl N-(2-aminoethyl)carbamate (0.056 ml, 0.4 mmol, 2.0 equiv.) was added and the reaction mixture was stirred at rt for 16 h. The reaction was then diluted with 10 mL of EtOAc and washed sequentially with 10 mL each of 0.1 N HCl, deionized water, and satd aq NaCl solution. The organic layer was dried over $MgSO_4$, filtered, and concentrated to a clear oil with was purified via column chromatography on 12 g of silica gel elluting with 5% MeOH/DCM to yield 0.068 g (85%) of **15** as a white solid: ^{1}H NMR (400 MHz, $CDCl_3$) δ 6.62 (br. s., 1H), 5.20 (br. s., 1H), 3.70 - 3.85 (m, 2H), 3.29 - 3.36 (m, 2H), 3.24 (d, *J* = 4.76 Hz, 2H), 2.24 - 2.37 (m, 2H), 2.06 - 2.22 (m, 2H), 1.92 - 2.04 (m, 6H), 1.80 - 1.92 (m, 3H), 1.72 - 1.80 (m, 3H), 1.69 (br. s., 1H), 1.67 (br. s., 3H), 1.42 (s, 9H); ^{13}C NMR (100 MHz, $CDCl_3$) δ 173.2, 148.0, 112.5, 110.7, 79.8, 60.6, 58.5, 40.8, 40.3, 37.9, 36.7, 36.4, 36.4, 35.0, 35.0, 34.9, 34.9, 31.8, 31.0, 29.8, 28.5, 26.9, 26.5, 21.2, 14.3; LRMS (ESI) *m/z* $[M+H]^+$ calcd for $C_{23}H_{39}N_2O_7$: 455.3; found:455.2.

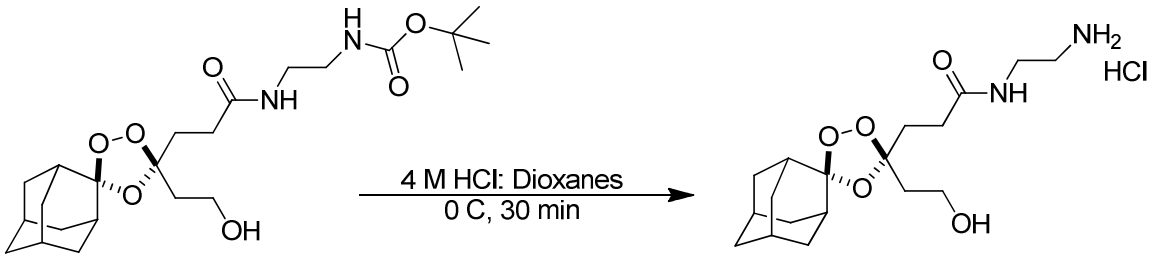

15 **46**

Preparation of N-(2-aminoethyl)-3-[5'-(2-hydroxyethyl)spiro[adamantane-2,2'-[1,3,4]trioxolane]-5'-yl]propanamide hydrochloride (46): A 20-mL scintillation vial equipped with a stirbar and screw cap was charged with alcohol **15** (0.040 g, 0.1 mmol, 1.0 equiv.) and 4 M HCl:Dioxanes (2.000 ml, 8.0 mmol, 90.9 equiv) The resulting mixture was stirred at 0 °C for 20 min then allowed to warm to rt. After 30 min at rt the reaction mixture was diluted with 5 mL of toluene and concentrated to a volume of ca 1 mL then diluted and concentrated from 5 mL of toluene twice more to afford the de-protected amine (**46**) as a white solid. This material was carried forward without further purification due to previous observations of stability issues with similar material. LRMS (ESI) *m/z* $[M+H]^+$ calcd for $C_{18}H_{31}N_2O_5$: 355.2; found:355.2.

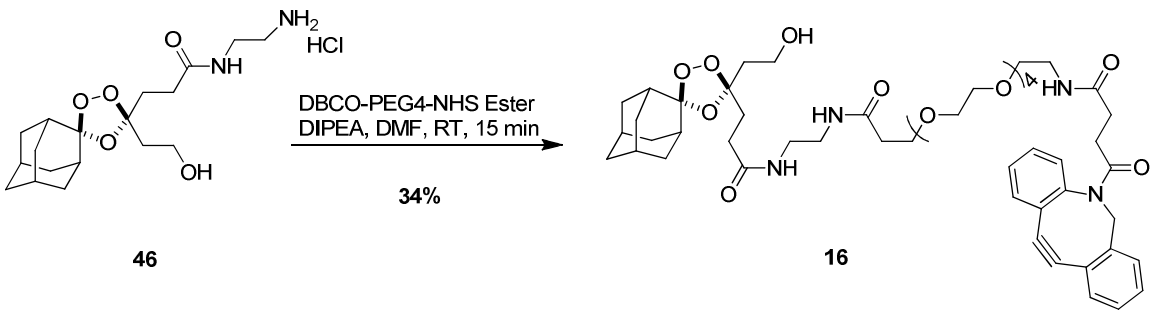

46 **16**

Preparation of N-(2-{2-azatricyclo[10.4.0.0^{4,9}]hexadeca-1(12),4(9),5,7,13,15-hexaen-10-yn-2-yl}-2-oxoethyl)-N'-(2-{3-[5'-(2-hydroxyethyl)spiro[adamantane-2,2'-[1,3,4]trioxolane]-5'-yl]propanamido}ethyl)-4,7,10,14-tetraoxaheptadecanediamide (16): A 20-mL scintillation vial containing amine **46** (0.034 g, 0.1 mmol, 1.0 equiv.) was equiped with a stir-bar, septa, and argon inlet and charged with 1 mL of DMF. To this solution was added N,N-diisopropylethylamine (0.150 ml, 0.9 mmol, 9.9 equiv.) followed by DBCO-PEG$_4$-NHS ester (0.100 g, 0.2 mmol, 1.8 equiv.) in a dropwise fashion while stirring. This solution was stirred at rt for 15 min then dilluted with 15 mL of DCM, washed with one 20 mL portion of water and one 20 mL portion of 0.1 N HCl solution. The aqueous layers were back extracted with 15 mL of DCM and the combined organic layers were washed with 20 mL of satd aq NaCl solution, dried over $MgSO_4$, filtered and reduced to a yellow oil. Purification via silica gel chromatography (25 g) elluting with 5-10% MeOH/DCM yielded the desired product with minor impurities. Further purification on 12 g of silica gel eluting with 10%MeOH/DCM yielded 0.026 g (34% over two steps) of **16**: ^{1}H NMR (400 MHz, $CDCl_3$) δ 7.60 - 7.67 (m, 1H), 7.54 (td, *J* = 2.50, 4.72 Hz, 1H), 7.36 - 7.43 (m, 1H), 7.22 - 7.35 (m, 2H), 7.13 (br. s., 1H), 6.88 (br. s., 1H), 6.78 (d, *J* = 14.28 Hz, 1H), 5.13 (d, *J* = 13.92 Hz, 1H), 3.71 - 3.80 (m, 1H), 3.64 - 3.70 (m, 1H), 3.54 - 3.63 (m, 8H), 3.41 - 3.49 (m, 2H), 3.27 - 3.37 (m, 4H), 2.77 - 2.88 (m, 1H), 2.47 (td, *J* = 7.51, 15.02 Hz, 2H), 2.24 - 2.36 (m, 3H), 2.09 - 2.23 (m, 3H), 1.94 - 2.03 (m, 4H), 1.91 (d, *J* = 4.76 Hz, 1H), 1.82 - 1.89 (m, 2H), 1.76 (d, *J* = 12.09 Hz, 2H),

1.63 - 1.71 (m, 3H), 1.25 (s, 1H); ^{13}C NMR (100 MHz, $CDCl_3$) δ 217.3, 173.0, 172.8, 172.7, 172.4, 151.5, 148.3, 132.3, 129.6, 128.9, 128.4, 128.3, 127.9, 127.2, 125.7, 123.4, 122.6, 114.8, 112.4, 110.9, 108.1, 70.7, 70.5, 70.4, 70.3, 70.3, 70.0, 67.3, 58.4, 55.8, 53.6, 43.8, 40.5, 39.4, 37.9, 36.8, 36.5, 35.1, 35.0, 35.0, 31.9, 31.2, 31.1, 30.3, 29.9, 26.9, 26.5, 25.8; LRMS (ESI) *m/z* $[M+H]^+$ calcd for $C_{48}H_{65}N_4O_{12}$: 889.4; found:889.5.

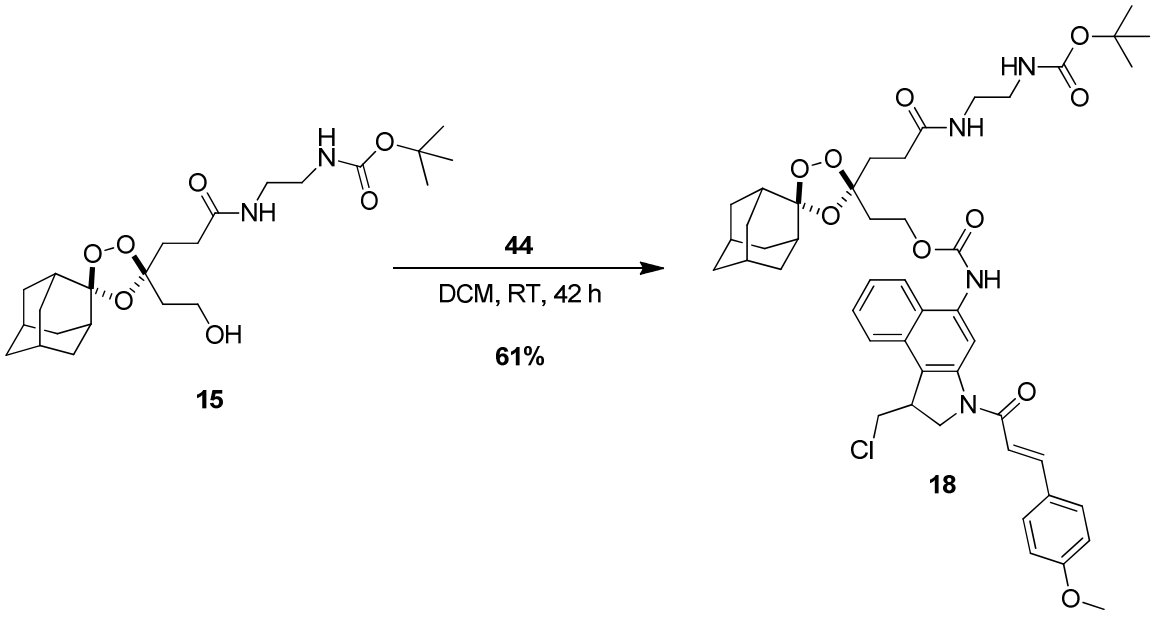

Preparation of 2-(5'-{2-[(2-{[(tert-butoxy)carbonyl]amino}ethyl)carbamoyl]ethyl}spiro[adamantane-2,2'-[1,3,4]trioxolane]-5'-yl)ethyl N-[1-(chloromethyl)-3-[(2E)-3-(4-methoxyphenyl)prop-2-enoyl]-1H,2H,3H-benzo[e]indol-5-yl]carbamate (18): A solution of alcohol **15** (0.024 g, 0.1 mmol, 1.0 equiv.) in 3 mL of drisolv DCM was added in bulk to isocyanate **44** while stirring under argon. The reaction was stirred under argon at rt and slowly concentrated to dryness overnight. Upon re-dissolving in dry DCM the next morning the reaction was observed to have gone to completion. The reaction was diluted with 15 mL of DCM and washed with 15-20 mL of water and satd aq NaCl solution then dried over $MgSO_4$, filtered, and reduced to give a yellow oil which was purified via column chromatography on 25 g of silica eluting with 5% MeOH/DCM to yield the desired product with minor impurities. This material was further purified on 25 g of silica gel eluting with 40-70% EtOAc/Hexanes to yield 0.028 g (61%) of **18** as a yellow film: ^{1}H NMR (500 MHz, d-DMF) δ 9.65 (br. s., 1H), 8.27 (d, *J* = 8.07 Hz, 1H), 7.97 - 8.05 (m, 2H), 7.84 (d, *J* = 8.56 Hz, 2H), 7.77 (d, *J* = 15.16 Hz, 1H), 7.59 (t, *J* = 7.46 Hz, 1H), 7.48 (t, *J* = 7.58 Hz, 1H), 7.24 (d, *J* = 15.16 Hz, 1H), 7.06 (d, *J* = 8.80 Hz, 2H), 6.76 (t, *J* = 5.14 Hz, 1H), 4.34 (t, *J*

= 6.11 Hz, 2H), 4.13 (dd, *J* = 2.93, 11.25 Hz, 1H), 4.06 (q, *J* = 7.09 Hz, 1H), 4.00 (dd, *J* = 8.19, 10.88 Hz, 1H), 3.87 - 3.90 (m, 2H), 3.26 (q, *J* = 5.95 Hz, 2H), 3.16 (q, *J* = 6.03 Hz, 2H), 2.35 - 2.40 (m, 2H), 2.13 - 2.29 (m, 4H), 1.98 - 2.04 (m, 4H), 1.67 - 1.89 (m, 10H), 1.39 (s, 9H), 1.25 - 1.32 (m, 1H), 1.18 - 1.22 (m, 1H); ^{13}C NMR (126 MHz, d-DMF) δ 172.0, 170.5, 164.3, 161.4, 156.2, 154.9, 142.7, 142.1, 135.3, 130.2, 130.1, 129.8, 128.0, 127.1, 124.1, 123.9, 123.3, 121.5, 117.4, 114.4, 111.8, 110.0, 77.8, 60.6, 59.9, 55.2, 53.2, 47.6, 41.7, 40.2, 39.4, 36.4, 36.4, 36.3, 36.3, 31.6, 30.4, 28.6, 27.9, 26.8, 26.4, 24.5, 23.3, 20.3, 13.8; LRMS (ESI) *m/z* $[M+H]^+$ calcd for $C_{47}H_{57}ClN_4O_{10}$: 873.4; found:873.4.

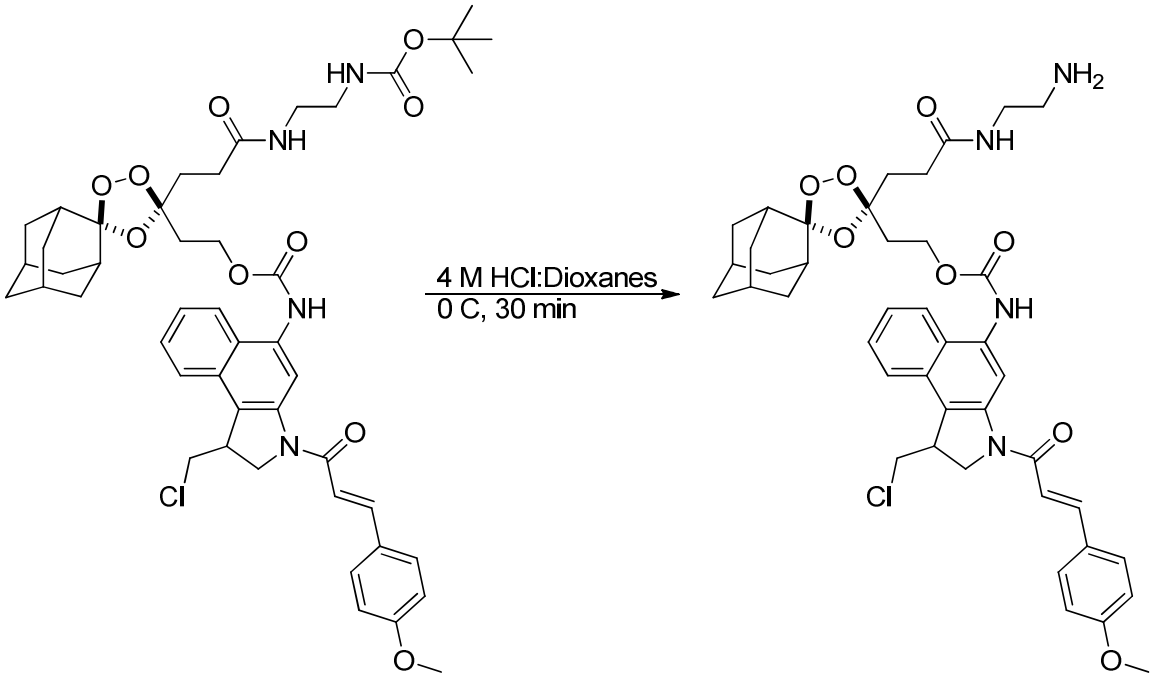

Preparation of 2-(5'-{2-[(2-aminoethyl)carbamoyl]ethyl}spiro[adamantane-2,2'-[1,3,4]trioxolane]-5'-yl)ethyl N-[1-(chloromethyl)-3-[(2E)-3-(4-methoxyphenyl)prop-2-enoyl]-1H,2H,3H-benzo[e]indol-5-yl]carbamate (47): A 4-mL scintillation vial charged with a stir bar and trioxolane **18 (15 mg, 0.02 mmol, 1.0 equiv.)** was dried overnight under high-vacuum. The material was then dissolved in dichloromethane (0.500 ml) and cooled to 0 °C. A solution of 4 M Hydrochloric acid (1.0 ml, 4.0 mmol, 232.9 equiv.) in dioxanes was then added dropwise and the reaction was stirred for 30 min at 0 °C then reduced to ca. 0.5 mL and dilluted with 1.5 mL of drisolv toluene. This procedure was repeated three times then the material was dried on high vac for > 2 h to yield **47**. This material was immediately carried forward due to previously noted instability of similar intermediates. LRMS (ESI) *m/z* $[M+H]^+$ calcd for $C_{42}H_{49}ClN_4O_8$: 773.3; found:773.3.

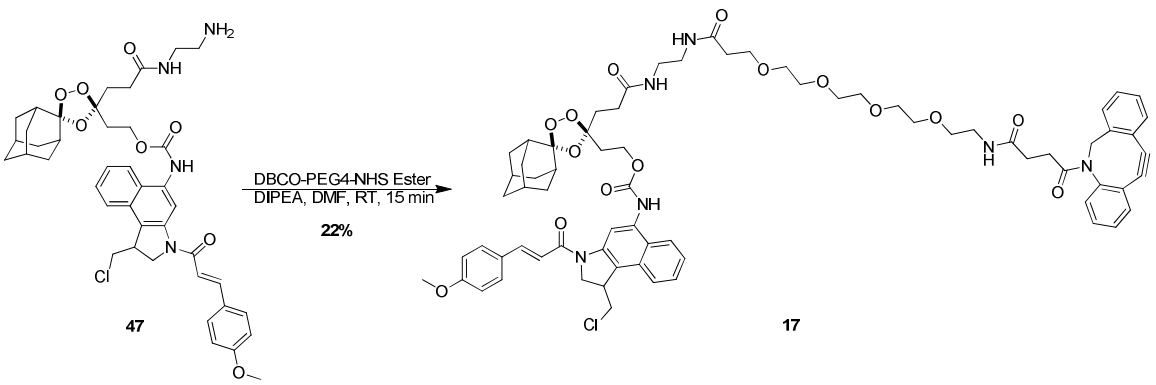

Preparation of 2-(5'-{2-[(2-{1-[(2-{2-azatricyclo[10.4.0.0^{4,9}]hexadeca-1(12),4(9),5,7,13,15-hexaen-10-yn-2-yl}-2-oxoethyl)carbamoyl]-3,6,9,13-tetraoxahexadecan-16-amido}ethyl)carbamoyl]ethyl}spiro[adamantane-2,2'-[1,3,4]trioxolane]-5'-yl)ethyl N-[1(chloromethyl)-3-[(2E)-3-(4-methoxyphenyl)prop-2-enoyl]-1H,2H,3H-benzo[e]indol-5-yl]carbamate (17): To a 4-mL scintillation vial charged with a stir bar and amine **47** (0.02 mmol, 1.0 equiv.) was added 0.5 mL of drisolv DMF and the resulting solution was cooled to 0 °C, a solution of DBCO-PEG4-NHS ester (17 mg, 0.03 mmol, 1.5 equiv.) in 1 mL of drisolv DMF was then added dropwise while stirring at 0 °C under argon. The reaction was stirred at 0 °C for ca. 15 min before being deemed complete by LCMS and diluted with 10 mL of DCM then washed with two, 15-mL portions of water and one 15 mL portion of satd aq NaCl . The organic layer was dried over $MgSO_4$, filtered and reduced to a yellow oil which was purified on 12 g of silica gel eluting with 5-10% MeOH/DCM to yield the desired product with minor impurities. This material was further purified via rp-HPLC with gradient elution from 10-90% MeCN:H_2O over 45 min with constant 10 mM NH_4OAc buffer to yield 0.005 g (22%) of **17**: ^{1}H NMR (400 MHz, $CDCl_3$) δ 8.12 (br. s., 1H), 7.84 (d, *J* = 15.22 Hz, 1H), 7.74 (d, *J* = 8.19 Hz, 1H), 7.61 (br. s., 2H), 7.48 - 7.56 (m, 2H), 7.40 - 7.45 (m, 1H), 7.33 - 7.40 (m, 2H), 7.18 - 7.24 (m, 2H), 7.13 (br. s., 1H), 6.95 (d, *J* = 8.97 Hz, 2H), 6.53 (br. s., 1H), 5.11 (d, *J* = 14.05 Hz, 1H), 4.56 (br. s., 1H), 4.38 (t, *J* = 5.66

Hz, 1H), 4.11 (br. s., 1H), 3.97 (d, *J* = 10.54 Hz, 1H), 3.87 (s, 3H), 3.48 - 3.68 (m, 18H), 3.41 - 3.47 (m, 2H), 3.32 (d, *J* = 4.68 Hz, 5H), 2.76 - 2.87 (m, 1H), 2.41 - 2.50 (m, 1H), 2.37 (d, *J* = 7.80 Hz, 2H), 2.27 (br. s., 4H), 2.09 - 2.20 (m, 3H), 1.65 - 2.06 (m, 17H), 1.60 (s, 23H), 1.27 (s, 4H); ^{13}C NMR (126 MHz, d-DMF) δ 172.2, 171.7, 171.6, 170.9, 164.5, 162.5, 162.3, 162.1, 159.4, 155.2, 152.3, 149.1, 142.9, 132.8, 130.4, 130.0, 129.2, 128.4, 128.2, 127.9, 127.1, 125.5, 124.3, 123.5, 123.3, 122.2, 117.6, 114.6, 114.5, 112.0, 110.2, 108.4, 70.5, 70.4, 70.2, 69.7, 67.4, 60.8, 55.4, 55.3, 39.2, 39.1, 39.0, 36.7, 36.5, 36.4, 31.7, 30.8, 30.6, 26.9, 26.6; LRMS (ESI) *m/z* $[M+H]^+$ calcd for $C_{72}H_{83}ClN_6O_{15}$: 1307.6; found:1308.

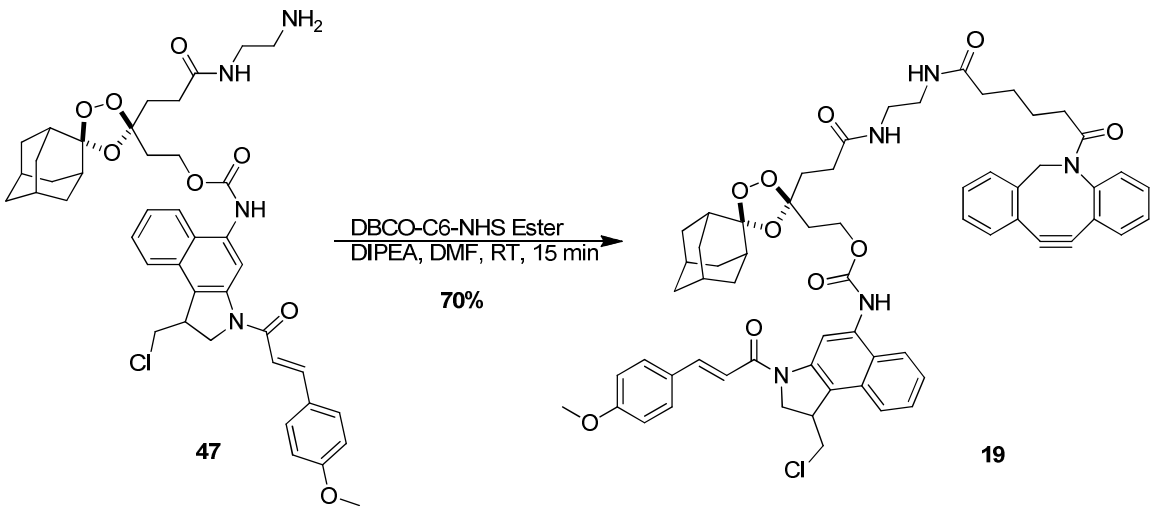

Preparation of 2-[5'-(2-{[2-(6-{2-azatricyclo[10.4.0.0^{4,9}]hexadeca-1(12),4(9),5,7,13,15-hexaen-10-yn-2-yl}-6-oxohexanamido)ethyl]carbamoyl}ethyl)spiro[adamantane-2,2'-[1,3,4]trioxolane]-5'-yl]ethyl N-[1-(chloromethyl)-3-[(2E)-3-(4-methoxyphenyl)prop-2-enoyl]-1H,2H,3H-benzo[e]indol-5-yl]carbamate (19): To a 4-mL scintillation vial charged with a stir bar and amine **47** (0.02 mmol, 1.0 equiv.) was added 0.5 mL of drisolv DMF and the resulting solution was cooled to 0 °C, a solution of DBCO-C6-NHS ester (7 mg, 0.02 mmol, 1.0 equiv.) in 1 mL of drisolv DMF was then added dropwise while stirring at 0 °C under argon. The reaction was stirred at 0 °C for ca. 15 min before being deemed complete by LCMS and dilluted with 10 mL of DCM then washed with two, 15-mL portions of water and one 15 mL portion of satd aq NaCl . The organic layer was dried over MgSO4, filtered and reduced to a yellow oil which was purified on 12 g of silica gel eluting with 5-10% MeOH/DCM to yield 0.013 g (70%) of **19**: ^{1}H NMR (500 MHz, d-DMF) δ 9.67 (br. s., 1H), 8.97 (br. s., 1H), 8.26 (d, *J* = 8.31 Hz, 1H), 8.03 (d, *J* = 2.20 Hz, 2H), 7.99 (s, 2H), 7.84 (d, *J* = 8.56 Hz, 2H), 7.77 (d, *J* = 15.16 Hz, 1H), 7.63 - 7.71 (m, 2H), 7.56 - 7.63 (m, 2H), 7.44 - 7.55 (m, 3H), 7.30 - 7.43 (m, 3H), 7.25 (d, *J* = 15.41 Hz, 1H), 7.06 (d, *J* = 8.56 Hz, 2H), 5.11 (d, *J* = 13.94 Hz, 1H), 4.33 (br. s., 1H), 4.13 (dd, *J* = 2.93, 11.25 Hz, 1H), 4.00 (dd, *J* = 8.31, 11.00 Hz, 1H),

3.89 (s, 3H), 3.67 (d, *J* = 13.69 Hz, 1H), 3.16 - 3.24 (m, 4H), 2.34 (t, *J* = 7.95 Hz, 2H), 2.22 (br. s., 0H), 2.13 - 2.29 (m, 3H), 1.96 - 2.05 (m, 5H), 1.93 (t, *J* = 6.97 Hz, 2H), 1.71 - 1.88 (m, 11H), 1.69 (br. s., 3H), 1.19 - 1.35 (m, 5H); ^{13}C NMR (126 MHz, d-DMF) δ 172.5, 172.1, 164.5, 159.4, 155.1, 152.5, 149.1, 142.9, 135.5, 132.8, 130.4, 130.3, 130.0, 129.8, 129.1, 128.3, 128.2, 127.9, 127.3, 127.1, 125.5, 124.3, 124.1, 123.5, 123.2, 122.2, 121.7, 117.6, 114.6, 114.6, 112.0, 110.2, 108.5, 60.8, 55.4, 55.4, 55.3, 55.2, 53.4, 47.7, 41.9, 39.3, 38.9, 36.5, 36.4, 35.6, 35.6, 31.9, 31.7, 30.5, 30.5, 28.1, 26.9, 26.6, 25.8, 25.2, 25.0, 24.5, 24.1, 13.8.; LRMS (ESI) *m/z* $[M+H]^+$ calcd for $C_{63}H_{66}ClN_5O_{10}$: 1088.4; found:1089.

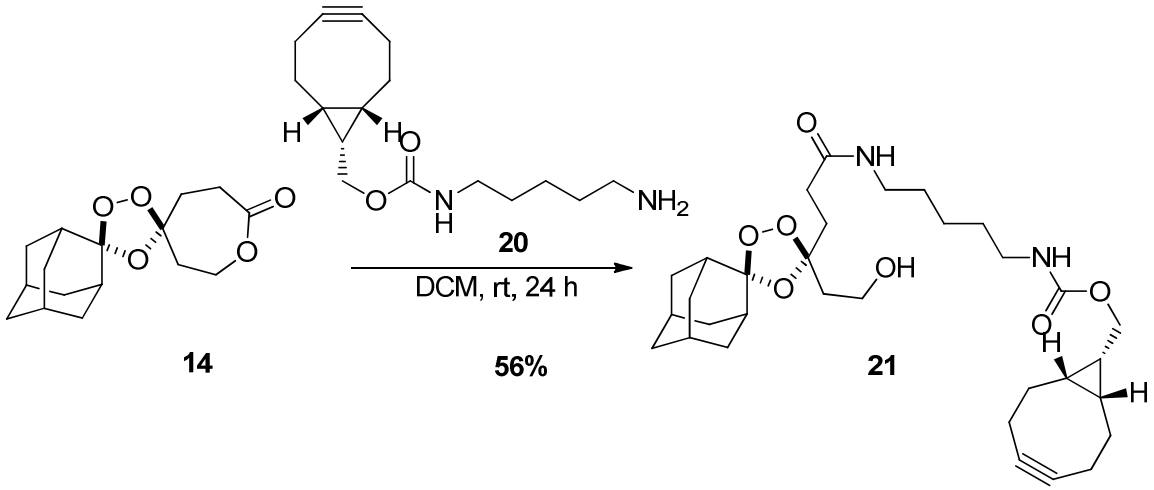

Preparation of (1R,8S,9S)-bicyclo[6.1.0]non-4-yn-9-ylmethyl N-(5-{3-[5'-(2-hydroxyethyl)spiro[adamantane-2,2'-[1,3,4]trioxolane]-5'-yl]propanamido}pentyl)carbamate (21): A 4-mL scintillation vial equipped with a stirbar and a screw-top cap was charged with Lactone **14** (0.064 g, 0.2 mmol, 1.0 equiv.), (1R,8S,9S)-bicyclo[6.1.0]non-4-yn-9-ylmethyl N-(5- aminopentyl)carbamate (**20**) (0.100 g, 0.4 mmol, 1.7 equiv.)**,** and DCM (ca. 0.5 mL) and the reaction mixture was stirred at rt for 24 h. The reaction was then concentrated to a light yellow oil and deposited onto ca. 2 g of silica in MeOH and DCM and purified via column chromatography on 12 g of silica (elluting with 30-50% EtOAc:Hex then 0-5%) to yield 0.070 g (56%) of **21** as a clear oil: ^{1}H NMR (400 MHz, $CDCl_3$) δ 6.01 (br. s., 1H), 4.90 (br. s., 1H), 4.11 (d, *J* = 7.02 Hz, 2H), 3.65 - 3.86 (m, 2H), 3.17 (dd, *J* = 6.20, 25.76 Hz, 3H), 2.07 - 2.35 (m, 11H), 1.91 - 2.04 (m, 5H), 1.80 - 1.90 (m, 3H), 1.71 - 1.78 (m, 2H), 1.61 - 1.70 (m, 3H), 1.42 - 1.59 (m, 5H), 1.26 - 1.38 (m, 2H), 0.91 (t, *J* = 8.59 Hz, 1H); ^{13}C NMR (100 MHz, $CDCl_3$) δ 172.2, 133.3, 112.3, 110.6, 98.8, 58.3, 39.3, 36.5, 36.3, 36.2, 34.9, 34.8, 34.7, 31.6, 29.6, 29.0, 26.7, 26.3, 23.8, 21.4, 20.1, 17.7; LRMS (ESI) *m/z* $[M+H]^+$ calcd for $C_{32}H_{48}N_2O_7$: 573.3; found: 573.7.

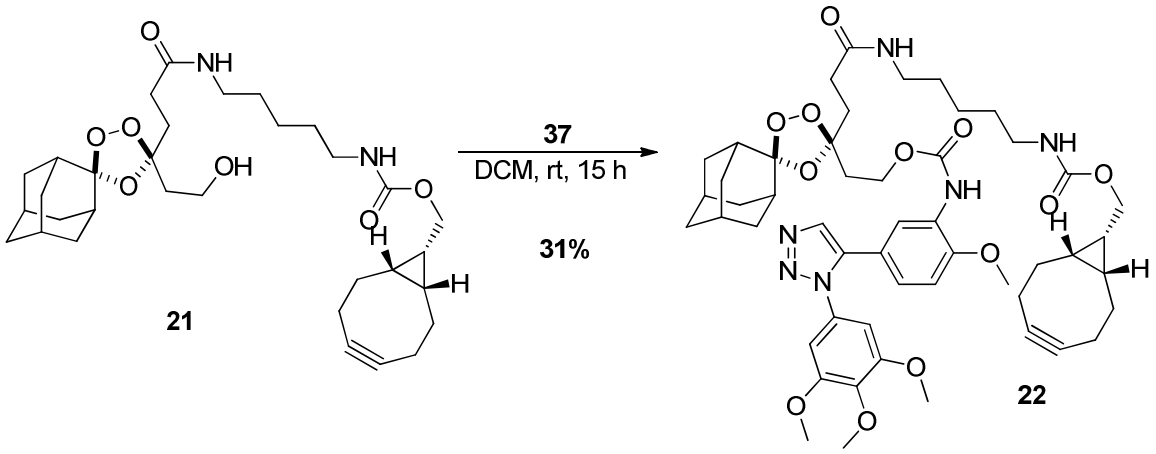

Preparation of (1R,8S,9R)-bicyclo[6.1.0]non-4-yn-9-ylmethyl N-{5-[3-(5'-{2-[({2-methoxy-5-[1-(3,4,5-trimethoxyphenyl)-1H-1,2,3-triazol-5-yl]phenyl}carbamoyl)oxy]ethyl}spiro[adamantane-2,2'-[1,3,4]trioxolane]-5'-yl)propanamido]pentyl}carbamate (22): A 5-ml round bottomed flask equipped with a rubber septa and argon inlet was charged with a teflon stirbar, isocyanate **37** (0.023 g, 0.06 mmol, 1 equiv.), and a solution of alcohol **21** (0.035 g, 0.06 mmol, 1 equiv.) in 1.5 mL of drisolv DCM which had been dried on activated molecular sieves followed by pyridine (0.050 ml, 0.6 mmol, 10.1 equiv.) and the reaction mixture was stirred under argon at rt for 15 h then diluted with 10 mL of DCM and washed with 10 mL of deionized water. The aqueous layer was extracted with 2, 10-mL portions of DCM and the organic layers were combined, washed with sat. aq. NaCl sol., dried over MgSO4, filtered and reduced to yield a yellow oil which was purified on 25 g of silica gel eluting with 75%-100 EtOAc/Hex to yield 0.018 g (31%) of **22**: ^{1}H NMR (500 MHz, Acetonitrile-d_3) δ 7.77 (s, 1H), 7.63 (s, 1H), 7.34 (br. s., 1H), 6.80 (dd, *J* = 2.40, 8.31 Hz, 1H), 6.75 (d, *J* = 8.56 Hz, 1H), 6.49 (s, 2H), 6.20 (br. s., 1H), 5.23 - 5.27 (m, 1H), 3.99 (dt, *J* = 2.40, 6.60 Hz, 2H), 3.86 (d, *J* = 8.07 Hz, 2H), 3.65 (s, 3H), 3.55 - 3.57 (m, 3H), 3.51 (s, 6H), 2.90 (q, *J* = 6.85 Hz, 2H), 2.83 (q, *J* = 6.77 Hz, 2H), 1.97 - 2.04 (m, 6H), 1.96 (d, *J* = 1.71 Hz, 3H), 1.81 - 1.91 (m, 5H), 1.76 (s, 3H), 1.74 (td, *J* = 2.41, 4.71 Hz, 8H), 1.48 - 1.67 (m, 13H),

1.32 - 1.40 (m, 2H), 1.22 (quin, *J* = 7.21 Hz, 5H), 1.04 - 1.11 (m, 4H), 0.66 - 0.71 (m, 2H); ^{13}C NMR (126 MHz, $CDCl_3$) δ 172.9, 154.9, 154.5, 150.3, 140.1, 139.5, 133.8, 133.6, 129.3, 125.0, 120.5, 113.4, 112.1, 111.2, 105.3, 100.1, 63.2, 62.0, 61.4, 57.4, 57.1, 41.7, 40.1, 37.6, 37.6, 37.5, 36.0, 35.8, 35.8, 35.7, 32.6, 31.6, 30.6, 30.2, 30.2, 28.1, 27.7, 25.0, 22.2, 21.2, 19.1; LRMS (ESI) *m/z* $[M+H]^+$ calcd for $C_{51}H_{66}N_6O_{12}$: 955.5; found: 955.8.

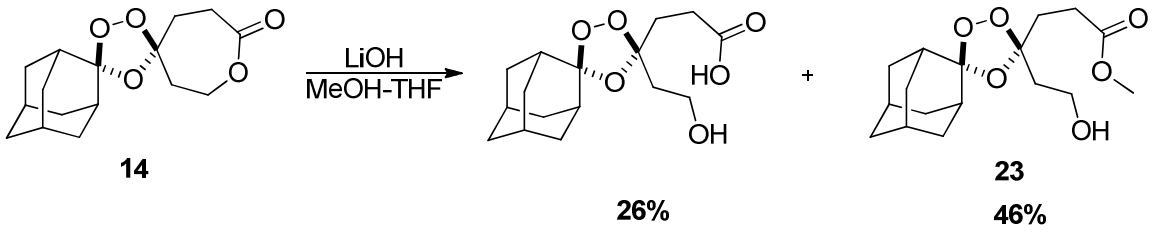

14 **26%** **23** **46%**

Preparation of methyl 3-[5'-(2-hydroxyethyl)spiro[adamantane-2,2'-[1,3,4]trioxolane]-5'-yl]propanoate (23): A 20-mL scintillation vial was charged with lactone **14** (0.228 g, 0.8 mmol, 1.0 equiv.) and a teflon stirbar. This material was dissolved in tetrahydrofuran (3.0 ml) and methanol (1.0 mL), and lithium hydroxide (0.053 g, 2.3 mmol, 3.0 equiv.) was added in bulk to the stirring solution at rt. The solution was stirred for 30 min then diluted with ca. 10 mL of deionized water and neutralized with 1 N HCl solution via dropwise addition. The aqueous fraction was extracted with three, 10-mL portions of DCM and the organic fraction was washed with 10 mL of satd aq NaCl solution then dried over MgSO4, filtered, and concentrated to a clear oil which was purified on 25 g of silica eluting with 40% EtOAc/Hex followed by 5% MeOH/DCM to yield 0.116 g (46%) of the methyl ester **23** and 0.062 g (26%) of the free acid. Methyl ester **23**: ^{1}H NMR (400 MHz, $CDCl_3$) δ 3.69 - 3.78 (m, 2H), 3.63 (s, 3H), 2.65 (br. s., 1H), 2.40 (ddd, *J* = 2.34, 6.93, 9.07 Hz, 2H), 2.02 - 2.21 (m, 3H), 1.95 - 2.01 (m, 4H), 1.78 - 1.94 (m, 7H), 1.66 - 1.77 (m, 5H), 1.64 (br. s., 3H); ^{13}C NMR (100 MHz, $CDCl_3$) δ 173.5, 112.5, 110.4, 73.3, 58.4, 51.8, 41.3, 37.8, 36.6, 36.3, 36.3, 35.8, 35.0, 34.8, 34.8, 33.8, 31.0, 30.9, 28.7, 26.7, 26.3, 25.9; LRMS (ESI) *m/z* $[M+Na]^+$ calcd for $C_{17}H_{26}O_6$: 349.2; found: 349.5. Carboxcylic Acid: LRMS (ESI) *m/z* $[M+Na]^+$ calcd for $C_{17}H_{26}O_6$: 335.1; found: 335.4.

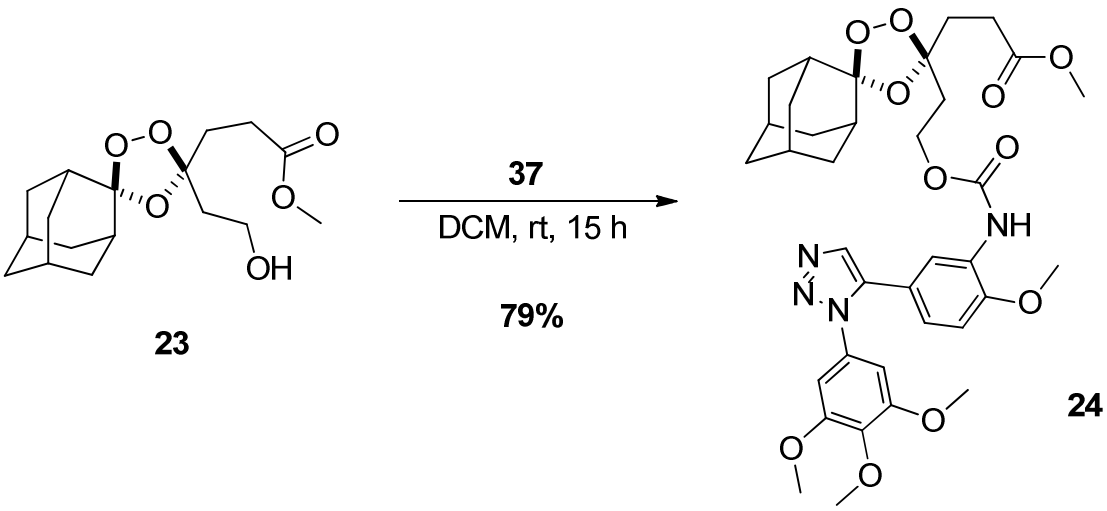

Preparation of methyl 3-(5'-{2-[({2-methoxy-5-[1-(3,4,5-trimethoxyphenyl)-1H-1,2,3-triazol-5-yl]phenyl}carbamoyl)oxy]ethyl}spiro[adamantane-2,2'-[1,3,4]trioxolane]-5'-yl)propanoate (24): A 5-mL round bottomed flask equipped with a rubber septa and argon inlet was charged with isocyanate **37** (0.026 g, 0.1 mmol, 1 equiv.), a solution of **23** (0.054 g, 0.2 mmol, 2.4 equiv.) in 1.0 mL of DCM, and a Teflon stirbar while stirring under argon to give a light yellow solution. The reaction mixture was slowly concentrated to dryness over 15 h under argon. Material was re-suspended in DCM (10 mL) and washed with 10 mL of water. The aqueous layer was extracted with two, 10-mL portions of DCM and the organic layers were combined, washed with 10 mL of satd aq NaCl solution, and then dried over $MgSO_4$, filtered, and concentrated to a light yellow oil which was purified via flash chromatography on 25 g of silica eluting with 50-70% EtOAc/Hex to yield 0.038 g (79%) of **24** as a colorless oil: ^{1}H NMR (400 MHz, $CDCl_3$) δ 8.19 (s, 1H), 7.83 (s, 1H), 7.27 (s, 1H), 6.80 (d, *J* = 1.56 Hz, 2H), 6.61 (s, 2H), 4.27 (dt, *J* = 1.56, 6.83 Hz, 2H), 3.88 (s, 3H), 3.87 (s, 3H), 3.75 (s, 6H), 3.68 (s, 3H), 2.44 - 2.50 (m, 2H), 2.08 - 2.26 (m, 4H), 1.96 (t, *J* = 10.93 Hz, 5H), 1.89 (br. s., 1H), 1.79 - 1.87 (m, 3H), 1.77 (br. s., 1H), 1.70 - 1.74 (m, 3H), 1.68 (br. s., 3H); ^{13}C NMR (100 MHz, $CDCl_3$) δ 189.9, 173.5, 153.6, 153.1, 148.2, 138.7, 137.9, 133.2, 132.4, 128.2,

123.4, 119.6, 112.6, 110.2, 109.2, 103.4, 61.2, 61.2, 56.5, 56.0, 52.0, 36.8, 36.6, 36.4, 35.3, 35.1, 34.9, 34.9, 34.7, 30.8, 28.8, 28.7, 26.9, 26.5, 22.3; LRMS (ESI) *m/z* $[M+H]^+$ calcd for $C_{36}H_{44}N_4O_{11}$: 709.3; found: 709.6.

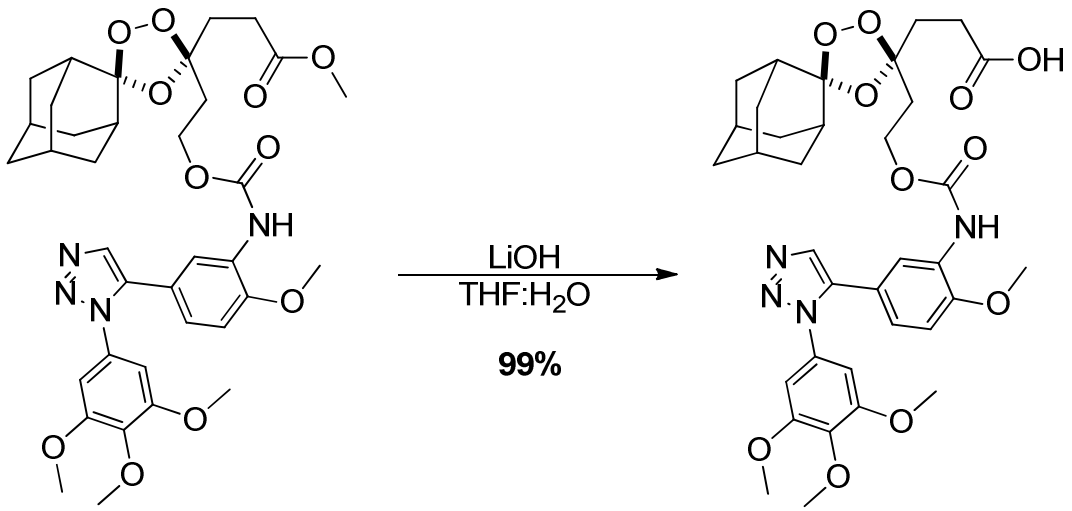

24 **48**

Preparation of 3-(5'-{2-[({2-methoxy-5-[1-(3,4,5-trimethoxyphenyl)-1H-1,2,3-triazol-5-yl]phenyl}carbamoyl)oxy]ethyl}spiro[adamantane-2,2'-[1,3,4]trioxolane]-5'-yl)propanoic acid (48): To a 20-mL scintillation vial charged with a teflon stir bar and methyl ester **24** (0.016 g, 0.0 mmol, 1.0 equiv.) was added tetrahydrofuran (1.000 ml) and Lithium hydroxide (0.002 g, 0.1 mmol, 3.0 equiv.) as a 1 M solution in water (69.4 μL) via microliter pipet. The resulting solution was stirred for 30 h at rt then dilluted with 5 mL of DCM and 5 mL of deionized water. The aqueous layer was acidified to pH ~2 with 100 μL of 1 N HCl and extracted with three, 5-mL portions of DCM. The organic layers were combined, washed with 10 mL of sat. NaCl, dried over MgSO4, and reduced to yield 0.015 g (99%) of **48** as a clear oil: ^{1}H NMR (400 MHz, $CDCl_3$) δ 8.18 (br. s., 1H), 7.85 (s, 1H), 7.26 (s, 1H), 6.79 - 6.82 (m, 2H), 6.62 (s, 2H), 4.29 (dt, *J* = 1.76, 6.73 Hz, 2H), 3.88 (s, 6H), 3.76 (s, 6H), 2.52 (t, *J* = 8.30 Hz, 2H), 2.10 - 2.27 (m, 5H), 1.99 (d, *J* = 11.71 Hz, 5H), 1.90 (br. s., 1H), 1.79 - 1.88 (m, 3H), 1.78 (br. s., 1H), 1.73 (d, *J* = 10.15 Hz, 2H), 1.69 (s, 2H); LRMS (ESI) *m/z* $[M+H]^+$ calcd for $C_{35}H_{42}N_4O_{11}$: 695.3; found: 695.6.

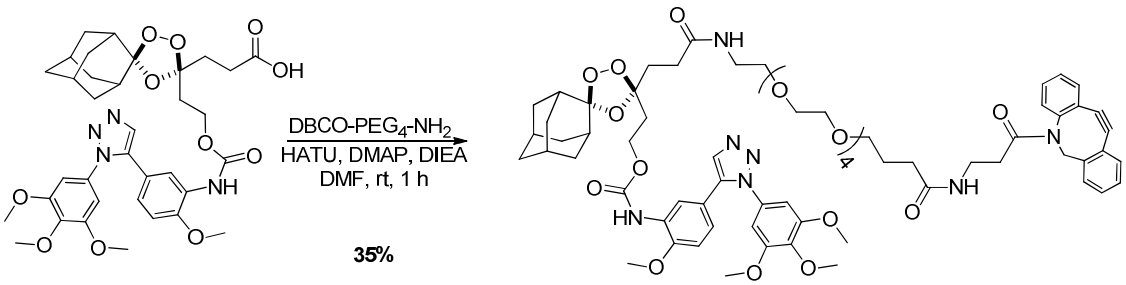

48 25

Preparation of 2-{5'-[2-({14-[(3-{2- azatricyclo[10.4.0.0^{4,9}]hexadeca-1(12),4(9),5,7,13,15-hexaen-10-yn-2-yl}-3- oxopropyl)carbamoyl]-3,6,9,12-tetraoxatetradecan-1- yl}carbamoyl)ethyl]spiro[adamantane-2,2'- [1,3,4]trioxolane]-5'-yl}ethyl N-{2-methoxy-5-[1- (3,4,5-trimethoxyphenyl)-1H-1,2,3-triazol-5-yl]phenyl}carbamate (25): A 4-mL scintillation vial was charged with carboxcylic acid **48** (0.015 g, 0.0 mmol, 1.0 equiv.), DBCO-Peg$_4$-NH$_2$ (0.012 g, 0.0 mmol, 1.0 equiv.), 4-dimethylaminopyridine (0.001 g, 0.0 mmol, 0.4 equiv.), and a teflon stirbar. The vial was fitted with a rubber septa and the atmosphere was exchanged for argon. N,N-dimethylformamide (0.500 ml, 6.5 mmol, 300.3 equiv.) and N,N-diisopropylethylamine (0.020 ml, 0.1 mmol, 5.3 equiv.) were added to the reaction mixture. The resulting yellow reaction mixture was stirred under argon at rt for 1 h then diluted with 500 μL of DMSO and directly purified via HPLC chromatography eluting from 40-90% MeOH/Water to yield 0.009 g (35%) of **25** : ^{1}H NMR (400 MHz, CD_3OD) δ 8.51 (br. s., 1H), 7.94 (s, 1H), 7.92 (s, 1H), 7.65 (d, *J* = 6.24 Hz, 1H), 7.45 - 7.50 (m, 1H), 7.41 - 7.45 (m, 2H), 7.29 - 7.38 (m, 2H), 7.23 - 7.27 (m, 1H), 7.03 - 7.07 (m, 1H), 6.99 - 7.03 (m, 1H), 6.71 (s, 2H), 5.12 (d, *J* = 14.05 Hz, 1H), 4.23 (t, *J* = 6.83 Hz, 2H), 3.88 (s, 3H), 3.81 (s, 3H), 3.74 (s, 6H), 3.69 (d, *J* = 14.05 Hz, 1H), 3.58 - 3.60 (m, 1H), 3.57 (s, 5H), 3.47 - 3.56 (m, 10H), 3.34 (d, *J* = 5.46 Hz, 1H), 3.23 - 3.28 (m, 2H), 3.13 (td, *J* = 7.07, 13.56 Hz, 2H), 2.50 (td, *J* = 6.73, 15.80 Hz, 1H), 2.33 (t, *J* = 7.80 Hz, 2H), 2.27 (t, *J* = 6.24 Hz,

2H), 2.07 - 2.17 (m, 4H), 1.93 - 2.07 (m, 6H), 1.87 (br. s., 2H), 1.70 - 1.80 (m, 9H); ^{13}C NMR (126 MHz, CD_3OD) δ 175.3, 174.0, 173.3, 155.2, 152.7, 149.7, 140.4, 140.1, 133.6, 133.5, 130.7, 130.2, 129.8, 129.4, 129.1, 128.3, 126.7, 124.5, 123.8, 120.0, 115.8, 113.5, 112.0, 111.0, 109.0, 105.1, 101.6, 71.7, 71.6, 71.5, 71.4, 70.7, 68.2, 62.1, 61.5, 57.1, 56.7, 56.7, 56.2, 40.6, 37.9, 37.8, 37.6, 36.8, 36.0, 35.9, 35.6, 32.9, 31.6, 28.4, 28.0.

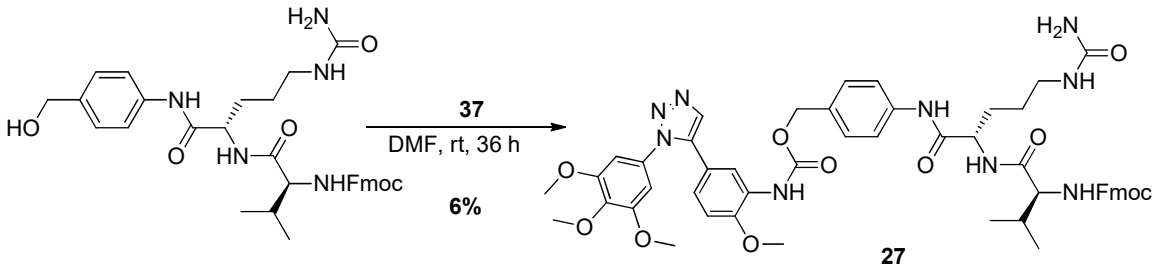

Preparation of 9H-fluoren-9-ylmethyl N-[(1S)-1-{[(1S)-4- (carbamoylamino)-1-[(4-{[({2-methoxy-5-[1-(3,4,5- trimethoxyphenyl)-1H-1,2,3-triazol-5-yl]phenyl}carbamoyl)oxy]methyl}phenyl)carbamoyl]butyl]carbamoyl}-2-methylpropyl]carbamate (27): A 5-mL round-bottomed flask equipped with a rubber septa and argon inlet was charged with a solution of **37** (0.026 g, 0.1 mmol, 1.0 equiv.) in 2.5 mL of DCM and Teflon stirbar. To this solution was added 9H-fluoren-9-ylmethyl N-[(1S)-1-{[(1S)-4- (carbamoylamino)-1-{[4-(hydroxymethyl)phenyl]carbamoyl}butyl]carbamoyl}-2- methylpropyl]carbamate (0.100 g, 0.2 mmol, 2.4 equiv.) in bulk while stirring under argon to giving a light yellow solution with a large amount of SM ppt. This solution was stirred o/n with no progress observed. N,N-dimethylformamide (4.0 ml) was then added and DCM was removed via argon stream. Upon warming to 35 °C all material went into solution to give a clear, yellow solution which was stirred at 35 °C under argon for 24 h. The reaction was then diluted with DCM and washed with 10 mL of deionized water, a white solid crashed from solution and this material was combined with the organic layer, reduced, and purified on rp-HPLC eluting with 40-90% MeOH:H_2O (0.05% formic acid) to yield 0.004 g (6%) of **27**:^{1}H NMR (400 MHz, d-DMF) δ 10.32 (s, 1H), 8.61 (br. s., 1H), 8.48 (s, 1H), 8.37 (d, *J* = 7.80 Hz, 1H), 7.79 (d, *J* = 7.02 Hz, 2H), 7.68 (d, *J* = 7.80 Hz, 1H), 7.62 - 7.66 (m, 3H), 7.43 (d, *J* = 8.97 Hz, 1H), 7.30 (dt, *J* = 3.51, 7.02 Hz, 2H), 7.17 - 7.26 (m, 4H), 6.96 (s, 2H), 6.74 (br. s., 2H), 6.44 (br. s., 1H), 5.54 - 5.62 (m, 1H), 4.97 (s, 2H), 4.50 (br. s., 1H), 4.11 - 4.20 (m, 3H), 3.97 - 4.06 (m, 1H), 3.73 - 3.76 (m, 3H), 3.67 (s, 6H), 3.66 (s, 3H),

3.04 - 3.12 (m, 1H), 2.92 - 3.00 (m, 1H), 2.03 - 2.13 (m, 1H), 1.78 (d, *J* = 8.58 Hz, 1H), 1.64 (br. s., 1H), 1.42 (d, *J* = 7.80 Hz, 2H), 1.28 (s, 1H), 1.14 (br. s., 2H), 0.85 (t, *J* = 7.61 Hz, 7H); LRMS (ESI) *m/z* $[M+H]^+$ calcd for $C_{52}H_{57}N_9O_{11}$: 984.4; found: 984.7.

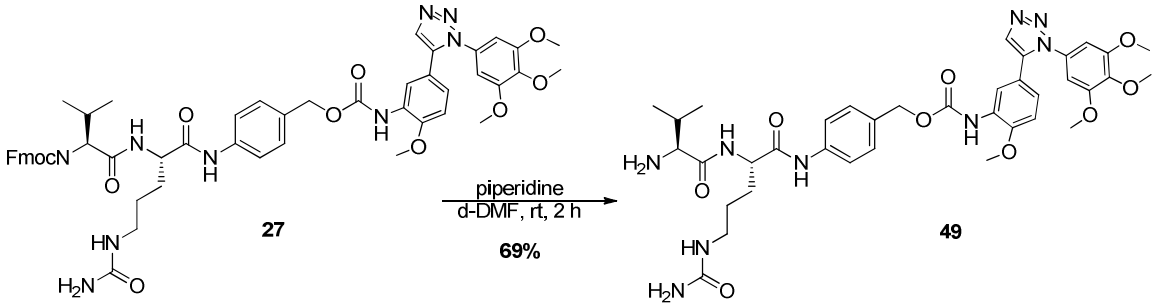

Preparation of {4-[(2S)-2-[(2S)-2-amino-3-methylbutanamido]-5-(carbamoylamino)pentanamido]phenyl}methyl N-{2- methoxy-5-[1-(3,4,5-trimethoxyphenyl)-1H-1,2,3- triazol-5-yl]phenyl}carbamate (49): A 4-mL scintillation vial containing a solution of **27** (4 mg, 0.0 mmol, 1.0 equiv.) in deutero-N,N-dimethylformamide (0.900 ml) and a Teflon stir bar was charged with piperidine (0.180 ml, 1.8 mmol, 417.0 equiv.) (20% v/v). This reaction was stirred at rt for 2 h then the reaction mixture was injected directly onto the HPLC for reverse phase purification eluting with 30-90% MeOH:H_2O to yield 0.0023 g (69%) of amine **49**: ^{1}H NMR (500 MHz, $CDCl_3$) δ 10.24 (s, 1H), 8.48 (s, 1H), 8.37 (br. s., 1H), 7.60 - 7.66 (m, 2H), 7.23 - 7.28 (m, *J* = 8.31 Hz, 2H), 6.93 - 6.98 (m, 2H), 6.71 - 6.76 (m, 2H), 6.27 (br. s., 1H), 5.55 (s, 2H), 4.98 (s, 2H), 3.74 - 3.76 (m, 3H), 3.67 - 3.68 (m, 6H), 3.65 - 3.67 (m, 3H), 3.14 (dd, *J* = 6.60, 13.69 Hz, 1H), 3.04 (d, *J* = 4.65 Hz, 1H), 2.90 - 2.98 (m, 1H), 1.91 - 1.98 (m, 1H), 1.71 - 1.78 (m, 1H), 1.52 - 1.59 (m, 1H), 1.40 (dt, *J* = 7.83, 14.06 Hz, 2H), 0.82 (d, *J* = 6.85 Hz, 3H), 0.72 (d, *J* = 6.85 Hz, 3H); LRMS (ESI) *m/z* $[M+H]^+$ calcd for $C_{37}H_{47}N_9O_9$: 762.3; found: 762.7.

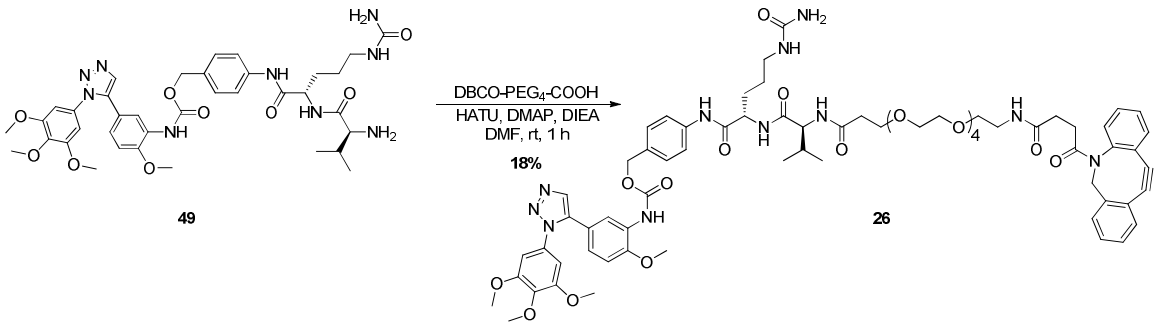

Preparation of {4-[(2S)-2-[(2S)-2-{1-[(3-{2-azatricyclo[10.4.0.0^{4,9}]hexadeca-1(12),4(9),5,7,13,15-hexaen-10-yn-2-yl}-3-oxopropyl)carbamoyl]-3,6,9,12-tetraoxapentadecan-15-amido}-3-methylbutanamido]-5-(carbamoylamino)pentanamido]phenyl}methyl N-{2-methoxy-5-[1-(3,4,5-trimethoxyphenyl)-1H-1,2,3-triazol-5-yl]phenyl}carbamate (26): A 4-mL vial was charged with a teflon stirbar, amine **49** (2 mg, 0.0 mmol, 1.0 equiv.), HATU (3 mg, 0.0 mmol, 2.9 equiv.), and 4-dimethylaminopyridine (2 mg, 0.0 mmol, 4.1 equiv.) and the atmosphere was replaced with argon. This material was dissolved in N,N-dimethylformamide (0.400 mL) and DBCO-PEG$_4$-Acid (2 mg, 0.0 mmol, 1.2 equiv.) was added as a solution (25 mg/mL in DMF, 0.08 mL) in bulk while stiring under argon. N,N-diisopropylethylamine (0.010 ml, 0.1 mmol, 19.0 equiv.) was added and the reaction was allowed to stir at rt for 2 h then diluted with 500 μL of DMSO and purified via rp-HPLC eluting with 40-90% MeOH/H_2O with 0.05% formic acid buffer to yield 0.0007 g (18%) of **26**: ^{1}H NMR (500 MHz, CD_3OD) δ 8.55 (br. s., 1H), 7.93 - 7.96 (m, 1H), 7.90 - 7.93 (m, 1H), 7.59 - 7.65 (m, *J* = 5.62, 8.56 Hz, 3H), 7.57 (d, *J* = 4.89 Hz, 1H), 7.46 (s, 1H), 7.42 (br. s., 1H), 7.32 - 7.37 (m, 2H), 7.28 - 7.32 (m, 1H), 7.22 (d, *J* = 6.85 Hz, 1H), 7.03 - 7.07 (m, 1H), 6.99 - 7.02 (m, 1H), 6.69 - 6.72 (m, 2H), 5.12 (d, *J* = 13.45 Hz, 2H), 4.21 (s, 1H), 3.85 - 3.89 (m, 3H), 3.78 - 3.80 (m, 3H), 3.71 - 3.75 (m, 6H), 3.70 (d, *J* = 3.42 Hz, 2H), 3.63 - 3.66 (m, 2H), 3.60 (br. s., 2H), 3.57 (s, 8H), 3.51 - 3.54 (m, 2H), 3.40 - 3.45 (m, 2H), 2.65 - 2.72 (m, 3H), 2.61 (d, *J* = 6.36 Hz, 1H), 2.53 (d, *J* = 11.98 Hz, 2H),

2.31 - 2.38 (m, 2H), 2.15 (dd, *J* = 7.09, 14.92 Hz, 4H), 1.93 - 2.00 (m, 3H), 1.72 - 1.78 (m, 2H), 1.54 - 1.62 (m, 3H), 1.36 (s, 2H), 1.28 - 1.30 (m, 2H), 1.22 (br. s., 2H), 0.95 - 1.01 (m, 6H); LRMS (ESI) *m/z* $[M+H]^+$ calcd for $C_{63}H_{73}N_{11}O_{14}$: 1297.4; found: 1297.3.

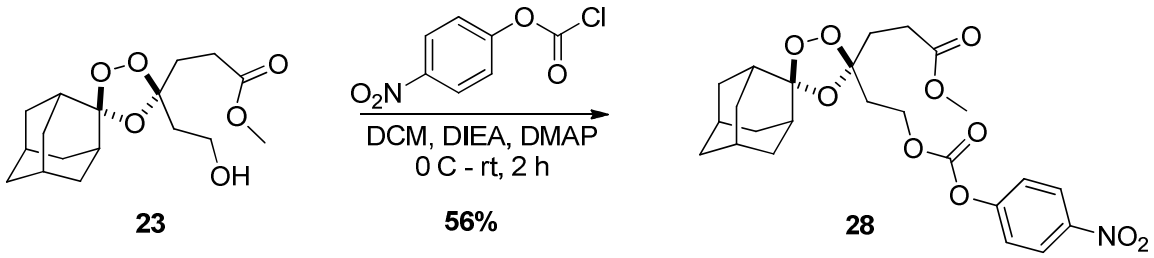

23 **56%** **28**

Preparation of methyl 3-[5'-(2-{[(4-nitrophenoxy)carbonyl]oxy}ethyl)spiro[adamantane- 2,2'-[1,3,4]trioxolane]-5'-yl]propanoate (28): Alcohol **23** (0.065 g, 0.2 mmol, 1.0 equiv.) was dissolved in 2mL of drisolv DCM under argon and transferred to a heat dried, 2-neck 25mL round-bottomed flask fitted with an argon inlet and charged with a teflon stirbar. This transfer was completed with an additional 2mL of DCM and N,N-diisopropylethylamine (160 μl, 0.9 mmol, 4.6 equiv.) was added to the solution which was then cooled to 0 °C. 4-Nitrophenyl chloroformate (123 mg, 0.6 mmol, 3.1 equiv.) and 4-dimethylaminopyridine (0.015 g, 0.1 mmol, 0.6 equiv.) were added in bulk and the reaction was allowed to warm slowly to rt over 2 h. The reaction was then diluted with 20 mL EtOAc and washed with five, 20-mL portions of sat. $NaHCO_3$ and one 20-mL portion of satd aq NaCl. The organic layer was dried over $MgSO_4$ and reduced to give a light yellow oil which was purified via column chromatography on 24 g of silica eluting with 0-15% EtOAc/Hexanes to yield the desired material contaminated with p-nitrophenol. This material was deposited onto 5 g of silica and further purified on 25 g of silica eluting with 5-10% EtOAc/Hexanes to yield 0.055 g (56%) of **28** as a clear oil: ^{1}H NMR (400 MHz, $CDCl_3$) δ 8.27 (d, J = 9.13 Hz, 2H), 7.38 (d, J = 9.13 Hz, 2H), 4.43 (t, J = 6.88 Hz, 2H), 3.69 (s, 3H), 2.45 - 2.51 (m, 2H), 2.22 - 2.27 (m, 2H), 2.09 - 2.20 (m, 1H), 1.87 - 2.03 (m, 6H), 1.71 - 1.86 (m, 6H), 1.69 (br. s., 3H); ^{13}C NMR (100 MHz, $CDCl_3$) δ 173.3, 155.7, 152.5, 145.6, 125.5, 122.0, 112.9, 108.9, 65.2, 52.0, 36.7, 36.6, 36.4, 35.2, 35.1, 35.0, 34.8, 34.6, 30.6, 28.5, 26.9, 26.5; LRMS (ESI) *m/z* $[M+Na]^+$ calcd for $C_{24}H_{29}NO_{10}$: 514.2; found: 514.6.

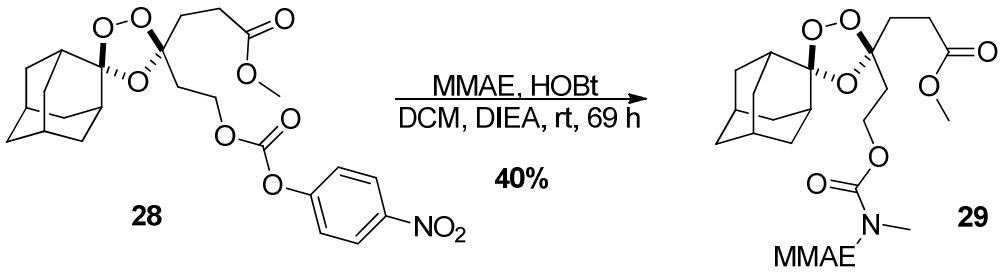

Preparation of methyl 3-{5'-[2-({[(1S)-1-{[(2S)-2-{[(3R,5S)-1-[(2S)-2-[(2R)-2-{[(1S,2R)-1-hydroxy-1-phenylpropan-2-yl]carbamoyl}-1-methoxy-2-methylethyl]pyrrolidin-1-yl]-3-methoxy-5-methyl-1-oxoheptan-4-yl](methyl)amino}-3-methylbutanoyl]carbamoyl}-2-methylpropyl](methyl)carbamoyl}oxy)ethyl]spiro[adamantane-2,2'-[1,3,4]trioxolane]-5'-yl}propanoate (29): a 5-mL round bottomed flask was charged with a teflon stir bar and heat dried under vacuum. The flask was charged with MMAE (10 mg, 0.0 mmol, 1.0 equiv.) and 1-hydroxybenzotriazole hydrate (1 mg, 0.0 mmol, 0.5 equiv.) and fitted with a rubber septa and argon inlet. The atmosphere was replaced with argon and a solution of p-nitrophenylcarbonate **28** (7 mg, 0.0 mmol, 1.0 equiv.) in 1 mL of DCM was added with N,N-diisopropylethylamine (0.030 ml, 0.2 mmol, 12.1 equiv.) while stirring under argon at rt. The reaction was allowed to stir for 69 h then purified via rp-HPLC to yield 0.006 g (40%) of **29**: ^{1}H NMR (500 MHz, $CDCl_3$) δ 7.37 - 7.41 (m, 2H), 7.32 - 7.37 (m, 3H), 6.52 (br. s., 1H), 4.70 (d, *J* = 7.34 Hz, 1H), 4.22 - 4.29 (m, 2H), 4.17 (br. s., 1H), 4.12 (d, *J* = 11.25 Hz, 1H), 4.07 (br. s., 1H), 3.86 (d, *J* = 8.56 Hz, 1H), 3.68 (s, 3H), 3.50 - 3.55 (m, 1H), 3.43 (s, 1H), 3.41 (s, 2H), 3.38 (d, *J* = 6.85 Hz, 1H), 3.34 - 3.36 (m, 1H), 3.33 (s, 2H), 3.02 (s, 2H), 2.87 (br. s., 1H), 2.46 (br. s., 3H), 2.39 (dd, *J* = 7.70, 15.28 Hz, 1H), 2.32 - 2.36 (m, 1H), 2.16 - 2.28 (m, 3H), 2.09 - 2.15 (m, 3H), 2.05 - 2.09 (m, 1H), 2.01 - 2.04 (m, 2H), 1.99 (br. s., 3H), 1.93 - 1.97 (m, 2H), 1.91 (br. s., 1H), 1.87 (br. s., 1H), 1.85 (br. s., 2H), 1.74 - 1.81 (m, 4H), 1.71 (br. s., 1H), 1.70 (br. s., 3H), 1.62 - 1.66 (m, 1H), 1.30 - 1.34 (m, 2H), 1.27 (s, 6H), 1.25 (br. s., 1H),

1.15 (d, *J* = 7.09 Hz, 1H), 1.04 (d, *J* = 6.85 Hz, 2H), 0.98 (d, *J* = 6.60 Hz, 3H), 0.92 - 0.97 (m, 3H), 0.86 - 0.91 (m, 8H), 0.81 - 0.85 (m, 3H); ^{13}C NMR (126 MHz, $CDCl_3$) δ 174.6, 173.2, 128.0, 127.2, 126.3, 109.1, 82.1, 65.1, 61.5, 60.9, 60.2, 58.0, 53.9, 51.6, 47.8, 44.9, 36.7, 36.4, 36.2, 35.5, 35.0, 34.7, 33.5, 31.9, 30.6, 29.7, 28.5, 26.8, 26.4, 25.8, 25.0, 22.7, 19.4, 18.5, 17.6, 14.3, 14.1, 13.9, 10.9; LRMS (ESI) *m/z* $[M+Na]^+$ calcd for $C_{57}H_{91}N_5O_{14}$: 1071.4; found: 1071.9.

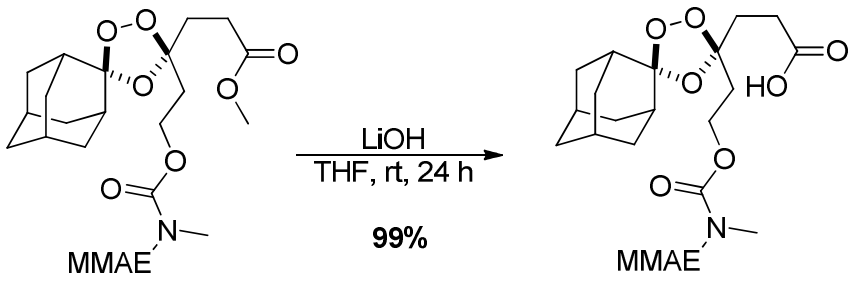

29 **50**

Preparation of 3-{5'-[2-({[(1S)-1-{[(2S)-2-{[(3R,5S)-1-[(2S)-2-[(2R)-2-{[(1S,2R)-1-hydroxy-1-phenylpropan-2-yl]carbamoyl}-1-methoxy-2-methylethyl]pyrrolidin-1-yl]-3-methoxy-5-methyl-1-oxoheptan-4-yl](methyl)amino}-3-methylbutanoyl]carbamoyl}-2-methylpropyl](methyl)carbamoyl}oxy)ethyl]spiro[adamantane-2,2'-[1,3,4]trioxolane]-5'-yl}propanoic acid (50): To a 20-mL scintillation vial charged with a teflon stir bar and methyl ester **24** (0.006 g, 0.006 mmol, 1.0 equiv.) was added tetrahydrofuran (1.000 ml) and Lithium hydroxide (0.0008 g, 0.04 mmol, 6.1 equiv.) as a 1 M solution in water (35 μL) via microliter pipet. The resulting solution was stirred for 30 h at rt then diluted with 5 mL of DCM and 5 mL of deionized water. The aqueous layer was acidified to pH ~4 with 35 μL of 1 N HCl and extracted with three, 5-mL portions of DCM. The organic layers were combined, washed with 10 mL of sat. NaCl, dried over $MgSO_4$, and reduced to yield 0.006 g (99%) of **50** which was carried forward without further purification: LRMS (ESI) *m/z* $[M+Na]^+$ calcd for $C_{56}H_{89}N_5O_{14}$: 1057.3; found: 1057.1.

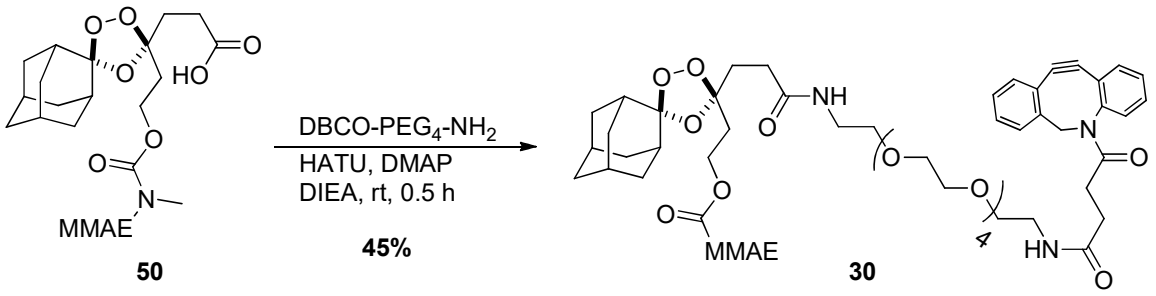

Preparation of 2-{5'-[2-({14-[(3-{2-azatricyclo[10.4.0.0^{4,9}]hexadeca-1(12),4(9),5,7,13,15-hexaen-10-yn-2-yl}-3-oxopropyl)carbamoyl]-3,6,9,12-tetraoxatetradecan-1-yl}carbamoyl)ethyl]spiro[adamantane-2,2'-[1,3,4]trioxolane]-5'-yl}ethyl N-[(1S)-1-{[(2S)-2-{[(3R,5S)-1-[(2S)-2-[(2R)-2-{[(1S,2R)-1-hydroxy-1-phenylpropan-2-yl]carbamoyl}-1-methoxy-2-methylethyl]pyrrolidin-1-yl]-3-methoxy-5-methyl-1-oxoheptan-4-yl](methyl)amino}-3-methylbutanoyl]carbamoyl}-2-methylpropyl]-N-methylcarbamate (30): A 5 mL round bottomed flask was heat dried under vacuum and charged with **50** (0.006 g, 0.0 mmol, 1.0 equiv.), 4-dimethylaminopyridine (0 mg, 0.0 mmol, 0.4 equiv.), HATU (0.010 g, 0.0 mmol, 4.6 equiv.) and a teflon stirbar. The vial was fitted with a rubber septa and the atmosphere was exchanged for argon. A solution of DBCO-PEG_4-NH_2 (5 mg, 0.0 mmol, 1.7 equiv.) in DMF (25 mg/mL) was added to the reaction (210 μL) and N,N-diisopropylethylamine (0.010 ml, 0.1 mmol, 10.1 equiv.) was added to the resulting solution. The resulting yellow reaction mixture was stirred under argon at rt for 30 min then diluted with 1000 μL of DMSO and directly purified via rp-HPLC chromatography eluting with 40-100% MeOH/Water to yield 0.004 g (45%) of **30**: ^{1}H NMR (500 MHz, $CDCl_3$) δ 7.68 (d, *J* = 7.34 Hz, 1H), 7.30 - 7.44 (m, 6H), 6.52 (br. s., 2H), 5.15 (d, *J* = 13.94 Hz, 1H), 4.95 (br. s., 1H), 4.69 (br. s., 1H), 4.21 - 4.35 (m, 2H), 4.13 - 4.21 (m, 1H), 4.08 (br. s., 2H), 3.85 (d, *J* = 8.31 Hz, 1H), 3.71 (d, *J* = 4.89 Hz, 1H), 3.68 (br. s., 1H), 3.63 (br. s., 4H), 3.60 (dd, *J* = 4.77, 7.70 Hz, 5H), 3.50 - 3.56 (m, 4H), 3.30 - 3.44

(m, 7H), 3.02 (s, 1H), 2.92 (br. s., 1H), 2.87 (br. s., 1H), 2.42 - 2.53 (m, 2H), 2.34 - 2.42 (m, 2H), 2.32 (dd, *J* = 4.77, 10.64 Hz, 2H), 2.20 - 2.25 (m, 2H), 2.17 (d, *J* = 6.36 Hz, 1H), 2.12 (br. s., 2H), 1.94 - 2.05 (m, 7H), 1.81 - 1.92 (m, 7H), 1.73 - 1.81 (m, 7H), 1.70 (br. s., 5H), 1.62 - 1.67 (m, 2H), 1.33 (br. s., 6H), 1.25 - 1.29 (m, 14H), 1.01 - 1.06 (m, 3H), 0.98 (d, *J* = 6.60 Hz, 2H), 0.94 (d, *J* = 6.11 Hz, 2H), 0.88 (td, *J* = 6.88, 14.37 Hz, 10H), 0.81 - 0.84 (m, 2H); LRMS (ESI) *m/z* $[M+Na]^+$ calcd for $C_{85}H_{124}N_8O_{19}$: 1562.9; found: 1562.6.

Supplementary Data:

Supplemental Figures:

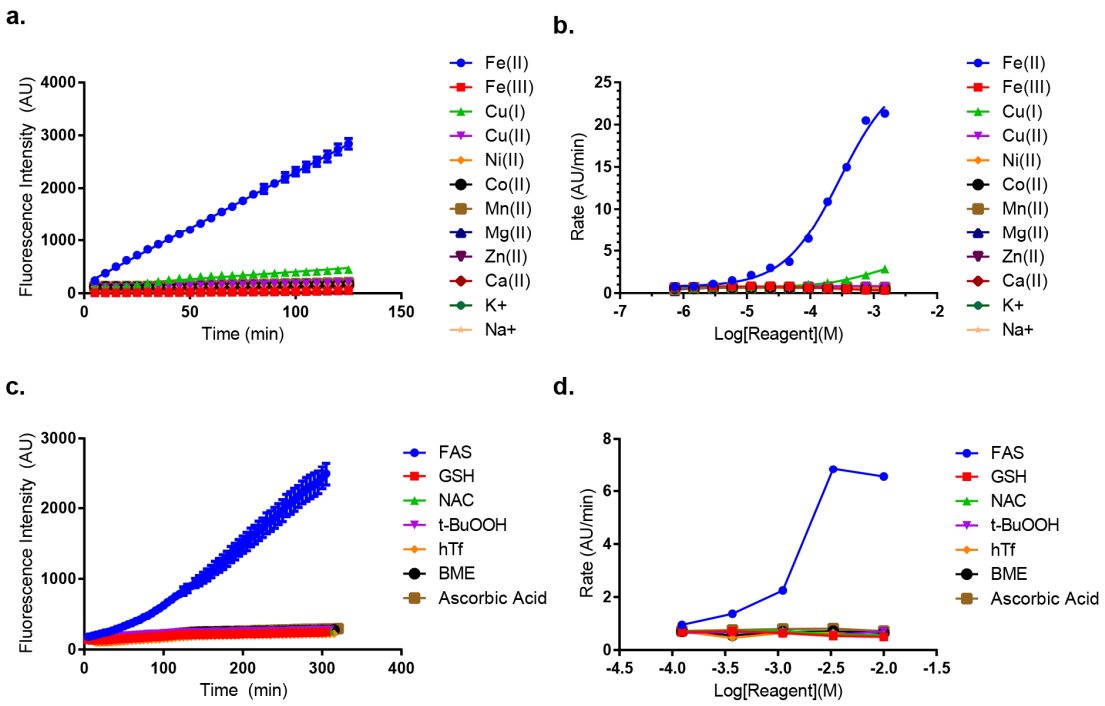

Supplementary Figure 1: Fluorescence intensity over time and rates of fluorescence increase from 1 treated with metal ions and redox active compounds.
(**a**) Fluorescence intensity over time from **1** (30 μM) when treated with 1.5 mM solutions of the indicated metal ions. (**b**) Initial rates of fluorescence increase from **1** (30 μM) when treated with solutions of the indicated metal ions at various concentrations. (**c**) Fluorescence intensity over time from **1** (15 μM) when treated with 3 mM solutions of the indicated biologically relevant redox active reagents. (**d**) Initial rates of fluorescence increase from **1** (15 μM) when treated with solutions of the indicated biologically relevant redox active reagents at various concentrations. Concentrations of **1** used for the assay were decreased from 30 to 15 μM to conserve material.

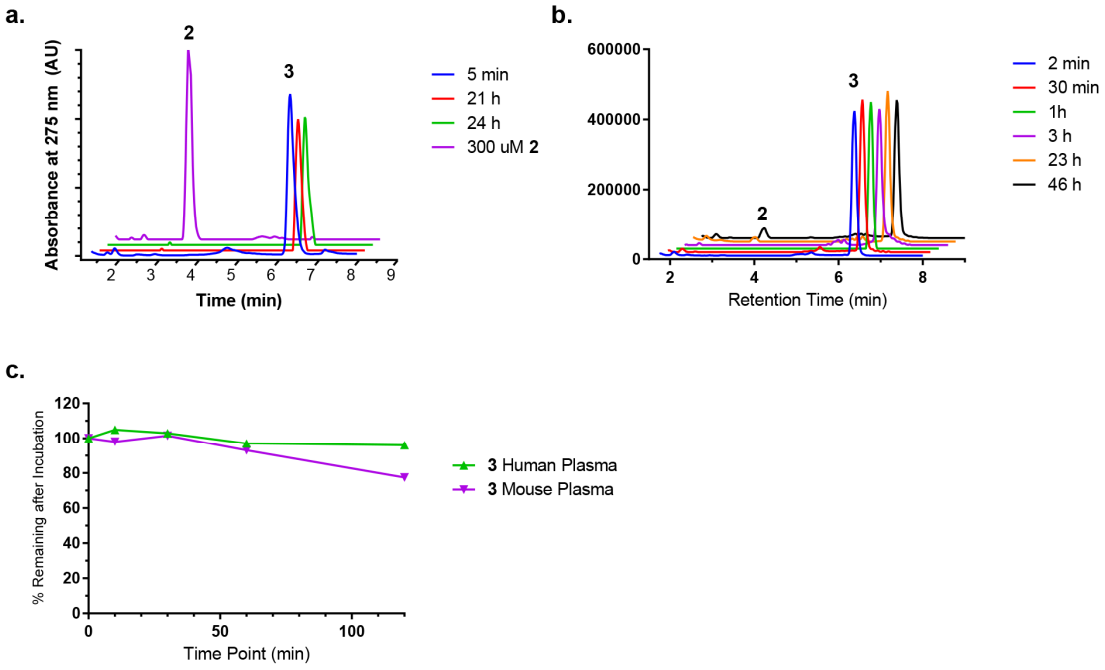

Supplementary Figure 2: Plasma and media stability of Trx-puro conjugate 3. (**a**) Stability of **3** for greater than 24 h when incubated at 37 °C in cell culture media. (**b**) Stability of **3** when exposed to 3 mM ferric sulfate in cell culture media at 37 °C for up to 2 days. Only very small amounts of free **2** is observed after 23 h as compared to essentially quantitative conversion of **3** to **2** when exposed to ferrous iron sources (**Fig. 2b**). (**c**) Plasma stability of **3** in mouse and human plasma with little loss of **3** observed over 2 h.

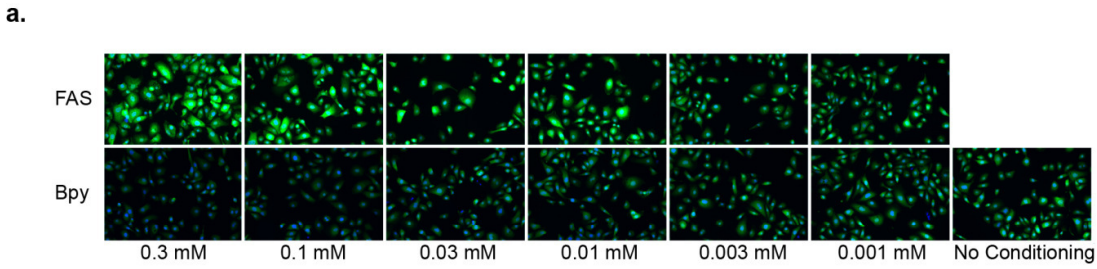

Supplementary Figure 3: Representative images of Fe(II)-conditioning dose responses.

Representative images of PC-3 cells treated with the indicated doses of FAS or Bpy for 2 h before washing with PBS and exposing to **3** for 4 h then washing fixing and imaging as described in the methods. Puromycin incorporation is visualized in green while Hoechst stained nuclei are shown in blue.

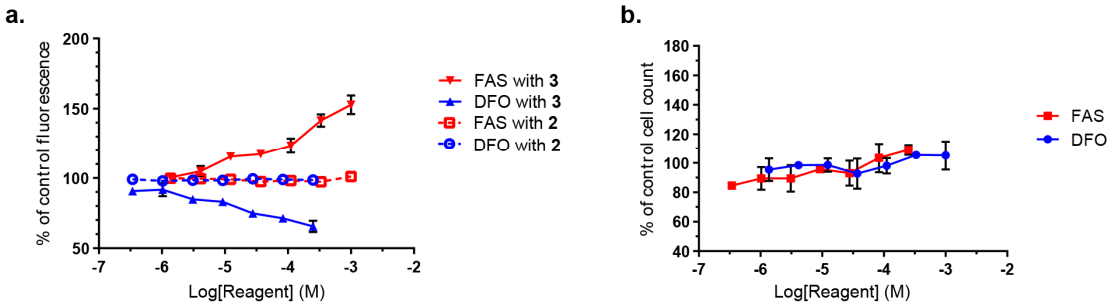

Supplementary Figure 4: Fe(II)-conditioning with FAS and DFO.
(a) Incorporation of puromycin in PC-3 cells pretreated with various concentrations of FAS or DFO in cell culture media for 2.5 h then washed and exposed to **2** or **3** for 4 h before fixing, staining, and imaging. Greater than 2000 cells were imaged and analyzed per condition and well mean intensity values across triplicates are reported with error bars depicting +/- s.e.m. Data is normalized to fluorescence in cells pretreated with vehicle instead of FAS or DFO then subsequently treated with **2**, or **3** as in all other conditions. **(b)** Effects of iron conditioning and puromycin treatment (1 μM for 4 h as in (a)) on cell viability as determined by nuclei count.

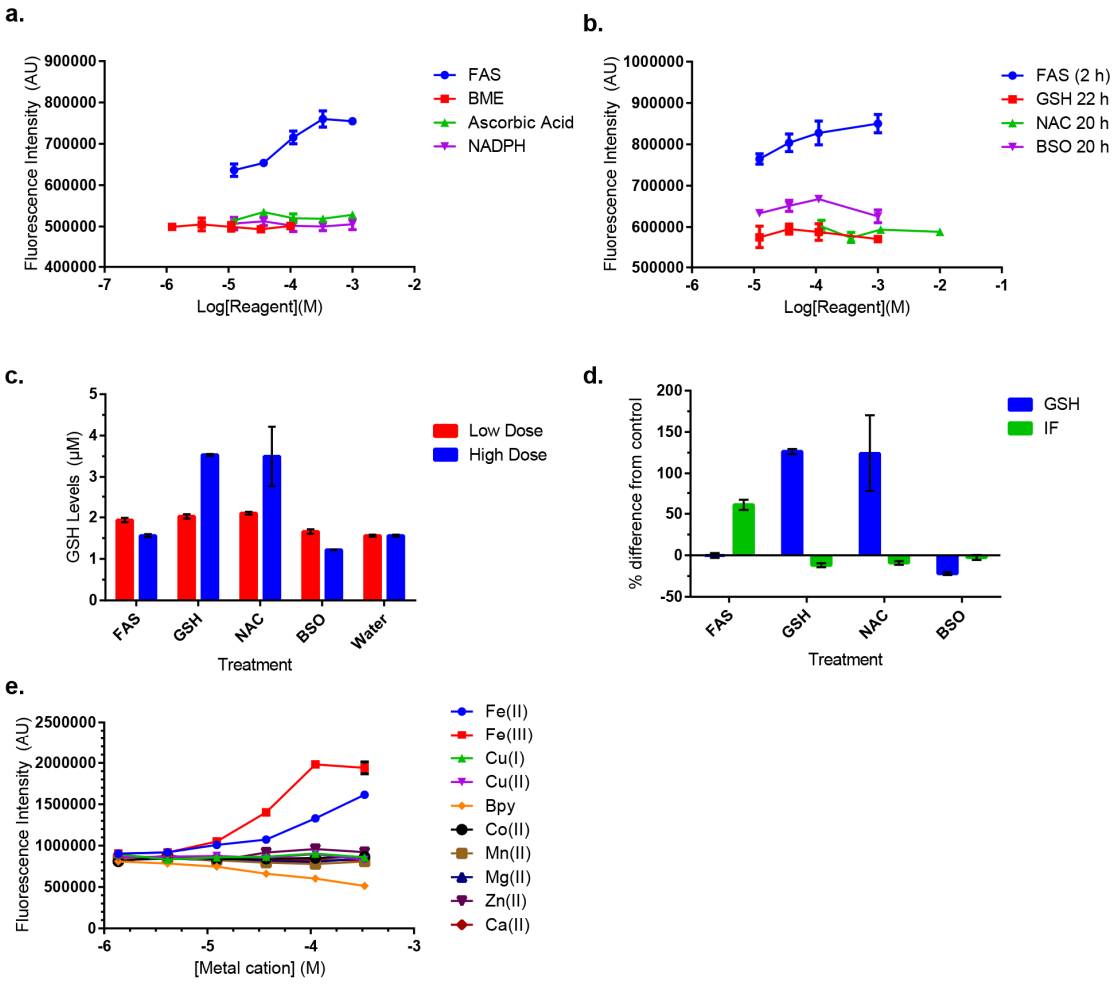

Supplementary Figure 5: Selectivity of Trx-puro probe 3 for reporting on Fe(II) in cells.

(**a**), (**b**), and (**e**) Raw fluorescence intensity data from selectivity experiments in figure 3. (**c**) Measured GSH levels from ca. 10,000 cells treated as in (**b**) with 1 mM (high dose) or 0.1 mM (low dose) of the indicated reagents (10 mM and 1 mM doses were used for the high and low NAC treatments). (**c**) Signal produced from probe **3** after dosing with the indicated reagents as in (**b**) at their highest doses compared to the effect the same treatments had on intracellular GSH levels.

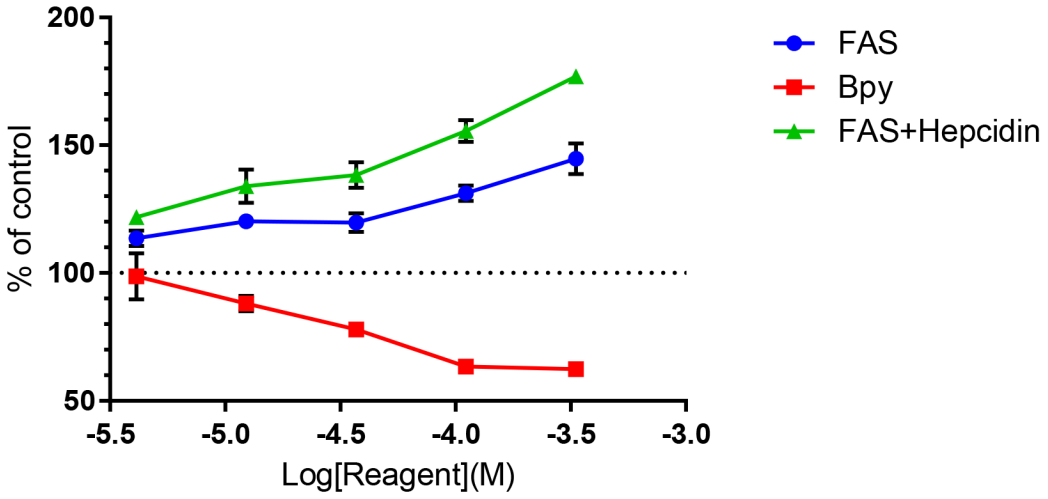

Supplementary Figure 6: Effects of hepcidin treatment on Fe(II) levels.
Levels of puromycin incorporation in PC-3 cells pretreated with a dose response of FAS or Bpy the washed and exposed to probe **3** for 4 h before washing, staining and imaging as described in the methods. Background from cells treated with DMSO instead of **3** was subtracted and values were normalized to those in cells pretreated with vehicle (water) instead of FAS or Bpy. Levels of incorporation in cells pretreated with HP for 16 prior to and during FAS treatment were higher at all doses, consistent with decreased iron export capacity increasing the Fe(II) pool in cells.

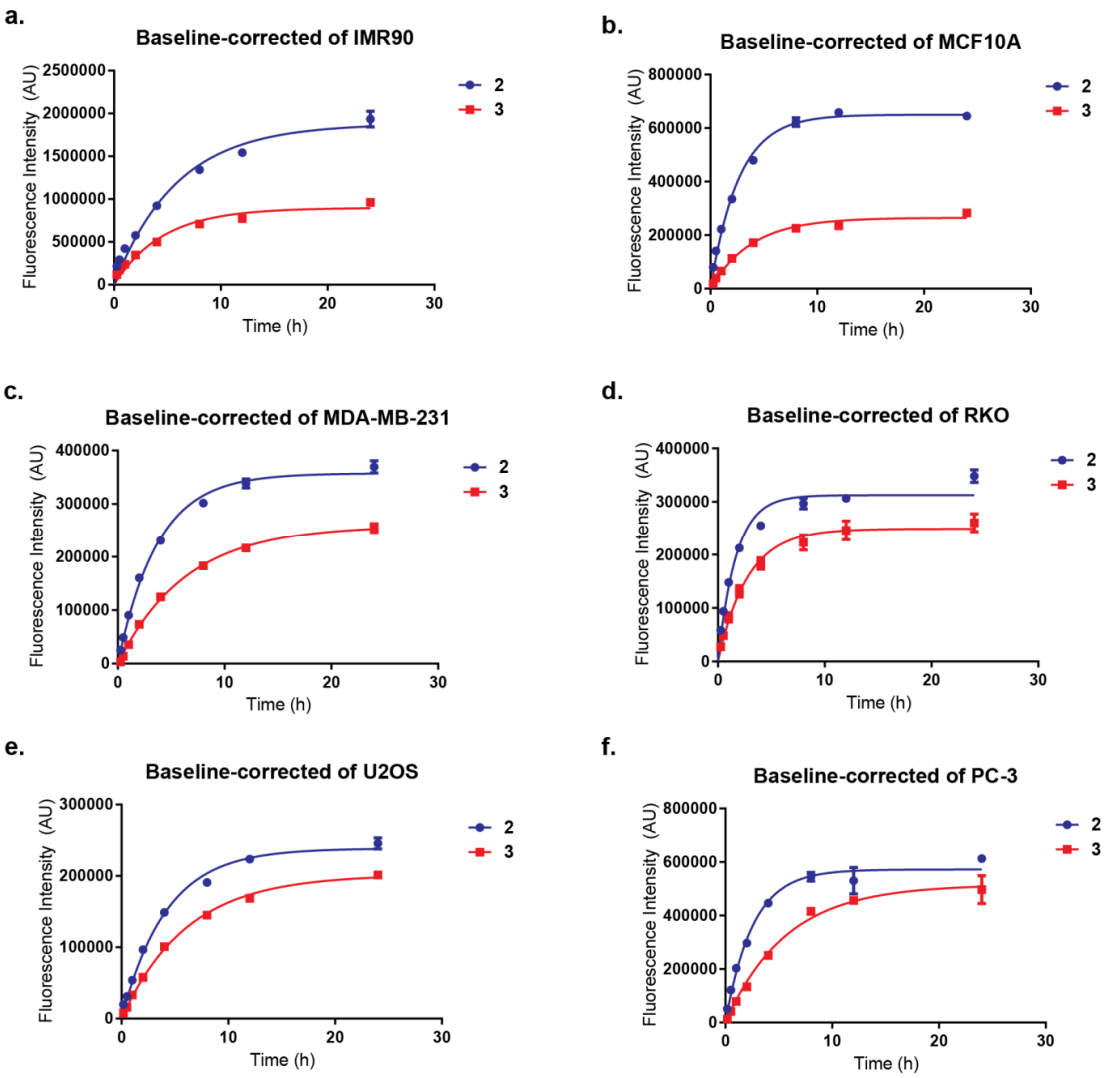

Supplementary Figure 7: Baseline-corrected puro incorporation for cell lines treated with 2 or 3

Puromycin incorporation over time in cell lines treated with trioxolane-conjugate **3** or free puromycin **2**. Signal at saturation in cells treated with **3** was normalized to that in cells treated with equimolar amounts of **2** as reported in figure 5 to compare reactive Fe(II) pools across cell lines.

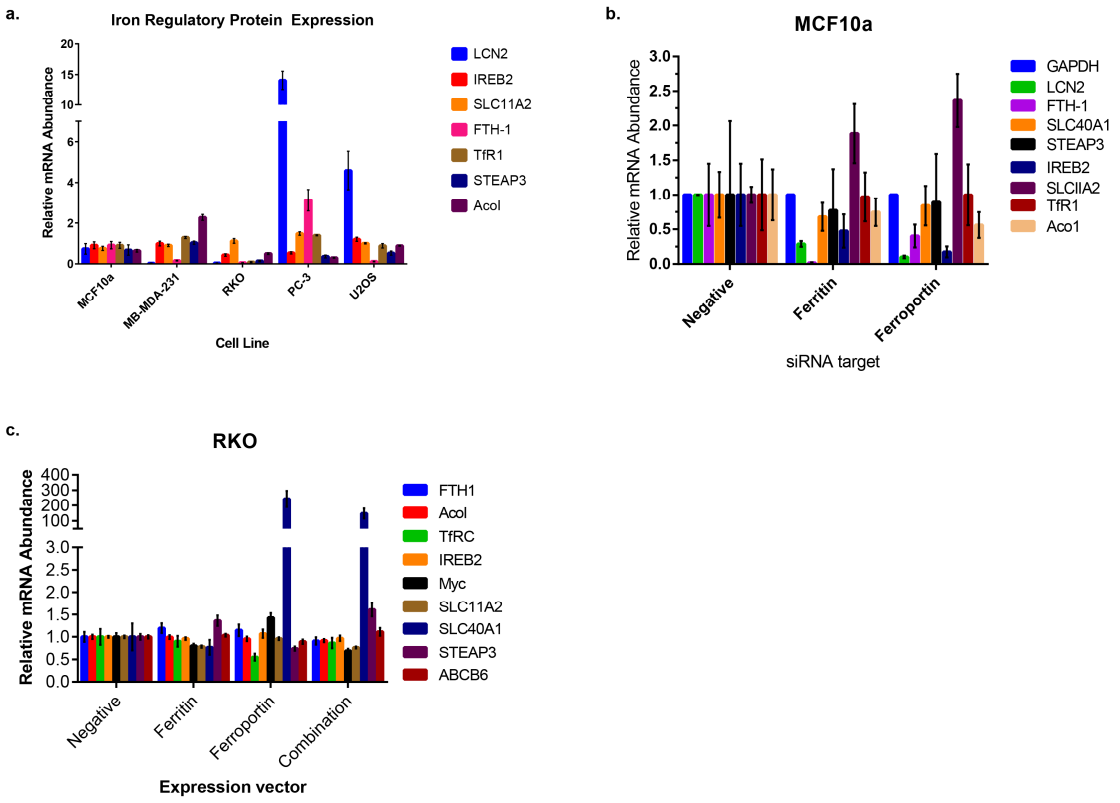

Supplementary Figure 8: qRT-PCR panels for iron regulator proteins across cells
(a) mRNA expression levels for iron regulatory proteins in cancer cell lines as compared to those in MCF10A cells. Measurements were taken of biological triplicates internally normalized to GAPDH expression. Relative mRNA levels were determined from a standard curve consisting of 4-fold dilutions of pooled cDNA samples from all of the cell lines for each set of qPCR primers. Error bars represent s.e.m. (n=3). (**b**) Full qRT-PCR panel for MCF10A cells treated with siRNA targeting SLC40A1 and FTH-1. (**c**) Full qRT-PCR panel for RKO cells ectopically expressing the same proteins. Measurements were taken of biological triplicates internally normalized to GAPDH expression. Relative mRNA levels were determined by normalizing to negative control treated cells. Error bars represent s.e.m. (n=3).

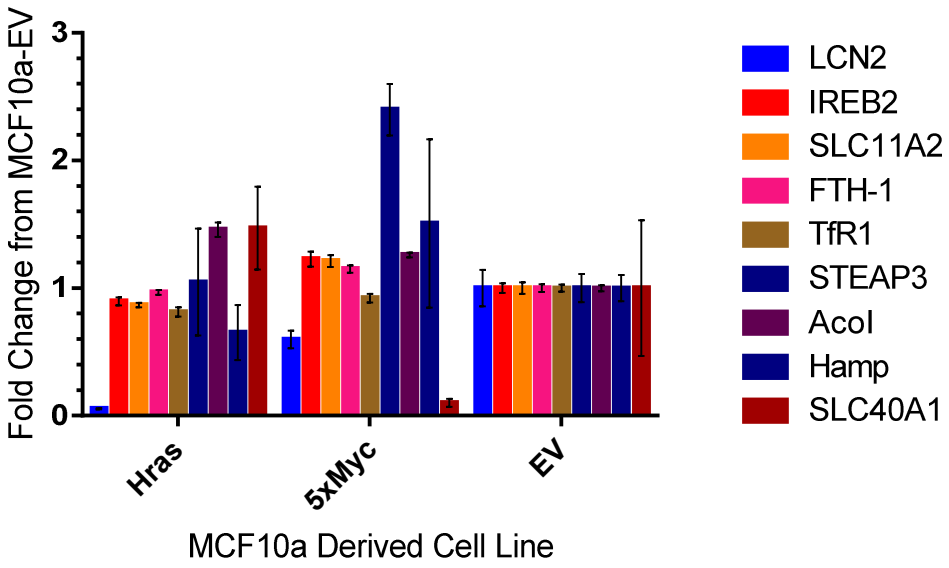

Supplementary Figure 9: Oncogenic perturbation of iron metabolism protein expression

qRT-PCR analysis of iron metabolism protein transcript levels in MCF10A cells stabily transfected with either the oncogenes Myc or Hras normalized to those in the empty vector. Measurements were taken of biological triplicates internally normalized to GAPDH expression. Error bars represent s.e.m. (n=3).

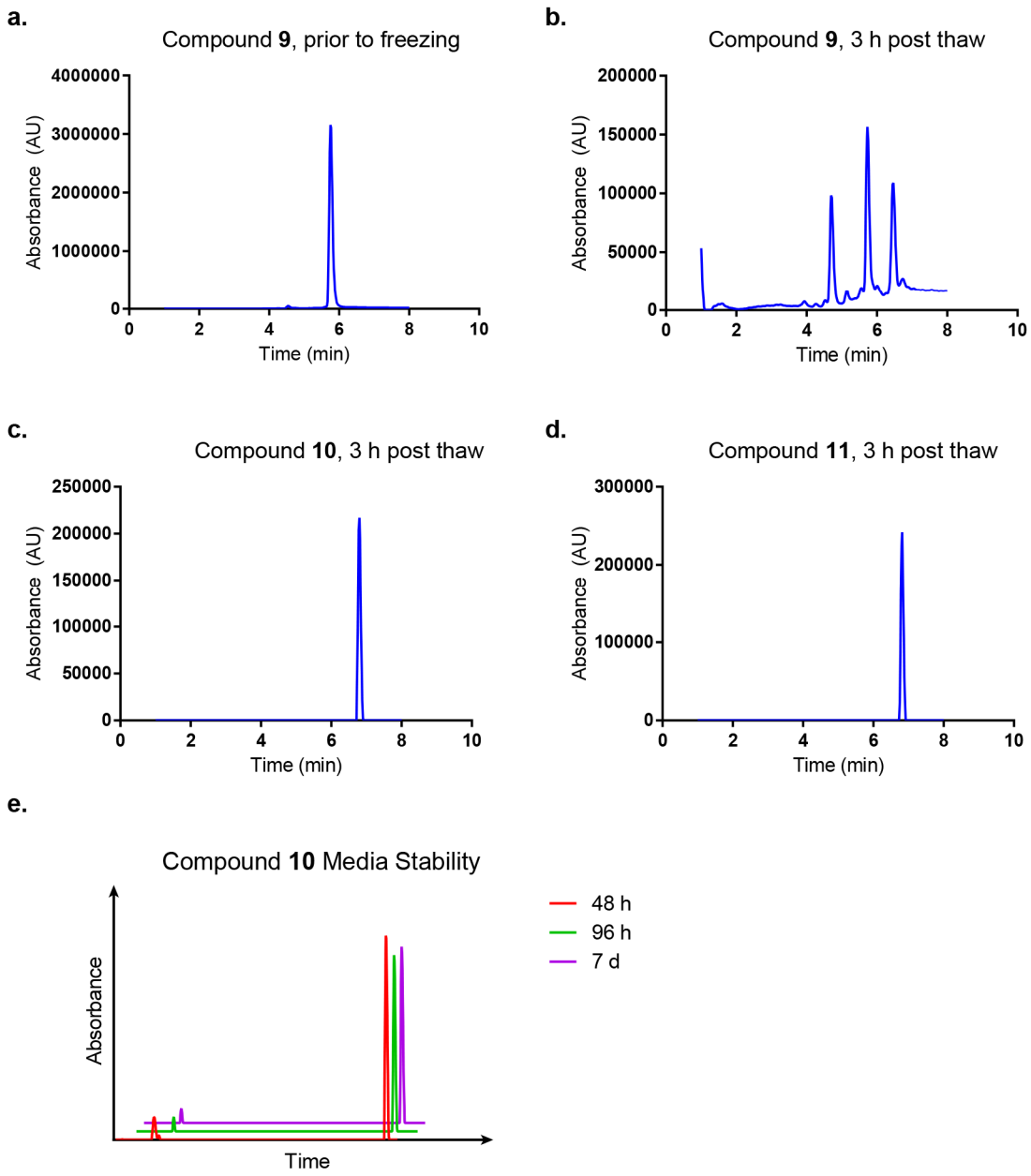

Supplementary Figure 10: Stability of amino-CBI analogs 9, 10, and 11
LCMS chromatograms of **9, 10,** and **11** after the indicated treatments.

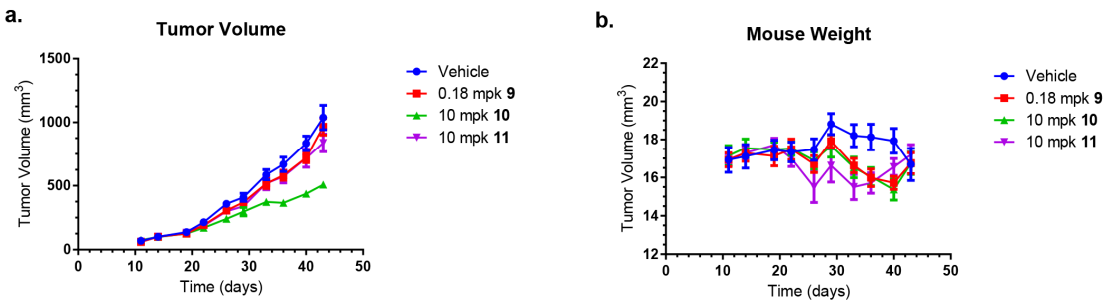

Supplementary Figure 11: Efficacy of amino-CBI analogs 9, 10, and 11 in xenograft models

(a) Changes in tumor volume over time as determined by calipers in MDA-MB-231 xenograft bearing mice treated with the indicated doses of free **9**, trioxolane-conjugate **10**, or dioxolane-control **11** as compared to mice treated with vehicle. **(b)** Changes in mouse weight over time for the mice in (a).

Schemes:

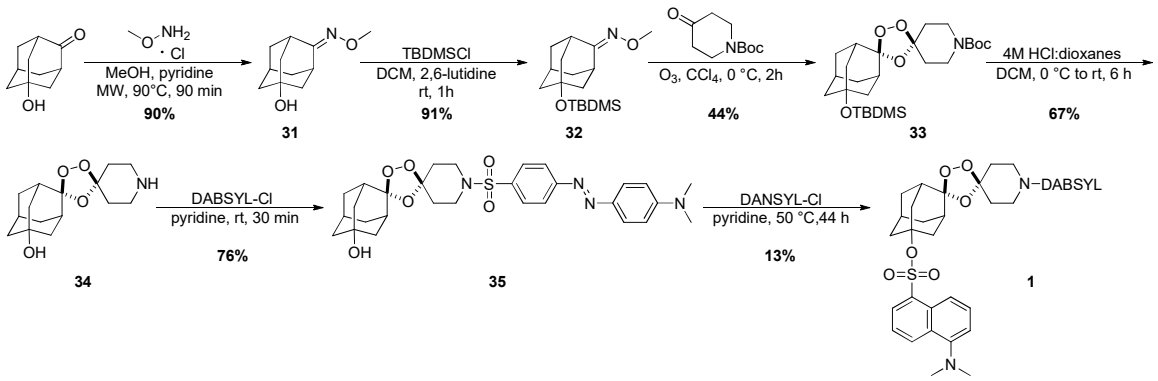

Supplementary Scheme 1: Synthesis of trioxolane-based FRET probe 1

Oxime **10** was prepared as previously described previously[151]. The modest yield obtained in the final step reflects the poor nucleophilicity of the hydroxyl function in **35** and thermal instability of the trioxolane moiety on prolonged heating.

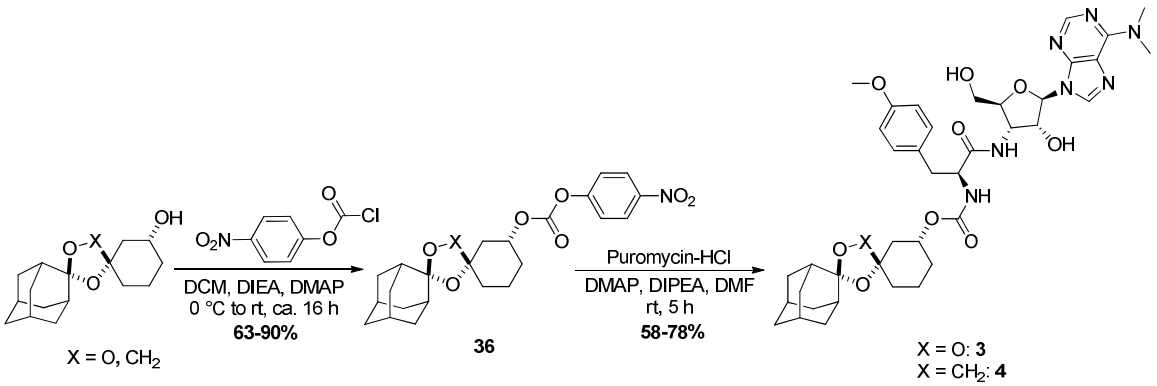

Supplementary Scheme 2: Synthesis of puromycin conjugates 3 and 4.
Key alcohol intermediate *trans*-**15** was prepared in racemic form as described in our recent communication[90] and converted to **3** in two steps as shown above. Dioxolane-control **4** was prepared in an analogous manner from alcohol **17** as described in the methods.

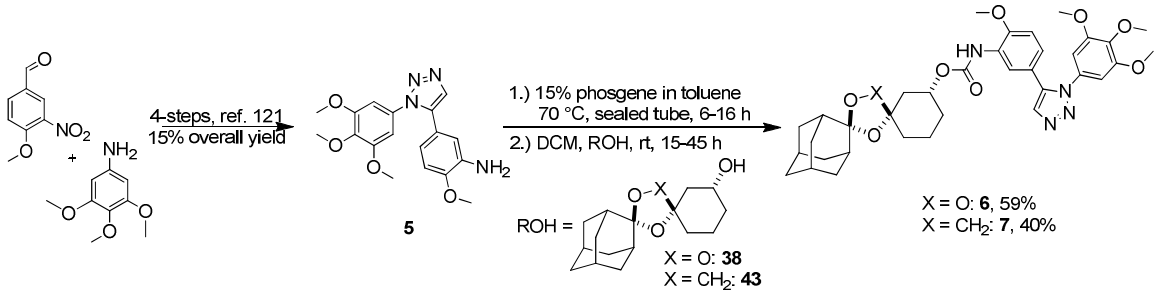

Supplemental Scheme 3: Synthesis of microtubule inhibitor conjugates 2 and 3.
The known microtubule inhibitor **5** was prepared following the previously reported procedure[121]. This material was converted to the corresponding isocyanate followed by reaction with alcohol intermediates **38** or **43** to yield conjugates **6** and **7** respectively.

Tables:

Compound	Pe (cm/s)	R(%)
Puromycin (**2**)	2E-07	2
Trx-Puro (**3**)	6.75E-07	11
Propranolol	1.59E-05	1
Metprolol	4.24E-06	1

Supplementary Table 1: Intrinsic permeability of puromycin and trioxolane-conjugate 3

Permeability of puromycin and trioxolane-conjugate **3** as determined by PAMPA assay. Positive controls of propranolol and metprolol run in parallel to confirm validity of the assay and match well with literature reported values[152].

EC_{50}	**6**	**7**	**6/7**
HeLa	4.76 ± 0.5 nM	15.82 ± 1.78 nM	0.30
U-2 OS	9.68 ± 1.63 nM	20.88 ± 3.80 nM	0.46
MDA-MB-231	11.23 ± 0.76 nM	20.87 ± 1.67 nM	0.54
MCF10A	8.85 ± 2.47 nM	238.8 ± 36.3 nM	0.04
PC-3	9.23 ± 0.87 nM	28.43 ± 3.27 nM	0.32
RKO	9.47 ± 0.59 nM	20.50 ± 1.00 nM	0.46

Supplementary Table 2: Toxicity of 6 and 7 across cell lines
Table of determined EC_{50} values for **6** and **7** in the indicated cell lines. Error values represent ±1 s.d. from three independent experiments run in triplicate.

Cell Line	EC_{50} of **7** (M)	95% CI (M)
EKVX	4.345e-008	2.939e-008 to 6.424e-008
NCI-H226	2.071E-08	1.504e-008 to 2.852e-008
MCF-7	9.876E-09	7.436e-009 to 1.312e-008
U-251	1.166E-07	7.856e-008 to 1.729e-007
K-562	1.87E-07	1.293e-007 to 2.703e-007
SKOV3	4.744E-08	3.695e-008 to 6.091e-008
UACC-257	9.147E-08	7.639e-008 to 1.095e-007
ACHN	6.893E-08	6.352e-008 to 7.480e-008
HeLa	4.155E-07	3.900e-007 to 4.426e-007
Jurkat	1.351E-07	8.923e-008 to 2.046e-007
OVCAR-8	1.895E-07	1.575e-007 to 2.279e-007
SF-539	4.93E-08	3.436e-008 to 7.073e-008
PC-3	2.025E-07	1.758e-007 to 2.333e-007

Supplementary Table 3: Expanded toxicity panel of trioxolane-conjugate 7
Table of determined EC50 values for **7** in the indicated cell lines with the 95% confidence interval for each value shown (n=3).

Dosed	Dosing (mg/kg)	Analyte	$T_{1/2}$ (h)	AUC (h*ng/mL)	AUC (h*umol/L)	CL/F pred. (mL/h/kg)	Vz/F pred. (mL/kg)
9	0.3	**9**	3.82	246.07	0.628	1208.8	6669.0
10	7.5	**10**	20.42	5050.2	7.233	1874.9	55233
10	7.5	**9**	n.d.	641.30	1.636	n.d.	n.d.

Supplementary Table 4: Pharmacokinetic parameters of compounds of 9 and 10
Table of calculated PK parameters of compounds **9** and **10** when dosed to at their respective MTD (0.3 mg/kg and 7.5 mg/kg) in healthy NSG mice (n=3).

References:

1. Wang, J. & Pantopoulos, K. Regulation of cellular iron metabolism. *Biochem. J.* **434,** 365–381 (2011).

2. Richardson, D. R. & Ponka, P. The molecular mechanisms of the metabolism and transport of iron in normal and neoplastic cells. *Biochim. Biophys. Acta* **1331,** 1–40 (1997).

3. Pantopoulos, K. Iron Metabolism and the IRE/IRP Regulatory System: An Update. *Ann. NY Acad. Sci* **1012,** 1–13 (2004).

4. Kurz, T., Eaton, J. W. & Brunk, U. T. The role of lysosomes in iron metabolism and recycling. *Int. J. Biochem. Cell Biol.* **43,** 1686–1697 (2011).

5. Fontecave, M. & Pierre, J. L. Iron: metabolism, toxicity and therapy. *Biochimie* **75,** 767–73 (1993).

6. S. Bandyopadhyay, K. Chandramouli, M. K. J. Iron-Sulphur Cluster Biosynthesis. *Biochem Soc Trans.* **36,** 1112–1119 (2008).

7. Johnson, D. C., Dean, D. R., Smith, A. D. & Johnson, M. K. Structure, function, and formation of biological iron-sulfur clusters. *Annu. Rev. Biochem.* **74,** 247–281 (2005).

8. Torti, S. V & Torti, F. M. Iron and cancer: more ore to be mined. *Nat. Rev. Cancer* **13,** 342–55 (2013).

9. O'Neill, P. M. & Posner, G. H. A medicinal chemistry perspective on artemisinin and related endoperoxides. *J. Med. Chem.* **47,** 2945–64 (2004).

10. Mercer, A. E. *et al.* Evidence for the involvement of carbon-centered radicals in the induction of apoptotic cell death by artemisinin compounds. *J. Biol. Chem.* **282,** 9372–82 (2007).

11. Dixon, S. J. & Stockwell, B. R. The role of iron and reactive oxygen species in cell death. *Nat. Chem. Biol.* **10,** 9–17 (2014).

12. Miller, L. D. *et al.* An iron regulatory gene signature predicts outcome in breast cancer. *Cancer Res.* **71,** 6728–37 (2011).

13. Daniels, T. R. *et al.* The transferrin receptor and the targeted delivery of therapeutic agents against cancer. *Biochim. Biophys. Acta* **1820,** 291–317 (2012).

14. Ponka, P. & Lok, C. N. The transferrin receptor: role in health and disease. *Int. J. Biochem. Cell Biol.* **31,** 1111–37 (1999).

15. Boult, J. *et al.* Overexpression of cellular iron import proteins is associated with malignant progression of esophageal adenocarcinoma. *Clin. Cancer Res.* **14,** 379–87 (2008).

16. Ohgami, R. S. *et al.* Identification of a ferrireductase required for efficient transferrin-dependent iron uptake in erythroid cells. *Nat. Genet.* **37,** 1264–9 (2005).

17. Radulescu, S. *et al.* Luminal iron levels govern intestinal tumorigenesis after Apc loss in vivo. *Cell Rep.* **2,** 270–82 (2012).

18. Leng, X., Wu, Y. & Arlinghaus, R. B. Relationships of lipocalin 2 with breast tumorigenesis and metastasis. *J. Cell. Physiol.* **226,** 309–14 (2011).

19. Pinnix, Z. K. *et al.* Ferroportin and Iron Regulation in Breast Cancer Progression and Prognosis. *Sci. Transl. Med.* **2,** (2010).

20. Wu, K. Coordinated Regulation of Iron-Controlling Genes, H-Ferritin and IRP2, by c-MYC. *Science (80).* **283,** 676–679 (1999).

21. Maffettone, C., Chen, G., Drozdov, I., Ouzounis, C. & Pantopoulos, K. Tumorigenic Properties of Iron Regulatory Protein 2 (IRP2) Mediated by Its Specific 73-Amino Acids Insert. *PLoS One* **5,** (2010).

22. Kakhlon, O. & Cabantchik, Z. I. The labile iron pool: Characterization, measurement, and participation in cellular processes. *Free Radic. Biol. Med.* **33,** 1037–1046 (2002).

23. Petrat, F., Rauen, U. & de Groot, H. Determination of the chelatable iron pool of isolated rat hepatocytes by digital fluorescence microscopy using the fluorescent probe, phen green SK. *Hepatology* **29,** 1171–9 (1999).

24. Meguro, R., Asano, Y., Odagiri, S., Li, C. & Shoumura, K. Cellular and subcellular localizations of nonheme ferric and ferrous iron in the rat brain: a light and electron microscopic study by the perfusion-Perls and -Turnbull methods. *Arch. Histol. Cytol.* **71,** 205–22 (2008).

25. Espósito, B. P., Epsztejn, S., Breuer, W. & Cabantchik, Z. I. A review of fluorescence methods for assessing labile iron in cells and biological fluids. *Anal. Biochem.* **304,** 1–18 (2002).

26. Epsztejn, S., Kakhlon, O. & Glickstein, H. Fluorescence analysis of the labile iron pool of mammalian cells. *Anal. Biochem.* **40,** 31–40 (1997).

27. Cabantchik, Z. I. Labile iron in cells and body fluids: physiology, pathology, and pharmacology. *Front. Pharmacol.* **5,** 45 (2014).

28. Petrat, F., Groot, H. de, Sustmann, R. & Rauen, U. The Chelatable Iron Pool in Living Cells: A Methodically Defined Quantity. *Biol. Chem.* **383,** 489–502

(2002).

29. Petrat, F., Groot, H. de, Sustmann, R. & Rauen, U. The Chelatable Iron Pool in Living Cells: A Methodically Defined Quantity. *Biol. Chem.* **383,** 489–502 (2002).

30. Hirayama, T., Okuda, K. & Nagasawa, H. A highly selective turn-on fluorescent probe for iron(ii) to visualize labile iron in living cells. *Chem. Sci.* **4,** 1250 (2013).

31. Au-yeung, H. Y., Chantarojsiri, T. & Chang, C. J. Molecular Imaging of Labile Iron(II) Pools in Living Cells with a Turn- On Fluorescent Probe. *J. Am. Chem. Soc.* **135,** 15165–15173 (2013).

32. Chaturvedi, D., Goswami, A., Saikia, P. P., Barua, N. C. & Rao, P. G. Artemisinin and its derivatives: a novel class of anti-malarial and anti-cancer agents. *Chem. Soc. Rev.* **39,** 435–454 (2010).

33. Valecha, N. *et al.* Arterolane, a new synthetic trioxolane for treatment of uncomplicated Plasmodium falciparum malaria: a phase II, multicenter, randomized, dose-finding clinical trial. *Clin. Infect. Dis.* **51,** 684–91 (2010).

34. Borstnik, K., Paik, I., Shapiro, T. a & Posner, G. H. Antimalarial chemotherapeutic peroxides: artemisinin, yingzhaosu A and related compounds. *Int. J. Parasitol.* **32,** 1661–7 (2002).

35. Stocks, P. a *et al.* Evidence for a common non-heme chelatable-iron-dependent activation mechanism for semisynthetic and synthetic endoperoxide antimalarial drugs. *Angew. Chem. Int. Ed. Engl.* **46,** 6278–83 (2007).

36. Burchard, G. D. World Malaria Report 2014. **55,** 165–176 (2014).

37. Edikpo, N., Ghasi, S., Elias, A. & Oguanobi, N. Artemisinin and biomolecules: The continuing search for mechanism of action. *Mol. Cell. Pharmacol.* **5 (2),** 75–89 (2013).

38. Robert, a, Benoitvical, F. & Meunier, B. The key role of heme to trigger the antimalarial activity of trioxanes. *Coord. Chem. Rev.* **249,** 1927–1936 (2005).

39. Amewu, R. *et al.* Design and synthesis of orally active dispiro 1,2,4,5-tetraoxanes; synthetic antimalarials with superior activity to artemisinin. *Org. Biomol. Chem.* **4,** 4431–6 (2006).

40. Harris, F. & Pierpoint, L. PhotodynamicTherapy Based on 5-Aminolevulinic Acid and Its Use as an Antimicrobial Agent. *Med. Res. Rev.* 1292–1327 (2012). doi:10.1002/med

41. Wang, X. *et al.* Spiro- and dispiro-1,2-dioxolanes: contribution of iron(II)-mediated one-electron vs two-electron reduction to the activity of

antimalarial peroxides. *J. Med. Chem.* **50,** 5840–7 (2007).

42. Kim, H. S. *et al.* Synthesis and antimalarial activity of novel medium-sized 1,2,4,5-tetraoxacycloalkanes. *J. Med. Chem.* **44,** 2357–2361 (2001).

43. Vennerstrom, J., Arbe-Barnes, S. & Brun, R. Identification of an antimalarial synthetic trioxolane drug development candidate. *Nature* **430,** 900–904 (2004).

44. Charman, S. A. *et al.* Synthetic ozonide drug candidate OZ439 offers new hope for a single-dose cure of uncomplicated malaria. *PNAS* (2011). doi:10.1073/pnas.1015762108

45. Opsenica, I. *et al.* Tetraoxane antimalarials and their reaction with Fe(II). *J. Med. Chem.* **49,** 3790–9 (2006).

46. Dong, Y. *et al.* The structure-activity relationship of the antimalarial ozonide arterolane (OZ277). *J. Med. Chem.* **53,** 481–91 (2010).

47. Jefford, C. W. New developments in synthetic peroxidic drugs as artemisinin mimics. *Drug Discov. Today* **12,** 487–95 (2007).

48. Haynes, R. K. *et al.* Artemisone--a highly active antimalarial drug of the artemisinin class. *Angew. Chem. Int. Ed. Engl.* **45,** 2082–8 (2006).

49. Wang, X., Dong, Y., Wittlin, S., Charman, S. A. & Chiu, F. C. K. antimalarial activities and ADME profiles of ozonides (1, 2, 4-trioxolanes) OZ277, OZ439, and their 1, 2-dioxolane, 1, 2, 4-trioxane, and 1, 2, 4, 5-tetraoxane isosteres. *J. Med. Chem.* **56,** 2547–2555 (2013).

50. Valecha, N. *et al.* Arterolane maleate plus piperaquine phosphate for treatment of uncomplicated plasmodium falciparum malaria: A comparative, multicenter, randomized clinical trial. *Clin. Infect. Dis.* **55,** 663–671 (2012).

51. Rubin, M. The History of Ozone. Part III. *Helv. Chim. Acta* **86,** 930–940 (2003).

52. Zhao, Q. *et al.* Structure-activity relationship of an ozonide carboxylic acid (OZ78) against Fasciola hepatica. *J. Med. Chem.* **53,** 4223–33 (2010).

53. Duan, W. *et al.* Praziquantel derivatives exhibit activity against both juvenile and adult Schistosoma japonicum. *Bioorg. Med. Chem. Lett.* **22,** 1587–90 (2012).

54. Hooft van Huijsduijnen, R. *et al.* Anticancer properties of distinct antimalarial drug classes. *PLoS One* **8,** (2013).

55. Terent'ev, A. O., Borisov, D. a, Vil', V. a & Dembitsky, V. M. Synthesis of five- and six-membered cyclic organic peroxides: Key transformations into peroxide ring-retaining products. *Beilstein J. Org. Chem.* **10,** 34–114 (2014).

56. Tang, Y., Dong, Y., Karle, J. M., DiTusa, C. a & Vennerstrom, J. L. Synthesis of tetrasubstituted ozonides by the Griesbaum coozonolysis reaction: diastereoselectivity and functional group transformations by post-ozonolysis reactions. *J. Org. Chem.* **69,** 6470–3 (2004).

57. Fontaine, S. D. *et al.* Drug Delivery to the Malaria Parasite Using an Arterolane-Like Scaffold. *ChemMedChem* **10,** 47–51 (2015).

58. Story, P., Hall, T., III, W. M. & Farine, J. Thermal decomposition of ozonides. *Tetrahedron Lett.* 5397–5400 (1968).

59. Harries, C. D. The History of Ozone. **86,** 930–940 (2003).

60. Griesbaum, K., Bandyopadhyay, A. R. & Meister, M. Monoozonides of chloro-substituted conjugated dienes: preparation, stability, and some chemical reactions. *Can. J. Chem.* **64,** 1553–1559 (1986).

61. Dong, Y. *et al.* Effect of functional group polarity on the antimalarial activity of spiro and dispiro-1,2,4-trioxolanes. *Bioorg. Med. Chem.* **14,** 6368–82 (2006).

62. Hull, L., Hisatsune, I. & Heicklen, J. Vapor-phase thermal decomposition of some simple ozonides. *J. Phys. Chem.* **76,** 2659–2665 (1972).

63. Griesbaum, K., Dong, Y. & McCullough, K. J. Ozonolyses of Acetylenes: Trapping of α-Oxo Carbonyl Oxides by Carbonyl Compounds and Stabilization of α-Oxo Ozonides by Derivatizations. *J. Org. Chem.* **62,** 6129–6136 (1997).

64. McCullough, K. Short path syntheses of α-diozonides by sequential ozonolyses of acetylenes and O-methyl oximes. *J. Chem. Soc. Perkin …* 1601–1604 (1997).

65. Kuwabara, H., Ushigoe, Y. & Nojima, M. Synthesis and reaction of cyano-substitued 1, 2, 4-trioxolanes. *J. Chem. Soc., Perkin Trans. 1* 871–874 (1996).

66. Griesbaum, K. & Schlindwein, K. Nucleophilic Substitution Reactions at Chloro-Substituted Ozonides and at a Chlorinated Dimeric Peroxide. *J. Org. Chem.* **60,** 8062–8066 (1995).

67. Wu, H.-J. & Lin, C.-C. First Exclusive Regioselective Fragmentation of Primary Ozonides Controlled by Remote Carbonyl Groups and a New Method for Determining the Regiochemistry of Carbonyl Oxide Formation. *J. Org. Chem.* **61,** 3820–3828 (1996).

68. Hon, Y.-S. & Yan, J.-L. Syntheses of bifunctional compounds from cycloalkenes via ozonide intermediates. *Tetrahedron* **53,** 5217–5232 (1997).

69. Tang, Y. *et al.* Weak base dispiro-1,2,4-trioxolanes: potent antimalarial ozonides. *Bioorg. Med. Chem. Lett.* **17,** 1260–5 (2007).

70. Padmanilayam, M. *et al.* Antimalarial activity of N-alkyl amine, carboxamide,

sulfonamide, and urea derivatives of a dispiro-1,2,4-trioxolane piperidine. *Bioorg. Med. Chem. Lett.* **16,** 5542–5 (2006).

71. Barton, V., Ward, S. a, Chadwick, J., Hill, A. & O'Neill, P. M. Rationale design of biotinylated antimalarial endoperoxide carbon centered radical prodrugs for applications in proteomics. *J. Med. Chem.* **53,** 4555–9 (2010).

72. Jin, H.-X., Liu, H.-H., Zhang, Q. & Wu, Y. On the susceptibility of organic peroxy bonds to hydride reduction. *J. Org. Chem.* **70,** 4240–7 (2005).

73. Hon, Y.-S. & Yan, J.-L. Chemoselective reaction on a hydroxy or aldehyde group tethered with a tri-substituted ozonide: A versatile methodology for the preparation of terminally differentiated compounds from cyclohexene. *Tetrahedron* **54,** 8525–8542 (1998).

74. Zhou, L. *et al.* Characterization of the two major CYP450 metabolites of ozonide (1,2,4-trioxolane) OZ277. *Bioorg. Med. Chem. Lett.* **18,** 1555–8 (2008).

75. Miura, M. & Nagase, S. Acidolysis of ozonides. An ab initio study. *J. Org. Chem.* **2366,** 2366–2370 (1983).

76. Park, S. & Huh, T. Acid-Catalyzed Rearrangements of Aldehydo Ozonides. *Bull. Korean Chem. Soc.* **22,** 308–310 (2001).

77. Perry, C. S. *et al.* Chemical Kinetics and Aqueous Degradation Pathways of a New Class of Synthetic Ozonide Antimalarials. *J. Pharm. Sci.* **95,** 737–747 (2006).

78. Dussault, P. H., Lee, H.-J. & Liu, X. Selectivity in Lewis acid-mediated fragmentations of peroxides and ozonides: application to the synthesis of alkenes, homoallyl ethers, and 1,2-dioxolanes†. *J. Chem. Soc. Perkin Trans. 1* 3006–3013 (2000). doi:10.1039/b001391i

79. Dussault, P. H., Liu, X. & Rr, S. R. O. O. SnCl4-mediated reaction of ozonides with allyltrimethylsilane: formation of 1,2-dioxolanes. *Tetrahedron Lett.* **40,** 6553–6556 (1999).

80. Fukagawa, R. & Nojima, M. Synthesis and silica gel-catalysed decomposition of 3-(1-arylcycloalkyl) substituted 1, 2, 4-trioxolanes and 1, 2, 4-dioxazolidines. *J. Chem. Soc., Perkin Trans. 1* (1994).

81. Hon, Y. Y.-S. & Yan, J. J.-L. Chemoselective reactions of a compound containing both aldehyde and ozonide groups. *Tetrahedron Lett.* **35,** 1743–1746 (1994).

82. Griesbaum, K., Quinkert, R.-O. & McCullough, K. J. C–C Bond Formation at Ozonide Rings by Substitution of Chlorinated Ozonides. *European J. Org. Chem.* **2004,** 3657–3662 (2004).

83. Abe, M., Inakazu, T., Munakata, J. & Nojima, M. O-Tracer Studies of Fe (II) -

Induced Decomposition of 1 , 2 , 4-Trioxolanes (Ozonides) Derived from Cyclopentenes and Indenes . Inner-Sphere Electron Transfer Reduction of the Peroxide Linkage. *J. Am. Chem. Soc.* **121,** 6556–6562 (1999).

84. Posner, G. & Oh, C. Regiospecifically oxygen-18 labeled 1, 2, 4-trioxane: a simple chemical model system to probe the mechanism (s) for the antimalarial activity of artemisinin (qinghaosu). *J. Am. Chem. Soc.* 8328–8329 (1992).

85. Jefford, C., Favarger, F., Vicente, M. & Jacquier, Y. The Decomposition of cis-Fused Cyclopenteno-1, 2, 4-Trioxanes induced by Ferrous Salts and some oxophilic reagents. *Helv. Chim. Acta* **78,** 452–458 (1995).

86. Creek, D. *et al.* Iron-mediated degradation kinetics of substituted dispiro-1, 2, 4-trioxolane antimalarials. *J. Pharm. Sci.* **96,** 2945–2956 (2007).

87. Creek, D. J., Chalmers, D. K., Charman, W. N. & Duke, B. J. Quantum chemical study of the intermediate complex required for iron-mediated reactivity and antimalarial activity of dispiro-1,2,4-trioxolanes. *J. Mol. Graph. Model.* **27,** 394–400 (2008).

88. Mahajan, S., Deu, E., Lauterwasser, E. M. W. & Leyva, M. J. A fragmenting hybrid approach for targeted delivery of multiple therapeutic agents to the malaria parasite. *ChemMedChem* **6,** 415–419 (2011).

89. Deu, E. *et al.* Ferrous iron-dependent drug delivery enables controlled and selective release of therapeutic agents in vivo. *Proc. Natl. Acad. Sci. U. S. A.* **110,** 18244–9 (2013).

90. Fontaine, S. D., Dipasquale, A. G. & Renslo, A. R. Efficient and Stereocontrolled Synthesis of 1,2,4-Trioxolanes Useful for Ferrous Iron-Dependent Drug Delivery. *Org. Lett.* **16,** 5776–5779 (2014).

91. Chen, C. & Paw, B. H. Cellular and mitochondrial iron homeostasis in vertebrates. *Biochim. Biophys. Acta - Mol. Cell Res.* **1823,** 1459–1467 (2012).

92. Yan, C. Y., Ferrari, G. & Greene, L. a. N-acetylcysteine-promoted survival of PC12 cells is glutathione-independent but transcription-dependent. *J. Biol. Chem.* **270,** 26827–26832 (1995).

93. Mukherjee, T. K., Mishra, A. K., Mukhopadhyay, S. & Hoidal, J. R. High concentration of antioxidants N-acetylcysteine and mitoquinone-Q induces intercellular adhesion molecule 1 and oxidative stress by increasing intracellular glutathione. *J. Immunol.* **178,** 1835–1844 (2007).

94. Frikke-Schmidt, H. & Lykkesfeldt, J. Keeping the intracellular vitamin C at a physiologically relevant level in endothelial cell culture. *Anal. Biochem.* **397,** 135–7 (2010).

95. Gao, J. P., Friedman, S. & Lanks, K. W. The Role of Reduced Nicotinamide Adenine Dinucleotide Phosphate in Glucose Dependent and Temperature Dependent Doxorubicin Cytotoxicity. *Cancer Chemother. Pharmacol.* **33,** 191–196 (1993).

96. Ishii, T., Sugita, Y. & Bannai, S. Regulation of glutathione levels in mouse spleen lymphocytes by transport of cysteine. *J. Cell. Physiol.* **133,** 330–336 (1987).

97. Kanc, Y. J. & Fenc, Y. I. Glutathione Stimulates A549 Cell Proliferation in Glutamine-Deficient Culture : The Effect of Glutamate Supplementation. *J. Cell. Physiol.* **161,** 589–596 (1994).

98. Mukaide, T. *et al.* Histological detection of catalytic ferrous iron with the selective turn-on fluorescent probe RhoNox-1 in a Fenton reaction-based rat renal carcinogenesis model. *Free Radic. Res.* **48,** 990–5 (2014).

99. Mercer, A. E., Copple, I. M., Maggs, J. L., O'Neill, P. M. & Park, B. K. The role of heme and the mitochondrion in the chemical and molecular mechanisms of mammalian cell death induced by the artemisinin antimalarials. *J. Biol. Chem.* **286,** 987–96 (2011).

100. Stringham, R. W. & Teager, D. S. Streamlined Process for the Conversion of Artemisinin to Artemether. *Org. Process Res. Dev.* **16,** 764–768 (2012).

101. Atkinson, J. M., Siller, C. S. & Gill, J. H. Tumour endoproteases: the cutting edge of cancer drug delivery? *Br. J. Pharmacol.* **153,** 1344–52 (2008).

102. Ueki, N., Lee, S., Sampson, N. S. & Hayman, M. J. Selective cancer targeting with prodrugs activated by histone deacetylases and a tumour-associated protease. *Nat. Commun.* **4,** 2735 (2013).

103. Walko, C. M. & Lindley, C. Capecitabine: a review. *Clin. Ther.* **27,** 23–44 (2005).

104. Ettmayer, P., Amidon, G. L., Clement, B. & Testa, B. Lessons Learned from Marketed and Investigational Prodrugs. *J. Med. Chem.* **47,** 2393–2404 (2004).

105. Rooseboom, M., Commandeur, J. a N. N. M. & Vermeulen, N. P. E. Enzyme-Catalyzed Activation of Anticancer Prodrugs. *Pharmacol Rev* **56,** 53–102 (2004).

106. DeFeo-Jones, D. *et al.* A peptide-doxorubicin 'prodrug' activated by prostate-specific antigen selectively kills prostate tumor cells positive for prostate-specific antigen in vivo. *Nat. Med.* **6,** 1248–1252 (2000).

107. Defeo-jones, D. *et al.* A Prostate-specific Antigen (PSA)-activated Vinblastine Prodrug Selectively Kills PSA-secreting Cells in Vivo. *Mol. Cancer Ther.* **1,** 451–459 (2002).

108. Kratz, F., Müller, I. a, Ryppa, C. & Warnecke, A. Prodrug strategies in anticancer chemotherapy. *ChemMedChem* **3,** 20–53 (2008).

109. Xu, G. & McLeod, H. L. Strategies for enzyme/prodrug cancer therapy. *Clin. Cancer Res.* **7,** 3314–24 (2001).

110. Denny, W. a. Tumor-activated Prodrugs—A New Approach to Cancer Therapy. *Cancer Invest.* **22,** 604–619 (2004).

111. Chen, C.-S. *et al.* Activation of the anticancer prodrugs cyclophosphamide and ifosfamide: identification of cytochrome P450 2B enzymes and site-specific mutants with improved enzyme kinetics. *Mol. Pharmacol.* **65,** 1278–1285 (2004).

112. Atwell, G. J. & Denny, W. a. Synthesis of3H- and2H4-labelled versions of the hypoxia-activated pre-prodrug 2-[(2-bromoethyl)-2,4-dinitro-6- [[[2-(phosphonooxy)ethyl]amino]carbonyl]anilino]ethyl methanesulfonate (PR-104). *J. Label. Compd. Radiopharm.* **50,** 7–12 (2007).

113. Jameson, M. B. *et al.* A phase I trial of PR-104, a nitrogen mustard prodrug activated by both hypoxia and aldo-keto reductase 1C3, in patients with solid tumors. *Cancer Chemother. Pharmacol.* **65,** 791–801 (2010).

114. McKeown, S. R., Cowen, R. L. & Williams, K. J. Bioreductive drugs: from concept to clinic. *Clin. Oncol. (R. Coll. Radiol).* **19,** 427–42 (2007).

115. Ashoorzadeh, A. *et al.* The effect of sulfonate leaving groups on the hypoxia-selective toxicity of nitro analogs of the duocarmycins. *Bioorg. Med. Chem.* **19,** 4851–60 (2011).

116. Wolfe, A. L. *et al.* Efficacious cyclic N-acyl O-amino phenol duocarmycin prodrugs. *J. Med. Chem.* **56,** 4104–15 (2013).

117. Brown, J. M. & Wilson, W. R. Exploiting tumour hypoxia in cancer treatment. *Nat. Rev. Cancer* **4,** 437–47 (2004).

118. Brown, J. M. & Giaccia, A. J. The Unique Physiology of Solid Tumors : Opportunities (and Problems) for Cancer Therapy. *Cancer Res.* **58,** 1408–1416 (1998).

119. Rockwell, S., Dobrucki, I. T., Kim, E. Y., Marrison, S. T. & Vu, V. T. Hypoxia and radiation therapy: past history, ongoing research, and future promise. *Curr. Mol. Med.* **9,** 442–458 (2009).

120. Marcu, L. & Olver, I. Tirapazamine: from bench to clinical trials. *Curr. Clin. Pharmacol.* **1,** 71–79 (2006).

121. Odlo, K. *et al.* 1,5-Disubstituted 1,2,3-triazoles as cis-restricted analogues of combretastatin A-4: Synthesis, molecular modeling and evaluation as

cytotoxic agents and inhibitors of tubulin. *Bioorg. Med. Chem.* **16,** 4829–38 (2008).

122. Martins, M. M. *et al.* Linking Tumor Mutations to Drug Responses via a Quantitative Chemical-Genetic Interaction Map. *Cancer Discov.* **5,** 154–167 (2014).

123. Boger, D. L. & Johnson, D. S. CC-1065 and the duocarmycins: unraveling the keys to a new class of naturally derived DNA alkylating agents. *Proc. Natl. Acad. Sci. U. S. A.* **92,** 3642–9 (1995).

124. Yang, S. & Denny, W. a. A new short synthesis of 3-substituted 5-amino-1-(chloromethyl)-1,2-dihydro-3H-benzo[e]indoles (amino-CBIs). *J. Org. Chem.* **67,** 8958–61 (2002).

125. Atwell, G. J., Milbank, J. J., Wilson, W. R., Hogg, A. & Denny, W. a. 5-Amino-1-(chloromethyl)-1,2-dihydro-3H-benz[e]indoles: relationships between structure and cytotoxicity for analogues bearing different DNA minor groove binding subunits. *J. Med. Chem.* **42,** 3400–11 (1999).

126. Jeffrey, S. C. *et al.* Design, synthesis, and in vitro evaluation of dipeptide-based antibody minor groove binder conjugates. *J. Med. Chem.* **48,** 1344–58 (2005).

127. McGovren, J. P., Clark, G. L., Pratt, E. A. & DeKoning, T. F. Preliminary Toxicity Studies with the DNA-binding antibiotic, CC-1065. *J. Antibiot. (Tokyo).* **XXXVII,** 63–70 (1984).

128. Greener, Y., Martis, L. & Indacochea-Redmond, N. Assessment of the toxicity of cyclohexanone administered intravenously to Wistar and Gunn rats. *J. Toxicol. Environ. Health* **10,** 385–96 (1982).

129. Markovic, S. N. *et al.* Phase II trial of KW2189 in patients with advanced malignant melanoma. *Am J Clin Oncol* **25,** 308–312 (2002).

130. Corrigan, P. a, Cicci, T. a, Auten, J. J. & Lowe, D. K. Ado-trastuzumab Emtansine: A HER2-Positive Targeted Antibody-Drug Conjugate. *Ann. Pharmacother.* (2014). doi:10.1177/1060028014545354

131. Beck, A. & Reichert, J. M. Antibody-drug conjugates. *MAbs* **6,** 15–17 (2014).

132. Chari, R. Targeted delivery of chemotherapeutics: tumor-activated prodrug therapy. *Adv. Drug Deliv. Rev.* **31,** 89–104 (1998).

133. Ritter, A. Antibody-Drug Conjugates: Looking Adead to an Emerging Class of Biotherapeutic. *Pharm. Technol.* 42–47 (2012).

134. Chari, R. V. J. Targeted cancer therapy: conferring specificity to cytotoxic drugs. *Acc. Chem. Res.* **41,** 98–107 (2008).

135. Perez, H. L. *et al.* Antibody-drug conjugates: current status and future

directions. *Drug Discov. Today* **19,** 869–881 (2014).

136. Bouchard, H., Viskov, C. & Garcia-Echeverria, C. Antibody-drug conjugates-A new wave of cancer drugs. *Bioorg. Med. Chem. Lett.* **24,** 5357–5363 (2014).

137. Turek, J. J., Leamon, C. P. & Low, P. S. Endocytosis of folate-protein conjugates: ultrastructural localization in KB cells. *J. Cell Sci.* **106 (Pt 1,** 423–30 (1993).

138. Lorusso, P. M. *et al.* Phase I study of folate conjugate EC145 (Vintafolide) in patients with refractory solid tumors. *J. Clin. Oncol.* **30,** 4011–6 (2012).

139. Leamon, C. P. *et al.* Folate targeting enables durable and specific antitumor responses from a therapeutically null tubulysin B analogue. *Cancer Res.* **68,** 9839–44 (2008).

140. Vlahov, I. R. & Leamon, C. P. Engineering folate-drug conjugates to target cancer: from chemistry to clinic. *Bioconjug. Chem.* **23,** 1357–69 (2012).

141. Li, H. & Qian, Z. M. Transferrin/transferrin receptor-mediated drug delivery. *Med. Res. Rev.* **22,** 225–250 (2002).

142. Macedo, M. F. & de Sousa, M. Transferrin and the transferrin receptor: of magic bullets and other concerns. *Inflamm. Allergy Drug Targets* **7,** 41–52 (2008).

143. Reddy, J. a *et al.* Preclinical evaluation of EC145, a folate-vinca alkaloid conjugate. *Cancer Res.* **67,** 4434–42 (2007).

144. Kovtun, Y. V *et al.* Antibody-drug conjugates designed to eradicate tumors with homogeneous and heterogeneous expression of the target antigen. *Cancer Res.* **66,** 3214–21 (2006).

145. Singleton, D. C. *et al.* The nitroreductase prodrug SN 28343 enhances the potency of systemically administered armed oncolytic adenovirus ONYX-411(NTR). *Cancer Gene Ther.* **14,** 953–67 (2007).

146. Senter, P. D. & Sievers, E. L. The discovery and development of brentuximab vedotin for use in relapsed Hodgkin lymphoma and systemic anaplastic large cell lymphoma. *Nat. Biotechnol.* **30,** 631–7 (2012).

147. Doronina, S. O. *et al.* Development of potent monoclonal antibody auristatin conjugates for cancer therapy. *Nat. Biotechnol.* **21,** 778–84 (2003).

148. Lewis Phillips, G. D. *et al.* Targeting HER2-positive breast cancer with trastuzumab-DM1, an antibody-cytotoxic drug conjugate. *Cancer Res.* **68,** 9280–90 (2008).

149. Abu Ajaj, K. *et al.* Comparative evaluation of the biological properties of reducible and acid-sensitive folate prodrugs of a highly potent doxorubicin derivative. *Eur. J. Cancer* **48,** 2054–65 (2012).

150. Mahajan, S. S. *et al.* A fragmenting hybrid approach for targeted delivery of multiple therapeutic agents to the malaria parasite. *ChemMedChem* **6,** 415–9 (2011).

151. Zhou, L. *et al.* Characterization of the two major CYP450 metabolites of ozonide (1,2,4-trioxolane) OZ277. *Bioorg. Med. Chem. Lett.* **18,** 1555–8 (2008).

152. Chen, X., Murawski, A., Patel, K., Crespi, C. L. & Balimane, P. V. A Novel Design of Artificial Membrane for Improving the PAMPA Model. *Pharm. Res.* **25,** 1511–1520 (2008).

Publishing Agreement

It is the policy of the University to encourage the distribution of all theses, dissertations, and manuscripts. Copies of all UCSF theses, dissertations, and manuscripts will be routed to the library via the Graduate Division. The library will make all theses, dissertations, and manuscripts accessible to the public and will preserve these to the best of their abilities, in perpetuity.

I hereby grant permission to the Graduate Division of the University of California, San Francisco to release copies of my thesis, dissertation, or manuscript to the Campus Library to provide access and preservation, in whole or in part, in perpetuity.

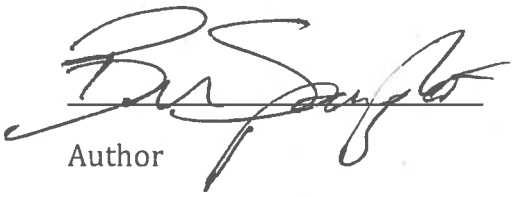

Author

01/14/2016

Signature Date